

Thesis for the degree of Doctor of Engineering

**Research on egg-shaped pressure hulls of
deep manned submersibles**

Jian Zhang

*Department of System Engineering
Graduate School of Engineering
Saitama Institute of Technology
2018*

Abstract

The deep-sea manned submersible plays an important role in oceanic exploration and deep-sea research, which demonstrates the frontier and height of ocean science and technology. The pressure hull is an important device and a buoyancy unit of submersible, which provides a safe living and working space for crews and some non-pressure resisting/non-water repellent equipment. The spherical pressure hull is the most extensively used configuration due to equally distributed stress and deformation. However, it has disadvantages of highly geometrical imperfection sensitivity, irrational hydrodynamics, and inefficient space utilization. In order to overcome these disadvantages, the author puts forward a new geometry, an egg-shaped pressure hull, to take place of the spherical pressure hull. In this case, bionics on egg-shaped pressure hulls and their buckling properties are proposed in this thesis.

Firstly, the buckling of spherical pressure hulls are analytically and numerically explored under various wall thicknesses, imperfection sizes, and material properties. On this basis, A semi-analytical formula to predict the load-carrying capacity of hulls is derived. To validate the numerical approach and obtained buckling performances, ten laboratory scale models are experimentally, analytically, and numerically evaluated. A good agreement (deviation $\leq 7\%$) is obtained between experiment and prediction. In this case, the obtained post buckling mode, the adopted material modelling, and imperfection assumption are confirmed experimentally.

Secondly, bionic egg-shaped pressure hulls are engineered based on biological properties of goose eggs and egg-shaped shell theories. Equivalent spherical pressure hulls are provided as a special case of egg-shaped ones for a like-for-like comparison. It is found that, with respect to hull strength, buoyancy reserve, and space efficiency etc., egg-shaped pressure hulls could be optimally coordinated, which appear to be leading to overall better performance than the spherical pressure hull. Especially, the egg-shaped pressure hull is quite less sensitive to the geometric imperfections, making it more convenient and lower costly to form the hull in manufacturing or to open

holes in applications.

On this basis, the effects of shape index and wall thickness on the buckling egg-shaped pressure hulls are numerically studied, along with two experimentations and non-uniform wall thickness design. It is indicated that the egg-shaped pressure hull is less sensitive to the material plasticity and shape deviation than the spherical one, especially in the case of thick wall. Also, there is a good agreement (deviation < 6%) between experiment and prediction of egg-shaped experimental models. Furthermore, the equivalent comparison between equivalent egg-shaped pressure hulls with non-uniform and uniform wall thicknesses is carried out. It is suggested that the load-carrying capacity of egg-shaped pressure hulls is significantly improved when the non-uniform wall thickness is implemented.

Finally, the buckling of spherical caps under various heights, geometrical imperfections, and wall-thickness reductions are numerically and experimentally studied. A good agreement (deviation < 9%) is obtained between simulation and experiment. The spherical cap with the height-to-span ratio of about 0.274 is an optimal configuration, and it can be applied as a manhole cover for manned cabins in deep-sea vehicles. The first linear buckling mode is the worst imperfection form. Both Wagner's and Evkin's formulae appear to yield the optimal performance in cases of both full and partial thickness reduction, which are much less conservative than the formula developed by NASA.

Contents

Chapter 1 Introduction	1
1.1 Background and significance	1
1.2 Overview of research status	3
1.2.1 Externally pressurized spherical shells.....	3
1.2.2 Externally pressurized untypical shells	3
1.2.3 Externally pressurized domed heads	4
1.2.4 Shell buckling research approaches.....	5
1.3 Problems and innovations	6
1.4 Structure of the thesis	9
References	11
Chapter 2 Buckling of deep sea spherical pressure hulls.....	17
2.1 Buckling analysis of geometrically perfect and imperfect hulls	18
2.1.1 Geometry and material	18
2.1.2 Buckling of geometrically perfect hulls	20
2.1.3 Buckling of geometrically imperfect hulls	24
2.2 Effect of yield strength on the buckling of hulls.....	26
2.2.1 Perfect geometry analysis.....	27
2.2.2 Imperfect geometry analysis.....	28
2.3 Experimental methodology of spherical shells	34
2.3.1 Shell manufacturing and testing	34
2.3.2 Material properties.....	39
2.4 Buckling analysis of spherical shells	40
2.4.1. Experimental and analytical results.....	40
2.4.2. Comparison between experimental and numerical results	43
2.4.3. Effect of constitutive models.....	46
2.4.4. Effect of geometrical imperfections	47
2.5 Summary	50
References	52
Chapter 3 Bionic design of egg-shape pressure hulls	55
3.1 Geometric properties of goose eggshells	56

3.2 Load carrying capacities of goose eggshells	65
3.3 Configuration and size egg-shaped pressure hulls	77
3.4 Wall thickness and buoyancy factor of egg-shaped and spherical pressure hulls	80
3.4.1 Strength and stability of egg-shaped pressure hull	80
3.4.2 Uniform wall thickness analysis of egg-shaped pressure hulls	81
3.4.3 Non-uniform wall thickness analysis of egg-shaped pressure hulls	83
3.5 Analytical results of egg-shaped and spherical pressure hulls	86
3.6 Numerical results of egg-shaped and spherical pressure hulls	89
3.7 Evaluation and comparison of main properties for pressure hulls	97
3.8 Summary	98
References	99
Chapter 4 Effect of geometrical parameters on buckling of egg-shaped pressure hulls	103
4.1 Effect of shape index on buckling of egg-shaped pressure hulls	104
4.1.1 Geometry of egg-shaped pressure hulls	104
4.1.2. Capacity and mass of egg-shaped pressure hull	106
4.1.3 Numerical modeling of egg-shaped pressure hulls	107
4.1.4. Linear buckling of egg-shaped pressure hulls	108
4.1.5. Nonlinear buckling of egg-shaped pressure hulls	110
4.2 Effect of wall thickness on buckling of egg-shaped pressure hulls	114
4.2.1 Buckling of geometrically perfect egg-shaped pressure hulls	114
4.2.2 Buckling of geometrically imperfect egg-shaped pressure hulls	117
4.2.3 Comparison between egg-shaped and spherical pressure hulls	120
4.3 Buckling of CNC-machined egg-shaped shells under uniform external pressure	123
4.3.1 Experimental buckling of CNC-machined egg-shaped shells	123
4.3.2 Numerical buckling of CNC-machined egg-shaped shells	128
4.4 Buckling of rapid prototyping egg-shaped shells under uniform external pressure	131
4.4.1 Experimental buckling of rapid prototyping egg-shaped shells	132
4.4.2 Numerical buckling of rapid prototyping egg-shaped shells	139
4.4.3 Effects of imperfection shape and size on buckling of egg-shaped shells	141

4.5 Summary	142
References	144
Chapter 5 Enhancement of egg-shaped pressure hulls using non-uniform wall thickness.....	147
5.1 Design and fabrication of egg-shaped pressure hulls.....	147
5.1.1 Geometrical design	147
5.1.2 Sample fabrication.....	149
5.2 Measurement and test.....	150
5.2.1 Shape scanning of samples	150
5.2.2 Hydrostatic test of samples.....	152
5.2.3 Tensile tests of material.....	156
5.3 Experimental analysis of egg-shaped pressure hulls.....	156
5.4 Numerical analysis of egg-shaped pressure hulls	158
5.5 Summary	162
References	163
Chapter 6 Spherical closures on access holes of pressure hulls.....	167
6.1 Spherical caps under various heights	168
6.1.1 Geometry and fabrication	169
6.1.2 Pretest measurement.....	169
6.1.3 Hydrostatic pressure test.....	171
6.1.4 Parent material properties.....	172
6.1.5 Experimental analysis of spherical caps.....	173
6.1.6 Numerical analysis of spherical caps.....	174
6.1.7 Buckling of spherical caps of various heights.....	177
6.2 Buckling of spherical caps under various imperfections	180
6.2.1 Geometry and imperfections	180
6.2.2 Finite element model	182
6.2.3 Numerical analysis of imperfect spherical caps	184
6.2.4 Experimentation of imperfect spherical caps	186
6.3 Buckling of spherical caps under various thickness reductions.....	193
6.3.1 Design and fabrication.....	193
6.3.2 Geometric measurement.....	195

6.3.3 Mechanical testing	197
6.3.4 Full thickness reduction analysis of spherical caps	200
6.3.5 Partial thickness reduction analysis of spherical caps	203
6.3.6 Numerical analysis of the tested caps	207
6.4 Summary	209
References	212
Chapter 7 Conclusions and future work.....	217
7.1 Conclusions	217
7.2 Future works.....	219
Publications associated with the thesis	221
Acknowledgements.....	223

Nomenclature

A : surface area

B : minor axis

d : nominal base diameter of caps

D : nominal diameter of plate

D_g : mean diameter of goose egg

E : Young modulus

$F_{net\ buoyant}$: net buoyancy

g : gravitational acceleration

K : safety factor

K_d : deviation factor

k_{imp} : imperfection reduction factor

k_p : plasticity reduction factor

L : major axis

m : mass

p_0 : initial uniform external pressure

p_{e-p} : buckling load obtained from geometrically and materially nonlinear analysis

p_{fy} : first yield pressure obtained from geometrically and materially nonlinear analysis

p_{fy1} : first yield pressure obtained from analytical analysis

p_{lin} : buckling load obtained from linear elastic buckling analysis

p_{m-t} : buckling load obtained from medium-thick-walled equation

p_t : buckling load obtained from the thin-walled equation

p_{test} : experimental buckling load

P_s : design load

P_{s1} : yielding load of egg-shaped pressure hull with uniform thickness

P_{s2} : yielding load of egg-shaped pressure hull with non-uniform thickness

P_{s3} : yielding load of spherical pressure hull

P_q : critical elastic buckling load

P_{q1} : critical elastic buckling load of egg-shaped pressure hull with uniform thickness

P_{q2} : critical elastic buckling load of egg-shaped pressure hull with non-uniform thickness
 P_{q3} : critical elastic buckling load of spherical pressure hull
 r : median radius of spherical pressure hull
 r_{in} : internal radius of spherical pressure hull
 r_m : mean radius of spherical pressure hull
 $R_1(x)$: meridional radius of curvature of egg-shaped pressure hull
 $R_2(x)$: circumferential radius of curvature of egg-shaped pressure hull
 R_m : middle radius of spherical pressure hull
 R_i : internal radius of spherical pressure hull
 \overline{R}_1 : meridional mean radius of curvature of egg-shaped pressure hull
 \overline{R}_2 : circumferential mean radius of curvature of egg-shaped pressure hull
 S_1 : meridional area of egg-shaped pressure hull
 S_2 : circumferential area of egg-shaped pressure hull
 t : wall thickness
 \bar{t} : mean thickness of egg-shaped pressure hull with non-uniform thickness
 t_0 : thickness normalization function of egg-shaped pressure hull with non-uniform thickness
 t_1 : thickness of egg-shaped pressure hull with uniform thickness
 $t_2(x)$: thickness function of egg-shaped pressure hull with non-uniform thickness
 t_3 : thickness of spherical pressure hull
 T : nominal wall thickness of plate
 T_2 : maximum thickness of egg-shaped pressure hull with non-uniform thickness
 U_x : x -direction displacement
 U_y : y -direction displacement
 U_z : z -direction displacement
 U_{max} : the maximum deflection
 V : volume of goose egg
 V_0 : water displacement volume of egg-shaped pressure hull
 V_{s0} : water displacement volume of spherical pressure hull
 V_1 : material volume of egg-shaped pressure hull with uniform thickness

V_2 : material volume of egg-shaped pressure hull with non-uniform thickness

V_3 : material volume of spherical pressure hull

w : radial deviation of imperfection

x : distance between a point on the egg-shaped curve and the sharp end

α : angle corresponding to the meridional extent of imperfection

δ : imperfection size of spherical pressure hulls

Δ : imperfection size of egg-shaped pressure hulls

δ_1 : buoyancy factor of egg-shaped pressure hull with uniform thickness

δ_2 : buoyancy factor of egg-shaped pressure hull with non-uniform thickness

δ_3 : buoyancy factor of spherical pressure hull

ε : strain

ε_φ : meridional strain

ε_θ : circumferential strain

λ : geometry parameter of cap

θ : the meridional position of imperfect centre axis

μ : Poisson ratio

ρ : mass density

ρ_w : seawater density

ρ_T : material density

ρ_{water} : water density

ρ_{steel} : steel density

σ : stress

σ_φ : meridional stress

σ_θ : circumferential stress

σ_y : yield strength

σ_t : tensile strength

$\sigma_{r4(x)}$: von Mises equivalent stress

$[\sigma]$: allowable stress

Chapter 1 Introduction

1.1 Background and significance

Ocean takes up approximately 2/3 of the Earth's surface. The average depth of ocean ranges from 4 – 5 km and the largest depth is about 11.52 km. Consequently, deep seas have generated considerable interest for centuries [1-2]. Details of human dive into oceans can be found in [3-5]. In 21st century, deep sea exploration and development are also important for the purpose of energy, research, and military. During this process, both manned and unmanned submersibles act as an important role [6-9]. Although unmanned submersibles have some advantages, manned submersibles are the first choice due to the in-situ operation and direct experience [7-10]. Therefore, the deep-sea manned submersible plays a key role in oceanic exploration and deep-sea research, which also demonstrates the frontier and height of ocean science and technology. Typical submersibles are Chinese JIAO LONG, Japanese SHIKAI, French NAUTILE, and Russian MIR [11].

As one of the most critical components and buoyancy units in a deep manned submersible system, the pressure hull provides a safe living and working space for crews and some non-pressure resisting/non-water repellent equipment. The weight of the manned pressure hull accounts for almost 1/3 of the total weight of a submersible. Therefore, the pressure hull should be designed to optimally coordinate safety, buoyancy reserve, space efficiency etc [12-18]. A typical pressure hull is a closed medium-thick shell of revolution under uniform external pressure, which is prone to nonlinear buckling. The buckling properties are greatly influenced by geometrical configuration, wall thickness, material properties, and inevitable initial geometrical imperfections [19-25].

As is well known, due to its efficiency to bear the external high hydrostatic pressure in deep sea, spherical pressure hull is the most extensively used configuration for the deep manned submersible, where the stress and deformation are equally distributed throughout when the pressure hull is subjected to high hydrostatic

pressure in deep sea. In brief, the spherical pressure hull has advantages of good mechanical properties, low buoyancy factor and efficient material utilization. However, the spherical pressure hull is meanwhile with difficult interior arrangement, and especially it is a highly imperfection-sensitive structure. Any small changes in geometry such as a tiny imperfection may lead to a significant drop of the buckling load [26-29]. These limitations have prevented to some extent from making a breakthrough on design for the better overall performance of a pressure hull of deep manned submersible.

Eggshell is a closed shell of revolution, with multifocal surfaces of positive Gaussian curvature. It has advantages of amazing weight-to-strength ratio, proper span-to-thickness ratio, rational streamline, satisfactory aesthetics and reasonable material distribution. Eggshell can withstand extremely high loads by membrane action when subjected to uniform pressures, for the material is used to its full strength [30-35]. For example, the eggshell provides the egg with an external support using the dome principle to obtain enough strength and stability, with economy in building material and without requirement of ribs. Likewise, the pressure hull is also a closed shell structure subjected to hydrostatic pressure, requiring excellent characteristics such as safety, material economy, inner space and hydrodynamics. Obviously the eggshell could provide effective biological information for the design of the pressure hull with unconventional geometry.

Therefore, this thesis is mainly devoted to bionics on egg-shaped pressure hulls of deep manned submersibles, along with traditional spherical pressure hulls and spherical caps used to close the inevitable hole of pressure hulls. The proposed egg-shaped configuration will play an important role in developing an original deep sea pressure hull, which may optimally coordinate safety, buoyancy reserve, space efficiency of deep manned submersible. The involved buckling exploration will make a potential contribution to the progress of instability theories of untypical shells of revolution.

1.2 Overview of research status

In order to achieve above research objectives, this section carries out a general overview of corresponding literatures with regard to externally pressurized spherical shells, untypical shells, and domed head, along with shell buckling research approaches. Details of overview are in following subsections.

1.2.1 Externally pressurized spherical shells

Buckling of spherical shells under uniform external pressure has always been an interesting problem in structural mechanics. Early in 1915, Zoelly first proposed a formula to evaluate the critical buckling load of a thin-walled spherical shell subjected to uniform external pressure [36]. For decades, this evaluation was found to be much higher than the experimental results due to geometrical imperfections and material properties. Later, in 1945, Koiter made a breakthrough to the buckling of spherical shells by putting forward the initial post-buckling theory for elastic systems subjected to conservative loading, and investigating the imperfection sensitivity of the buckling of shells [37]. Furthermore, Pan et al. experimentally and numerically explored the critical buckling load of spherical pressure hulls used in deep manned submersibles. According to the results obtained from nonlinear finite element analysis with equivalent geometrical imperfection included, they proposed a phenomenological model to predict the ultimate strength of spherical pressure hulls [38, 39]. In addition, Blachut et al. performed a series of experimental and numerical studies regarding elastic-plastic buckling of medium-thick shells of revolution with positive Gaussian curvature, including spherical shells considered as a special case, under external pressure. They found that both geometrical imperfections and material plasticity could lead to a severe decrease in the load carrying capacity of shells [40-45].

1.2.2 Externally pressurized untypical shells

An effective means for increasing the load carrying capacity of shells is the incorporation of a shell of revolution that has a positive Gaussian curvature. The barreled shell is an apt example that combines the advantages of spherical and cylindrical shells. It is a cylindrical shell that has a meridional curvature. The

buckling properties of barreled shells have been investigated in recent years. Jasion and Magnuki, for instance, proposed a set of barreled shells with the Cassini oval [46], clothoidal-spherical [47], and circular arc meridians [48]. They provided buckling results for these shells that were obtained using analytical or numerical methods. Furthermore, Blachut detailed the results of the numerical and experimental study into the buckling behavior of barreled shells that have meridians in the form of circular arcs [49] and generalized ellipses [50]. Close agreement between the numerical predictions and the experimental data was obtained. However, as we know, due to the manufacturing difficulties in welding and machining these novel shaped metal body made of either HY steel, or titanium alloy, or aluminium alloy, and required with very high accuracy standard, these novel structural geometries have not been extensively applied, and most of these investigations and designs were theoretical research, or say, mostly just on “paper work” stage [51-52]. With the rapid development of new manufacturing techniques such rapid prototype, it may provide a big space to improve the optimization of design for pressure hull, including geometry design.

1.2.3 Externally pressurized domed heads

Studies have extensively focused on the buckling of domed caps of various shapes. For example, Blachut et al. numerically and experimentally investigated the buckling of hemispherical [53, 54], torispherical [55,56], toriconical [57], and ellipsoidal [58] caps under external pressure along with the effects of initial geometrical imperfections on buckling [59]. The shapes of mass-equivalent generalized ellipsoidal domes were optimized by defining the exponents of the ellipsoidal equation as design variables to obtain the maximum buckling load [60]. More recently, Zhang et al. studied bionic designs for egg-shaped shells and their applications in ocean engineering [61, 62]. They proposed a prolate egg-shaped dome to optimally trade-off the work safety and service performance of submarines [63]; their experimental and numerical results suggest that this dome affords good load-carrying capacity and eliminates the need for complicated ring-stiffened prolate structures [64].

Meanwhile, the buckling performances of various dome forms with other geometrical imperfections under uniform external pressure have also attracted

considerable research attention. For example, Blachut and Galletly explored the effects of amplitude and the meridional extent of the local inward dimple imperfection (LIDI) on buckling pressure for spherical domes [53]. Furthermore, Blachut systematically investigated the effects of LIDI, increased-radius imperfection (IRI) and force-induced dimple imperfections (FIDI) on the buckling performance of hemispherical domes [59]. Additionally, the formulae most widely used to predict the buckling pressures of spherical caps include Zoelly's analytical linear buckling formula [60], NASA's classical knockdown factor formula [65], Alexander's empirical formula [66], and Wagner's new knockdown factor formula [67].

1.2.4 Shell buckling research approaches

The manned pressure hull is a shell structure with closed space. One of the limit states considered during its design process is the loss of stability, which generates considerable recent interest. There are mainly three ways to tackle this problem: analytical formulations, numerical simulations and experimental investigations. Analytical solutions have the advantage to use abacuses and simple formula to give the global and local buckling load of shell. However, this method is not appropriate for shells with complex shapes, boundary conditions and loadings. And it is difficult to analyze imperfect shells considering geometrical and material nonlinearity [68, 69]. As a result, analytical approaches always lead to apparent discrepancies between theoretical and experimental results. Numerical simulations are then commonly accepted to undertake buckling analyses of shell structures, for which reliable analytical solutions are not available in current literature. The realistic buckling resistance of a shell structure with imperfections can be determined by both geometry and material nonlinear analysis (GMNIA) [70]. Finally, experimental investigations are straightforward ways to perform buckling analysis for shell structures. However, it is impossible to directly investigate buckling behavior of a shell structure by experiments during the early design stage. Moreover, experimental investigations are time consuming and require high cost and complex equipment. Consequently, the use of numerical simulations is widely considered as a replacement of experimental investigations, although some complex physical problems can be only solved by

combination of experimental and numerical activities [71].

1.3 Problems and innovations

According to above literature review, the existing problems in regard to deep pressure hulls can be concluded as follows:

Problem 1: Although the effects of geometrical imperfections and material properties on the buckling of spherical shells were demonstrated in previous studies, little attention has been paid on the establishment of a mechanism model to predict the load-carrying capacity of deep sea spherical pressure hulls at the preliminary design stage or being used in the classification society rules, considering the sensitivities of shape deviations and material plasticity simultaneously to the buckling.

Problem 2: The spherical pressure hull has disadvantages of difficult interior arrangement or low space efficiency, and is highly sensitive to geometrical imperfections. Most importantly, various holes must be opened and numerous components need to be installed on the pressure hulls. Such requirements considerably destroy the symmetry of spherical configuration. Therefore, it is even necessary to put forward an untypical configuration, which can overcome the disadvantages of spherical configuration.

Problem 3: Although many investigators focused on non-spherical or untypical shells of revolution with positive Gaussian curvature, but most of these investigations and designs were mostly just on “paper work” stage neglecting effect of geometrical parameters. Furthermore, all of these investigations have been considered with uniform wall thickness, and less attention has been paid to the enhancement of shells of revolution using non-uniform wall thickness.

Problem 4: Although the properties buckling of several untypical caps have been widely demonstrated, little is known about the buckling of an externally pressurized spherical cap resembling a circular arc, which is an attractive configuration. Further, few experimental studies of domes have examined the influence of various configurations of imperfections on the buckling, and little attention has been paid on the buckling of domed caps with wall-thickness reduction, particularly to the case of

partial thickness reduction.

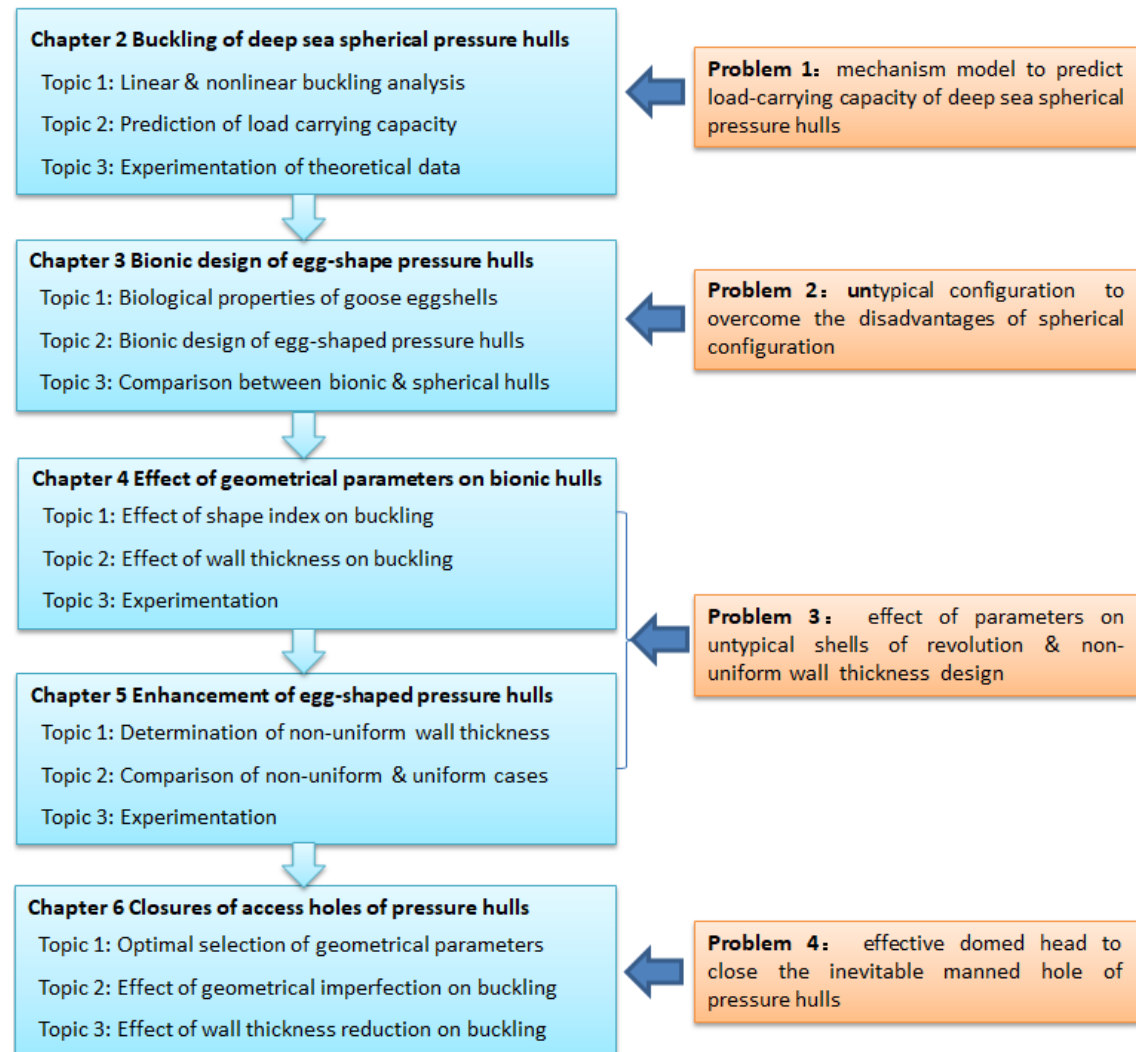


Fig.1-1 Research map of the thesis

In order to tackle above problems, this thesis is dedicated to bionics on egg-shaped pressure hulls of deep manned submersibles, along with traditional spherical pressure hulls and spherical caps used to close the inevitable hole of pressure hulls. The research map is shown in Fig.1-1. Firstly, an analytical, numerical, and experimental study into the buckling of spherical pressure hulls is carried out under different wall thicknesses, material properties, and imperfection amplitude. A mechanism formula to predict the load-carrying capacity of spherical pressure hulls is derived semi-analytically. Secondly, a bionic study into egg-shaped pressure hulls is

performed based on the biological properties of goose eggs. A like-for-like comparison is made between spherical and egg-shaped hulls as well. Thirdly, the effects of geometric shape and wall thickness on the linear and nonlinear buckling of pressure hulls are deeply explored, along with corresponding experimentation. Subsequently, an equivalent comparison between the buckling of mass equivalent egg-shaped pressure hulls with non-uniform and uniform wall thicknesses is conducted under uniform external pressure. Finally, the buckling of spherical laboratory-scale caps under various heights, geometrical imperfections, and wall-thickness reductions are numerically and experimentally studied.

Through above research, the following innovations can be obtained:

(1) A mechanism formula to predict the load-carrying capacity of spherical pressure hulls is derived semi-analytically, which includes analytical buckling equation of medium-thick externally pressurized spherical shell, plasticity reduction factor, and geometrical imperfection reduction factor. Such formula extends the previous phenomenological model and could be used to evaluate the load-carrying capacity of deep sea spherical pressure hulls at preliminary design stage.

(2) A new geometry, an egg-shaped pressure hull, is put forward to replace the spherical configuration. It is found that, with respect to hull strength, buoyancy reserve, and space efficiency etc., egg-shaped pressure hulls could be optimally coordinated, which appear to be leading to overall better performance than the spherical pressure hull. Especially, the egg-shaped pressure hull is quite less sensitive to the geometric imperfections, making it more convenient and low costly to form the hull in manufacturing or to open holes in applications.

(3) Both linear and nonlinear buckling of medium-thick untypical egg-shaped shells subjected to uniform external pressure are analytically, numerically, and experimentally explored, along with the effect of geometrical shape, wall thickness, and initial geometrical imperfections. It is hoped that this work could promote an upsurge on the buckling of medium-thick untypical shells of revolution under external pressure and motivate further studies into the effect of other imperfections and materials on the buckling.

(4) An optimal configuration of spherical cap with the height-to-span ratio of about 0.274 is determined, which can be applied as an end-closure for cylindrical pressure hulls or as a manhole cover for manned cabins in deep-sea vehicles. Based on such configuration, the effects of geometrical imperfection shape, full and partial wall thickness reduction on the buckling are explored, which will instigate a resurgence of interest on the buckling of imperfect or corroded shells.

1.4 Structure of the thesis

The structure of this thesis is as follows:

Chapter 1 mainly presents background and significance of research topics, overview of current research status, existing problems and research innovations, and structures of the thesis.

Chapter 2 focuses on the buckling of spherical pressure hulls subjected to uniform external pressure under different wall thicknesses, material properties, and imperfection amplitude, as well as buckling of ten laboratory scale spherical models for experimentation. The linear and nonlinear buckling of geometrically perfect hulls are examined numerically and verified analytically in linear range. The nonlinear buckling of hulls with eigenmode geometrical imperfections are evaluated numerically using the modified Riks method. Also, the geometry, wall thickness, buckling load, and final collapsed mode of each spherical shell are measured, as well as the material properties of the corresponding sheet. The buckling behaviors of these shells are demonstrated analytically and numerically according to experimental data. The research can provide a reference and comparison model for the bionics on egg-shaped pressure hulls. Also, the obtained nonlinear buckling analyzing and testing approaches can form a foundation for an analytical, numerical, and experimental study into buckling of bionic pressure hulls.

Chapter 3 is devoted to the bionic design of egg-shaped pressure hulls in order to overcome spherical limitations, as well as comparison between egg-shaped and spherical configurations. Firstly, the geometric properties of goose eggs are measured to obtain the best shape function as well as the shape index range. The geometric

result can provide a reference for the bionic design of egg-shaped shells and pressure hulls. Then, the load-carrying capacities of five goose eggshells are explored experimentally and numerically, which indicates that eggshell is a good bionic prototype for shells of revolution subjected to uniform external pressure. On these basis, the configuration and size of egg-shaped pressure are determined. Using linear elastic strength and stability formulae, the wall thickness of egg-shaped pressure are determined analytically. In this way, two egg-shaped pressure hulls respectively with uniform and non-uniform thickness are proposed, along with the buckling properties. Meanwhile, the equivalent spherical pressure hull is evaluated for comparison.

Chapter 4 evaluates the effect of wall thickness and geometrical shape on the linear and nonlinear buckling of pressure hulls. On the one hand, a family of egg-shaped pressure hulls with constant capacity and mass are evaluated under various shape indices. According to the experimental results, eight shape indices in the 0.65 to 0.72 range are selected for creating the egg-shaped pressure hull. Besides, to extend the shape index range, six pressure hulls with shape indices of 0.4, 0.5, 0.6, 0.8, 0.9 and 1.0 are also proposed. On the other hand, a range of egg-shaped pressure hulls in the case of uniform wall thickness varying from 10-80 mm with 5 mm increment are assessed, along with three equivalent spherical ones for a comparison. Nonlinear material properties and geometrical imperfections sensitivities are considered in both cases. In addition, a numerical and experimental study into the buckling performances of three CNC-machined stainless egg-shaped shells and nine rapid prototyping ones is performed to validate the adopted analyzing approach.

Chapter 5 is dedicated to egg-shaped pressure hulls with non-uniform wall thickness. An equivalent comparison between the buckling of mass equivalent egg-shaped pressure hulls with non-uniform and uniform wall thicknesses is conducted under uniform external pressure. First, a pair of resin egg-shaped pressure hulls with non-uniform and uniform wall thicknesses are designed and fabricated using rapid prototyping. Subsequently, the geometrical and buckling performance of the shells and the parent material properties of the shells are experimentally studied. Finally, the nonlinear elastic buckling performances of fabricated shells with

measured imperfections and perfect shells with first eigenmode imperfections are numerically explored using the arc length method. The results reveal that the load-carrying capacity of egg-shaped pressure hulls is significantly improved when the shells have non-uniform thickness.

Chapter 6 evaluates the buckling of spherical caps under various heights, geometric imperfections, and wall-thickness reductions. Firstly, the buckling of stainless steel spherical caps under uniform external pressure is analyzed. Caps with a circular arc meridian have a nominal base diameter of 146 mm and various heights. Then, the buckling of spherical caps with four different geometric imperfections are examined, including local inward dimple, increased-radius, force-induced dimple, and linear buckling mode. Finally, the buckling of spherical caps fabricated under different conditions of wall-thickness reduction is investigated. The effects of site, magnitude, and range of the thickness reduction on the buckling properties are evaluated experimentally, analytically, and numerically.

Chapter 7 contains main conclusions and provides future works.

References

- [1] W.C. Cui. Development of the jiaolong deep manned submersible, *Mar Technol Soc J.* 47 (2013) 37-54.
- [2] C.T.F. Ross, A conceptual design of an underwater vehicle, *Ocean Eng.* 33 (2006) 2087-2104.
- [3] W.Forman. From Beebe and Barton to Piccard and Trieste, *Mar Technol Soc J.* 43 (2009) 27-36.
- [4] W. Kohnen. Human exploration of the deep seas: fifty years and the inspiration continues, *Mar Technol Soc J.* 43 (2009) 42-62.
- [5] A. Sagalevitch. From the bathyscaph trieste to the submersibles mir, *Mar Technol Soc J.* 43 (2009) 79-86.
- [6] H. Momma. Deep ocean technology at JAMSTEC, *Mar Technol Soc J.* 33(1999) 49-64.
- [7] Committee on Future Needs in Deep Submergence Science. 2004. *Future Needs in Deep Submergence Science: Occupied and Unoccupied Vehicles in Basic Ocean Research*, National Research Council, ISBN: 0-309-52917-4, 152 pages, The National Academies Press. This PDF is available from the National Academies Press at: <http://www.nap.edu/catalog/10854.html>.

- [8] Committee on Evolution of the National Oceanographic Research Fleet. 2009. Science at Sea: Meeting Future Oceanographic Goals with a Robust Academic Research Fleet, National Research Council, ISBN: 0-309-14558-9, 120 pages, The National Academies Press. This free PDF was downloaded from <http://www.nap.edu/catalog/12775.html>.
- [9] J.P. Barry & J. Hashimoto. Revisiting the challenger deep using the ROV kaiko, Mar Technol Soc J. 43 (2009) 77-8.
- [10] P.A. Rona. Deep diving manned research submersibles, Mar Technol Soc J. 33 (2000) 13-25.
- [11] W. Kohnen. Review of deep ocean manned submersible activity in 2013. Mar Technol Soc J. 47 (2013) 56-68.
- [12] L. Ma. Conceptual design of 1000-meter light operating manned submersible. Harbin: Harbin Engineering University. (2012).
- [13] J.R. MacKay. Department of precision and microsystems engineering on lightweight design of submarine pressure hulls. Delft: Delft University of Technology. (2012).
- [14] T. Reynolds, O. Lomacky & M. Krenzke. Design and analysis of small submersible pressure hulls, Computers and Structures. 3 (1973) 1125-1143.
- [15] J. Blachut & Smith. P. Buckling of multisegment underwater pressure hull, Ocean Engineering, 35 (2008) 247-260.
- [16] B.B. Pan, W.C. Cui. A comparison of different rules for the spherical pressure hull of deep manned submersibles, Journal Ship Mechanics. 15 (2011) 276-285.
- [17] J. Blachut. Developments in strength and stability of shell components used in submersibles, Shell Struct Theory Appl 2 (2010).
- [18] K.R. Yamamoto. 5.2 construction technology of deep sea research boat: development of 'deep sea 6500'. Techno Marine. 885 (2005) 389-392.
- [19] A Zingoni. Liquid-containment shells of revolution: A review of recent studies on strength, stability and dynamics, Thin-Walled Struct 87 (2015) 102-114.
- [20] S. Knoche, J. Kierfeld. Buckling of spherical capsules, Phys. Rev. E - Stat. Nonlinear, Soft Matter Phys. 84 (2011).
- [21] J. Blachut, K. Magnucki. Strength, Stability, and Optimization of Pressure Vessels: Review of Selected Problems, Appl. Mech. Rev. 61 (2008) 1517-1526.
- [22] S.S. Datta, S.H. Kim, J. Paulose, A. Abbaspourrad, D.R. Nelson, D.A. Weitz. Delayed buckling and guided folding of inhomogeneous capsules, Phys. Rev. Lett. 109 (2012).
- [23] B.B. Pan, W.C. Cui. An overview of buckling and ultimate strength of spherical pressure hull under external pressure, Mar. Struct. 23 (2010) 227-240.
- [24] J. Blachut. Experimental perspective on the buckling of pressure vessel components. Appl Mech Rev 66 (2013) 11003.
- [25] O. Ifayefunmi, J. Blachut. Imperfection sensitivity: a review of buckling behaviour of cones, cylinders and domes. J Press Vessel Technol 140 (2018) 1-8.

- [26] AC. Morandi. Computer aided reliability based design of ring-stiffened cylindrical shells under external pressure. University of Glasgow. (1994).
- [27] SI. Wong. On lightweight design of submarine pressure hulls. Delft University of Technology. (2012).
- [28] Z.L. Wang, R.H. Wang, M.H. Yu, L.B. Li. The influence of the initial imperfections on the ultimate strength of manned deep-sea submersible pressure sphere hull. Shipbuilding of China. 2 (2007) 45-50 [in Chinese].
- [29] B. Lu, T. Liu, W.C. Cui. Ultimate strength of pressure spherical hull in deep-sea manned submersibles. Journal of Ship Mechanics. 8 (2004) 51-8 [in Chinese].
- [30] DV. Babich. Stability of shells of revolution with multifocal surfaces. International Applied Mechanics. 29 (1993) 935-8.
- [31] HT. Wong. Behaviour and modeling of steel-concrete composite shell roofs. The Hong Kong Polytechnic University. (2005).
- [32] B. Prabu. Investigations on the effects of general initial imperfections on the buckling of thin cylindrical shells under uniform axial compression. Pondicherry Engineering College. (2007).
- [33] F. Cheng, S. Sha. An introduction to bridge design based on bionics. In: Proceedings of the 24th Southern African Transport Conference (SATC 2005). 2005 July 11-13. (2005) 951-8.
- [34] A. Ar, H. Rahn, CV. Paganelli. The avian egg: mass and strength. Condor. 81 (1979) 331-337.
- [35] P. Woelke. Computational model for elasto-plastic and damage analysis of plates and shells. Louisiana state university and agricultural and mechanical college. (2005).
- [36] R. Zoelly. Über ein Knickungs problem an der Kugelschale (Thesis). Zürich. (1915).
- [37] WT. Koiter. Over de stabiliteit van het elastisch evenwicht. Mech Marit Mater Eng. (1945).
- [38] B.B. Pan, W.C. Cui, YS Shen. Experimental verification of the new ultimate strength equation of spherical pressure hulls, Mar Struct. 29 (2012) 169-176.
- [39] B.B. Pan, W.C. Cui, YS Shen, T Liu. Further study on the ultimate strength analysis of spherical pressure hulls. Mar Struct. 23 (2010) 444-461.
- [40] J. Blachut. Buckling of externally pressurized steel toriconical shells. Int J Pres Ves Pip. 144 (2016) 25-34.
- [41] J. Blachut. Locally flattened or dented domes under external pressure. Thin-Walled Struct. 97 (2015) 44-52.
- [42] J. Blachut. Buckling of multilayered metal domes. Thin-Walled Struct. 47 (2009) 1429-1438.
- [43] J. Blachut, K. Magnucki. Strength, Stability, and Optimization of Pressure Vessels: Review of Selected Problems. Appl Mech Rev. 61 (2008) 1517-1526.
- [44] J. Blachut, P. Smith. Buckling of multi-segment underwater pressure hull. Ocean Eng. 35 (2008) 247-260.

- [45] J. Blachut. Buckling of externally pressurised barrelled shells: a comparison of experiment and theory. *Int J Press Vessel Pip.* 79 (2002) 507-517.
- [46] P. Jasion, K. Magnucki. Elastic buckling of cassini ovaloidal shells under external pressure – theoretical study. *Archives of Mechanics* 67 (2005) 179-192.
- [47] P. Jasion, K. Magnucki. Elastic buckling of clothoidal-spherical shells under external pressure – theoretical study. *Thin-Walled Structures* 86 (2015) 18-23.
- [48] P. Jasion, K. Magnucki. Elastic buckling of barreled shell under external pressure. *Thin-Walled Structures*. 45 (2007) 393-399.
- [49] J. Blachut. Buckling of externally pressurized barreled shells: a comparison of experimental and theory. *International Journal of Pressure Vessels and Piping*. 79 (2002) 507-517.
- [50] J. Blachut. Optimal barreling of steel shells via simulated annealing algorithm. *Computers and Structures*. 81 (2003) 1941-1956.
- [51] J. Blachut. Buckling and first ply failure of composite toroidal pressure hull. *Computers and Structures*. 82 (2004) 1981-1992.
- [52] P. Gou, W.C. Cui. Study of structural optimization problem for multiple intersecting spherical pressure hulls. *Journal of Ship Mechanics*. 13 (2009);:269-277.
- [53] J. Blachut, G.D. Galletly. Buckling strength of imperfect steel hemispheres, *Thin-Walled Struct.* 23 (1995) 1-20.
- [54] J. Blachut. Buckling of multilayered metal domes, *Thin-Walled Struct.* 47 (2009) 1429-1438.
- [55] J. Blachut, G.D. GALLETLY, D.N. MORETON. Buckling of near-perfect steel torispherical and hemispherical shells subjected to external pressure, *AIAA J.* 28 (1990) 1971-1975.
- [56] J. Blachut. Buckling of composite domes with localised imperfections and subjected to external pressure, *Compos. Struct.* 153 (2016) 746-754.
- [57] J. Blachut. Buckling of externally pressurized steel toriconical shells, *Int. J. Press. Vessel. Pip.* 144 (2016) 25-34.
- [58] P. Smith, J. Blachut. Buckling of externally pressurized prolate ellipsoidal domes, *J Press Vessel Technol.* 130 (2008) 11210.
- [59] J. Blachut. Locally flattened or dented domes under external pressure, *Thin-Walled Struct.* 97 (2015) 44-52.
- [60] J. Blachut, P. Smith. Tabu search optimization of externally pressurized barrels and domes, *Eng. Optim.* 39 (2007) 889-918.
- [61] J. Zhang, M. Wang, W. Wang, W. Tang. Buckling of egg-shaped shells subjected to external pressure, *Thin-Walled Struct.* 113 (2017) 122-128.
- [62] J. Zhang, M. Wang, W. Wang, W. Tang, Y. Zhu. Investigation on egg-shaped pressure hulls, *Mar. Struct.* 52 (2017) 50-66.
- [63] J. Zhang, B. Zhu, F. Wang, W. Tang, W. Wang, M. Zhang. Buckling of prolate

- egg-shaped domes under hydrostatic external pressure, *Thin Walled Struct.* 119 (2017) 296-303.
- [64] C.T.F. Ross, A.P.F. Little, L. Chasapides, J. Banks, D. Attanasio. Buckling of ring stiffened domes under external hydrostatic pressure, *Ocean Eng.* 31 (2004) 239-252.
 - [65] NASA, NASA SP-8032: Buckling of thin-walled doubly curved shells, Washington (DC): NASA Space Vehicle Design Criteria (Structures). (1969).
 - [66] A.Y. Evkin, O.V. Lykhachova. Energy barrier as a criterion for stability estimation of spherical shell under uniform external pressure, *Int. J. Solids Struct.* 118-119 (2017) 1339-1351.
 - [67] H. N. R. Wagner, C. Hühne, S. Niemann. Robust knockdown factors for the design of spherical shells under external pressure: Development and validation, *Int. J. Mech. Sci.* 141 (2018) 58-77.
 - [68] S.J. Medwadowski. Buckling of concrete shells: an overview. *Journal of the International Association for Shell and Spatial Structures* 45 (2004) 51-63.
 - [69] M. Andres, R Harte. Buckling of concrete shells: a simplified numerical approach. *Journal of the International Association for Shell and Spatial Structures* 47(2006) 279-290.
 - [70] H. Schmidt. Stability of steel shell structures general report. *Journal of Constructional Steel Research* 55(2000) 159-181.
 - [71] C. Bisagni. Numerical analysis and experimental correlation of composite shell buckling and post-buckling. *Composites* 31B (2000) 655-667.

Chapter 2 Buckling of deep sea spherical pressure hulls

It is well known that the spherical pressure hull is the most extensively used configuration for the deep manned submersible. To conduct an innovative design of pressure hulls, the buckling mechanism of deep sea spherical pressure hulls must be first clarified. Therefore, this chapter focuses on the buckling of spherical pressure hulls subjected to uniform external pressure. Hulls were spherical shells with 1000 mm median radius and had uniform wall thickness of 25-80 mm. The linear and nonlinear buckling of geometrically perfect hulls were examined numerically and verified analytically in linear range. The nonlinear buckling of hulls with eigenmode geometrical imperfections were evaluated numerically using the arc length method, in which imperfection size ranged from 2-10 mm. The critical buckling load of geometrically perfect and imperfect hulls was obtained based on elastic-perfectly plastic material modelling, in which the yield strength varied from 800-1300 MPa. A semi-analytical formula to predict the load-carrying capacity of hulls was derived based on the numerical computations.

In addition, to further validate the obtained buckling mechanism, the adopted material modeling and imperfections assumption, ten laboratory scale models, each with a nominal diameter of 150 mm, were tested. Half of them were manufactured from a 0.4-mm stainless steel sheet, whereas the remaining five shells were manufactured from a 0.7-mm sheet. The geometry, wall thickness, buckling load, and final collapsed mode of each spherical shell were measured, as well as the material properties of the corresponding sheet. The buckling behaviors of these shells were demonstrated analytically and numerically according to experimental data. Analyses involved considering the average geometry, average wall thicknesses, and average elastic material properties. Numerical calculations entailed considering the true geometry, average wall thicknesses, and elastic-plastic modeling of true stress–strain

curves. Moreover, the effects of purely elastic and elastic-perfectly plastic models on the buckling loads of spherical shells were examined numerically.

2.1 Buckling analysis of geometrically perfect and imperfect hulls

This section examines the buckling of geometrically perfect and imperfect spherical pressure hulls in line with ENV 1993-1-6 (2007) [1]. For the geometrically perfect hulls, linear elastic buckling analysis was carried out, along with geometrically and materially nonlinear analysis. For the geometrically imperfect hulls, geometrically and materially nonlinear analysis with eigenmode imperfections included was conducted. The study is entirely numerical and partially theoretical.

2.1.1 Geometry and material

Consider a spherical pressure hull with its geometry given by the median radius, $r=1000$ mm, uniform wall thickness t ranging from 25 mm to 80 mm, and subjected to uniform external pressure, p_0 , see Fig.2-1. Let the pressure hull be made from Ti-6Al-4V(TC4), the material properties were as follows: Young modulus $E = 110$ GPa, yield strength $\sigma_y = 830$ MPa, tensile strength $\sigma_t = 869.7$ MPa, Poisson ratio $\mu = 0.3$.

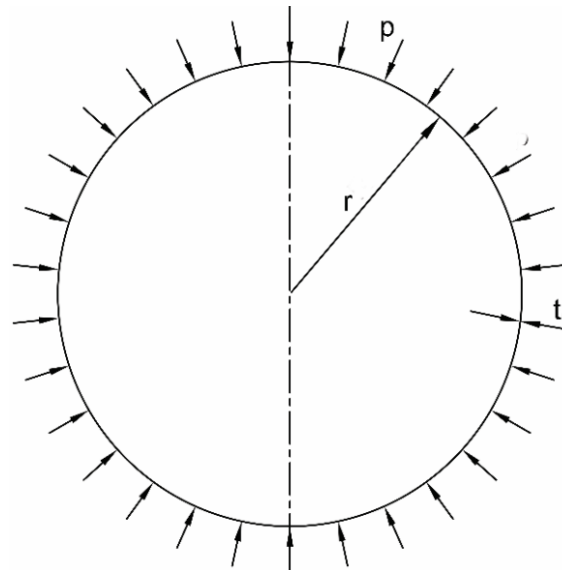


Fig.2-1 Geometry of a spherical pressure hull

All material properties except Poisson ratio were obtained from the experimental results of a tension coupon tested according to Chinese Standard (GB/T 228.1-2010)

[2]. Test details could be found in ref. [3]. In the test, the high-precision load cell and extensometer were adopted, which could produce the exact engineering stress-strain curve, see Fig.2-2a. From this curve, tensile strength could be determined as the peak value of the nonlinear range, which was presented only for the evaluation of the material and not adopted in the following analysis.

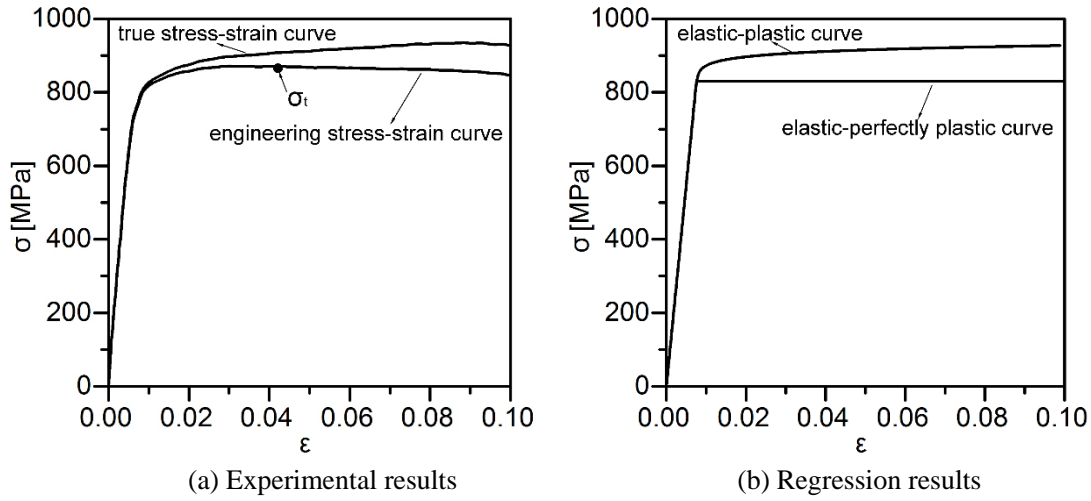


Fig.2-2 Stress versus strain of Ti-6Al-4V(TC4)

According to this curve, true stress-strain relationship could be determined according to Eqs.(2-1, 2-2):

$$\varepsilon_{true} = \ln(1 + \varepsilon_{eng}) \quad (2-1)$$

$$\sigma_{true} = \sigma_{eng} (1 + \varepsilon_{eng}) \quad (2-2)$$

Its relationship between true stress and true strain could be defined as follows:

$$\sigma = E\varepsilon, \text{ for } \sigma < \sigma_y \quad (2-3a)$$

and

$$\sigma = \sigma_y \left[\left(\frac{E\varepsilon}{\sigma_y} - 1 \right) n \right]^{\frac{1}{n}}, \text{ for } \sigma \geq \sigma_y \quad (2-3b)$$

In this way, Young modulus, yield strength, and the strain hardening parameter ($n=59.327$) were obtained from experimental results – plot of true stress versus strain, see Fig.2-2a. Young modulus was determined from the slop of the linear range. The yield point was determined based on the 0.2% proof stress. The strain hardening

parameter was regressed based the nonlinear range. The regression result was shown as elastic-plastic curve in Fig.2-2b. Also, the elastic-perfectly plastic curve was generated by assuming that the stress tended to be horizontal after the yield point. Both material curves were employed in the following analysis.

2.1.2 Buckling of geometrically perfect hulls

A total of 24 numerical analyses were performed for geometrically perfect spherical pressure hulls using the FE code ABAQUS 6.13. Half of them with 5 mm thickness increment were used for linear elastic buckling analysis, while others with the same thickness increment were adopted for geometrically and materially nonlinear analysis based on the arc length method. The fully integrated S4 shell element was employed to avoid hourglassing. The number of elements was determined using mesh convergence analysis in the case of linear elastic buckling analysis [4, 5]. It was noted that the different shell thickness might result in a different critical element number. Nevertheless, to keep the uniformity and simplify the problem, the maximum element number among shells with various wall thicknesses was employed in each model according to mesh convergence analysis of shells. This employment was due to fact that the buckling of a shell could vary slightly beyond the critical element number. As a result, each numerical model had the same shell elements of 6534 and the nodes of 8750. The uniform external pressure, $p_0 = 1$ MPa was imposed on the whole surface of each spherical pressure hull. In this way, the eigenvalue obtained from linear elastic buckling analysis corresponded directly to the linear buckling load, while the arc length value obtained from geometrically and materially nonlinear analysis was the nonlinear buckling load. To avoid rigid body motion, three spatial points of each model are fixed according to CCS2013 [4], as follows: $U_y=U_z=0$, $U_x=U_y=0$, $U_y=U_z=0$. These constraints did not lead to excessive constraint of the models, because the pressure was applied uniformly.

The linear buckling performances of a geometrically perfect spherical pressure hull were greatly affected by its thickness. For example, the linear buckling load, p_{lin} , significantly increased with an increase in the wall thickness (Table 2-1), which was consistent with previous studies given by Zoelly [6] for thin-walled spherical shells

(Eq.2-4), and Wang [7] for medium-thick-walled spherical shells (Eq.2-5):

$$p_t = \frac{2E}{\sqrt{3(1-\mu^2)}} \left(\frac{t}{r} \right)^2 \quad (2-4)$$

$$p_{m-t} = \frac{2Et}{r(1-\mu^2)} \left[\sqrt{\frac{(1-\mu^2)}{3}} \frac{t}{r} - \frac{\mu t^2}{2r^2} \right] \quad (2-5)$$

Table 2-1 Buckling loads of geometrically perfect spherical pressure hulls obtained from numerical and analytical analysis, as well as their first yield analysis.

t/r	p_t	p_{m-t}	p_{lin}	p_{e-p}	p_{fy}	p_{fyl}
[MPa]						
0.025	83.219	82.652	83.468	42.147	41.479	41.500
0.030	119.835	118.856	119.660	50.559	49.790	49.800
0.035	163.109	161.554	162.610	59.011	58.083	58.100
0.040	213.040	210.719	211.640	67.462	66.400	66.400
0.045	269.629	266.324	266.880	75.890	74.707	74.700
0.050	332.875	328.342	328.280	84.343	83.000	83.000
0.055	402.779	396.746	398.730	92.778	91.299	91.300
0.060	479.340	471.507	470.020	101.257	99.604	99.600
0.065	562.559	552.600	549.780	109.653	107.904	107.900
0.070	652.435	639.997	638.340	118.062	116.198	116.200
0.075	748.969	733.670	733.780	130.539	124.512	124.500
0.080	852.160	833.593	827.780	140.695	132.800	132.800

Notations: p_t = buckling load obtained from the thin-walled equation; p_{m-t} = buckling load obtained from medium-thick-walled equation; p_{lin} = buckling load obtained from linear elastic buckling analysis; p_{e-p} = buckling load obtained from geometrically and materially nonlinear analysis; p_{fy} = first yield pressure obtained from geometrically and materially nonlinear analysis; p_{fyl} = first yield pressure obtained from analytical analysis (Eq.2-6).

The difference between these two equations was that the medium-thick-walled equation (Eq.2-5) contained an extra higher order term, which led to a decrease in the buckling load with an increase in the wall thickness, and resulted in a more precise prediction than the thin-walled equation (Eq.2-4). In this way, the numerical results agreed well with the theoretical ones given by Eq.2-5, as these deep sea spherical pressure hulls were shells of revolution with medium-thick wall thickness. In addition, the linear buckling modes of all spherical pressure hulls were identical and took the form of several circumferential and meridional half waves. These buckling modes are

typical for highly symmetrical spherical shells [8]. As can be seen from Fig.2-3 (colors of buckling shape indicate eigenvector), the number of the wave crest decreased with an increase in the wall thickness. For instance, the number, n , of the wave crest is 11 for the 25 mm spherical pressure hull, while the number reduced to 6 for the 80 mm spherical pressure hull.

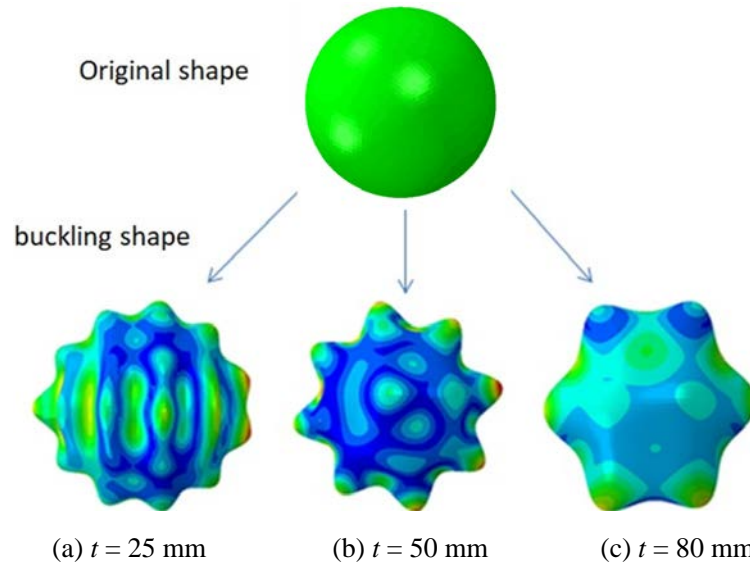


Fig.2-3 Linear buckling modes of deep sea spherical pressure hulls with various wall thickness

The nonlinear buckling performances of a geometrically perfect spherical pressure hull were completely different from the linear one. As can be observed from Table 2-1, the nonlinear buckling load, p_{e-p} , of each hull significantly decreased compared to the corresponding value obtained from linear elastic buckling analysis. This difference increased with an increase in the wall thickness. These findings suggested that material plasticity played a very important role in the buckling of deep sea pressure hull. The more sensitive to the plasticity the buckling load of a spherical pressure hull was, the thicker its wall thickness was.

In the same table, the first yield pressures of spherical pressure hulls were provided using the same post-processing procedure as [9]. The first yield pressure of the mid-surface of each hull could be obtained in accordance with the mechanics of elasticity – dividing the yield stress of the material by the maximum Von Mises stress given by linear analysis, in the case of 1 MPa external pressure. It must be noted that

these yield loads were obtained based on the median surface of the spherical pressure hulls. The yield load derived from the internal surface could be less than these values, because the maximum stress located at the internal surface for the medium-thick spherical pressure hulls under external pressure [10]. The first yield pressure of each spherical pressure hull was less than its nonlinear buckling load. These findings indicated that all of the spherical pressure hulls could buckle in the elastic-plastic range, which was consistent with previous studies regarding medium-thick shells subjected to external pressure [9, 11]. In addition, according to Eq.2-6, the analytical first yield pressure was listed in a separate column of Table 2-1.

$$p_{fy1} = \frac{2t\sigma_y}{r} \quad (2-6)$$

where $\sigma_y = 830$ MPa. As can be seen from the table, the numerical results were nearly the same as the analytical results.

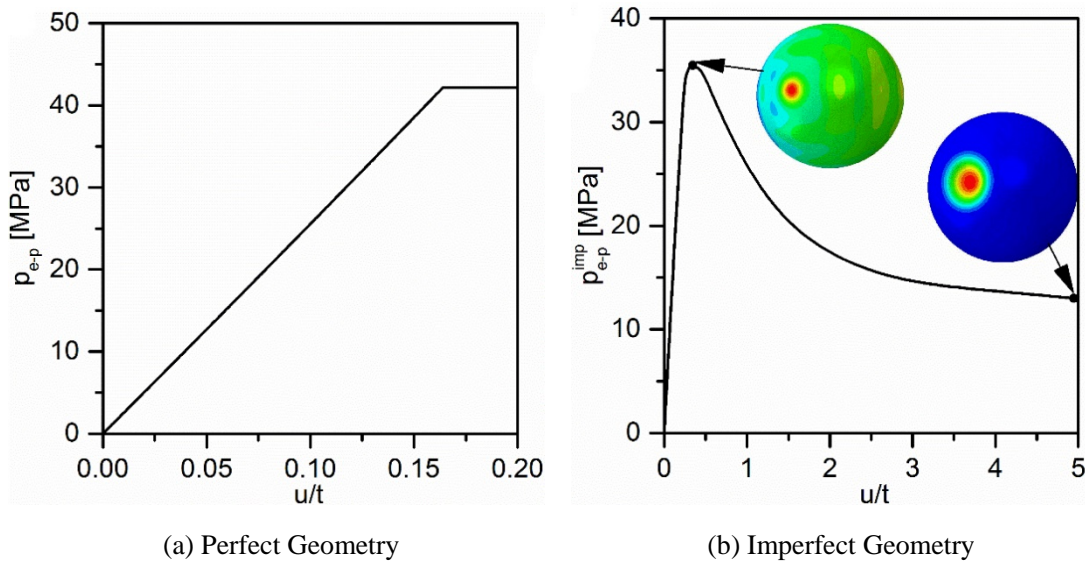


Fig.2-4 Equilibrium paths of the 25 mm spherical pressure hull obtained from geometrically and materially nonlinear analysis

Moreover, the equilibrium path of the 25 mm spherical pressure hull was illustrated in Fig.2-4. The path provided the applied pressure and the maximum deflection, u , normalized by its wall thickness. As can be identified, the applied pressure first increased monotonically with an increase in the deflection; this continued for up to the critical or buckling point, beyond which the path levelled off. This trend was

identical with the equilibrium path of medium-thick and geometrically perfect conical shells under external pressure [12].

Table 2-2 Buckling loads [MPa] of spherical pressure hulls obtained from geometrically and materially nonlinear analysis with eigenmode imperfections included; the parentheses show non-dimensional buckling load that is the ratio of each buckling load to the one in the case of $t/r = 0.025$ and $\delta = 2$ mm, along with the ratios of the elastic-perfectly plastic buckling loads to the elastic-plastic ones, respectively.

t/r	δ [mm]				
	2	4	6	8	10
0.025	35.465 (1.000,0.990)	30.265 (0.853,0.988)	26.268 (0.741,0.988)	23.180 (0.654,0.988)	20.777 (0.586,0.987)
0.030	45.149 (1.273,0.988)	39.714 (1.120,0.985)	35.191 (0.992,0.983)	31.500 (0.888,0.984)	28.486 (0.803,0.984)
0.035	55.698 (1.571,0.994)	52.183 (1.471,0.986)	48.402 (1.365,0.982)	44.857 (1.265,0.981)	41.658 (1.175,0.981)
0.040	64.578 (1.821,0.994)	61.308 (1.729,0.979)	57.795 (1.630,0.985)	54.250 (1.530,0.983)	50.933 (1.436,0.982)
0.045	73.765 (2.080,0.995)	71.282 (2.010,0.991)	68.642 (1.935,0.987)	65.846 (1.857,0.985)	62.985 (1.776,0.982)
0.050	82.246 (2.319,0.994)	79.553 (2.243,0.991)	76.689 (2.162,0.987)	73.654 (2.077,0.985)	70.524 (1.989,0.983)
0.055	90.567 (2.554,0.992)	87.458 (2.466,0.989)	84.150 (2.373,0.987)	80.683 (2.275,0.984)	77.007 (2.171,0.982)
0.060	99.925 (2.818,0.991)	97.378 (2.746,0.989)	94.662 (2.669,0.988)	91.833 (2.589,0.986)	88.920 (2.507,0.984)
0.065	108.865 (3.070,0.988)	106.243 (2.996,0.988)	103.468 (2.917,0.987)	100.579 (2.836,0.986)	97.620 (2.753,0.984)
0.070	118.037 (3.328,0.983)	115.623 (3.260,0.986)	113.046 (3.188,0.985)	110.358 (3.112,0.985)	107.599 (3.034,0.984)
0.075	128.165 (3.614,0.975)	125.374 (3.535,0.982)	123.041 (3.469,0.983)	120.781 (3.406,0.983)	118.482 (3.341,0.983)
0.080	136.857 (3.859,0.977)	135.021 (3.807,0.977)	132.653 (3.740,0.980)	130.433 (3.678,0.982)	128.263 (3.617,0.982)

2.1.3 Buckling of geometrically imperfect hulls

A total of 60 numerical analyses were performed for geometrically imperfect spherical pressure hulls with 5 mm thickness increment, using the FE code ABAQUS 6.13. In each analysis, the imperfection was introduced into the perfect model by means of equivalent geometrical imperfection. The equivalent geometrical

imperfection took the shape of the same linear buckling mode as that mentioned in Section 2.1.2, which may lead to conservative results [13]. The imperfection sizes were defined as 2 mm, 4 mm, 6 mm, 8 mm, and 10 mm, respectively. This imperfection assumption was in accordance with [14]. The mesh, load, boundary condition, and material specifications were the same as geometrically and materially nonlinear analysis. The modified Riks method was used to obtain solution due to the unstable problem. The calculating parameters were set as follows: initial increment in arc length along the static equilibrium path in scaled load-displacement space was set as 0.1; total arc length scale factor associated with this step is 200; Minimum arc length increment is 5E-5; Maximum arc length increment is 0.5; Maximum value of the load proportionality factor is 500. The obtained results are shown in Fig.2-4 and Table 2-2.

The critical buckling load, p_{e-p}^{imp} , of the spherical pressure hull decreased sharply with an increase in the imperfection size at the same wall thickness. For example, comparing Table 2-1 and Table 2-2, the critical buckling load of the 25 mm spherical pressure hull (35.465 MPa) is about 84% of that obtained from geometrically and materially nonlinear analysis at 2 mm imperfection size, and about 49% at 10 mm imperfection size. This decrease suggested that the spherical pressure hull was an imperfection sensitive structure, in which small shape deviations change its buckling load significantly. From Table 2-1 and Table 2-2, it is also inferred that sensitivity of imperfection to the buckling load of the spherical pressure hull decreased with an increase in its wall thickness. At the same imperfection size, the critical buckling load, p_{e-p}^{imp} , of the spherical pressure hull increased linearly with an increase in the wall thickness (Table 2-1), which was consistent with [14].

All equilibrium paths of imperfect spherical pressure hulls were unstable, which was typical for shell structures [15]. For instance, as illustrated in Fig.2-4, for the 25 mm spherical pressure hull, the applied pressure first increased monotonically with an increase in the deflection up to a peak value corresponding to the critical buckling load, p_{e-p}^{imp} , beyond which the pressure decreased significantly. Prior to buckling,

hulls initially exhibit a linear regime from the view of elastic mechanics, which is similar to the linear elastic shell analysis. Therefore, the deflection increases linearly with an increase in the applied load, which leads to the cusp. The deflection is measured on the maximum deflection point of shell, which is found at the end of the equilibrium path. Its critical buckling mode corresponding to the peak point was also listed in the same figure, as well as the post buckling mode corresponding to the end of the path. As can be seen, the critical buckling load of the pressure hull was similar to its linear buckling one; while the post buckling mode was in the form of a local dent, which was typical for shells of revolution with positive Gaussian curvature [11, 16]. Similar trends were found in other cases. Also, the first yield loads of these spherical pressure hulls were less than their critical buckling load, suggesting that all imperfect spherical pressure hulls buckled in the elastic-plastic range.

In addition, to examine the effect of constitutive models on the buckling spherical pressure hulls, another 60 numerical analyses were performed for the same imperfect spherical pressure hulls. All analyses were the same as the geometrically and materially nonlinear analysis with imperfections included mentioned in first paragraph of this section, except that the material properties were modeled as elastic-perfectly plastic. The parentheses in Table 2-2 detailed the ratio of the elastic-perfectly plastic buckling load, p_{e-pp}^{imp} , to the elastic-plastic buckling load, p_{e-p}^{imp} . This ratio varied from 0.975 to 0.995, indicating that the elastic-perfectly plastic could result in relatively conservative results. This finding extended previous works [9, 16], confirming that the elastic-perfectly plastic assumption could be used to predict the critical buckling load of shells of revolution subjected to uniform external pressure. This assumption were used to study the effect of yield strength on the buckling of spherical pressure hulls in the following sections.

2.2 Effect of yield strength on the buckling of hulls

The section examines the effect of yield strength on the buckling load of geometrically perfect and imperfect spherical pressure hulls. Elastic-perfectly plastic material modelling was assumed in all of the analyses. The yield strength of the

material varied from 800 to 1300 MPa with an increment of 100 MPa. This range corresponded to the varying range of titanium alloys used to manufacture deep sea spherical pressure hulls [17]. The wall thickness of spherical pressure hulls ranged from 25 to 80 mm with an increment of 5mm. The other modelling parameters of this section were assumed to be the same as those of Section 2.1.1. According to the analysis results, a semi-analytical formula was put forward to evaluate the load carrying capacity of deep see spherical pressure hulls.

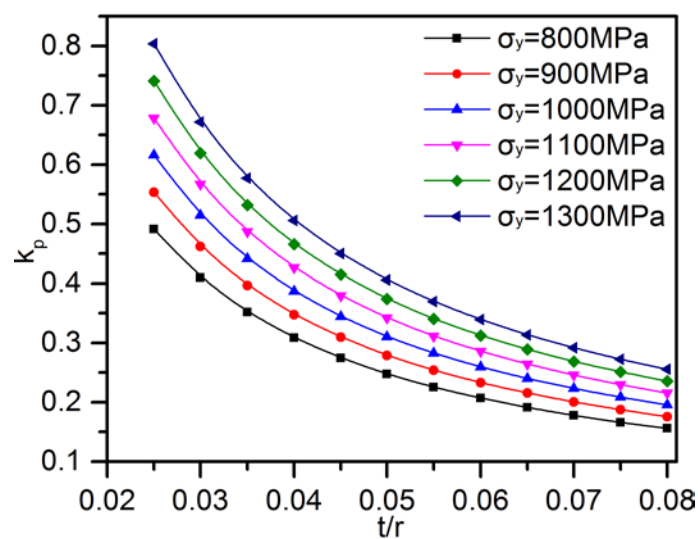


Fig.2-5 Plasticity reduction factor, k_p , versus the wall thickness-to-radius ratio, t/r , under six yield strengths, σ_y

2.2.1 Perfect geometry analysis

A family of $6 \times 12 = 72$ geometrically and materially nonlinear analysis was carried out for geometrically perfect spherical pressure hulls with various plasticity parameters and wall thicknesses. Fig.2-5 demonstrates the plasticity reduction factor, k_p , versus the wall thickness, t under six yield strengths, σ_y . The plasticity reduction factor was defined as the critical buckling load obtained from geometrically and materially nonlinear analysis divided by the linear buckling load obtained from the medium-thick-walled equation (Eq.2-5) at the same wall thickness mentioned in Section 2.1.2. As can be seen, the sensitivity of critical buckling load of deep sea spherical pressure hull to the material plasticity increased with an increase in its wall thickness and with a decrease in its yield strength. Using the nonlinear and linear regression analysis based on Origin analysis software, we found that the plasticity

reduction factor could be given by

$$k_p = k_0 \left(\frac{t}{r} \right)^{-0.986} \quad (2-7)$$

$$k_0 = 1.62 \times 10^{-5} \sigma_y \quad (2-8)$$

These findings suggested that the nonlinear critical buckling load, p_{non} , of geometrically perfect spherical pressure hulls could be obtained from the product of the plastic reduction factor, k_p , and the linear buckling load, p_{m-t} , obtained from the medium-thick-walled equation (Eq.2-5), as follows:

$$p_{non} = k_p p_{m-t} \quad (2-9)$$

2.2.2 Imperfect geometry analysis

A family of $6 \times 12 \times 5 = 360$ geometrically and materially nonlinear analysis with the first buckling mode (eigenmode) imperfections included was carried out for geometrically imperfect spherical pressure hulls with various yield strengths, imperfection sizes and wall thicknesses. Fig.2-6 demonstrates the geometrical imperfection reduction factor, k_{imp} , versus the wall thickness, t under six yield strengths, σ_y , and five imperfection sizes, δ . The geometrical imperfection reduction factor was defined as the critical buckling load obtained from geometrically and materially nonlinear analysis with eigenmode imperfections included divided by the corresponding one obtained from geometrically and materially nonlinear analysis at the same wall thickness and yield strength mentioned in Section 2.2.1. As can be seen, the sensitivity of critical buckling load of deep sea spherical pressure hull to the geometrical imperfection increased with a decrease in its wall thickness and yield strength, and with an increase in its imperfection size. At the same yield strength and imperfect size, the geometrical imperfection reduction, k_{imp} , increased nearly linearly with an increase in the wall thickness ($0.025 < t/r < 0.045$) with a high slope, then tends to level off in the range $0.045 < t/r < 0.055$, and finally increased linearly with an increase in the wall thickness ($0.055 < t/r < 0.08$) with a small slope. The reason for this trend was mainly due to the nonlinear material behaviour. Therefore, different regression formulas can be derived for these three ranges.

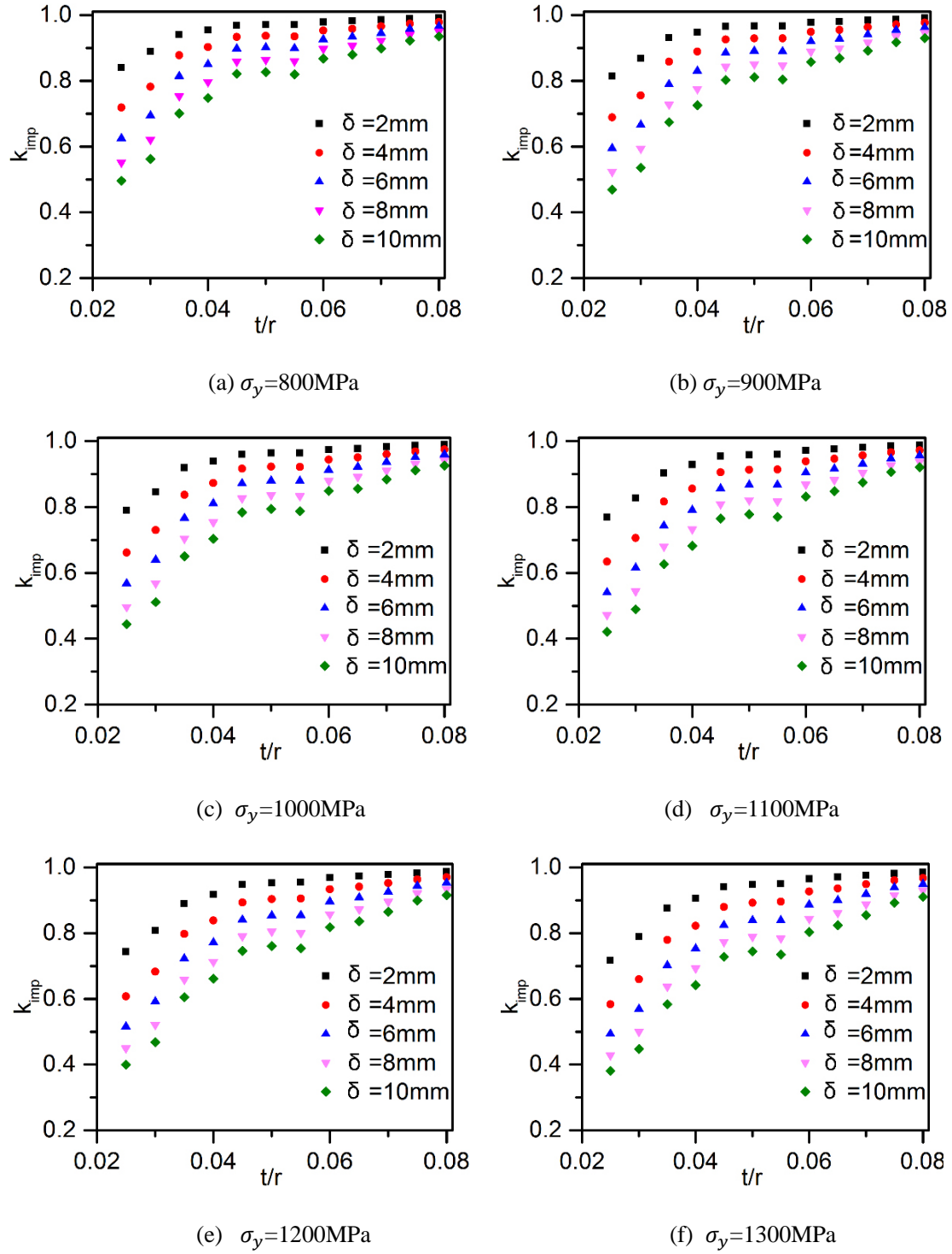


Fig.2-6 Geometrical imperfection reduction factor, k_{imp} , versus the wall thickness-to-radius ratio, t/r , under six yield strengths, σ_y , and five imperfection sizes, δ

Combining the linear and nonlinear regression analysis based on Origin analysis software, it was found that the geometrical imperfection reduction factor, k_{imp} can be determined as:

$$k_{imp} = \begin{cases} k_1\left(\sigma_y, \frac{\delta}{r}\right)\frac{t}{r} + k_2\left(\sigma_y, \frac{\delta}{r}\right), & (0.025 < \frac{t}{r} < 0.045) \\ \left[\begin{aligned} &0.045k_1\left(\sigma_y, \frac{\delta}{r}\right) + 0.055k_a\left(\sigma_y, \frac{\delta}{r}\right) \\ &+ k_2\left(\sigma_y, \frac{\delta}{r}\right) + k_4\left(\sigma_y, \frac{\delta}{r}\right) \end{aligned} \right] / 2, & (0.045 < \frac{t}{r} < 0.055) \\ k_3\left(\sigma_y, \frac{\delta}{r}\right)\frac{t}{r} + k_4\left(\sigma_y, \frac{\delta}{r}\right)\frac{t}{r}, & (0.055 < \frac{t}{r} < 0.080) \end{cases} \quad (2-10)$$

where, $k_1\left(\sigma_y, \frac{\delta}{r}\right)$, $k_2\left(\sigma_y, \frac{\delta}{r}\right)$, $k_3\left(\sigma_y, \frac{\delta}{r}\right)$, and $k_4\left(\sigma_y, \frac{\delta}{r}\right)$ can be obtained from Fig.2-7.

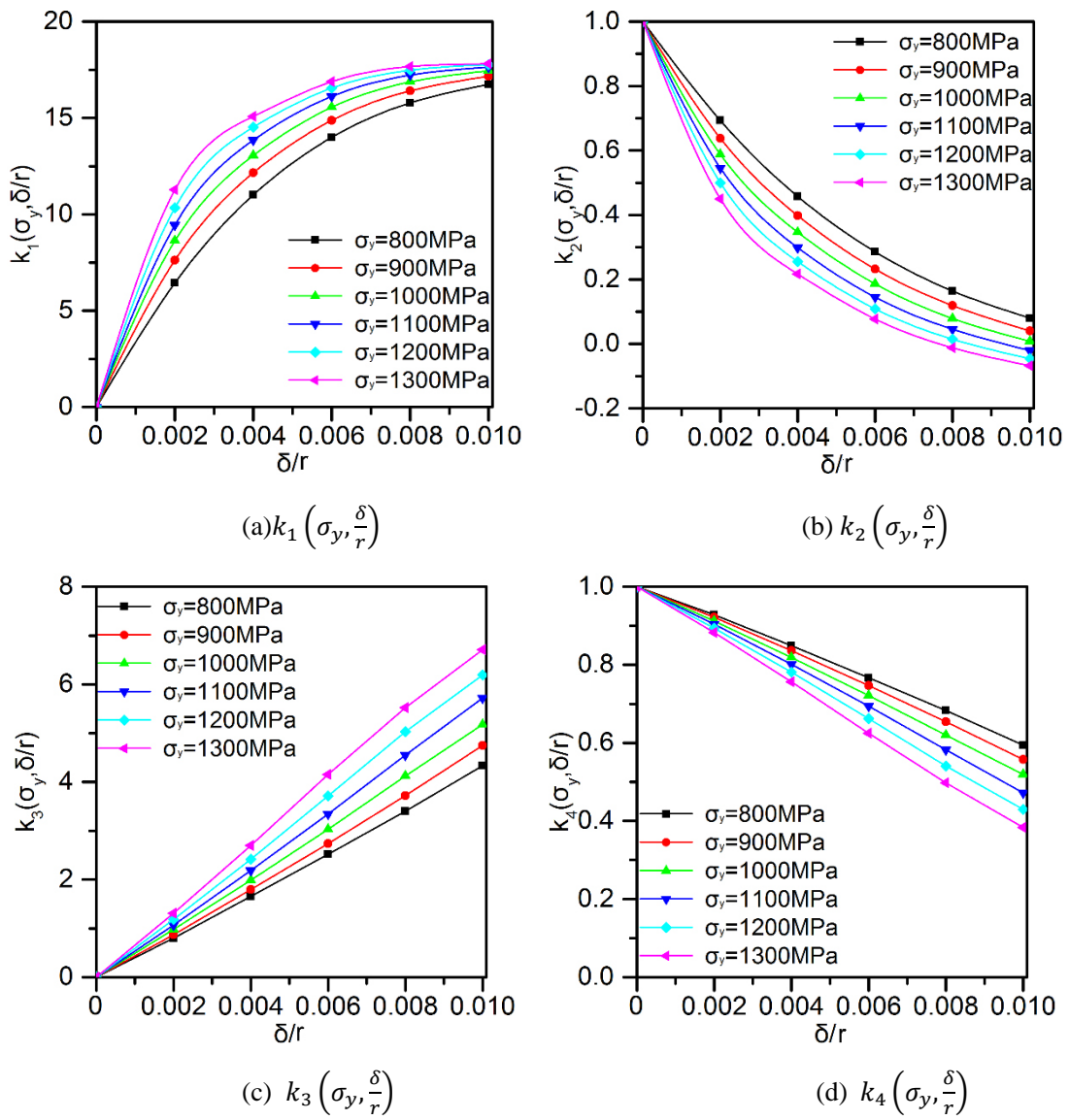


Fig.2-7 Coefficients, $k_1\left(\sigma_y, \frac{\delta}{r}\right)$, $k_2\left(\sigma_y, \frac{\delta}{r}\right)$, $k_3\left(\sigma_y, \frac{\delta}{r}\right)$, and $k_4\left(\sigma_y, \frac{\delta}{r}\right)$, of the equations versus the imperfection size-to-radius ratio, δ/r , under six yield strengths, σ_y

As can be seen from Fig.2-7, the coefficients, $k_1\left(\sigma_y, \frac{\delta}{r}\right)$ and $k_2\left(\sigma_y, \frac{\delta}{r}\right)$, varied nonlinearly with the imperfection size and yield strength. We can obtain their values using the graphing method. On the other hand, the coefficients, $k_3\left(\sigma_y, \frac{\delta}{r}\right)$, and $k_4\left(\sigma_y, \frac{\delta}{r}\right)$, varied linearly with the imperfection size and yield strength. Using the linear and nonlinear regression analysis based on Origin analysis software, these two coefficients can be given as:

$$k_3\left(\sigma_y, \frac{\delta}{r}\right) = (0.5087\sigma_y + 11.231)\frac{\delta}{r} \quad (2-11)$$

$$k_4\left(\sigma_y, \frac{\delta}{r}\right) = 1 - (0.0447\sigma_y + 3.2321)\frac{\delta}{r} \quad (2-12)$$

As a result, in line with the generalized reduction factor approach (RFA) for shell buckling design [18], the load carrying capacity p_{real} of deep sea pressure hulls could be determined from Eqs(2-5, 2-7~2-12), in the following semi-analytical formula:

$$p_{real} = k_p k_{imp} p_{m-t} \quad (2-13)$$

where, k_p was determined from Eqs(2-7 and 2-8), k_{imp} was determined from Eqs(2-10~2-12) and Fig.2-7, p_{m-t} was determined from Eq.2-5.

Furthermore, an example containing full sequence of a step-by-step calculations using the semi-analytical formula for a typical case was provided, in the following:

Step 1: The geometry and material parameters of the spherical shell were as follows: a spherical pressure hull was assumed that the median radius, $r=1000$ mm, uniform wall thickness $t=30$ mm, the imperfection sizes $\delta=2$ mm. In addition, let the pressure hull be made from Ti-6Al-4V(TC4) with Young modulus $E=110$ GPa, yield strength $\sigma_y = 850$ MPa, and Poisson ratio $\nu = 0.3$.

Step 2: The buckling load obtained, p_{m-t} , could be determined from Eq.2-5, the value was 118.856MPa. The details were as follows:

$$\begin{aligned}
P_{m-t} &= \frac{2Et}{r(1-\nu^2)} \left[\sqrt{\frac{(1-\nu^2)}{3}} \frac{t}{r} - \frac{\nu t^2}{2r^2} \right] \\
&= \frac{2 \times 110000 \times 30}{1000 \times (1-0.3^2)} \times \left[\sqrt{\frac{(1-0.3^2)}{3}} \times \frac{30}{1000} - \frac{0.3 \times 30^2}{2 \times 1000^2} \right] \approx 118.856;
\end{aligned}$$

Step 3: The plasticity reduction factor, k_p , could be calculated based on Eqs.2-7~2-8, this value was 0.437. The details were as follows:

$$k_p = k_0 \left(\frac{t}{r} \right)^{-0.986} = 1.62 \times 10^{-5} \sigma_y \left(\frac{t}{r} \right)^{-0.986} = 1.62 \times 10^{-5} \times 850 \times \left(\frac{30}{1000} \right)^{-0.986} \approx 0.437;$$

Step 4: The geometrical imperfection reduction factor, k_{imp} , could be acquired by first segment function of Eq.2-10 due to $t/r = 0.03$. The coefficients, $k_1 \left(\sigma_y, \frac{\delta}{r} \right)$ and $k_2 \left(\sigma_y, \frac{\delta}{r} \right)$, varied nonlinearly with the imperfection size and yield strength. One could obtain their values using the graphing method from Fig.2-7. Therefore, the value of k_{imp} was 0.8766 based on Eq.2-10. The details were summarized as follows:

- (1) when $\delta/r = 0.002$ and $\sigma_y = 800$ MPa, the corresponding values of $k_1 \left(\sigma_y, \frac{\delta}{r} \right)$ and $k_2 \left(\sigma_y, \frac{\delta}{r} \right)$ were 6.430 and 0.694; when $\delta/r = 0.002$ and $\sigma_y = 900$ MPa, the corresponding values of $k_1 \left(\sigma_y, \frac{\delta}{r} \right)$ and $k_2 \left(\sigma_y, \frac{\delta}{r} \right)$ were 7.610 and 0.638.
- (2) The yield strength ($\sigma_y = 850$ MPa) was between 800 MPa and 900 MPa, the final values were obtained by the linear interpolation, as follows:

$$k_1 \left(\sigma_y, \frac{\delta}{r} \right) = \frac{50}{100} \times (7.610 - 6.430) + 6.430 = 7.02;$$

$$k_2 \left(\sigma_y, \frac{\delta}{r} \right) = \frac{50}{100} \times (0.694 - 0.638) + 0.638 = 0.666;$$

- (3) The value of k_{imp} was calculated, as follows:

$$k_{imp} = k_1 \left(\sigma_y, \frac{\delta}{r} \right) \frac{t}{r} + k_2 \left(\sigma_y, \frac{\delta}{r} \right) = 7.02 \times \frac{30}{1000} + 0.666 = 0.8766$$

Step 5: The load carrying capacity of deep sea pressure hulls, p_{real} , could be determined from Eq.2-13. The value of p_{real} was 45.531MPa. The details were as follows:

$$p_{real} = k_p k_{imp} p_{m-t} = 118.856 \times 0.437 \times 0.8766 = 45.531$$

This semi-analytical formula included the medium-thick-walled analytical buckling equation to determine the linear elastic buckling load of deep sea spherical pressure hulls, along with the quantitative evaluation of reduction of this load due to the nonlinearity of material and the shape deviation of geometry. The formula involved most of the geometrical, material, and manufacturing parameters that affected the buckling of deep sea spherical pressure hulls, such as the ratio of wall thickness, r , to radius, t , the conservative imperfection size, δ , Young modulus, E , yield strength, σ_y , and Poisson ratio, ν . The interrelationship and interaction among these parameters were considered by defining the plasticity reduction factor as a function of the yield strength and the wall thickness-radius-ratio, and by defining the plastic imperfection factors as a function of the imperfection size-to-radius-ratio, the yield strength, and the wall thickness-radius-ratio. Most importantly, this formula was a kind of mechanism model corresponding to the buckling regime of deep sea spherical pressure hulls.

It is known that an empirical formula (Eqs.2-14 and 2-15) to predict the critical buckling load of deep sea spherical pressure hulls was given in Chapter 16 of CCS2013 [4]. This empirical formula was proposed by our previous studies [14, 19] to estimate the ultimate strength of the spherical pressure hull at preliminary design stage with the first eigenmode imperfection included. This empirical formula was obtained from geometrically and materially nonlinear analysis with imperfections included for deep sea pressure hulls with the same imperfection sizes and wall thicknesses as the current work (Section 2.1.2). However, all of the analyses used only one elastic-plastic material modelling, and did not consider the effect of material plasticity on the buckling of spherical pressure hulls. Furthermore, this empirical formula directly established a quantitative relationship between the critical buckling load of a deep sea spherical pressure hull and its thickness, internal radius, median radius, tensile strength, and imperfection size; but the tensile strength seemed to be irrelevant with the critical buckling of a spherical shell. Also, it did not involve as many geometrical and material parameters as the proposed formula of this work, and

was not associated with the buckling regime of deep sea spherical pressure hulls, although the empirical formula could accurately evaluate the load carrying capacity of deep sea spherical pressure hulls in some cases. In other cases, for example, if Young modulus, E , yield strength, σ_y , or Poisson ratio, ν changes, this empirical formula could not adapt to these variations and may give an incorrect result. Therefore, this empirical formula was a kind of phenomenological model, which could be considered as the special case of the current work. Our proposed semi-analytical formula extended previous work and could be used to evaluate the load carrying capacity of deep sea spherical pressure hulls at preliminary design stage.

$$p_{real} = (1 - k \frac{\delta}{r_{in}}) (\frac{\sigma_t}{r_{in}} t + \frac{\sigma_t}{m} t) \quad (2-14)$$

$$k = a + b \cdot \exp(-c \frac{\delta}{r_{in}} - d \frac{t}{r_{in}} + j (\frac{\delta}{r_{in}})^2 + f (\frac{t}{r_{in}})^2 - g (\frac{\delta}{r_{in}})^3 - h (\frac{t}{r_{in}})^3) \quad (2-15)$$

where, r_{in} = internal radius; δ = imperfection size; r_m = mean radius; σ_t = ultimate strength; t = wall thickness; a, b, c, d, j, f, g , and h are constants.

2.3 Experimental methodology of spherical shells

This section involved sampling and analyzing 10 spherical shells to determine their buckling behaviors. A series of tests were performed to obtain the geometrical and buckling properties of these shells in addition to their material properties.

2.3.1 Shell manufacturing and testing

Each spherical shell was manufactured using the tungsten inert gas butt welding of two coupled hemispherical shells, after which the excess of the weld has been removed by grinding and then been polished. Each hemispherical shell was cut and stamped from 304 thin stainless steel sheets with a nominal thickness of either 0.4 mm or 0.7 mm due to the good ductility. Ten spherical shells with a nominal diameter of 150 mm were manufactured for the tests. Five of them were fabricated from a 0.4-mm-thick sheet and were denoted as t0.4-1, t0.4-2, t0.4-3, t0.4-4, and t0.4-5. Five other shells were fabricated from a 0.7-mm-thick sheet and were denoted as t0.7-1, t0.7-2, t0.7-3, t0.7-4, and t0.7-5. In addition, all the shells were not stress relieved

during the manufacturing process because the ratios of the wall thickness to the nominal diameter were very low. Before the spherical shells were tested, the wall thickness and geometric shape were measured for all the shells.

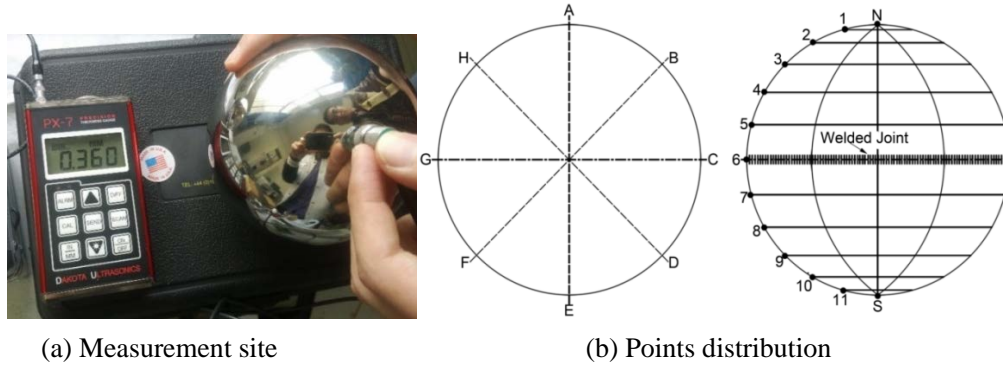


Fig.2-8 Measurement site and typical distribution of testing points for wall thickness

First, the thickness of each wall was measured using an ultrasonic probe at 13 equidistant points along a meridian for eight equally spaced meridians, as detailed in Fig.2-8. Each shell was measured at $8 \times 11 + 2 = 90$ points. The values of the minimum (t_{min}), maximum (t_{max}), and average wall thicknesses (t_{ave}), as well as the corresponding standard deviations (t_{std}), are listed in Table 2-3. Overall average wall thickness profile from the North-Pole to the South Pole for a t0.4-1 spherical shell and its thicknesses of all measure points are also showed in Fig.2-9 and Table 2-4 respectively. The average variation between the maximal and minimal wall thicknesses was approximately 17%, which may be attributed to the stamping process. Second, the geometries of all the spherical shells were obtained using a three-dimensional optical scanner, developed by Open Technologies Corporation. The scanned accuracy is not more than 0.02 mm referring to operating manual provided by the corporation. Each shell surface was scanned in the form of a point cloud and automatically transformed into a CAD model. Each model demonstrated the real geometric shape of the corresponding shell, which contained deterministic geometric imperfections caused by manufacturing processes. Furthermore, the minimum (r_{min}), maximum (r_{max}), and average radii (r_{ave}) of each shell were also obtained from the CAD model in addition to the corresponding standard deviations (r_{std}); these values are listed in the final four columns of Table 2-3, while contours of local radii of

curvature for a t0.4-1 spherical shell are presented in Fig.2-10.

Table 2-3 Testing values of the wall thickness and radius for spherical shells (minimum, maximum, average, and standard deviation).

	t_{min} (mm)	t_{max} (mm)	t_{ave} (mm)	t_{std} (mm)	r_{min} (mm)	r_{max} (mm)	r_{ave} (mm)	r_{std} (mm)
t0.4-1	0.382	0.476	0.422	0.022	73.903	74.485	74.248	0.174
t0.4-2	0.396	0.496	0.432	0.024	73.843	74.517	74.163	0.170
t0.4-3	0.378	0.488	0.426	0.024	74.067	74.285	74.157	0.046
t0.4-4	0.382	0.436	0.401	0.010	74.304	74.754	74.548	0.133
t0.4-5	0.382	0.476	0.414	0.016	73.817	74.501	74.185	0.158
t0.7-1	0.650	0.754	0.708	0.024	74.231	75.005	74.710	0.249
t0.7-2	0.614	0.766	0.715	0.024	74.391	75.291	74.926	0.242
t0.7-3	0.644	0.746	0.723	0.02	74.282	75.102	75.023	0.142
t0.7-4	0.652	0.756	0.724	0.019	74.300	75.062	74.840	0.184
t0.7-5	0.648	0.762	0.716	0.021	74.317	75.001	74.983	0.252

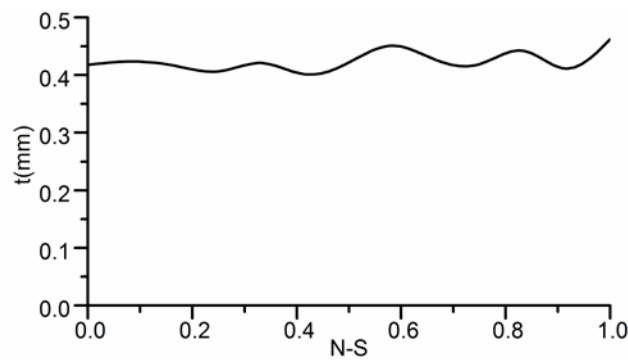
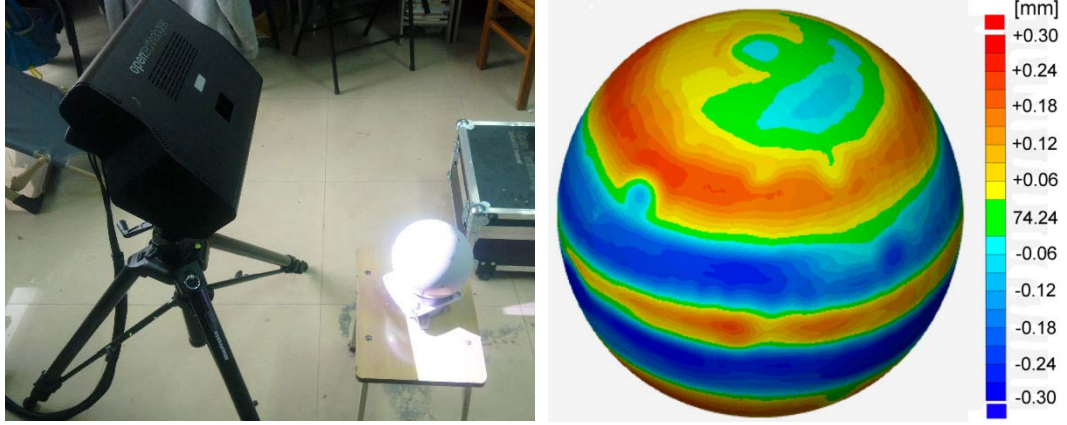


Fig.2-9 Overall average wall thickness profile from the North-Pole to the South Pole for a t0.4-1 spherical shell

Table 2-4 Thickness (mm) at 13 equidistant points along 8 meridians for a t0.4-1 spherical shell.

Longitude no.	Latitude no.							
	A	B	C	D	E	F	G	H
1	0.416	0.422	0.420	0.410	0.426	0.458	0.426	0.412
2	0.436	0.410	0.408	0.404	0.436	0.416	0.410	0.408
3	0.426	0.426	0.398	0.382	0.422	0.408	0.394	0.396
4	0.428	0.432	0.412	0.464	0.410	0.422	0.398	0.400
5	0.402	0.396	0.418	0.388	0.402	0.398	0.408	0.398
6	0.425	0.415	0.418	0.420	0.419	0.416	0.432	0.431
7	0.406	0.466	0.408	0.408	0.392	0.396	0.396	0.418
8	0.414	0.434	0.432	0.432	0.456	0.470	0.476	0.424
9	0.398	0.438	0.418	0.406	0.416	0.416	0.446	0.414
10	0.428	0.446	0.406	0.414	0.424	0.420	0.458	0.414
11	0.456	0.446	0.436	0.450	0.446	0.450	0.472	0.454

The thicknesses at the North-Pole and South-pole are 0.418 and 0.462 respectively.



(a) Shape scanning site

(b) Deviation distribution

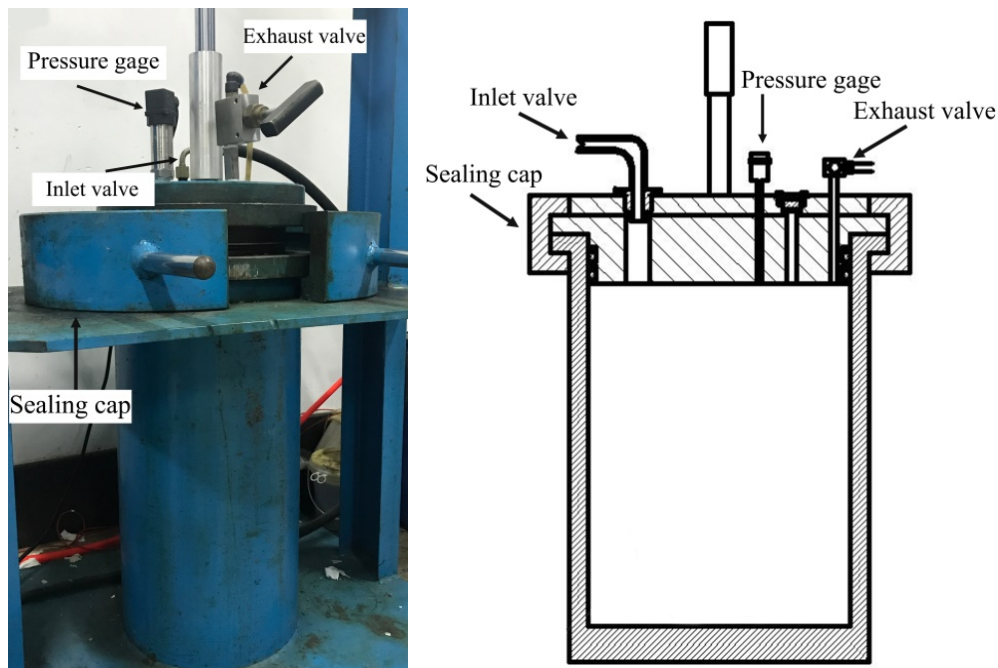
Fig.2-10 Shape scanning site and result for a t0.4-1 spherical shell

The spheres were empty and they were floating in the test vessel (Fig.2-11). This floating was expected to exert a strong influence on the buckling behavior of spherical shells. The net buoyancy values of the spherical shells were considerably high because their buoyant loads were higher than their dead-weight values. The net buoyancy was obtained by:

$$F_{net\ buoyant} = \frac{4}{3}\pi r^3 g \rho_{water} - \frac{4}{3}\pi (r^3 - (r-t)^3) g \rho_{steel} \quad (2-16)$$

where, r , t are the nominal radius and nominal thickness of a spherical shell, ρ_{steel} is the density of stainless steel, ρ_{water} is the density of water inside the vessel, g is the gravitational acceleration. Assume that: $r=75\text{mm}$, $t=0.4\text{mm}$ for a $t=0.4\text{-mm}$ spherical shell, $t=0.7\text{mm}$ for a $t=0.7\text{-mm}$ spherical shell, $\rho_{steel} = 7930\text{ kg/m}^3$, $\rho_{water} = 1000\text{ kg/m}^3$, $g=9.8\text{ m/s}^2$. Therefore, the net buoyancy of a $t=0.4\text{-mm}$ spherical shell is 15.12N, whereas the results of calculation can be approximately is 13.50N for a $t=0.7\text{-mm}$ spherical shell. To minimize this effect, each spherical shell was encased in a string bag connected to a ballast pig. The weight of the pig was slightly higher than the buoyant load of the spherical shell. The shell, bag, and pig were then immersed together in a cylindrical pressure chamber with a 200-mm inner diameter, 400-mm total length, and 20-MPa maximum pressure. The chamber (located at Jiangsu University of Science and Technology) entailed using water as a pressurizing medium. The pressure inside the chamber was controlled automatically by a programmable logic controller and measured using a pressure transducer. All the spherical shells

failed suddenly with substantial decreases in pressure. Thus, determining the buckling load was very simple.



(a) Photograph and schematic

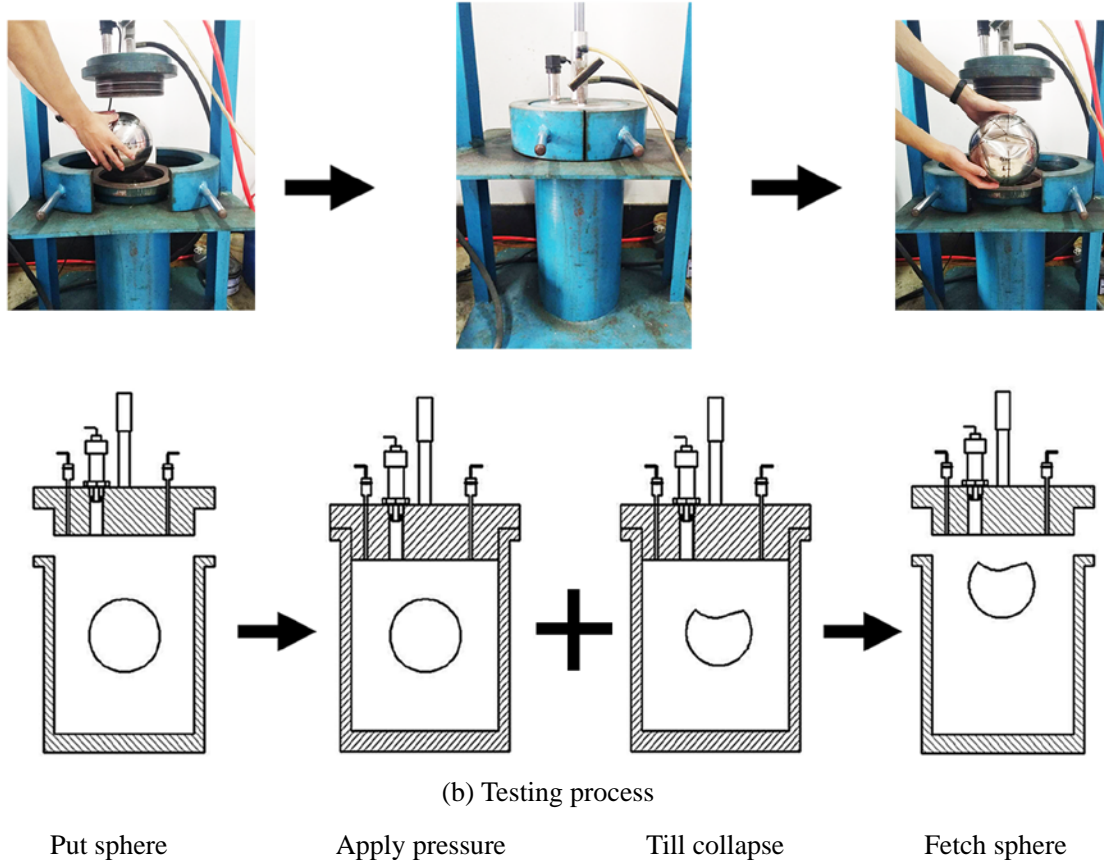


Fig.2-11 Test set-up and testing process

2.3.2 Material properties

In cases of uniform external pressure, the buckling behaviors of spherical shells are determined according to the compression stress–strain behavior of the relevant material. However, experiments to demonstrate such behaviors with thin-walled structures are extremely difficult to conduct. Therefore, the compression behavior of steel is assumed to be the same as its tension behavior. This hypothesis has been frequently used in the buckling prediction of various shells of revolution loaded by external pressure [18, 20, 21]. Thus, the material properties of steel sheets can be established by testing a series of flat tension coupons.

The coupons for this work were designed and tested according to Chinese Standard (GB/T 228.1-2010) [2], which is in line with ISO 6892-1: 2009 [22]. They were cut along the rolling directions of the same sheets that were used to manufacture spherical shells for ensuring accurate material data. Five coupons were selected for each thickness and subjected to uniaxial tension. Two of them were strain-gauged in the transverse and longitudinal directions to obtain Poisson ratio (ν) for the material and to verify the extensometer readings. The average values were 0.277 for the 0.4-mm-thick sheet and 0.291 for the 0.7-mm-thick sheet. Other coupons were tested to obtain accurate stress–strain curves, which can be demonstrated in the following form:

$$\sigma = E\varepsilon, \text{ for } \sigma < \sigma_y \quad (2-17a)$$

and

$$\sigma = \sigma_y \sqrt[k]{\left(\frac{E\varepsilon}{\sigma_y} - 1\right)^n} \quad (2-17b)$$

where E is Young modulus, σ_{yp} is the yield strength based on 0.2% proof stress, and n and k are the strain hardening parameters. The values of these coefficients, as well as the average values, are listed in Table 2-5. The testing coupons were numbered and named according to the thickness and coupon number; one name, for example, was t0.4-c1, where t0.4 indicates that the thickness of the sheet was 0.4 mm, and c1 indicates that the coupon number was one. The variance of coefficients for each thickness was very small.

Table 2-5 Material properties of 304 stainless steel obtained from uniaxial tension tests (E -Young modulus; σ_{yp} -yield strength; n and k -strain hardening parameter).

	E (GPa)	σ_{yp} (MPa)	n	k
t0.4-c1	193.1	250.9	0.108	4.154
t0.4-c2	188.4	241.4	0.101	3.896
t0.4-c3	190.5	246.2	0.091	4.319
t0.4-average	190.7	246.1	0.100	4.123
t0.7-c1	187.2	288.5	0.081	4.291
t0.7-c2	180.3	292.0	0.088	4.733
t0.7-c3	197.1	294.2	0.118	4.972
t0.7-average	188.2	291.6	0.096	4.665

2.4 Buckling analysis of spherical shells

Previous studies have indicated that the experimental buckling loads of spherical shells are lower than theoretical predictions [23, 24]. This phenomenon may result from inevitable geometric imperfections and from nonlinear material properties. This problem of classical mechanics is far from being solved; the buckling analysis of spherical shells remains to be vivid and is still challenging.

This section reports how the buckling loads and final collapsed modes of a family of spherical shells were determined from hydrostatic tests. The results of analytical and numerical investigations into these shells are presented and compared with the experimental findings. The effects of constitutive models on the buckling load are discussed.

2.4.1. Experimental and analytical results

The experimental buckling loads are listed in column 2 of Table 2-6, and graphed in Fig.2-12. Photographs of the final collapsed modes for 10 spherical shells are presented in Fig.2-13. Notably, the buckling load of the t0.7-2 spherical shell was not recorded because of an incorrect operation during the testing process. However, the final collapsed mode of this shell was still obtained. The buckling loads of the 0.4-mm-thick spherical shells ranged between 1.330 and 1.956 MPa, whereas the 0.7-mm-thick shell buckling loads ranged between 3.178 and 4.692 MPa. The buckling loads of the 0.7-mm-thick shell loads were more than twice those of the 0.4-mm-thick shell loads. This variance mainly affected by the ratio of the average

wall thickness (t_{ave}) to the average radius (r_{ave}), as illustrated in Fig.2-12. The experimental buckling load increased monotonically with an increase in t_{ave}/r_{ave} . As shown in Fig.2-13, the final collapsed modes of all shells are identical, and all of them have the form of a local dent because of the high ductility of stainless steel and the initial geometric imperfections of the shells. This failure mode is consistent with previous experimental results regarding shells of revolution with a positive Gaussian curvature, such as those for spherical shells reported by Quilliet [25], for ellipsoidal shells reported by Healey [26], and for barreled shells reported by Blachut [21, 27].

Table2-6 Experimental (p_{test}), analytical (p_{zoelly}), and numerical ($p_{ABAQUS}^{elastic-plastic}$) buckling loads of spherical shells. The analytical and numerical values were normalized by the experimental values in parentheses.

	P_{test} (MPa)	p_{zoelly} (MPa)	$P_{ABAQUS}^{elastic-plastic}$ (MPa)
t0.4-1	1.708	7.586(4.44)	1.745(1.02)
t0.4-2	1.956	7.968(4.07)	1.946(0.99)
t0.4-3	1.773	7.749(4.37)	1.708(0.96)
t0.4-4	1.330	6.795(5.11)	1.332(1.00)
t0.4-5	1.594	7.313(4.59)	1.708(1.07)
t0.7-1	3.178	21.089(6.64)	3.155(0.99)
t0.7-2	NA	21.384(NA)	4.317(NA)
t0.7-3	4.496	21.809(4.85)	4.716(1.05)
t0.7-4	4.692	21.976(4.68)	4.397(0.94)
t0.7-5	3.974	21.412(5.39)	4.006(1.01)

A theory derived by Zoelly [6] predicts the elastic buckling load (p_{cr}) of spherical shells, which is obtained using

$$p_{cr} = \frac{2E}{\sqrt{3(1-\mu^2)}} \left(\frac{t}{r} \right)^2 \quad (2-18)$$

where the wall thickness t , radius r , Young modulus E , and Poisson ratio μ are assumed to be average values of the experimental results (Tables 2-3 and 2-5). This analytical formula is widely accepted in ocean and aerospace engineering as a rule for designing spherical shells [4, 23, 28]. The results of Eq. 2-18 are listed in column 3 of Table 2-6, followed by the ratio of the experimental load p_{test} to the elastic buckling

load p_{zoelly} in parentheses. As shown in the table, the experimental load of a spherical shell was as little as 15.07%–24.55% of that shell's elastic buckling load, confirming that the spherical shell is a highly imperfection-sensitive structure. A small imperfection may lead to a substantial decrease in the magnitude of the buckling load. Furthermore, the average ratio of the experimental load p_{test} to the elastic buckling load p_{zoelly} for 0.4-mm-thick spherical shells was approximately 3% lower than the ratio for 0.7-mm-thick shells. It appears that the nonlinear properties of spherical shells' materials may play a major role in the buckling behaviors of shells with various wall thicknesses.

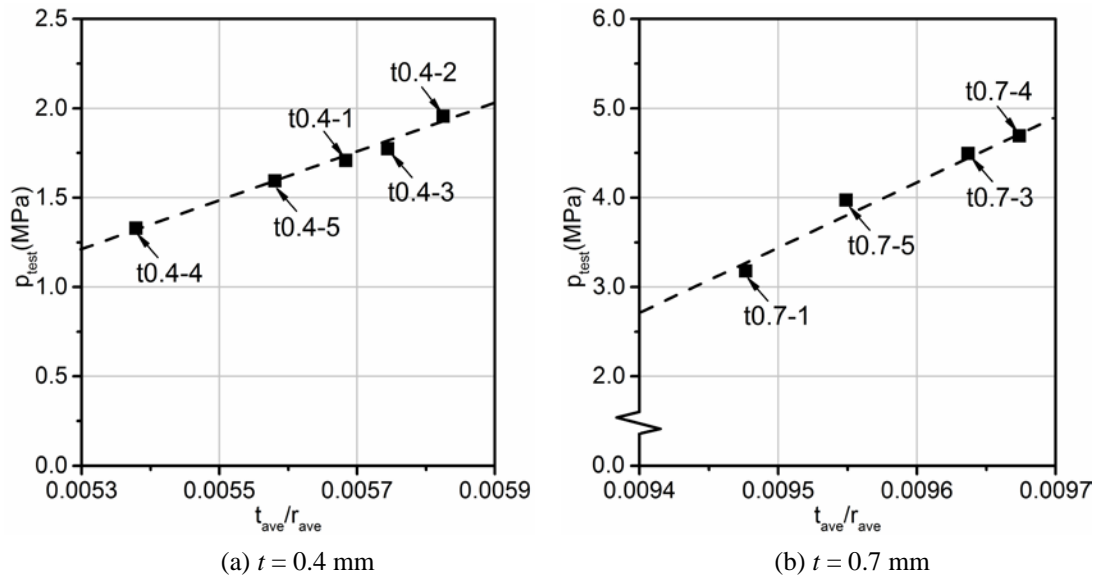


Fig.2-12 Plots of experimental buckling load versus ratio of average wall thickness (t_{ave}) to average radius (r_{ave}) of spherical shells

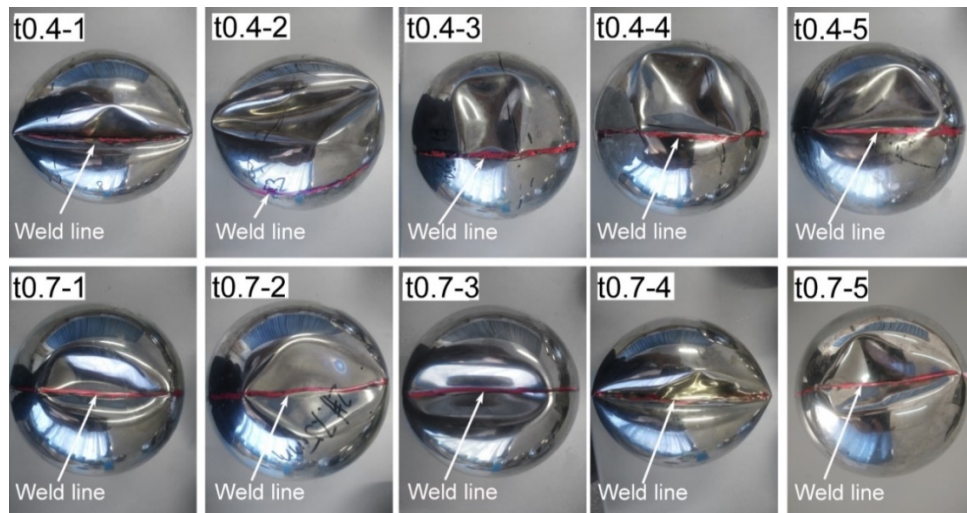


Fig.2-13 Views of spherical shells after collapse caused by external hydrostatic pressure

2.4.2. Comparison between experimental and numerical results

Prior work has demonstrated the effectiveness of the finite element method in predicting the buckling behaviors of thin-walled structures. Schmidt, for example, suggested that the real buckling load of a shell can be determined using geometrically and materially nonlinear analyses of shells that include imperfections [1, 13]. However, most studies have focused on equivalent geometric imperfections, such as eigenmode imperfections, in numerically analyzing the buckling of spherical shells.

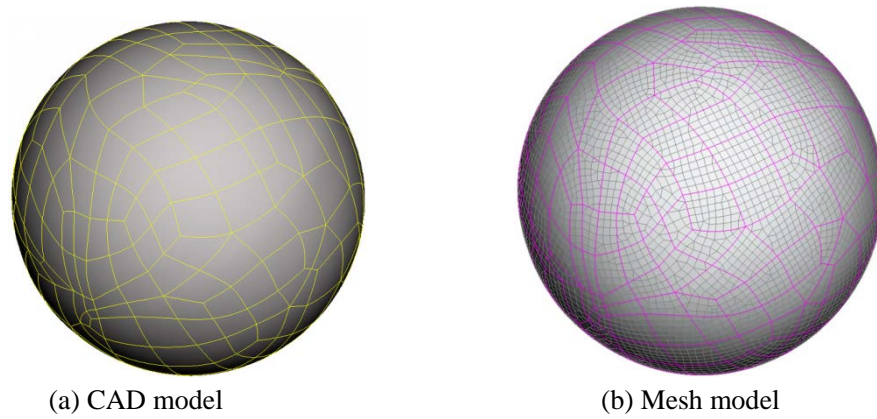


Fig.2-14 Scanned CAD model for a t0.4-1 spherical shell and its mesh

Table 2-7 Number of the FE elements for each spherical shell.

	t0.4-1	t0.4-2	t0.4-3	t0.4-4	t0.4-5	t0.7-1	t0.7-2	t0.7-3	t0.7-4	t0.7-5
S4	6746	6643	6820	6298	6264	6430	6348	6287	6436	6447
S3	1064	448	1110	1134	1064	1118	1212	1180	1170	1216

In this study, we carried out nonlinear buckling analysis for the same types of spherical shells as would be tested for deterministic imperfections. The analysis was performed using the arc length method in ABAQUS software [29]. The finite element model of each spherical shell was established according to the real geometric shape obtained from the experimental data. The shapes and sizes of the initial geometric imperfections were automatically included in the models. A fully integrated S4 and S3 shell was selected to avoid hourglassing and the number of elements was determined using mesh density convergence analysis in line with [5], shown in Fig.2-14 and Table 2-7. The mesh of each spherical shell was generated freely based on its real geometry in the form of numerous small surface pieces, where the local apex area was included.

In all the analyses, a $p_0 = 1 \text{ MPa}$ external pressure was applied on the whole area of each shell. To avoid rigid body motion, three random spatial points were respectively constrained in the three orthogonal directions. These constraints did not lead to over constrained models because the pressure was equally applied. The steel was assumed to be elastic-plastic as described in Eq.2-17. In addition, the average wall thickness (column 4 of Table 2-3) and material properties (Table 2-5) were defined in the analyses. This averaging assumption has been implemented by Blachut et al. and resulted in a good agreement between experiment and theory [30]. Fig.2-15 and the final column of Table 2-6 show the results obtained using numerical analysis.

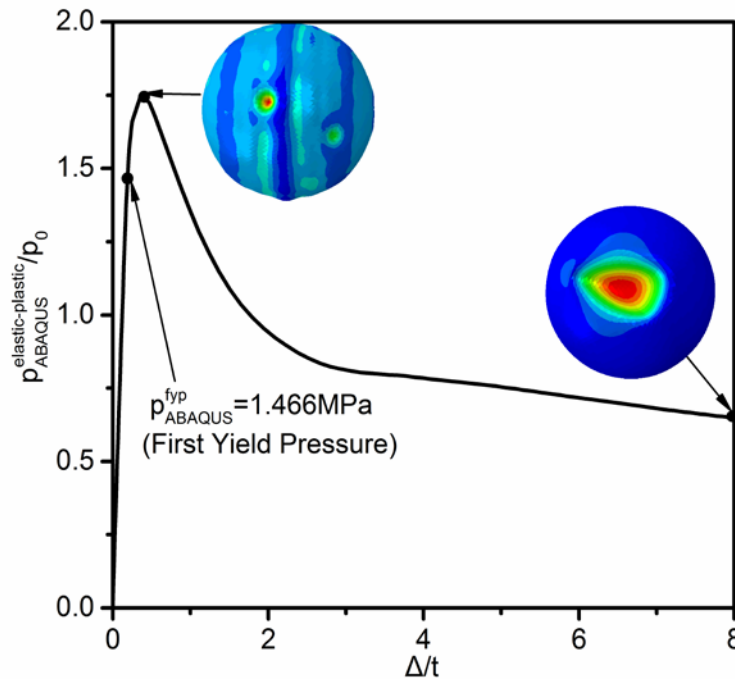


Fig.2-15 Equilibrium path, critical buckling mode, and postbuckling mode of a t0.4-1 spherical shell

Because the equilibrium paths, critical buckling, and postbuckling modes of all the analyzed shells were similar, detailed results are provided only for the case of t0.4-1. Fig.2-15 shows the equilibrium path of a shell; the vertical axis shows the applied load normalized by the initial applied load $p_0 = 1 \text{ MPa}$, and the horizontal axis shows the maximum deflection (Δ) normalized by the wall thickness (t). The path has an unstable characteristic that is typical of shell structures: At first, the load increases nearly linearly with an increase in the deflection up to a peak corresponding to the

critical buckling load, beyond which the load decreases sharply. The same figure shows that the buckling and post buckling modes are similar and assume the form of a local dent. This may have been caused by the initial deterministic imperfections of the shell. Comparing Fig.2-13 and 2-15 show that the predicted final failure mode is highly consistent with the experimental one. In addition, as indicated in the final column of Table 2-6, very good correlation between the numerical buckling loads and the experimental ones was obtained ($\pm 7\%$). This slight difference may be attributed to small variations of the material properties for the steel sheets, in addition to the assumption of the average wall thickness used to perform numerical calculation. These findings indicate that the real buckling resistance of a spherical shell can be determined numerically on the basis of its true geometry as well as its average wall thickness and material properties.

Table 2-8 First yield load P_{ABAQUS}^{fyd} values of spherical shells and the ratio of the first yield and critical buckling load $P_{ABAQUS}^{fyd} / P_{ABAQUS}^{elastic-plastic}$.

	P_{ABAQUS}^{fyd} (MPa)	$P_{ABAQUS}^{fyd} / P_{ABAQUS}^{elastic-plastic}$
t0.4-1	1.466	0.840
t0.4-2	1.407	0.723
t0.4-3	1.531	0.896
t0.4-4	0.907	0.681
t0.4-5	1.528	0.895
t0.7-1	2.392	0.758
t0.7-2	3.401	0.788
t0.7-3	3.904	0.828
t0.7-4	3.905	0.888
t0.7-5	3.402	0.849

In the same figure, the first yield load of t0.4-1 is plotted at the value of 1.466 MPa, which was obtained using the post processing procedure as in Ref. [31]. The first yield load was approximately 84% of the critical buckling load. At the first stage of testing up to this value, the spherical shell had an elastic characteristic. At the second stage of testing higher than this value, the spherical shell appeared to be elastic-plastic. This phenomenon was observed for all the cases shown in Table 2-8. For spherical

shells, the ratio of the first yield to the critical buckling load, $P_{ABAQUS}^{fyd} / P_{ABAQUS}^{elastic-plastic}$, varied between 0.681 and 0.895. It is suggested that all the spherical shells could lose stability within the elastic-plastic regime. This finding is similar to those regarding medium-thick conical shells subjected to external pressure [20].

2.4.3. Effect of constitutive models

It is well known that the modeling of materials strongly influences the accuracy of numerical results. Most recent numerical investigations on the buckling of shell structures have assumed the material properties to be either purely elastic [32] or elastic-perfectly plastic [21, 27]. To examine this assumption, the effect of constitutive models on the buckling of spherical shells was investigated in the present study. The same numerical models as those mentioned in Section 2.4.2 were employed, except that the steel was assumed to be elastic and elastic-perfectly plastic. The material parameters were determined on the basis of the average values listed in Table 2-5; 20 models were accounted for. Because the equilibrium paths, critical buckling modes, and post buckling modes of these cases were almost identical with the elastic-plastic results for t0.4-1 shown in Fig.2-15, the effects of constitutive models were examined according to the critical buckling load only. Table 2-9 shows the buckling loads $P_{ABAQUS}^{elastic}$ and $P_{ABAQUS}^{elastic-perfectly plastic}$ obtained from elastic and elastic-perfectly plastic assumptions, respectively, and the values normalized by elastic-plastic $P_{ABAQUS}^{elastic-plastic}$ and experimental p_{test} buckling loads are in parentheses.

As shown in Table 2-9, the elastic assumption yielded an increase of 53.98%–135.55% in the magnitude of the buckling load over that of the elastic-plastic assumption. A fairly large difference existed between the results obtained according to the purely elastic assumption and those of the experiments. This finding indicates that numerical predictions based on the purely elastic assumption are extremely nonconservative and are not suitable for engineering applications. However, the differences between the elastic and elastic-plastic results for 0.4-mm-thick spherical shells are always higher than those for 0.7-mm-thick shells. This implies that the failures of spherical shells vary gradually from elastic buckling to elastic-plastic

buckling as the wall thicknesses increase. It is more reasonable to include plastic material properties when performing buckling analysis on a medium-thick shell structure.

Table 2-9 Buckling loads of spherical shells obtained from elastic and elastic-perfectly plastic models. Values in parentheses were normalized by the elastic-plastic and experimental buckling loads, respectively.

	$P_{ABAQUS}^{elastic}$ (MPa)	$P_{ABAQUS}^{elastic-perfectly\ plastic}$ (MPa)
t0.4-1	3.146(1.80,1.84)	1.722(0.99,1.01)
t0.4-2	3.389(1.74,1.73)	1.823(0.94,0.93)
t0.4-3	2.941(1.72,1.65)	1.630(0.95,0.92)
t0.4-4	2.051(1.54,1.54)	1.332(1.00,1.00)
t0.4-5	3.174(1.86,1.99)	1.712(1.00,1.07)
t0.7-1	5.930(1.88,1.87)	2.953(0.94,0.92)
t0.7-2	9.549(2.21 ,NA)	4.206(0.97, NA)
t0.7-3	10.174(2.16,2.31)	4.483(0.95,1.02)
t0.7-4	10.357(2.36,2.21)	4.383(1.00,0.93)
t0.7-5	9.035(2.26,2.27)	3.953(0.99,0.99)

As shown in Table 2-9, the elastic-perfectly plastic predictions deviated from the elastic-plastic predictions by as little as 6%. Very good agreement was obtained between the elastic-plastic and elastic-perfectly plastic results. The maximum difference between a prediction from the elastic-perfectly plastic assumption and that from the experiment was only 8%. This confirms that the buckling of a shell is greatly determined according to its stress behavior, particularly its yield [33]. It could be inferred that aside from the elastic material properties, the buckling load of a shell strongly depends on the yield strength of the material. This finding extends those of Bluchat [21, 27], confirming that the elastic-perfectly plastic assumption can be made in the buckling analysis of shells, and tends to result in extremely accurate predictions.

2.4.4. Effect of geometrical imperfections

Measurements carried out on the ten laboratory scale models have shown that their geometry has been ‘near-perfect’. In practice however shape deviation from perfect geometry do occur. These will, by and large, appear either during manufacturing or

exploitation. An attempt has therefore been made to compare the sensitivity of buckling pressures, for tested and analyzed model geometries, to the initial shape deviations from perfect geometry. The initial deviations from perfect geometry can take various shapes and magnitudes. Traditionally, the most critical shape deviations are considered in order to ascertain the possible loss of the load carrying capacity. For this purpose, initial geometrical imperfections have been assumed in the form of the first eigenmode imperfection.

To further study the load-carrying capacity of spherical shell, a series of numerical analyses—namely linear elastic bifurcation (eigenvalue) analysis (LBA), geometrically materially nonlinear analysis with imperfections included (GMNIA) were performed according to EN 1993-1-6 (2007)[1]. The radii of spherical shells were assumed be 75 mm; the thickness of two different series spherical shells were assumed be 0.419 mm and 0.7172 mm, respectively. For GMNIA, the first eigenmode derived from the LBA of the perfect geometry was set as the initial geometrical imperfection. The imperfection size δ was assumed to be 0.2 mm, 0.4 mm, 0.6 mm, 0.8 mm and 1.0 mm. The material properties, load, and boundary conditions of all domes were the same as those of the four manufactured egg-shaped domes discussed in Section 2.3.2. For each model, mesh convergence examination was conducted through LBA; the number of elements obtained was 6534. For LBA, elastic material modelling was assumed, whereas elastic–perfectly plastic material was assumed for GMNIA.

According to the LBA, the linear buckling load (p_{LBA}) of the spherical shell with 0.419 mm thickness was 7.59 MPa, and that of 0.7172 mm spherical shell was 21.55 MPa. The number of circumferential waves was $n = 21$ for the spherical shell with 0.4 mm thickness, $n = 17$ for the spherical shell with 0.7 mm thickness (Fig.2-16); it seems to be more sensitive for the thinner spherical shell. Because the equilibrium paths, critical buckling, and postbuckling modes of the shells obtained through the nonlinear analyses were identical, only the GMNIA results for the shell with imperfection size $\delta = 0.6$ were reported herein. All spherical shell tended to be unstable and exhibited similar postbuckling modes (a local dent; Fig.2-17). The

critical buckling modes of spherical domes were similar to their linear buckling modes. The collapse loads of these shells decreased substantially relative to their linear buckling loads, which may be attributed to the material nonlinearity and initial geometric imperfections.

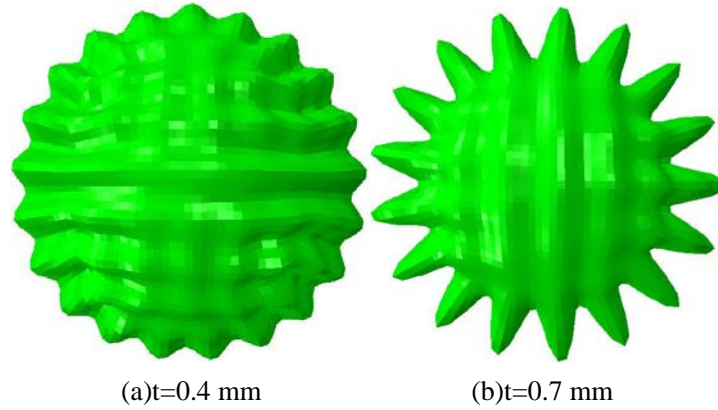


Fig.2-16 Linear buckling modes of spherical pressure hulls

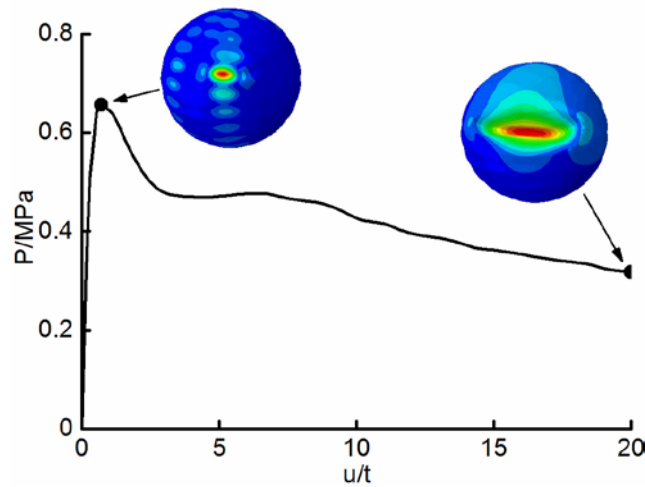


Fig.2-17 Equilibrium path, critical buckling mode, and postbuckling mode of a spherical shell with $\delta = 0.6$

Buckling loads of spherical shells obtained from GMNIA are listed in Table 2-10 and Fig.2-18. It could be seen that the spherical shell was very sensitive to imperfection. At the same time, the thinner shell was lower in the case of the same imperfection amplitude. This indicates that a thinner structure for spherical shell seems to be more sensitive to imperfection. First eigenmode imperfection was considered to be the worst initial imperfect forms used for many standard. The related formulae introduced in this chapter were also based on first eigenmode imperfections.

In fact, the calculation results of first eigenvalue imperfection were far lower than the numerical solutions under deterministic imperfection, (see Fig.2-18).

Table 2-10 Buckling loads of spherical shells obtained from GMNIA, the parentheses show non-dimensional buckling load that is the ratio of each buckling load to the one in the case.

$\delta=0$ mm.

δ	$p_{GMNIA}^{0.4mm}$ (MPa)	$p_{GMNIA}^{0.7mm}$ (MPa)
0	2.473 (1.00)	5.593 (1.00)
0.2	1.228 (0.50)	3.784 (0.68)
0.4	0.881 (0.36)	2.855 (0.51)
0.6	0.656 (0.27)	2.272 (0.41)
0.8	0.552 (0.22)	1.814 (0.32)
1	0.482 (0.19)	1.514 (0.27)

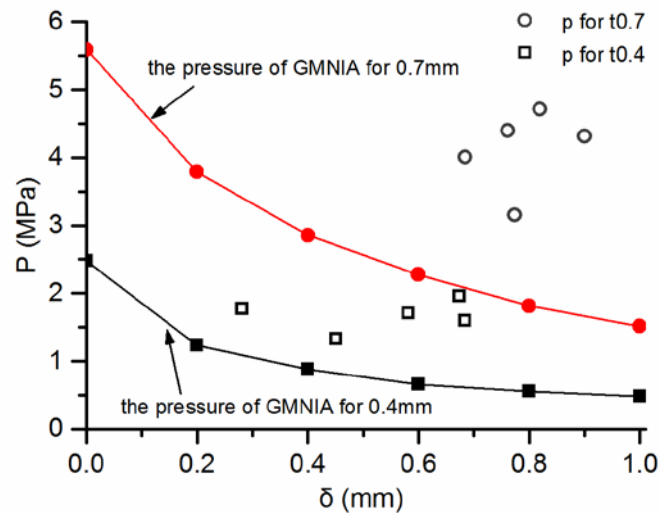


Fig.2-18 Buckling pressure from GMNIA and numerical analyses with determining imperfection

2.5 Summary

In the present chapter, the results of analytical and numerical study into the buckling and post-buckling performance of titanium alloy spherical pressure hulls were presented, along with ten laboratory scale stainless spherical shells for validation. The conclusions are as follows:

(1) The linear elastic buckling performance of geometrically perfect pressure hulls was described numerically and analytically. Good agreement was obtained between the numerical results obtained from the linear elastic buckling analyses and analytical ones obtained from the medium-thick-walled equation. The linear buckling mode of

pressure hulls was typical for highly symmetrical spherical shells: several circumferential and meridional half waves. The number of the wave crest decreased with an increase in the wall thickness. The nonlinear elastic-plastic buckling performance of geometrically perfect hulls was analyzed numerically. Hulls buckled in the elastic-plastic range, the buckling loads of which significantly reduced due to the decrease of the material plasticity. The plasticity reduction factor was a negative exponential function of the wall thickness-to-radius ratio with an amplification factor linearly increasing with an increase in the yield strength. An extremely distinct difference was obtained between results obtained using the elastic-plastic and elastic-perfectly plastic material modelling.

(2) The nonlinear elastic-plastic buckling performance of geometrically imperfect pressure hulls was evaluated numerically. Hulls buckled in the elastic-plastic range, which had an unstable character and a dimple post buckling mode. Hulls were imperfection-sensitive structures, the buckling loads of which significantly reduced due to the increase of the imperfection size. The geometrical imperfection reduction factor was a piecewise linear function of the wall thickness-to-radius ratio pieced in three ranges. The slope and intercept of this function could be obtained from several charts involving the yield strength and the imperfection size-to-radius ratio. According to the buckling of geometrically perfect and imperfect hulls, a mechanism formula was derived semi-analytically. This formula extended the previous phenomenological model and could be used to evaluate the load-carrying capacity of deep sea spherical pressure hulls at preliminary design stage. It is hoped that this work could promote an upsurge on the buckling of medium-thick spherical shells under external pressure and motivate further studies into the effect of other imperfections and materials on their buckling performance.

(3) Very good agreement was obtained among the elastic-plastic, elastic-perfectly plastic, and experimental results of ten stainless spherical shells. The elastic-perfectly plastic assumption resulted in a highly accurate prediction. The elastic assumption yielded a fairly large increase in the magnitude of the buckling load above the elastic-plastic assumption and experiment. The experimental and numerical data

indicates that the real load-carrying capacity of a spherical shell can be obtained numerically from measured geometric shape and average wall thickness, as well as from the assumption of elastic-perfectly plastic material properties. Also, the first buckling mode imperfection appears to be worse than deterministic imperfection caused by fabrication, which could result in a conservative design at preliminary design stage of spherical shells.

However, although spherical pressure hulls have an ideal mechanical performance and are widely applied in deep sea submersibles, they are highly sensitive to inevitable initial geometrical imperfections possibly caused by manufacture, installation, transportation, and service, and have disadvantages of difficult interior arrangement and poor hydrodynamics. Most importantly, various holes, including manned hole, view window, and wire through hole, must be opened on the pressure hulls. Also, numerous components need to be installed on both outer and inner surfaces. All of these requirements considerably destroy the symmetry of spherical configuration and cause some critical disadvantages and difficulties of design. Therefore, it is even necessary to put forward an untypical configuration, which can overcome the disadvantages of spherical configuration.

References

- [1] [CEN] Comité Européen de Normalisation, EN 1993-1-6: Eurocode 3 – Design of steel structures – Part 1.6: Strength and Stability of shell structures. Brussels: CEN. (2007)
- [2] [SAC] Standardization Administration of the People's Republic of China, GB/T 228.1: Metallic materials – Tensile Testing – Part 1: Method of Test at Room Temperature, China: SAC. (2010)
- [3] L. Li, R. Wang, M. Yu, Z. Wang, Nonlinear finite element analysis of pressurized spherical shell for manned deep submersible, *Shipbuild. China.* 46 (2005) 11-18.
- [4] [CCS] China Classification Society, Rules for the Classification and Construction of Diving Systems and Submersibles, Beijing: CCS. (2013).
- [5] P. Jasion, K. Magnucki, Elastic buckling of clothoidal-spherical shells under external pressure - Theoretical study, *Thin-Walled Struct.* 86 (2015) 18-23.
- [6] R. Zoelly, Über ein Knickungs problem an der Kugelschale, (1915).
- [7] C.M. Wang, C.Y. Wang, Exact solutions for buckling of structural members, CRC press, 2004.
- [8] Z. Wang, R. Wang, M. Yu, L. Li, The influence of the initial imperfections on the ultimate

- strength of manned deep-sea submersible pressure sphere hull, *Shipbuild. China.* 48 (2007) 45-50.
- [9] O. Ifayefunmi, J. Blachut, Combined stability of unstiffened cones—theory, experiments and design codes, *Int. J. Press. Vessel. Pip.* 93 (2012) 5-68.
 - [10] J. Zhang, J. Gao, W. Wang, W. Tang, T. Zhou, Investigation on mechanical properties of deep sea spherical pressure hull, *Shipbuild. China.* 56 (2015) 129-140.
 - [11] J. Blachut, Experimental perspective on the buckling of pressure vessel components, *Appl. Mech. Rev.* 66 (2014) 10803.
 - [12] O. Ifayefunmi, J. Blachut, Instabilities in imperfect thick cones subjected to axial compression and external pressure, *Mar. Struct.* 33 (2013) 297-307.
 - [13] H. Schmidt, Stability of steel shell structures: General Report, *J. Constr. Steel Res.* 55 (2000) 159-181.
 - [14] B.B. Pan, W.C. Cui, Y.S. Shen, T. Liu, Further study on the ultimate strength analysis of spherical pressure hulls, *Mar. Struct.* 23 (2010) 444-461.
 - [15] P. Jasion, Stability analysis of shells of revolution under pressure conditions, *Thin-Walled Struct.* 47 (2009) 311-317.
 - [16] J. Zhang, M. Zhang, W. Tang, W. Wang, M. Wang, Buckling of spherical shells subjected to external pressure: A comparison of experimental and theoretical data, *Thin-Walled Struct.* 111 (2017) 58-64.
 - [17] W.C. Cui, F. Wang, B.B. Pan, Y. Hu, Q.H. Du, Issues to be solved in the design, manufacture and maintenance of full ocean depth manned cabin, *Adv Eng Res.* 11 (2016) 1-29.
 - [18] Schmidt H, Swadlo P. Part C - Shells of revolution with Arbitrary meridional shapes - Buckling design by use of computer analysis, ECSC contract No.7210-SA/208: Enhancement of ECCS design recommendations and development of Eurocode 3 parts related to shell buckling: Final Report, Universität GH Essen, FB Bauwesen • Stahlbau; 1996.
 - [19] B.B. Pan, W.C. Cui, Y.S. Shen, Experimental verification of the new ultimate strength equation of spherical pressure hulls, *Mar. Struct.* 29 (2012) 169-176.
 - [20] J. Blachut, A. Muc, J. Ryś, Plastic buckling of cones subjected to axial compression and external pressure, *J. Press. Vessel Technol.* 135 (2013) 011205.
 - [21] J. Blachut, Optimal barreling of steel shells via simulated annealing algorithm, *Comput. Struct.* 81 (2003) 1941-1956.
 - [22] [ISO] International Organization for Standardization, SO 6892-1: Metallic Materials – Tensile Testing - Part 1: Method of Test at Room Temperature. Geneva: ISO. (2009)
 - [23] B.-B. Pan, W.-C. Cui, A comparison of different rules for the spherical pressure hull of deep manned submersibles, *J. Ship Mech.* 15 (2011) 276-285.
 - [24] T. Von Kármán, The buckling of spherical shells by external pressure, *J. Aeronaut. Sci.* 7 (1939) 43-50.
 - [25] C. Quilliet, Depressions at the surface of an elastic spherical shell submitted to external pressure, *Phys. Rev. E.* 74 (2006) 046608.
 - [26] J.J. Healey, Hydrostatic tests of two prolate spheroidal shells, *J. Ship Res.* 9 (1965) 77-78.
 - [27] J. Blachut, Buckling of externally pressurised barrelled shells: A comparison of experiment and theory, *Int. J. Press. Vessel. Pip.* 79 (2002) 507-517.

- [28] NASA SP-8032. Buckling of thin-walled doubly curved shells, National Aeronautics and Space Administration, Washington, 1969.
- [29] K. Hibbitt, S. Inc, ABAQUS - Theory and Standard User's Manual Version 6.3, USA, 2006.
- [30] J. Blachut, G.D. Galletly, D.N. Moreton, Buckling of near-perfect steel torispherical and hemispherical shells subjected to external pressure, AIAA J. 28 (1990) 1971-1975.
- [31] J. Blachut, O. Ifayefunmi, Buckling of unstiffened steel cones subjected to axial compression and external pressure, J. Offshore Mech. Arct. Eng. 134 (2012) 031603.
- [32] P. Jasion, K. Magnucki, Elastic buckling of Cassini ovaloidal shells under external pressure - theoretical study, Arch. Mech. 67 (2015) 179-192.
- [33] M. Barski, J. Kruzelecki, Optimal design of shells against buckling under overall bending and external pressure, Thin-walled Struct. 43 (2005) 1677-1698.

Chapter 3 Bionic design of egg-shape pressure hulls

Spherical shells are presently most extensively used for pressure hull in the deep manned submersible. However, it is known that the spherical pressure hull has disadvantages of difficult interior arrangement/low space efficiency, and is highly sensitive to geometric imperfections. These limitations have prevented further developments of the deep manned submersible to some extent. In order to overcome these limitations, this chapter is devoted to the bionic design of egg-shaped pressure hulls.

Firstly, to provide a reference for the bionic design of egg-shaped pressure hulls, the geometric properties of goose eggshells were examined. The author measured goose egg sizes and performed statistical tests, and found that the major axis, minor axis, and egg-shape index had normal distributions. The thickness of goose eggshells first increased and then decreased from the blunt end to the sharp end. Then, the shape of each goose eggshell was measured with a 3D scanner. The volume equation, surface equation, and contour function of goose eggshell shape were obtained, exhibiting a highly symmetrical structure.

Secondly, to validate the excellent load-carrying capacity of eggshells, mechanical characteristics of 5 goose eggshells under uniform external pressure were investigated. The contour sizes of goose eggshells were shown with the use of 3D scanning. The Young modulus and Poisson ratio of goose eggshells with combination of compression testing and theoretical calculation were given. The collapse load of goose eggshells under uniform external pressure by hydraulic testing was presented. The thickness and density of goose eggshells with the use of measuring apparatus were measured. The buckling and strength analyses of 5 goose eggshells were carried out with using finite element methods.

Finally, two egg-shaped pressure hulls respectively with the constant and variable thickness were proposed, where the equivalent spherical pressure hull was also presented for comparison. Buckling of these pressure hulls with geometric

imperfections were further studied using numerical analyses at a given design load. It was found that, with respect to hull strength, buoyancy reserve, and space efficiency etc., egg-shaped pressure hulls could be optimally coordinated, which appear to be leading to overall better performance than the spherical pressure hull. Especially, the egg-shaped pressure hull is quite less sensitive to the geometric imperfections, making it more convenient and low costly to form the hull in manufacturing or to open holes in applications. It is anticipated that egg-shaped pressure hulls will play a key role in the future developments of deep-sea manned submersibles.

3.1 Geometric properties of goose eggshells

A sample of 333 fresh eggs was collected from 2-year-old geese, as shown in Fig.3-1. The geese were raised using free-range technology at a commercial breeding farm in Jiangshan, Zhejiang province, China. The goose eggs were numbered from 1 to 333. First, the sizes of the major and minor axes of all the goose eggs were measured to analyze the shape index distributions. Second, the 3D shapes of the goose eggs numbered 1–50 were scanned to examine the axial symmetry, meridian, volume, wall thickness and surface area. Finally, wall thicknesses of the goose eggs numbered 51-100 were measured.

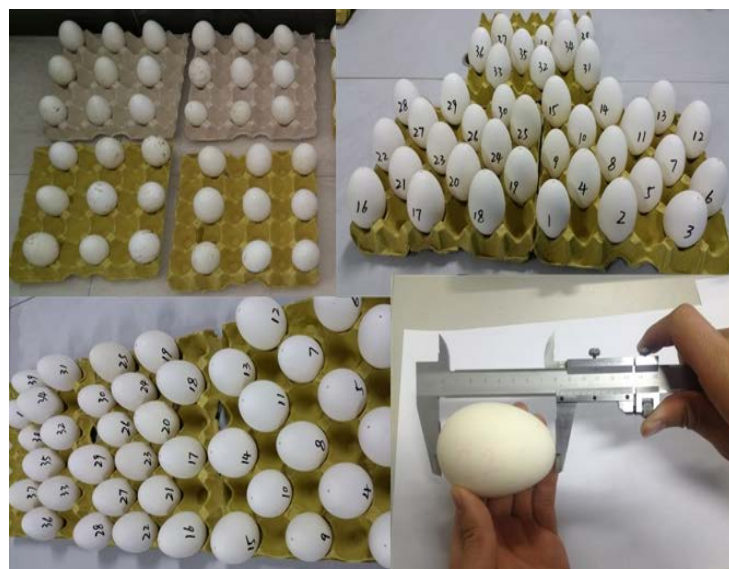


Fig.3-1 Photographs of goose eggs and size measurement

In the geometrical characteristics test, the L and B of goose eggs were measured to

the nearest 0.01 mm by using a digital caliper. Each parameter was measured four times and their averages were used in this study. To obtain more accurate geometric shapes, goose eggs 1–50 were scanned with an Aurum 3D scanner to the nearest 0.004 mm (Fig.3-2). A 3D model was obtained that included contour shape characteristics. Goose eggs 51–100 were then halved along their major axes, and five points were marked along the generatrix of the eggshell (Fig.3-3). Point 1 was located at the top of the blunt end, Point 3 was marked at the equatorial position of the eggshell, and Point 2 was located between them. Point 5 was placed at the top of the sharp end, and Point 4 was located between it and Point 3. The thickness of every point was measured with a screw micrometer to the nearest 0.01 mm. Each point was measured four times and the averages were used in this study.

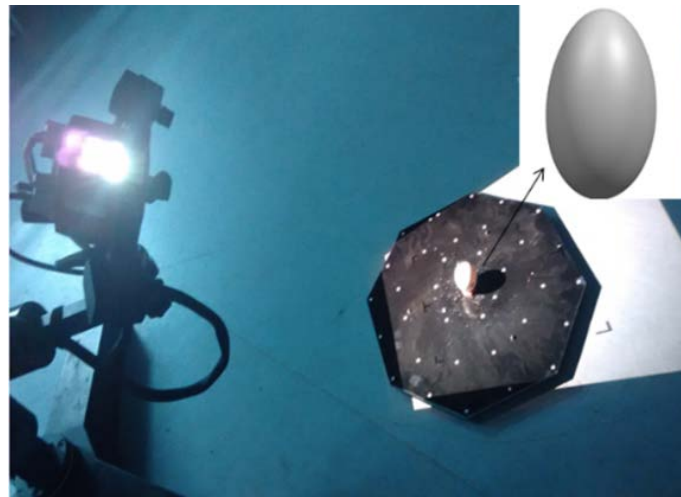


Fig.3-2 Shape scanning of a goose egg

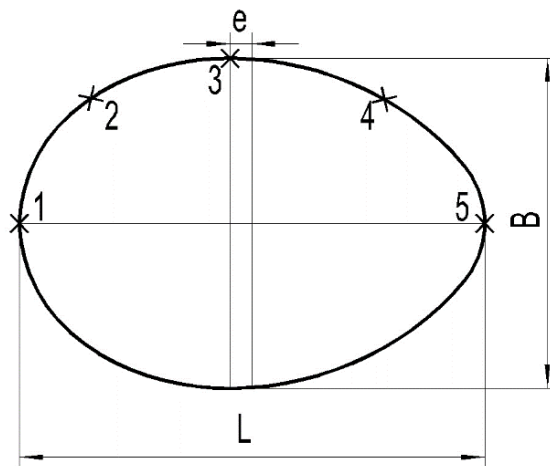


Fig.3-3 Mark points adopted to measure wall thicknesses

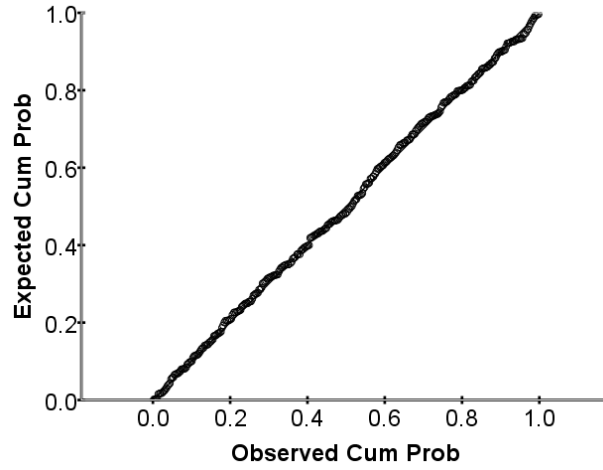
3.1.1 Size of goose eggshells

This type of measurement includes values of L , B , and $SI=B/L$, which are given in Table 3-1. L and B are the most intuitive descriptors of shape parameters. The data for L ranged from 60.79 to 91.02 mm, with an average of 78.26 mm. The data for B ranged from 44.87 to 63.05 mm, with an average of 53.62 mm. The parameter SI is crucial for describing goose egg shape. Eggs were characterized as sharp, normal, or round if they had an SI value of < 0.72 , $0.72-0.76$, or > 0.76 , respectively [1]. Nedomová examined 226 goose eggs and found that their SI was distributed between 55.75% and 108.63%, with an average of 65.03% [2]. This study used more eggs than did the study by Nedomová, and found a distribution of 61%–80%, with an average of 69%. Thus, these results indicate that regionalism influences the geometrical size of goose eggs.

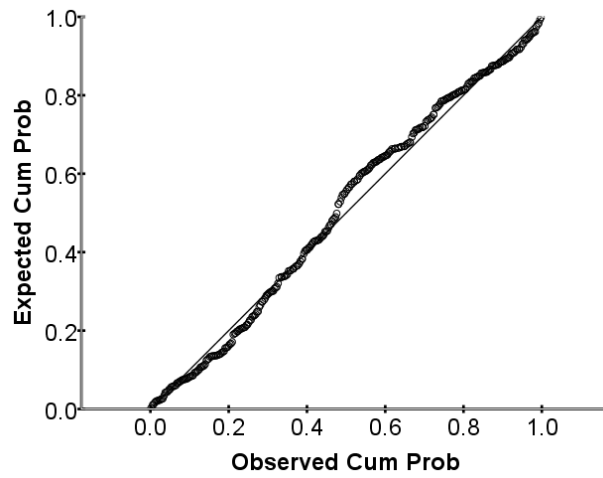
Table 3-1 Geometric size of goose eggs (No. 1-333).

Value	L [mm]	B [mm]	SI
Minimum	60.79	44.87	61%
Mean	78.26	53.62	69%
Maximum	91.02	63.05	80%
St.deviation	4.742	3.159	0.029
Skewness	-0.187	-0.151	0.407
Kurtosis	0.333	-0.499	0.653

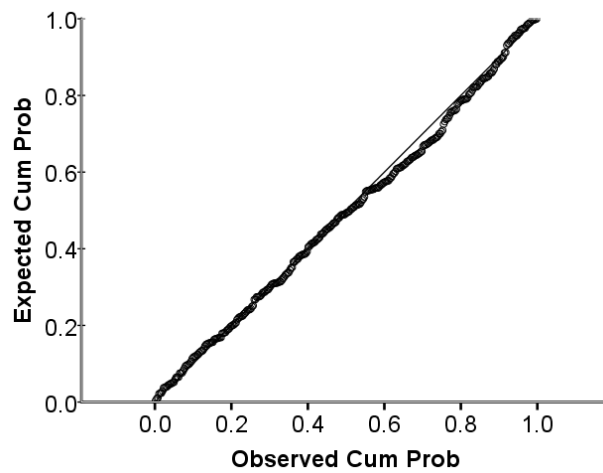
As listed in Table 3-1, the skewness and kurtosis of data for L were -0.187 and 0.333 , respectively. The skewness and kurtosis of data for B were -0.151 and -0.499 , respectively, and for SI were 0.407 and 0.653 , respectively. The data points of the measurement all approximated a straight line in the P-P diagram (Fig.3-4), a test for normal distribution. As a result, the L , B , and SI of goose eggs were found to present normal distributions.



(a) P-P diagram for L



(b) P-P diagram for B



(c) P-P diagram for SI

Fig.3-4 P-P diagram of normal distribution examination

The distribution functions of L , B , and SI were as follows:

$$F(x) = \frac{1}{4.742\sqrt{2\pi}} \int_{-\infty}^x e^{-\frac{(t-78.26)^2}{44.97}} dt \quad (3-1)$$

$$F(x) = \frac{1}{3.159\sqrt{2\pi}} \int_{-\infty}^x e^{-\frac{(x-53.62)^2}{19.96}} dt \quad (3-2)$$

$$F(x) = \frac{1}{0.029\sqrt{2\pi}} \int_{-\infty}^x e^{-\frac{(x-0.69)^2}{0.00168}} dt \quad (3-3)$$

3.1.2 Surface area and volume of goose eggshells

The 3D models of goose eggs were constructed using UG NX software [3]. The test results were obtained for S and V by measuring 3D models directly in the software, and the theoretical calculation results were determined using the equations detailed by Mohsenin [4], as follows:

$$D_g = (LB^2)^{\frac{1}{3}} \quad (3-4)$$

$$A = \pi D_g^2 \quad (3-5)$$

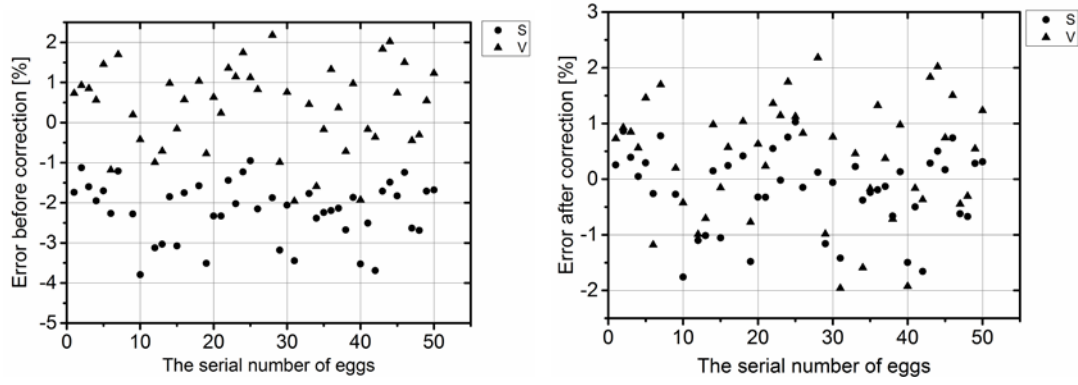
$$V = \frac{\pi}{6} LB^2 \quad (3-6)$$

Table 3-2 Surface area and volume of goose eggs (No. 1-50).

Value	Test		Calculation	
	A [mm ²]	V [mm ³]	A [mm ²]	V [mm ³]
Minimum	9262.98	82017.66	9056.43	81043.11
Mean	11705.49	115043.00	11455.90	115538.30
Maximum	12844.18	133358.60	12701.60	134607.00

The data obtained from the test and theoretical calculations were highly similar (Table 3-2). The largest relative errors of S and V were -3.79% and 2.18%, respectively; their averages were -2.19% and 0.38%, respectively. However, the error of S was greater than that of V. A correction coefficient, $\delta = 1.02$, was introduced to correct the calculation results for S (Eq.3-7). This study maintained an average error of less than 0.5% in calculating S (Fig.3-5). The average error for S was -0.19% after the correction coefficient was used. Therefore, the S and V of goose eggs could be calculated using functions (3-6) and (3-7).

$$A = \pi D_g^2 \delta \quad (3-7)$$



(a) Error before correction.

(b) Error after correction.

Fig.3-5 Error between the theoretical calculation and scanning method

3.1.3 Symmetry of goose eggshells

The 3D scanning model of goose eggs was created using UG NX software. A coordinate system was built in the barycenter of the 3D models. Three cross-sections (M, B, and S) were constructed perpendicular to the major axes (Fig.3-6). The M cross section passed through the barycenter, the B cross-section passed through the middle of the blunt end and barycenter, and the S cross-section passed through the middle of the sharp end and barycenter. Three concentric circles of weft were positioned approximately on the cross sections.

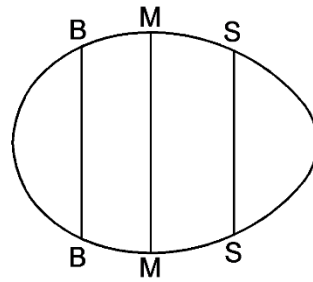


Fig.3-6 Cross sections of the goose egg

A total of 80 equally spaced points were marked on each weft by using CAXA 2013 software to calculate the coordinates of these points. The following formula was used to calculate the radius (Eq.3-8) of each point. The P (Eq.3-9) of each weft and U (Eq.3-10) were then calculated as well.

$$R = \left(x^2 + y^2 \right)^{\frac{1}{2}} \quad (3-8)$$

$$P = R_{\max} - R_{\min} \quad (3-9)$$

$$U = \frac{P}{R_{\text{mon}}} \times 100\% \quad (3-10)$$

The data for P and U are presented in Table 3-3. The average of P was between 0.19 and 0.22 mm, and the maximum was 0.53 mm. The average of U was between 0.80% and 0.88%, with the maximum being 2.30%. The test results were far lower than 5%, indicating that the weft of a goose egg is circular.

Table 3-3 Roundness (U), average radius of goose eggs (R_{mon}), and percentage (U) (No. 1-50).

Value	M			B			S		
	P	U	R_{mon}	P	U	R_{mon}	P	U	R_{mon}
	[mm]	[%]	[mm]	[mm]	[%]	[mm]	[mm]	[%]	[mm]
Minimum	0.07	0.27	24.08	0.10	0.36	21.68	0.06	0.27	20.63
Mean	0.22	0.87	26.30	0.19	0.80	24.45	0.20	0.88	22.65
Maximum	0.45	1.66	28.73	0.53	2.30	28.00	0.43	1.96	25.59
St.deviation	0.10	0.37	1.08	0.08	0.34	1.59	0.07	0.33	1.26

Three meridians were labeled (M1, M2, and M3) for each goose eggshell, intersecting at 120° angles (Fig.3-7). The Pearson similarity between the meridians was then analyzed.

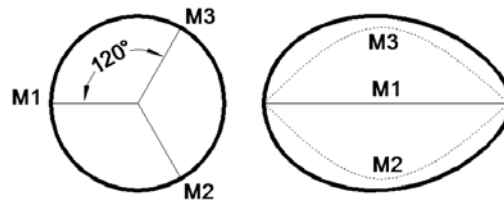


Fig.3-7 Goose egg meridians

The Pearson similarity test results are shown in Table 3-4. As can be seen, the similarity between the meridians were all measured as 0.99. The goose egg was determined to be a strongly revolving body with a symmetrical structure through a combination of similar analysis results for roundness and meridians. Therefore, a meridian could be used to represent the profile curve when building a mathematical model of a goose egg. A 3D mathematical model could then be derived by rotating the profile curve around the major axis.

Table 3-4 Pearson's coefficient of similarity for goose egg meridians (No. 1-50).

Value	M1 & M2	M2 & M3	M1 & M3	Mean
Minimum	0.990516	0.998815	0.992894	0.995854
Mean	0.999579	0.999865	0.999576	0.999721
Maximum	0.999988	0.999984	0.999989	0.999986
St.deviation	0.001588	0.000225	0.001328	0.000742

3.1.4 Shape function of goose eggshells

The contour lines of the goose eggs were extracted from the scanning results to express the egg shape in mathematical formulas. Subsequently, 300 points were marked in every contour line and the coordinates of each point were obtained and fitted to the curve by using Origin software and the existing function of egg shape [5]. The degree of coincidence of the two curves was determined using the simple Pearson correlation coefficient of these point sets.

The most common functions that are currently used to describe the contour lines of goose eggs are the Cassini oval (Eq.3-11) [6], N-R (Eq.3-12) [7-8], U (Eq.3-13) [9], and K equations (Eq.3-14) [10].

$$\sqrt{(x-a)^2 + y^2} \times \sqrt{(x+a)^2 + y^2} = b^2 \quad (3-11)$$

$$\begin{cases} y = \pm \sqrt{L^{\frac{2}{n+1}} x^{\frac{2n}{n+1}} - x^2} \\ n = 1.057 \left(\frac{L}{B} \right)^{2.372} \end{cases} \quad (3-12)$$

$$\frac{x^2}{a^2} + \frac{y^2}{(b + x \tan \theta)^2} = 1 \quad (3-13)$$

$$\begin{cases} X = \frac{B}{2} \\ Y = \left(\frac{L}{2} + e \cdot \sin \alpha \right) \cdot \sin \alpha \end{cases} \quad (3-14)$$

The curves of the Cassini oval, N-R, U, and K functions are highly similar to the contour lines of goose eggs; the average similarities are 94.76%, 99.36%, 95.25%, and 99.70%, respectively. The similarity of the N-R and K functions are all greater

than 99%, indicating that these two functions can be determined with greater accuracy by comparing averages. However, the standard deviation of the N-R function is 0.43 and is 0.82 for the K function, meaning that the data of the N-R function is more concentrated than that of the K function. The N-R function is therefore the most satisfactory means of describing the contour lines of goose eggs. The degrees of similarity are shown in Table 3-5.

Table 3-5 Information of similarity for functions compared with actual goose eggs (No. 1-50).

Value	Cassini's oval[%]	N-R Function[%]	Upadhyaya Function[%]	Kitching Function[%]
Maximum	97.70	99.92	99.95	99.99
Minimum	90.82	97.05	90.66	94.97
Mean	94.77	99.36	95.25	99.70
St.deviation	1.72	0.43	2.73	0.82

3.1.5 Thickness of goose eggshells

The thickness of each measurement point is shown in Table 3-6. As can be seen, the smallest average thickness was 0.479 mm at Point 1, and the largest one was 0.516 mm at Point 4. These results showed that the goose eggshells were thickest at the blunt end and thinnest in the middle. The eggshells become thicker and then thinner along the path from the blunt end to the sharp end (Fig.3-8). This is most likely because an air chamber is located in the blunt end of a goose egg, and the thin section in the blunt end enables convenient gas exchange with the outside environment.

Table 3-6 Thickness of each measurement point (No. 51-100).

Value	1 Point [mm]	2 Point [mm]	3 Point [mm]	4 Point [mm]	5 Point [mm]
Minimum	0.374	0.381	0.431	0.420	0.326
Mean	0.479	0.483	0.510	0.516	0.503
Maximum	0.633	0.599	0.613	0.671	0.631
St.deviation	0.044	0.043	0.042	0.052	0.049

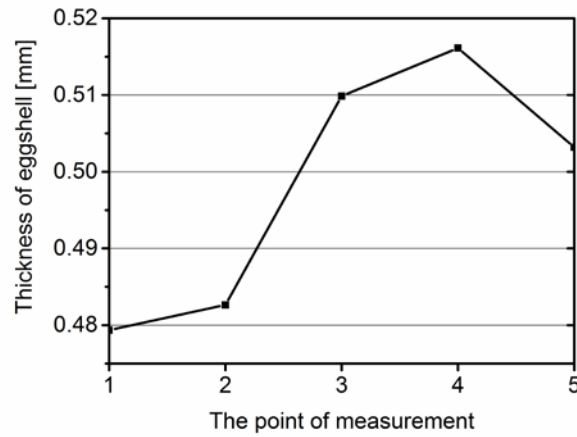


Fig.3-8 Thickness of each measurement point

3.2 Load carrying capacities of goose eggshells

A sample of 5 goose eggs was selected from 2-year-old geese, which are consistent with Section 3.1. The geese were raised using free-range technology at a commercial breeding farm located in Jiangshan of Zhejiang province in China. These goose eggs were numbered from 1# to 5#. Counter sizes of five goose eggs were measured. Then the axial compression testing and external radial pressure testing were carried out. Finally the thickness and density of 5 goose eggshells were measured.

Firstly, the major axis L and minor axis B of the goose eggshell were measured by using a digital caliper with an accuracy of 0.01 mm. Each parameter value was measured for four times, then the parameter value was finally determined by the average of these values. To get more accurate contour of the eggshell, 5 goose eggshells were scanned with an Aurum 3D scanner. Aurum 3D scanner has two internal industrial cameras with a resolution of 2×3 MPix. It also has a 3d-coordinate system with an accuracy of 0.05mm in the X and Y axes and an accuracy of 0.004mm in the Z axis.

Secondly, the equator area of the goose eggshell was pasted with strain gauges, which were welded with some signal input lines. The type of strain gauge is BE120-1AA with resistance value of $120.2 \pm 0.1 \Omega$ and a sensitive coefficient of $2.14 \pm 1\%$. A total of 6 strain gauges were used for each goose eggshell in the testing. Three strain gauges pasted along the circumferential direction and three strain gauges

pasted along the meridional direction were placed alternatively at the equator area. The goose eggshell pasted with strain gauges at the equator is shown in Fig.3-9.

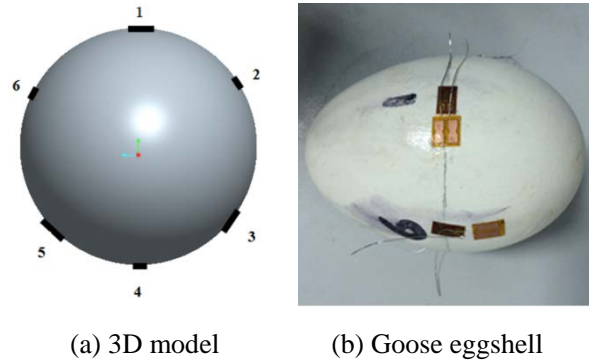


Fig.3-9 View of the goose eggshell Pasted with strain gauges at the equator

Thirdly, the process of axial compression testing of the goose eggshell is presented in Fig.3-10. As can be seen from Fig.3-10, when tested on the electronic universal testing machine, the goose eggshell was placed vertically between the bottom and upper plate with the sharp end maintaining up. The bottom plate was fixed in the machine, while the upper plate could move along the axial direction. The type of electronic universal testing machine is MZ-5001D1 with the max compression load of 50KN. During the process of axial compression testing, the load range of $250\text{N} \pm 5\%$ was chosen. Besides, the compression velocity of upper plate was set to be 6mm/min. Through the axial compression testing, the plot of the load applied to the goose eggshell versus the time could be obtained. At the same time, the plot of the meridional strain of the goose eggshell versus the time could also be obtained, as well as the circumferential strain of the goose eggshell versus the time.

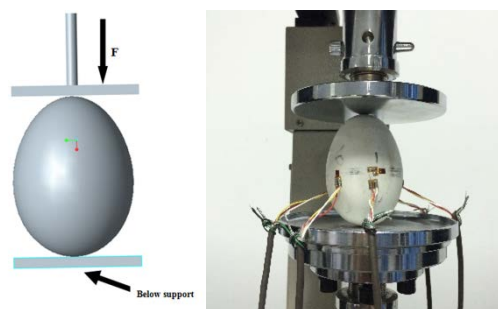


Fig.3-10 Axial compression testing of the goose eggshell

Fourthly, the primary processing of the goose eggshell is presented in Fig.3-11. After finishing the axial compression testing, the signal lines welded on the surface of strain gauges were removed. As can be seen from Fig.3-11 (a), a center point at the sharp end of the goose eggshell was marked. Then at the mark a hole with a diameter of 2 mm was drilled. Here, it is noted that the drill should be parallel to the major axis of the goose eggshell. After drilling a hole, a syringe was used to inject the air into the goose eggshell, as shown in Fig.3-11 (b). Then the goose egg was placed with the sharp end maintaining down to make the internal liquid outflow from the hole. When the internal liquid was cleaned up, the goose eggshell was exposed under the sun for 3 hours to make the internal membrane come off from the shell. This could make the experimental result more reliable. Finally, the hole of the goose eggshell was sealed with curing silicone rubber, as shown in Fig.3-11 (c). To ensure the seal property of the goose eggshell, the hole was sealed for 3 times. Generally, the diameter of cover area of curing silicone rubber was in the range from 5 mm to 6 mm. The curing silicone rubber would have no effect on mechanical characteristic of the goose eggshell, because collapse usually occurs at the equator area of the shell. In addition, the blunt end of the goose eggshell would be attached with some heavy weights to ensure the shell suspend in the water. This can reduce the influence of water wave on the goose eggshell.



Fig.3-11 Primary processing of the goose eggshell

Fifthly, External radial pressure testing of five prepared goose eggshells was carried out in the hydrostatic test device (HMT-G64A). The test rig mainly consists of the holder, quick opening flanges, pressure transmitter, valve, lifting cylinder and air interface. The control panel is mainly composed of air source pressure gauge, air pressure regulator valve, hand valve and high pressure gauge. Air compressor part

mainly includes the oil circulation system, air circulation system, water circulation system, power distribution system, screen protection system, DC power supply system, and DTC control system. The pressure applied to the goose eggshell was obtained mainly from the air compressor part. The working principle of the hydrostatic test device is shown in Fig.3-12. As can be seen in Fig.3-12, the working principle includes the following steps: operating air compressor to increase the pressure to 0.8 MPa; regulating the pressure valve to open air controller slightly to maintain the primary pressure about 0.1 MPa; putting the goose eggshell into the pressure chamber, then injecting water into the pressure chamber; closing the pressure chamber cover and opening the exhaust valve to exhaust air; regulating the gas pressure regulating valve to make the pressure zero; opening the hand valve and regulating the gas pressure regulating valve again to make the controller work; closing the hand exhaust valve when the water outflows from the pipe; connecting the computer with the PLC device and opening the electric valve. The external radial pressure testing of the goose eggshell was begun. The plot of the uniform pressure applied to the goose eggshell versus the time was recorded. When the goose eggshell was collapsed, the external radial pressure testing was complete. The next minute the electric valve was closed and the pressure of the gas source valve was controlled to be zero. Then the pressure cabin was opened, and the collapsed goose eggshell was taken out from the pressure cabin. The process of external radial pressure testing was the same for 5 goose eggshells.

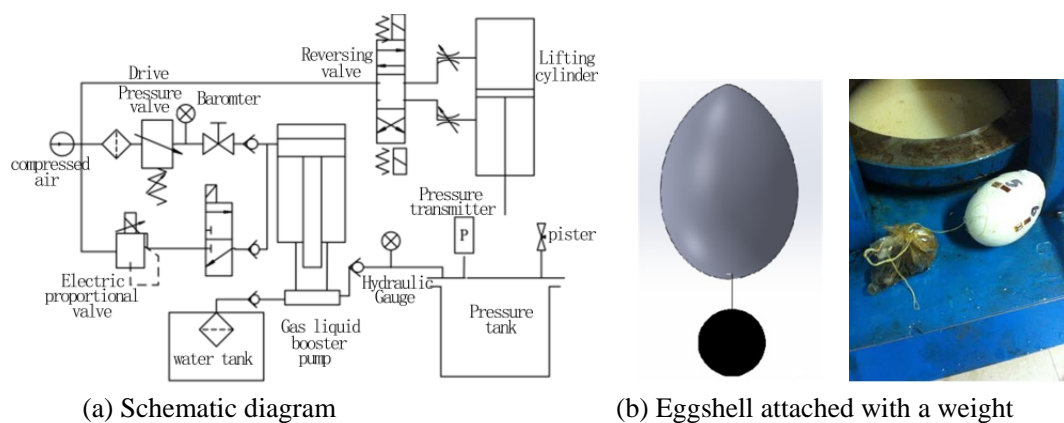


Fig.3-12 External radial pressure testing of the goose eggshell

Finally, five destroyed goose eggshells were cut apart by using an egg-cutting machine. The thickness of each goose eggshell along the meridional and circumferential direction was measured with a micrometer. When reading the graduation value, the eyes of us should be maintain horizontal to ensure the readings was exact. Ten points of the half of the goose eggshell was measured along the meridional direction. Ten points of the 1/4 of the goose eggshell was measured along the circumferential direction. Each point was measured for 3 times and the thickness value of each point was determined by the average. The process of thickness measuring of the goose eggshell is presented in Fig.3-13.

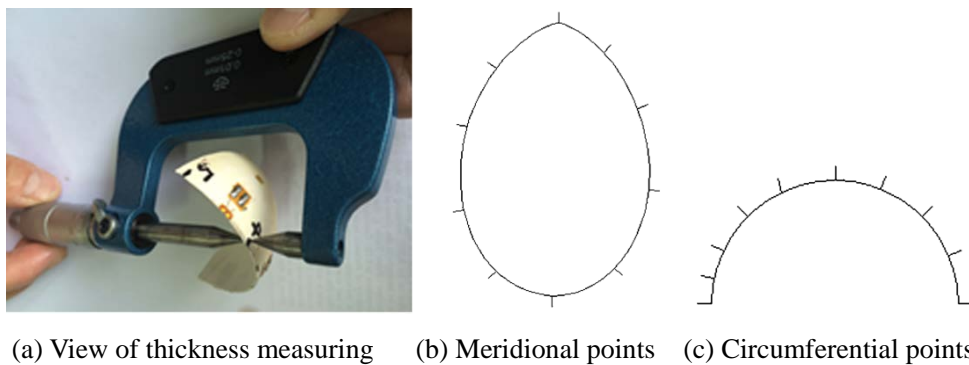


Fig.3-13 Measurement of thickness for the goose eggshell

After the thickness measurement, densities of 5 goose eggshells were measured with the use of a digital electronic balance (DH-300). Density of each goose eggshell was measured repeatedly for 3 times and obtained the average. The view of density measuring of the goose eggshell is shown in Fig.3-14.

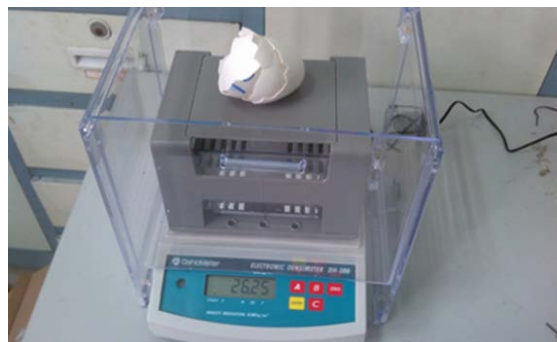


Fig.3-14 Measurement of density for the goose eggshell

According to the tested contour and size, the eggshell shape, surface area, major

axis, minor axis, eggshell-shaped index and roundness of the goose eggshell could be gained. The stress and strain of the goose eggshell subjected to axial loading could be obtained from the axial compression testing. The stress and strain could be introduced into a series of equations to calculate the Young modulus and Poisson ratio of the goose eggshell. In this section, numerical analyses of 5 goose eggshell were also carried out with the use of finite element methods. Both buckling and strength analyses of the goose eggshell were implemented. The result obtained from numerical prediction is compared with that obtained from experimental data. The effects of buckling and strength on the stability of the goose eggshell subjected to uniform external pressure could be studied.

3.2.1 Experimental results of goose eggshells

The major axis, minor axis and egg-shaped index of 5 goose eggshells are presented in Table 3-7. The roundness of 5 goose eggshells is given in Table 3-8. As can be seen from Table 3-7, the major axes of five goose eggshell were close to each other as well as the minor axes. The egg-shaped index of each goose eggshell was around 0.69, which corresponded to the experimental average value in Section 3.1. Three planes of each goose eggshell were chosen to be measured for roundness. Three planes were through the center of mass, a point at the area of blunt end and a point at the area of sharp end, respectively. As can be seen from Table 3-8, the maximum and minimum roundness of 5 goose eggshells were 1.39 and 0.53 respectively. This also shows that all of 5 goose eggshells are highly symmetrical structures of revolution.

The circumferential and meridional thicknesses of 5 goose eggshells are presented in Table 3-9 and Fig.3-15 respectively. As can be seen from Table 3-9, the circumferential thickness of a goose shell was almost constant, and the circumferential thickness of 5 goose eggshell was close to each other. But the meridional thickness of a goose shell was not constant, as shown in Fig.3-15. The thicker shell occurred at middle area of the goose eggshell and the thinner shell occurred at the two ends of the goose eggshell. Especially, the thinnest shell corresponded to the area of the blunt end the goose eggshell. These findings are consistent with those of Section 3.1.

Table 3-7 Contour size of 5 goose eggshells.

Egg number	1#	2#	3#	4#	5#
Major axis	77.32	78.465	78.66	80.57	79.545
Minor axis	54.46	54.47	54.8	55.76	55.615
Egg-shaped index	0.704346	0.694195	0.696625	0.692069	0.699164

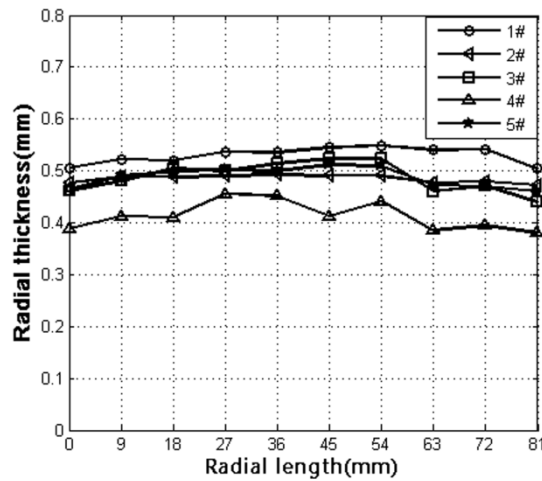
Table 3-8 Roundness values of 5 goose eggshells.

Egg number		M	B	S
1#	U(%)	0.57	0.53	0.55
2#	U(%)	0.59	1.02	0.96
3#	U(%)	0.83	0.60	0.84
4#	U(%)	0.97	0.76	0.89
5#	U(%)	1.36	0.87	1.34

Table 3-9 Circumferential thickness of 5 goose eggshells.

Egg number	1#	2#	3#	4#	5#
Maximum value	0.59	0.52	0.52	0.44	0.53
minimum value	0.52	0.46	0.48	0.37	0.48
average value	0.555	0.49	0.5	0.4	0.51
standard deviation	0.022773	0.019842	0.016768	0.025977	0.016469

Footnote: M, B, and S correspond to Fig.3-6.

**Fig.3-15** Meridional thickness of 5 goose eggshells

The concentrated load F_{max} , meridional strain ε_{φ} and circumferential strain ε_{θ} of 5 goose eggshells could be obtained from axial compression testing. The meridional stress σ_{φ} and circumferential stress σ_{θ} could be calculated by the following equations:

$$\sigma_{\phi} = \frac{F_{\max}}{2\pi R_2 t}, \quad (3-15)$$

$$\sigma_{\theta} = -\frac{R_2}{R_1} \sigma_{\phi}, \quad (3-16)$$

Where R_1 , R_2 are the mean radius of curvature of the goose eggshell, t is the average thickness at the equator of the goose eggshell. The mean meridional strain $\overline{\varepsilon_{\phi}}$ and the mean circumferential strain $\overline{\varepsilon_{\theta}}$ could be obtained in the following forms:

$$\overline{\varepsilon_{\phi}} = \frac{\sum_{j=1}^m \varepsilon_{3j}}{m} \quad (3-17)$$

$$\overline{\varepsilon_{\theta}} = \frac{\sum_{i=1}^n \varepsilon_{2i}}{n} \quad (3-18)$$

Where m is the number of strain gauge in the meridional direction, n is the number of strain gauge in the circumferential direction. The mean meridional strain $\overline{\varepsilon_{\phi}}$ and the mean circumferential strain $\overline{\varepsilon_{\theta}}$ also could be expressed as the following form:

$$\overline{\varepsilon_{\phi}} = \frac{1}{E}(\sigma_{\phi} - \mu \cdot \sigma_{\theta}), \overline{\varepsilon_{\theta}} = \frac{1}{E}(\sigma_{\theta} - \mu \cdot \sigma_{\phi}) \quad (3-19)$$

$$\overline{\varepsilon_{\theta}} = \frac{1}{E}(\sigma_{\theta} - \mu \cdot \sigma_{\phi}), \quad (3-20)$$

The Eqs. (3-19) and (3-20) could be written as follows:

$$E = \frac{\sigma_{\theta} - \mu \cdot \sigma_{\phi}}{\overline{\varepsilon_{\theta}}}, \quad (3-21)$$

$$\mu = \frac{\overline{\varepsilon_{\theta}} \cdot \sigma_{\phi} - \overline{\varepsilon_{\phi}} \cdot \sigma_{\theta}}{\overline{\varepsilon_{\theta}} \cdot \sigma_{\theta} - \overline{\varepsilon_{\phi}} \cdot \sigma_{\phi}}. \quad (3-22)$$

Table 3-10 Poisson ratio and Young modulus of 5 goose eggshells.

Egg number	1#	2#	3#	4#	5#
Poisson ratio	0.414	0.368	0.450	0.471	0.331
Young modulus / GPa	48	43	53	41	48

Therefore, Young modulus E and Poisson ratio μ of 5 goose eggshells could be calculated by Eqs. (3-21) and (3-22). Values of them are listed in Table 3-10. As can be seen from Table 3-10, the rang of Young modulus is from 41 GPa to 53 GPa. In the current paper, the range of Young modulus from 45.7GPa to 46.9GPa was given by Tung [11]. Besides, the Young modulus of 20.7GPa was adopted by Rehkugler [12]. In addition, the range of Young modulus from 26.3GPa to 34.1GPa could also be given by Bain [13]. In the paper, the Poisson ratio and Young modulus calculated by Eqs. (3-21) and (3-22) are in a good agreement with those obtained by the paper of Tung [11].

The plots of pressure applied to five goose eggshells versus the sampling points are presented in Fig.3-16. As can be seen in Fig.3-16, when subjected to external pressure, the pressure values of five goose eggshell first increased, then decreased and increased again. When the pressure first increased to the peak point, the goose eggshell was at a critical state. Then the pressure decreased quickly because the goose eggshell started to collapse with the water flowing into the inside of the goose eggshell. After filling the goose eggshell, the pressure increased again. The range of the pressure at the peak point for 5 goose eggshells was from 2.87 MPa to 3.31 MPa, listed in Table 3-11. The results may be a little larger, because the internal membrane of 5 goose eggshells may not come off completely.

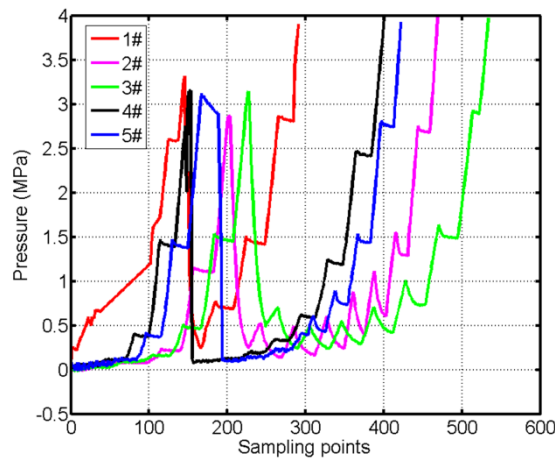


Fig.3-16 Plots of the pressure versus sampling points for 5 goose eggshells

Table 3-11 Pressure values of 5 goose eggshells.

Egg number	1#	2#	3#	4#	5#
Pressure at the peak point/ MPa	3.31	2.87	3.14	3.15	3.12

The surface area of the goose eggshell could be obtained from the 3D scanning model. The hand grip could be calculated by the multiplication between pressure and half of surface area. The surface areas, pressure values and hand grips of 5 goose eggshells are presented in Table 3-12. As shown in Table 3-12, the range of hand grips was from 17368.2 N to 19916.5 N. The result showed that the goose eggshell could have a high load carrying ability when subjected to external uniform pressure.

Table 3-12 Hand grips of 5 goose eggshells.

Egg number	Surface area (mm ²)	Pressure value (MPa)	Hand grip (N)
1#	11958.37	3.31	19813.5
2#	12120.44	2.87	17368.2
3#	12150.13	3.14	19098.5
4#	12768.28	3.12	19916.5
5#	12719.92	3.12	19843.1

3.2.2 Numerical results of goose eggshells

Both buckling and strength of the goose eggshell were investigated. Before numerical analyses of 5 goose eggshells were carried out, the 3D scanning models should be pre-treated. Firstly, the surface of 3D scanning models should be regenerated with the Geomagic Studio software because of its rough surface; secondly, the 3D scanning models should be meshed by automatic mesh generation available in ANSA, as presented in Fig.3-17; finally, the 3D scanning models was input into ABAQUS for finite element analysis. A shell element S3R was chosen corresponding to the randomness of mesh. The number of elements and nodes of five goose eggshells is presented in Table 3-7. To prevent the model from moving six degree of freedom was restricted. The constraints did not produce excessive reaction force. It is noted that the boundary condition was applicable for buckling analysis of the goose

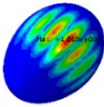
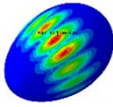
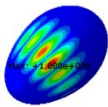
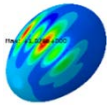
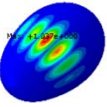
eggshell. No boundary condition was defined when the strength analysis of the goose eggshell was conducted. The external uniform pressure $P_0=1\text{MPa}$ was applied to the whole surface of the goose eggshell. Material properties of 5 goose eggshells are listed in Table 3-10.

The buckling load and buckling shape of the goose eggshell obtained from buckling analysis are presented in Table 3-14. Besides, the meridional stress and circumferential stress of the goose eggshell obtained from strength analysis are given in Fig.3-18. As can be seen from Table 3-14, the area of losing stability was at the equator of the goose eggshell. In the Fig.3-18, the meridional stress at the equator of the goose eggshell was the largest, and that at the two ends of the goose eggshell was the smallest. The circumferential stress of the goose eggshell had the same distribution trends. These results are the same for all goose eggshells considered.

Table 3-13 Elements and nodes of 5 goose eggshells.

Egg number	1#	2#	3#	4#	5#
Element	13573	13475	13198	13573	13662
Node	12777	12687	12349	12777	12799

Table 3-14 Buckling loads and shapes of 5 goose eggshells.

Egg number	1#	2#	3#	4#	5#
Buckling load/MPa	7.97	5.33	5.76	3.26	4.37
Buckling shape					

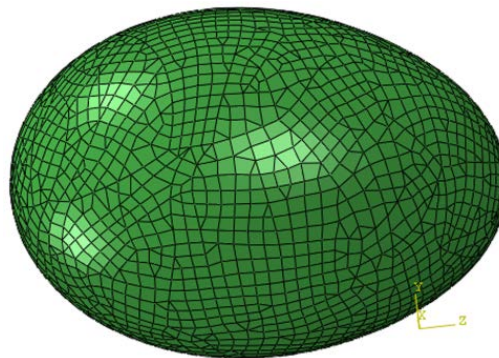


Fig.3-17 FE mesh of the goose eggshell

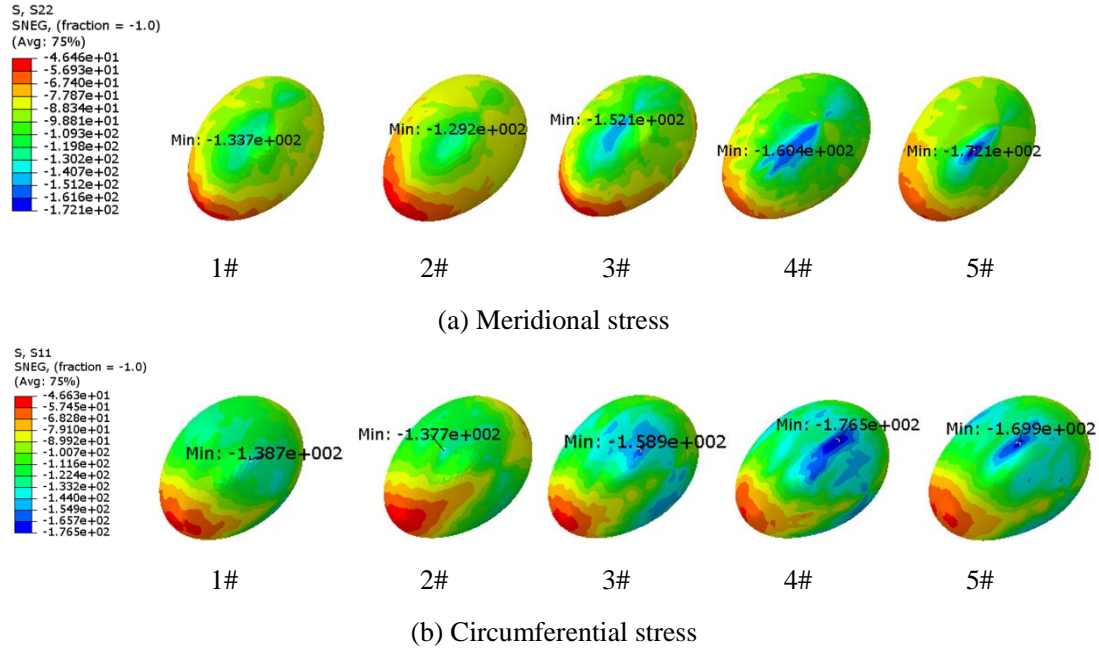


Fig.3-18 Strength results of 5 goose eggshells

3.2.3 Comparison between experimental and numerical data

One of main factors resulting in the collapse of the goose eggshell is the instability of strength. The meridional and circumferential stresses obtained from numerical analysis are given in Table 3-15. As can be seen from Table 3-15, the value of circumferential stress was slightly more than that of meridional stress. But both of them had fairly large values of stress. When the circumferential stress or meridional stress was more than the allowable stress, the goose eggshell would be collapsed.

Table 3-15 Meridional and circumferential stress of 5 goose eggshells.

Egg number	1#	2#	3#	4#	5#
Circumferential stress	138.7	137.7	158.9	176.5	169.9
Meridional stress	133.7	129.2	152.1	160.4	172.1

Compressive strength and relative density of 4 types of calcium carbonate are presented in Table 3-16, as well as the goose eggshell. The compressive strength and relative density of the goose eggshell were obtained from the experiment. As can be seen from Table 3-16, compressive strength and relative density of the goose eggshell were similar to those of other 4 types of calcium carbonate. The relative density of the

goose eggshell was smaller than other calcium carbonate due to its porous structure. The above results showed that the collapse of the goose eggshell may mainly result from the instability of strength. In other words, when the circumferential stress or meridional stress of the eggshell was more than the allowable stress, the goose eggshell would be collapsed with losing stability.

Table 3-16 Compressive strength and relative density of 4 types of calcium carbonate and the goose eggshell.

Type	Marble	Granite	limestone	calcite	goose-egg
compressive strength/(MPa)	250-260	100-300	60-140	100	137.7-169.9
relative density/(g/cm ³)	2.60-2.8	2.63-3.3	2.93	2.60-2.8	2.357

Numerical and experimental results of 5 goose eggshells are given in Table 3-17. As can be seen from Table 3-17, the critical load of the goose eggshell obtained from experiment was less than that obtained from numerical simulation. This phenomenon is the same for all goose eggshells analyzed. If the collapse of the goose eggshell resulted from the instability of buckling, the critical load obtained from experiment would be close to that given from numerical simulation. Therefore, the buckling was not the main factor to result in the collapse of the goose eggshell.

Table 3-17 Comparison of critical loads obtained from numerical simulation and experiment.

Egg number	1#	2#	3#	4#	5#
Numerical value/MPa	7.9671	5.3296	5.7576	3.2568	4.3734
Experimental value/MPa	3.31	2.87	3.14	3.15	3.12

3.3 Configuration and size egg-shaped pressure hulls

In this section, the configuration of egg-shaped pressure hulls can be directly obtained from the shape function of eggshells. The performance mapping in Fig.3-19 for eggshells, pressure hull and submersible demonstrates bionic evidence of such work.

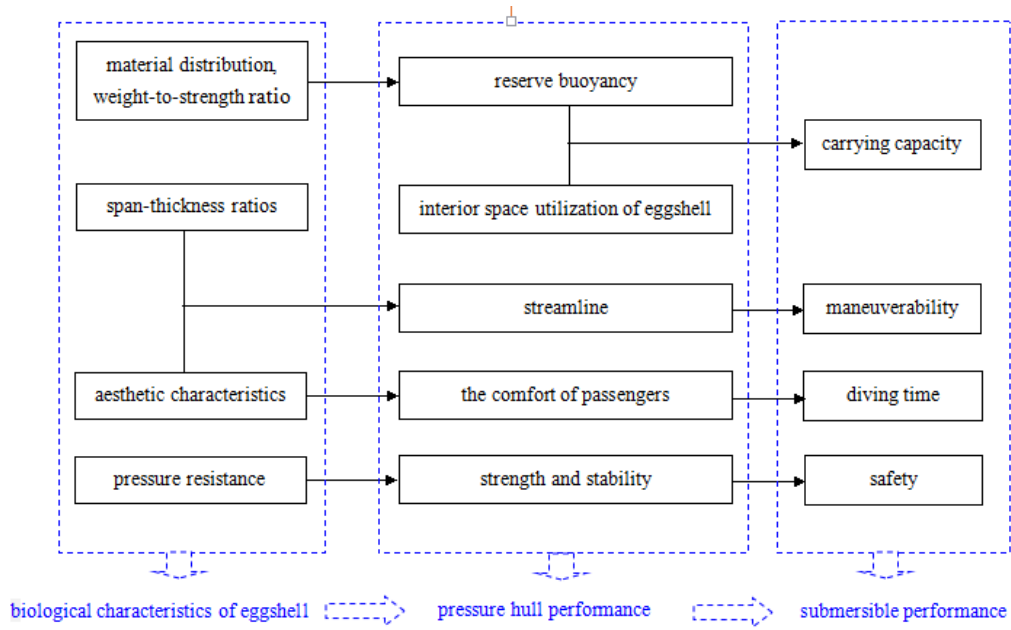


Fig.3-19 Schematic diagram of performance mapping for eggshells, pressure hull and submersible

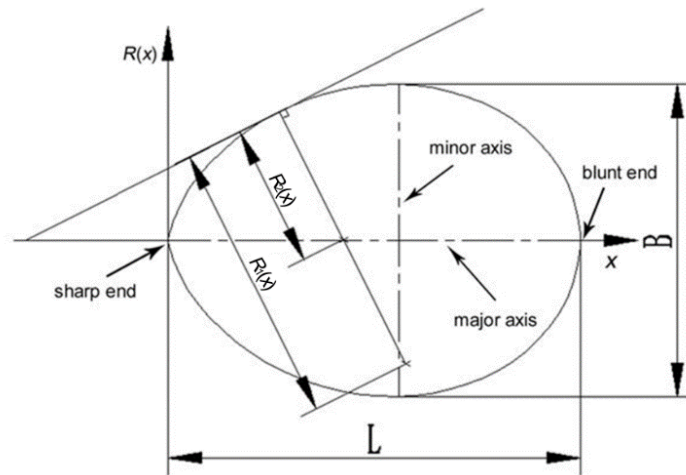


Fig.3-20 Sketch of a typical egg-shaped pressure hull

It is well known that many of the spherical pressure hulls in current deep manned submersibles are with radius of around 1m, such as ‘Jiaolong’ of China for example [14]. This size provides a suitable working condition for crews of three and necessary equipment. This size was then used to be equivalent reference for designing the compared egg-shaped pressure hulls. The contour of egg-shaped pressure hull was determined based on the goose egg-shaped function, as shown in Equation (3-13) of Section 3.2. The size of egg-shaped pressure hull was designed to be the same as the volume of the spherical pressure hull with radius of 1m. According to Equation (3-13),

the length L and the width B of egg-shaped pressure hull are 2.561 m and 1.767 m, respectively. In this case, the shape index of hull is 0.69, which corresponds to the geometrical data of goose eggs. Fig.3-20 shows the contour of a typical egg-shaped pressure hull. The obtained shape function of egg-shaped pressure hull is as follows,

$$R(x) = \pm \sqrt{1.6988x^{1.4365} - x^2}, \quad (0 \leq x \leq 2.561) \quad (3-23)$$

For the spherical pressure hull subjected to the hydrostatic pressure, stress is equally distributed, so the thickness was designed to be constant. But for the egg-shaped pressure hull with the constant thickness, stress of the material along the major axis is variable. Therefore, both of the constant and variable wall thicknesses were proposed in this paper. For the egg-shaped pressure hull with the constant thickness with variable wall thickness, in order to save material and reduce buoyancy factor, thickness in the middle part was designed to be variable, so as to make the von Mises equivalent stress in this part constant. The thickness of each pressure hull is detailed in section 3.4.

In addition, the design load of pressure hulls is calculated with Equation (3-24) [15]. Since some reduction factors are included in this equation, it is suitable for classical design of pressure hulls. It should be noted that no additional reduction factors will be added when geometry and material nonlinear analyses with imperfections (GMNIA) were implemented to determine the buckling load of the pressure hull.

$$P_s = K \rho_0 g h / 0.9 \quad (3-24)$$

where h is set to be 0-4 km. K , ρ_0 and g is 1.5, 1g/cm^3 and 9.8 m/s^2 , respectively.

Other reduction factors associated with material and manufacturing in this paper were assumed to be 1. For simplicity reasons the properties of the pressure hull material were assumed to be temporarily referring to that of Ti-6Al-4V(TC4), which has been frequently used in deep manned submersibles [16]. Its mechanical parameters were as follows: Young modulus $E = 110\text{GPa}$, Poisson ration $\mu = 0.3$, Yield strength $\sigma_y = 830\text{MPa}$, tensile strength $\sigma_b = 869.7\text{MPa}$, mass density $\rho = 4.5\text{ g/cm}^3$.

Details can be found in Chapter 2.

3.4 Wall thickness and buoyancy factor of egg-shaped and spherical pressure hulls

In this section, yielding and buckling load of a perfect egg-shaped shell were analyzed firstly. Then, thickness and buoyancy factor of egg-shaped and spherical pressure hulls were determined.

3.4.1 Strength and stability of egg-shaped pressure hull

In accordance with membrane theory in shells of revolution under external pressure [17], the meridional stress $\sigma_\phi(x)$ and the circumferential stress $\sigma_\theta(x)$ of the egg-shaped shell are calculated with Equations (3-25) and (3-26), respectively. Then, the von Mises equivalent stress $\sigma_{r4}(x)$ of the egg-shaped shell is obtained from Equations (3-25) and (3-26), listed in Equation (3-27).

$$\sigma_\phi(x) = -\frac{P_s R_2(x)}{2t} \quad (3-25)$$

$$\sigma_\theta(x) = \sigma_\phi(x) \cdot \left(2 - \frac{R_2(x)}{R_1(x)} \right) \quad (3-26)$$

$$\sigma_{r4}(x) = \sqrt{\frac{1}{2} \cdot \left[\left(\sigma_\theta(x) - \sigma_\phi(x) \right)^2 + \sigma_\theta^2(x) + \sigma_\phi^2(x) \right]} \quad (3-27)$$

Where:

$$R_1(x) = \left| \frac{\left[1 + \left(R'(x) \right)^2 \right]^{\frac{3}{2}}}{R''(x)} \right| \quad (3-28)$$

$$R_2(x) = R(x) \cdot \sqrt{1 + \left(R'(x) \right)^2} \quad (3-29)$$

Fig.3-21 illustrates the meridional and circumferential radii of curvature of egg-shaped pressure hull along the major axis by Equations (3-23), (3-28) and (3-29). It could be seen that both of the meridional and circumferential radii firstly increased and then decreased from the sharp end to the blunt end. The meridional radius was always higher than the circumferential radius that changes slightly. The ratio of the circumferential radius and the meridional radius is plotted in Fig.3-22. It was indicated that this ratio gradually increases from the sharp end to the blunt end of

egg-shaped pressure hull. And this value was less than 1, which indicated that the circumferential stress of the egg-shaped pressure hull is higher than the meridional stress in accordance with Equation (3-26).

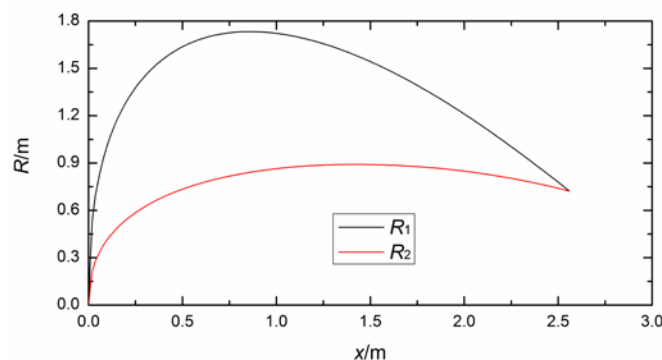


Fig.3-21 Meridional and circumferential radii of curvature of egg-shaped pressure hull

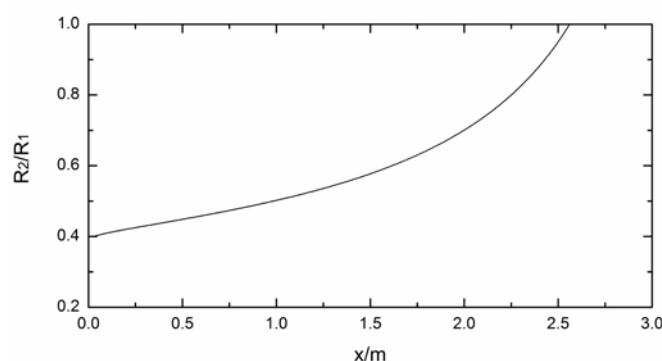


Fig.3-22 Ratio of the circumferential radius and the meridional radius

The critical elastic buckling load P_q of the egg-shaped shell is calculated with Equation (3-30), which is derived by Mushtari [18].

$$P_q = \frac{2Et^2}{(2R_1 - R_2) \cdot R_2} \cdot \sqrt{\frac{1}{3(1-\mu^2)}} \quad (3-30)$$

3.4.2 Uniform wall thickness analysis of egg-shaped pressure hulls

The thickness of egg-shaped pressure hull with uniform or constant thickness can then be calculated:

$$\sigma_{r4}(x) = \frac{P_s R_2(x) \cdot \sqrt{3 - 3 \cdot \frac{R_2(x)}{R_1(x)} + \left(\frac{R_2(x)}{R_1(x)} \right)^2}}{2t} \quad (3-31)$$

$$t = \frac{P_s R_2(x) \cdot \sqrt{3 - 3 \cdot \frac{R_2(x)}{R_1(x)} + \left(\frac{R_2(x)}{R_1(x)} \right)^2}}{2\sigma_{r4}(x)} \quad (3-32)$$

If strength is the main factor, Equation (3-32) is rewritten for clarification as:

$$t_1 = \frac{P_s}{2[\sigma]} \left(R_2(x) \cdot \sqrt{3 - 3 \cdot \frac{R_2(x)}{R_1(x)} + \left(\frac{R_2(x)}{R_1(x)} \right)^2} \right)_{\max} \quad (3-33)$$

Where the allowable stress $[\sigma]$ is assumed to be equal to the yield strength σ_y .

Then the yielding load of egg-shaped pressure hull P_{s1} can be expressed as:

$$P_{s1} = \frac{2t_1[\sigma]}{\left(R_2(x) \cdot \sqrt{3 - 3 \cdot \frac{R_2(x)}{R_1(x)} + \left(\frac{R_2(x)}{R_1(x)} \right)^2} \right)_{\max}} \quad (3-34)$$

The critical elastic buckling load of egg-shaped pressure hull P_{q1} is obtained by Equation (3-30):

$$P_{q1} = \frac{2Et_1^2}{(2\bar{R}_1 - \bar{R}_2) \cdot \bar{R}_2} \cdot \sqrt{\frac{1}{3(1 - \mu^2)}} \quad (3-35)$$

If buckling is the main factor, the minimum thickness should be:

$$t_1 = \sqrt{\frac{P_s \bar{R}_2 (2\bar{R}_1 - \bar{R}_2) \cdot \sqrt{3(1 - \mu^2)}}{2E}} \quad (3-36)$$

Combined with Equations (3-33) and (3-36), the thickness of egg-shaped pressure hull t_1 is determined by:

$$t_1 = \left\{ \frac{P_s}{2[\sigma]} \left(R_2(x) \cdot \sqrt{3 - 3 \cdot \frac{R_2(x)}{R_1(x)} + \left(\frac{R_2(x)}{R_1(x)} \right)^2} \right)_{\max}, \sqrt{\frac{P_s \bar{R}_2 (2\bar{R}_1 - \bar{R}_2) \cdot \sqrt{3(1 - \mu^2)}}{2E}} \right\}_{\max} \quad (3-37)$$

The buoyancy factor of egg-shaped pressure hull δ_1 is:

$$\delta_1 = \frac{V_1 \rho_T}{V_0 \rho_W} \quad (3-38)$$

where:

$$V_1 = t_1 \int_0^L 2R(x) \pi dx \quad (3-39)$$

$$V_0 = \int_0^L \pi R^2(x) dx \quad (3-40)$$

3.4.3 Non-uniform wall thickness analysis of egg-shaped pressure hulls

The egg-shaped pressure hull with non-uniform or variable thickness was designed to have three parts along the major axis: sharp area, middle area and blunt area. The lengths of them were 5%, 90% and 5% of the general length L respectively. In the middle area, the thickness was designed to be variable so that the von Mises equivalent stress in shell was constant and equal to the allowable stress $[\sigma]$. For the sharp area, the thickness was set to be that of the left end of the middle area, and the thickness of the blunt area was equal to that of the right end of the middle area.

If strength is the main factor, the thickness of egg-shaped pressure hull $t_2(x)$ is calculated by Equations (3-31) and (3-41):

$$t_2(x) = \frac{P_s}{2[\sigma]} \left[R_2(x) \cdot \sqrt{3 - 3 \cdot \frac{R_2(x)}{R_1(x)} + \left(\frac{R_2(x)}{R_1(x)} \right)^2} \right] \quad (3-41)$$

For comparison with other pressure hulls, $t_2(x)$ is normalized as follows:

$$t_2(x) = T_2 t_0(x) \quad (3-42)$$

$$T_2 = \{t_2(x)\}_{\max} \quad (3-43)$$

$$t_0(x) = t_2(x) / \{t_2(x)\}_{\max} \quad (3-44)$$

Thus the yielding load of egg-shaped pressure hull P_{s2} is:

$$P_{s2} = \frac{2T_2[\sigma]}{\left[R_2(x) \cdot \sqrt{3 - 3 \cdot \frac{R_2(x)}{R_1(x)} + \left(\frac{R_2(x)}{R_1(x)} \right)^2} \right]_{\max}} \quad (3-45)$$

So:

$$T_2 = \frac{P_s \left[R_2(x) \cdot \sqrt{3 - 3 \cdot \frac{R_2(x)}{R_1(x)} + \left(\frac{R_2(x)}{R_1(x)} \right)^2} \right]_{\max}}{2[\sigma]} \quad (3-46)$$

The critical elastic buckling load of egg-shaped pressure hull P_{q2} by Equation (3-30):

$$P_{q2} = \frac{2Et^2}{(2\bar{R}_1 - \bar{R}_2) \cdot \bar{R}_2} \cdot \sqrt{\frac{1}{3(1-\mu^2)}} \quad (3-47)$$

$$\bar{t} = \frac{T_2 \int_{\frac{(1-a)L}{2}}^{\frac{(1+a)L}{2}} t_0(x) dx}{aL} \quad (3-48)$$

Where a is the percentage of L along the major axis.

If buckling is the main factor:

$$T_2 = \frac{aL}{\int_{\frac{(1-a)L}{2}}^{\frac{(1+a)L}{2}} t_0(x) dx} \cdot \sqrt{\frac{P_s \bar{R}_2 (2\bar{R}_1 - \bar{R}_2) \cdot \sqrt{3(1-\mu^2)}}{2E}} \quad (3-49)$$

Combined with Equations (3-46) and (3-49), the design thickness of egg-shaped pressure hull T_2 is determined by:

$$T_2 = \left\{ \frac{P_s \left[R_2(x) \cdot \sqrt{3 - 3 \cdot \frac{R_2(x)}{R_1(x)} + \left(\frac{R_2(x)}{R_1(x)} \right)^2} \right]_{\max}}{2[\sigma]}, \frac{aL}{\int_{\frac{(1-a)L}{2}}^{\frac{(1+a)L}{2}} t_0(x) dx} \cdot \sqrt{\frac{P_s \bar{R}_2 (2\bar{R}_1 - \bar{R}_2) \cdot \sqrt{3(1-\mu^2)}}{2E}} \right\}_{\max} \quad (3-50)$$

The buoyancy factor:

$$\delta_2 = \frac{V_2 \rho_T}{V_0 \rho_w} \quad (3-51)$$

Where:

$$V_2 = T_2 \left(\int_0^{0.2L} 2\pi R(x) t_0(0.2L) dx + \int_{0.2L}^{0.75L} 2\pi R(x) t_0(x) dx + \int_{0.75L}^L 2\pi R(x) t_0(0.75L) dx \right) \quad (3-52)$$

3.4.4 Spherical pressure hulls analysis

In addition, the spherical pressure hull can be considered as a special case of the

egg-shaped shell, where $R_1(x) = R_2(x) = R_m$. Then $\sigma_\varphi(x) = \sigma_\theta(x) = \sigma_{r4}(x)$ is calculated by [19-21].

$$\sigma_{r4}(x) = |\sigma_\theta(x)| = |\sigma_\varphi(x)| = \frac{P_s R_m}{2t_3} \quad (3-53)$$

If strength is the main factor, the thickness of spherical pressure hull :

$$t_3 = \frac{P_s R_m}{2[\sigma]} \quad (3-54)$$

Then the yielding load:

$$P_{s3} = \frac{3t_3[\sigma]}{R_m} \quad (3-55)$$

The critical elastic buckling load of spherical pressure hull P_{q3} [28,29,30]:

$$P_{q3} = \frac{2Et_3^2}{R_m^2} \cdot \sqrt{\frac{1}{3(1-\mu^2)}} \quad (3-56)$$

If the buckling is the main factor:

$$t_3 = \sqrt{\frac{P_s R_m^2 \cdot \sqrt{3(1-\mu^2)}}{2E}} \quad (3-57)$$

Combining Equations (3-54) and (3-57), the thickness of spherical pressure hull t_3 is determined by:

$$t_3 = \left\{ \frac{P_s R_m}{2[\sigma]}, \sqrt{\frac{P_s R_m^2 \cdot \sqrt{3(1-\mu^2)}}{2E}} \right\}_{\max} \quad (3-58)$$

The buoyancy factor of spherical pressure hull:

$$\delta_3 = \frac{V_3 \rho_T}{V_{s0} \rho_w} \quad (3-59)$$

where:

$$V_3 = 4\pi R_m^2 t_3 \quad (3-60)$$

$$V_{s0} = \frac{4\pi R_m^3}{3} \quad (3-61)$$

3.5 Analytical results of egg-shaped and spherical pressure hulls

Yielding load and buckling load are both very important parameters to evaluate safety of a pressure hull. Fig.3-23 shows different classical yielding loads and critical elastic buckling loads of the egg-shaped pressure hull with constant thickness (EPHC), the egg-shaped pressure hull with variable thickness (EPHV) and the spherical pressure hull (SPH). For the EPHV, abscissa was the maximum thickness, and for the other two pressure hulls it was the real thickness.

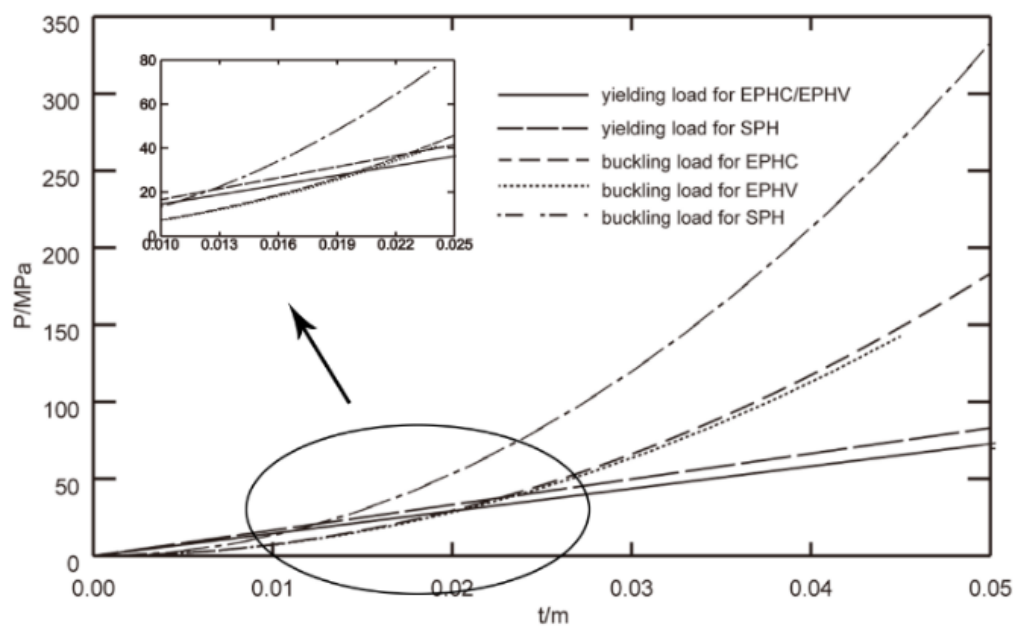


Fig.3-23 Comparison of yielding load and critical elastic buckling load for pressure hulls

It was evident from the results that there existed an intersection between classical yielding load and critical elastic buckling load for each pressure hull. Before the intersection, buckling was the main factor, in which case elastic or elastic-plastic buckling might lead to collapse of the pressure hull. After the intersection, strength was the main factor, in which case the maximum stress reached the yield condition and then might lead to collapse of the pressure hull. The results for the SPH are in line with previous findings given in [22].

For the EPHC, the load and thickness at the intersection were 28.81 MPa and 0.01982 m, respectively. If the design load was less than 28.81 MPa, the thickness is

calculated by Equation (3-36), otherwise by Equation (3-33). For the EPHV, the load and thickness at the intersection were 30 MPa and 0.02064 m, respectively. If the design load was less than 30 MPa, the thickness was calculated by Equation (3-49), otherwise by Equation (3-46). For the SPH, the intersection point was 20.7 MPa and 0.01247 m.

In addition, under the same critical elastic buckling load, the thickness of the EPHV (here it actually means the maximum value at the whole span along axis, as thickness of EPHV is variable) was the maximum, then the EPHC was following, and the thickness of the SPH was the minimum. And under the same yielding load, the thickness of the SPH was less than the thickness of the EPHC that was equal to the maximum thickness the EPHV.

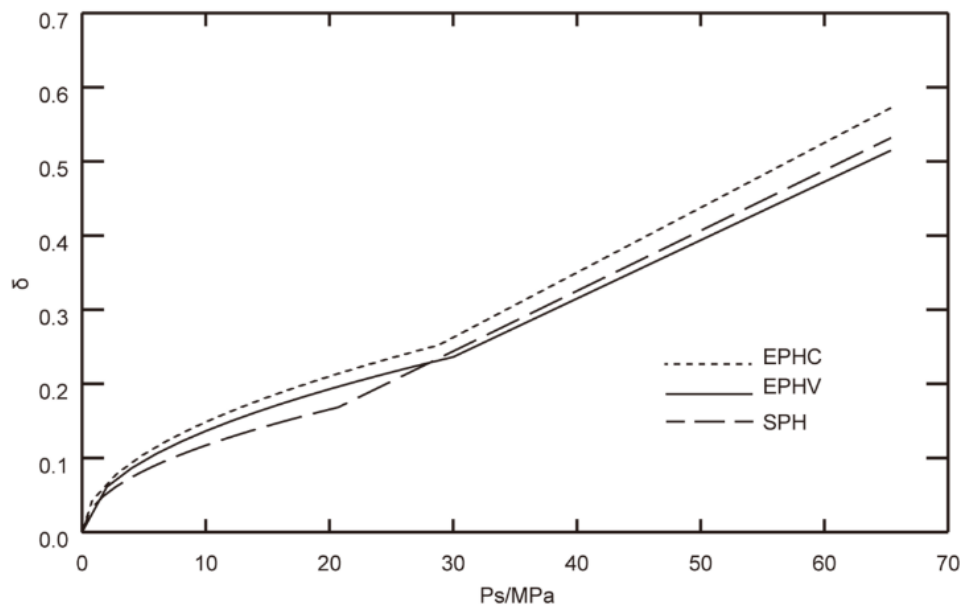


Fig.3-24 Comparison of buoyancy factor for pressure hulls

Buoyancy factor is an index to evaluate buoyancy reserve of a pressure hull. Fig.3-24 shows the buoyancy factor versus the design load for the EPHC, the EPHV and the SPH. It can be seen in Fig.3-24, the buoyancy factor of each pressure hull was non-linear with respect to the design load before the intersection point in Fig.3-23, and was linear with respect to the design load after that. The buoyancy factor of the EPHC was always higher than that of the EPHV by approximately 10%. When the

design load was less than 20.7 MPa, the buoyancy factors of both EPHC and EPHV were higher than that of the SPH. However, when the design load was more than 30 MPa, the buoyancy factor of EPHV became lower than SPH, by approximately 3.2%, meanwhile the buoyancy factor of EPHC was higher than SPH by approximately 7.6%. Therefore, it is expected that the buoyancy reserve of EPHV can be better than that of SPH in deep sea.

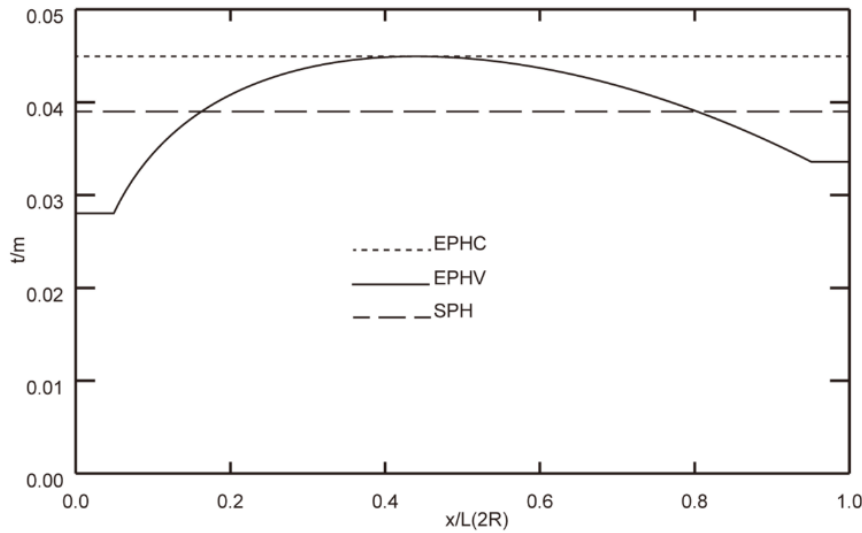


Fig.3-25 Comparison of thickness for pressure hulls

Assume that the working depth was 4 km. Then, the design load at this depth was 65.33 MPa by Equation (3-24). In accordance with Fig.3-25, the thickness of each pressure hull should be determined in the case that strength was the main factor. Fig.3-25 shows thickness variations of pressure hulls along the axis of EPHC/EPHV or the radial direction of the SPH. For comparison, the abscissa was assumed to be ratio of x and L for EPHC/EPHV or ratio of x and $2R$ for the SPH. From Fig.3-26, the thickness of EPHC t_1 , the maximum thickness of EPHV T_2 and the thickness of the SPH t_3 were 44.95 mm, 44.95 mm and 39.36 mm, respectively. The thickness of sharp area of EPHV was 28.04 mm. Likewise, the thickness of blunt area of EPHV was 33.58 mm. In this case, yielding loads of three pressure hulls obtained by Fig.3-24 were equal with the value of 65.33. Similarly, critical elastic buckling loads

of EPHC P_{q1} , EPHV P_{q2} and SPH P_{q3} were 148.11 MPa, 142.25 MPa and 206.28 MPa, respectively. Besides, buoyancy factors of EPHC δ_1 , that of EPHV δ_2 and that of SPH δ_3 obtained by Fig. 6 were 0.572, 0.513 and 0.531, respectively.

The von Mises equivalent stresses for pressure hulls were calculated by Equation (3-27), as shown in Fig.3-26. The stress of EPHC firstly increased and then decreased along the major axis, with the maximum value of 830 MPa. The stress was equal everywhere in SPH or in the equator area of EPHV, which was 830 MPa. In the sharp area of EPHV, the stress increased along the major axis, but the stress decreased in the blunt area. From Fig.3-26, it is implied that holes are appropriate to be opened at the sharp or blunt ends of egg-shaped pressure hulls, where the von Mises equivalent stresses are relatively small.

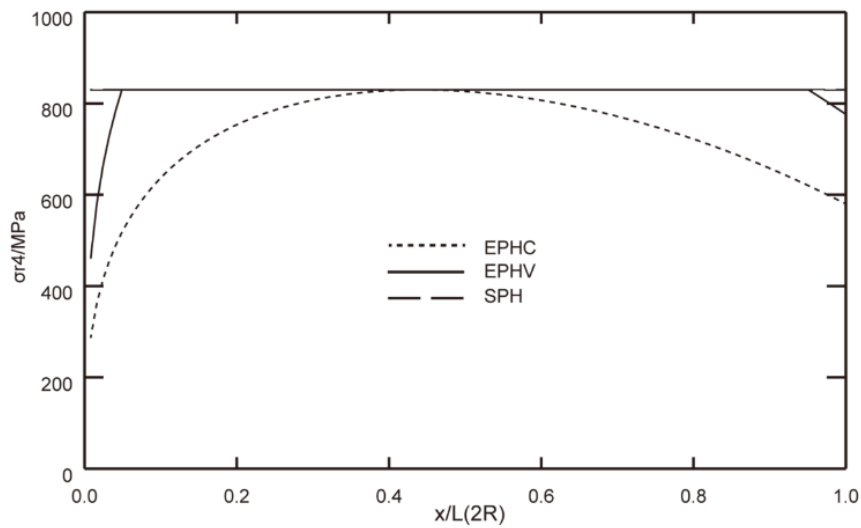


Fig.3-26 Comparison of von Mises equivalent stress for pressure hulls

3.6 Numerical results of egg-shaped and spherical pressure hulls

Two techniques are usually employed to investigate buckling behaviors of pressure hulls by finite element method: linear buckling analysis and nonlinear buckling analysis [23]. Since the linear buckling analysis only predicts the theoretical buckling behaviors of perfect elastic pressure hulls, in which imperfections and nonlinearities cannot be involved. Therefore, this technique was only adopted as the base of the afterwards nonlinear buckling analysis and to be compared with the analytical

solutions. Instead, more realistic buckling behaviors of pressure hulls can be determined by the nonlinear buckling analysis, for which geometric imperfections, plastic behavior of the material and large deflection response were all considered.

For shell structures, the initial geometric imperfections due to the manufacturing process usually have big effects on buckling behavior, which results in apparent discrepancies between the experimental results and the theoretical results [24]. However, real imperfections are mostly unknown in the design phase, thus patterns of imperfections are often assumed to be equivalent ones. Linear buckling mode shapes have sometimes been considered as the base of equivalent imperfections [25-26]. It is always a common practice to consider the imperfection pattern to be the worst that is affined to the lowest eigenmode [25-26]. Nevertheless, this imperfection pattern may not be usually the worst for shell structures with closely spaced eigenvalues. For such cases, higher modes are sometimes correlated to lower buckling loads [24]. Therefore, rather than one (only the first), many eigenmodes of each pressure hull were analyzed and then the corresponding one was selected as initial imperfections, respectively for different pressure shell.

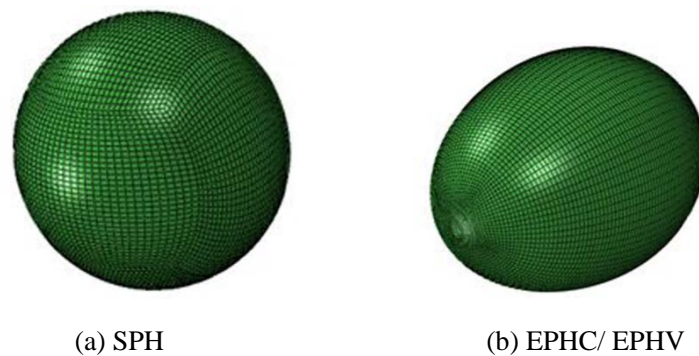


Fig.3-27 FE mesh of pressure hulls

A total of 39 linear buckling analysis models were presented and solved with aid of the subspace iteration technique as implemented in ABAQUS. The numerical models of three pressure hulls with perfect geometry were proposed by mesh generation program ANSA in conjunction with the FE program ABAQUS. Shell elements S4 based on a finite membrane strain formulation are selected to avoid Hourglassing. The material was assumed to be elastic with the mechanical properties given in section 3.3.

The number of elements has been determined with the use of the mesh convergence analysis. As a result, the FE model of the SPH composed of 7146 shell elements and 8172 nodes, the model of the EPHC composed of 9534 shell elements and 9536 nodes, similar to the EPHV except different thickness distribution in its model, as shown in Fig.3-27.

A total of 195 nonlinear buckling analyses were implemented with modified Riks method in ABAQUS. In these nonlinear buckling analyses, the initial geometric imperfections were introduced with the every eigenmode shapes which were obtained from the above linear buckling analyses. According to current rules for pressure hulls, the imperfection size should be considered as 1 mm, 2 mm, 3 mm, 4 mm and 5 mm, respectively. Plastic behavior of the material can also be defined, where the material parameters were given in section 3.3. Mesh and element type were the same as the linear buckling analysis. In this way, the real buckling loads of pressure hulls were obtained with geometry and material nonlinear imperfection analysis, without adding any additional preliminary reduction conditions. Then knock-down factors (KDFs) for each pressure hull were calculated as the ratio of buckling loads of imperfect and perfect pressure hull.

The first 13 eigenvalues of each perfect pressure hull obtained from the linear buckling analysis are listed in Table 3-18. The first buckling loads of the egg-shaped pressure hull with the constant thickness (EPHC), the egg-shaped pressure hull with the variable thickness (EPHV) and the spherical pressure hull (SPH) were 144.03 MPa, 135.29 MPa and 204.87 MPa, respectively. It is evident that the numerical results are in good agreement with the analytical solutions. It can be also seen from Table 3-18 that eigenvalues were increasing with 30.48% for the EPHC, 20.98% for the EPHV, 0.61% for the SPH, from the 1st to the 13th eignvalue. Furthermore, the first 12 eigenvalues of SPH presented differences within 0.5%, while only the first 2 eigenvalues of the EPHC and the first 4 eigenvalues of the EPHV yielded this range. It is reasonable to expect that the spherical pressure hull is more sensitive to such imperfection than egg-shaped pressure hulls. This was specially investigated in the following nonlinear buckling analyses.

Table 3-18 Eigenvalues and eigenmodes from the linear buckling analysis for pressure hulls.

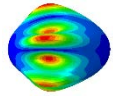
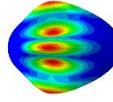
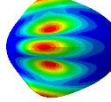
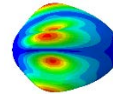
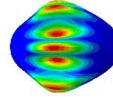
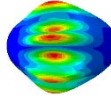
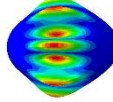
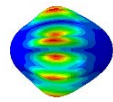
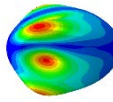
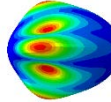
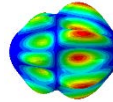
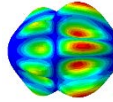
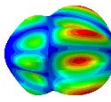
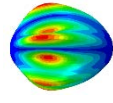
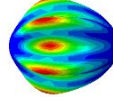
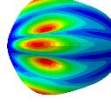
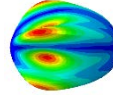
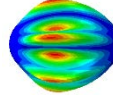
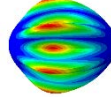
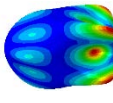
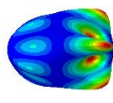
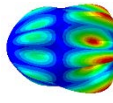
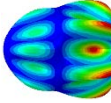
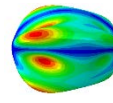
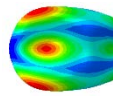
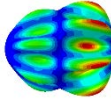
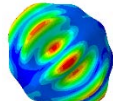
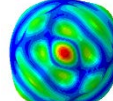
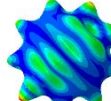
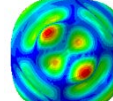
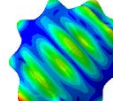
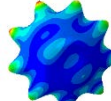
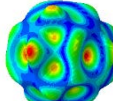
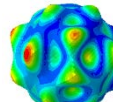
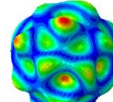
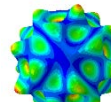
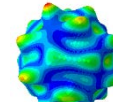
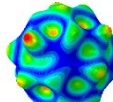
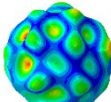
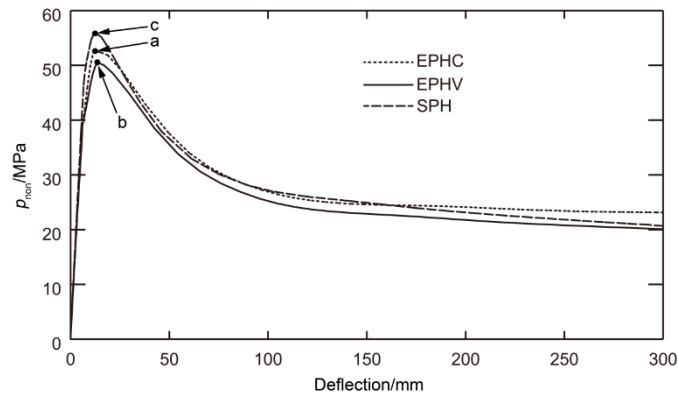
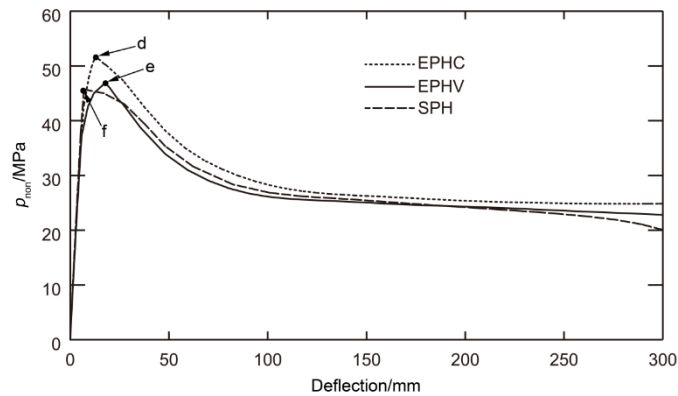
EPHC	1 st mode	2 nd mode	3 rd mode	4 th mode	5 th mode	6 th mode	7 th mode
	144.03 MPa	144.03 MPa	146.87 MPa	146.87 MPa	155.56 MPa	155.56 MPa	176.60 MPa
							
	8 th mode	9 th mode	10 th mode	11 th mode	12 th mode	13 th mode	P_{q1}
	176.60 MPa	177.15 MPa	177.15 MPa	180.65 MPa	180.65 MPa	187.93 MPa	148.11 MPa
							N/A
EPHV	1 st mode	2 nd mode	3 rd mode	4 th mode	5 th mode	6 th mode	7 th mode
	135.29 MPa	135.29 MPa	135.61 MPa	135.61 MPa	147.73 MPa	147.73 MPa	148.74 MPa
							
	8 th mode	9 th mode	10 th mode	11 th mode	12 th mode	13 th mode	P_{q2}
	148.74 MPa	150.50 MPa	150.51 MPa	159.63 MPa	159.63 MPa	163.68 MPa	142.25 MPa
							N/A
SPH	1 st mode	2 nd mode	3 rd mode	4 th mode	5 th mode	6 th mode	7 th mode
	204.87 MPa	204.89 MPa	204.91 MPa	204.93 MPa	204.95 MPa	204.97 MPa	205.50 MPa
							
	8 th mode	9 th mode	10 th mode	11 th mode	12 th mode	13 th mode	P_{q3}
	205.50 MPa	205.52 MPa	205.52 MPa	205.53 MPa	205.82 MPa	206.12 MPa	206.28 MPa
							N/A

Fig.3-28 presents the equilibrium paths of three pressure hulls with the maximum

imperfection size (5 mm) and with the imperfection shape of the first eigenmodes (Fig.3-29 (a)) and the worst eigenmodes (Fig.3-29 (b)). The paths presented applied loads versus maximum deflections of pressure hulls. As shown in Fig.3-28, all equilibrium paths have an unstable character. The applied load initially increased up to a peak value with an increase in deflection, after which the applied load substantially decreased with an increase in deflection. The character of equilibrium paths was similar for all cases considered.



(a) Lowest eigenmode imperfections



(b) Worst eigenmode imperfections

Fig.3-28 Equilibrium paths of pressure hulls with imperfection size of 5 mm

Critical buckling modes for EPHC (a,d), EPHV (b,e) and SPH (c,f) corresponding to Fig.3-28 are given in Fig.3-29; ‘a-c’ correspond to the lowest eigenmode imperfections, whilst ‘e-f’ correspond to the worst eigenmode imperfections. These marks are also designated in Fig.3-29. As can be seen from Fig.3-30, for EPHC, the nonlinear buckling modes (a) and (d) took the form of 6 and 7 circumferential waves along with a longitudinal half-wave, which are similar to their corresponding linear

buckling modes (Table 3-18). Likely, for EPHV, both the nonlinear buckling modes (b) and (e) took the same form of 6 circumferential waves together with a longitudinal half-wave, which are also in line with their corresponding linear buckling modes (Table 3-18). In addition, in the case of the lowest eigenmode imperfection, the nonlinear buckling mode (c) of the SPH was of the form of 9 circumferential waves and a longitudinal half-wave, while its buckling mode (f) in the case of the worst eigenmode imperfection had the shape of 9 circumferential and 9 longitudinal waves. These nonlinear buckling modes for the SPH are consistent with their corresponding linear buckling modes, listed in Table 3-18.

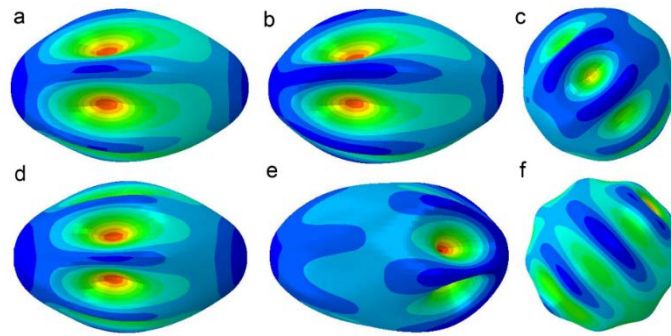


Fig.3-29 Critical buckling modes for EPHC (a,d), EPHV (b,e) and SPH (c,f); ‘a-c’=lowest eigenmode imperfections, ‘d-f’=worst eigenmode imperfections

Fig.3-30 shows Knock-down curves obtained from the nonlinear buckling analyses for pressure hulls with geometric imperfection of five different imperfection sizes of 1 mm, 2 mm, 3 mm, 4 mm and 5 mm (and each size correlating to the amplitudes of 13 mode shapes respectively, resulting in the total of 195 simulations). Some critical results are listed in Table 3-19 and Table 3-20. From Fig.3-30, nonlinear imperfection analyses gave a wide range of KDFs for pressure hulls, from 0.3576 to 0.4658 for EPHC, 0.3466 to 0.4789 for EPHV and 0.2231 to 0.3163 for the SPH. It is found that shape and size of the geometric imperfections have significant effects on the buckling loads of pressure hulls.

Table 3-19 and Table 3-20 summarize KDFs obtained from the lowest eigenmode and the ‘worst eigenmode’ respectively. This factor is an index of the sensitivity of the buckling load with respect to the considered geometric imperfections. From Table

3-19 and Table 3-20, it can be seen that the buckling modes causing the lowest KDFs were usually not the lowest eigenmodes in the cases. For example, the 9th mode produces the lowest KDF for the EPHV, and the 5th mode produced the lowest KDF for the EPHC and the SPH.

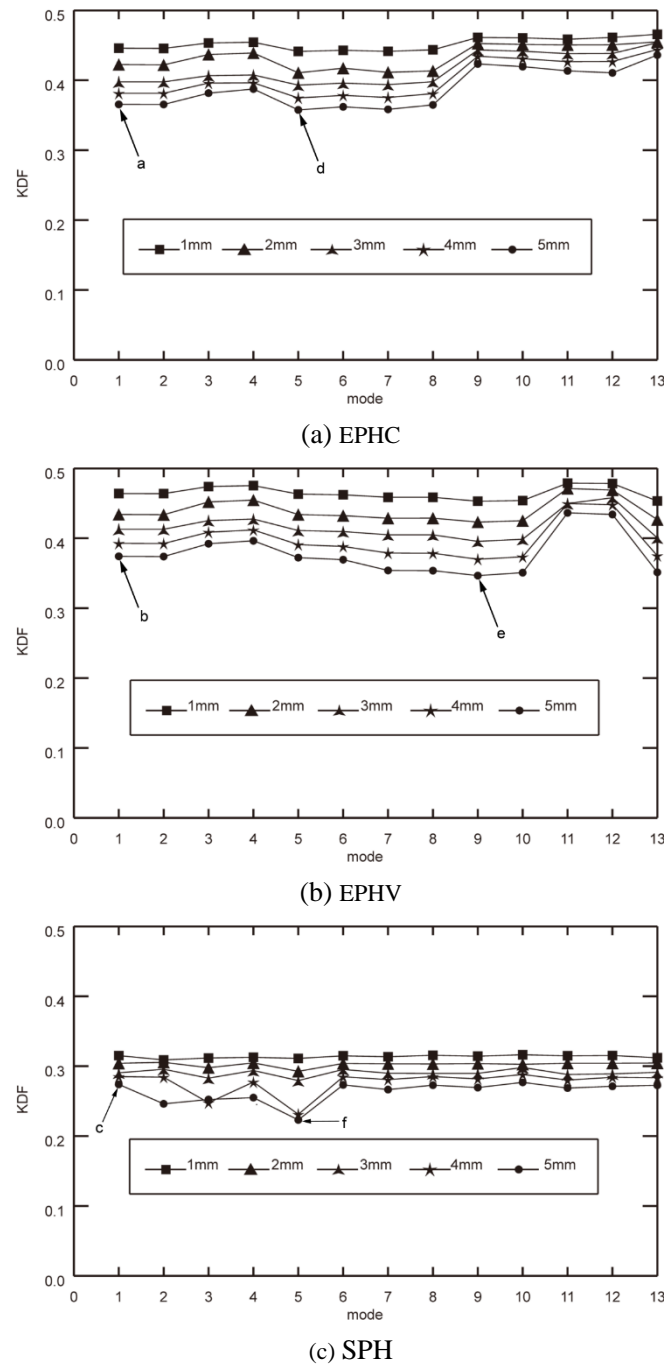


Fig.3-30 Knock-down curves for pressure hulls

It is found that the lowest eigenmode imperfection analysis of shell structures may be often yield dangerous results, therefore higher eigenmodes should be used to

characterize the deformation shape corresponding to the lowest buckling load for shell structures with densely spaced eigenvalues. In addition, by comparing Table 3-18, Table 3-19 and Table 3-20, it shows that, the more densely spaced eigenvalues existed, the more geometric imperfection sensitivity was the shell with.

Table 3-19 KDFs for imperfection pressure hulls with the lowest eigenmodes.

Imperfection size/mm	EPHC	EPHV	SPH
1	0.4459	0.4640	0.3151
2	0.4225	0.4340	0.3041
3	0.3977	0.4129	0.2905
4	0.3813	0.3927	0.2851
5	0.3655	0.3742	0.2739

Table 3-20 KDFs for imperfection pressure hulls with the worst eigenmodes.

Imperfection size /mm	EPHC		EPHV		SPH	
	mode	KDF	mode	KDF	mode	KDF
1	5 th	0.4413	9 th	0.4530	2 nd	0.3090
2	5 th	0.4107	9 th	0.4232	5 th	0.2926
3	5 th	0.3931	9 th	0.3956	5 th	0.2794
4	5 th	0.3747	9 th	0.3700	5 th	0.2311
5	5 th	0.3576	9 th	0.3466	5 th	0.2231

In each case, the buckling load decreased with an increase in the imperfection size. And this decrease was sharper for small amplitude imperfections. For an imperfection size of 1 mm, the buckling load of SPH was only about 1/3 of the buckling load of the hull without imperfections. It is thus indicated that the SPH is highly sensitive to the geometric imperfections. Compared with the SPH, the EPHV and the EPHC are less sensitive to geometric imperfections. As seen From Table 3-20, KDFs of the EPHC, EPHV and SPH were minimum with the imperfection size of 5mm. KDF of the SPH was as little as 0.2231 with this size of imperfection. This value is consistent with

classical literatures reported by scientists such as Karman, Tsien and Hutchinson [27-28]. The buckling loads of the EPHC, the EPHV and the SPH are 51.51 MPa, 46.89 MPa and 45.71 MPa, respectively. The buckling load of each pressure hull is more than 40 MPa, indicating that these pressure hulls could operate safely at the water depth of 4 km. And also, it seems that the stability of egg-shaped shell (EPHC/EPHV) is even better than that of the equivalent spherical shell (SPH), which is surprisingly beyond the conventional expectation.

3.7 Evaluation and comparison of main properties for pressure hulls

Main properties of the egg-shaped pressure hull with constant thickness (EPHC), egg-shaped pressure hull with variable thickness (EPHV) and spherical pressure hull (SPH) were evaluated and compared as follows:

First of all, safety is the most important property of the manned pressure hull, which provides a safe living space for crews and scientists. Since three pressure hulls were designed at the same strength level, the yielding loads of EPHC, EPHV and SPH were equal. However, the above investigation has documented that the SPH is more sensitive to geometric imperfections than the EPHC/EPHV. And the buckling load of SPH with the worst geometric imperfections is always less than that of EPHC/EPHV. It seems that safety of SPH was somewhat ‘worse’ than that of EPHC/EPHV.

Secondly, buoyancy reserve is also a critical property of the manned pressure hull, which affects total weight of the manned submersible. As discussed in the above, the buoyancy factor of EPHV was 96.6% of SPH, which indicates that buoyancy reserve of EPHV are better than SPH. The buoyancy factor of EPHC is slightly more than SPH by 7.7%.

Thirdly, space efficiency is another key property of the manned pressure hull, which provides convenient interior arrangement and a proper space for working and living. Hence, space efficiency was evaluated by the meridional radius of curvature and the meridional area of pressure hulls in this study. As outlined in section 2, the meridional radius of curvature and the area of meridional cross section of the EPHC/EPHV were 1.30 m and 3.27 m². Likely, these two values of the SPH were 1 m

and 3.14 m^2 , respectively. It is indicated that space efficiency of the EPHC/EPHV are better than that of the SPH.

Consequently, it is of great interest to discover that safety, buoyancy reserve, space efficiency of egg-shaped pressure hulls can be optimally coordinated, and perform better than spherical pressure hull. It is also convenient to open holes on the EPHC/EPHV. Furthermore, the EPHC/EPHV has advantages of satisfactory aesthetics, which may provide a crew comfort. It is anticipated that egg-shaped pressure hulls will play a key role in future development of the deep manned submersible.

3.8 Summary

It is until now that the spherical pressure hull is the most extensively used structure for the deep manned submersible. However, low buckling resistance, difficult interior arrangement and poor hydrodynamics are found with this type of pressure hull at the given design load. In this study, bionics on egg-shaped pressure hulls are performed to improve these problems possessed by the spherical pressure hull, the conclusions were as follows:

(1) The major axis, minor axis, and shape index of goose eggs were all determined to possess normal distributions, with averages of 78.26 mm, 53.62 mm, and 69%, respectively. The thickness of the eggshells first increased and then decreased from the blunt end to the sharp end. There is a considerable amount of error between the theoretical calculations and experiments conducted to determine eggshell surface area. As a result, the correction coefficient was increased to $\delta = 1.02$ to correct the calculation results for surface area. Goose eggs have a symmetrical structure with circular wefts. The N-R equation is the most satisfactory method of describing the contour lines and can be used to build the profile curve of a goose egg. A 3D mathematical model can then be built by rotating the profile curve around the major axis.

(2) Results of experiments showed that the critical loads of 5 goose eggshells were at the range from 2.87 to 3.31 MPa. Numerical results showed that the range of critical buckling loads was from 3.26 to 7.97 MPa. Comparison of results obtained

from experiment and numerical stimulation, it could be implied that buckling is not the main factor to result in instability of each goose eggshell. Besides, considering of meridional stress and circumferential stress of each goose eggshell, compared to some other calcium carbonates, it is suggested that strength is the main factor to result in instability of each goose eggshell. Goose eggshell would have a higher loading carry ability with using other pressure-resistant materials, such as titanium alloy. This finding could provide efficient bionic information for pressure hulls in deep-sea manned submersible.

(4) The shape and size of the geometric imperfections have a big effect on the buckling load of pressure hulls. For shell structures with densely spaced eigenvalues, higher rather than the first eigenmode imperfection is often the worst equivalent buckling mode which might lead to the lowest buckling load. The more densely spaced eigenvalues exists, the more geometric imperfection sensitivity is the shell with. Egg-shaped pressure hulls are less sensitive to the geometric imperfections compared with the spherical pressure hull. At the given design load, it is found that safety, buoyancy reserve, and space efficiency of egg-shaped pressure hulls could be optimally coordinated, which appears to be better than spherical pressure hull. This research work offers a new concept of pressure hull designs for future development of the deep-sea manned submersible.

However, this chapter is only a preliminary exploration into buckling of egg-shaped pressure hulls, although the results are encouraging. Also, it does not examine the effect of shape index and wall thickness on the buckling of egg-shaped pressure hulls. Since these two factors are very important in the preliminary design stage, further study into such effect is strongly required.

References

- [1] M Sarica, & C Erensayin. (2004). Poultry products. Bey-Ofset, Ankara-Turkey (in Turkish).
- [2] Š Nedomová, J Buchar, & J Strnková. Goose's eggshell strength at compressive loading. *Potravinárstvo Scientific Journal for Food Industry*. 8 (2014) 54-61.
- [3] X Wang, L. I Sen. 3D modeling and assembly design based on ug nx. *Manufacturing*

- Technology & Machine Tool. 29 (2007) 78-81.
- [4] N. N. Mohsenin, Physical properties of plant and animal material. Gordon and Breach, New York, 1970.
 - [5] E Seifert. Originpro 9.1: scientific data analysis and graphing software—software review. Journal of Chemical Information & Modeling 2014;54(5):1552.
 - [6] J Zhang, W. M Wang, F Wang, W. X Tang, W. C Cui, W. B Wang. Elastic buckling of externally pressurized Cassini oval shells with various shape indices. Thin-Walled Struct. 122 (2018) 83-89.
 - [7] Š Nedomová & J Buchar. Goose eggshell geometry. Res.Agr.Eng. 60 (2014) 100-106.
 - [8] Š Nedomová, L Severa, et al. Influence of hen egg shape on eggshell compressive strength. Int.Agrophysics. 23 (2009) 249-256.
 - [9] S. K Upadhyaya, J. R Cook, R. S Gates, et al. A finite element analysis of the mechanical and thermal strength of avian eggs. J Agric Engng Res, 33 (1986) 57-58.
 - [10] K M Entwistle, T Y Reddy. The fracture strength under internal pressure of the eggshell of domestic fowl . Biological Science. 263 (1996) 433-438.
 - [11] M. A Tung. Estimation of Young modulus and failure stresses in the hen's egg shell. Canadian Agricultural Engineering. (1969).
 - [12] G. E Rehkugler. Modulus of elasticity and ultimate strength of the hen's eggs shell. Journal of Agricultural Engineering Research. 8 (1963) 352-354.
 - [13] M. M Bain. Eggshell strength: a mechanical/ultrastructural evaluation. University of Glasgow, Scotland. (1990).
 - [14] W. C Cui. Development of the Jiaolong deep manned submersible. Marine Technology Society Journal. 47 (2013) 37-54.
 - [15] W. X Qu, D. F Han, F Liu. Research on critical buckling pressure of manned submersible pressure hull. Ship & Boat. 3 (2013) 42-47 (in Chinese).
 - [16] L. B Li, R. H Wang, M. H Yu, Z. L Wang. Nonlinear finite element analysis of pressurized spherical shell for manned deep submersible. Shipbuilding of China. 46 (2005) 11-18 (in Chinese).
 - [17] E Ventsel, T Krauthammer. Thin plates and shells: theory, analysis and applications. Marcel Dekker. (2001).
 - [18] H. M Mushtari. On elastic equilibrium of a thin shell with initial irregularities of the form of a middle surface. PMM. 15 (1915) 743-750 (in Russian).
 - [19] Rules for the classification and construction of diving systems and submersibles. Published by China Classification Society (CCS) in 2013.(2013)
 - [20] Rules for classification and construction, 1-ship technology, 5-underwater technology, 3-unmanned submersibles. Published by Germanischer Lloyd (GL) in 2009.(2009)
 - [21] Rules for the classification of underwater vehicles. Published by Korean Register of shipping (KR) in 2012. (2012).
 - [22] B. B Pan, W. C Cui. An overview of buckling and ultimate strength of spherical pressure hull under external pressure. Marine Structures. 23 (2010) 227-240.
 - [23] Review of Buckling Analysis by Finite Element Method (FEM). Published by American Bureau of Shipping (ABS) in 2005. (2005).
 - [24] SGP Castro, R Zimmermann, MA Arbelo, R Khakimova, MW Hilburgerd, R Degenhardt. Geometric imperfections and lower-bound methods used to calculate knock-down factors

- for axially compressed composite cylindrical shells. *Thin-walled Structures*. 74 (2014) 118-132.
- [25] Eurocode 3 – Design of steel structures – Part 1-6: Strength and Stability of shell structures. published by European Committee for Standardisation in 2007. (2007).
- [26] YV Narayana, JB Gunda, PR Reddy, R Markandeya. Non-linear buckling and post-buckling analysis of cylindrical shells subjected to axial compressive loads: A study on imperfection sensitivity. *Nonlinear Engineering*. 2 (2013) 83-95.
- [27] TV Karman, HS Tsien. The buckling of spherical shells by external pressure. *Journal of the Aeronautical Sciences*. 7 (1939) 43-50.
- [28] JW Hutchinson. Imperfection sensitivity of externally pressurized spherical shells. *J Appl Mech*. 34 (1967) 49-55.

Chapter 4 Effect of geometrical parameters on buckling of egg-shaped pressure hulls

In previous chapter, considering the advantages of eggshell, such as high load-carrying capacity, rational streamline, span-to-thickness ratio etc., the authors developed deep egg-shaped pressure hulls to replace the deep spherical ones. It was found that, compared with spherical pressure hulls, egg-shaped pressure hulls could meet the requirements of safety, space utilization, riding comfort, and hydrodynamics. However, the role of shape index and wall thickness on the buckling behaviours of egg-shaped pressure hulls has not been explored. In this case, one cannot determine in which shape or depth egg-shaped pressure hulls are most possibly suitable to work. Also, the corresponding computational method of egg-shaped pressure hulls is refer to that of spherical pressure hulls, which still requires experimentation. Therefore, this chapter is devoted to the effect of geometrical parameters on the buckling of egg-shaped pressure hulls, along with corresponding experimentations.

Firstly, a family of egg-shaped shells with various shape index (ratio of the minor B to the major L axis) were proposed by keeping capacity and mass constant. According to the experimental results, eight shape indices in the 0.65 to 0.72 range were selected for creating the egg-shaped pressure hull. Besides, to extend the shape index range, six pressure hulls with S /s of 0.4, 0.5, 0.6, 0.8, 0.9 and 1.0 were also proposed. The effects of shape index on both linear and nonlinear buckling of such pressure hulls were numerically studied.

Secondly, a further investigation on a range of externally pressurized egg-shaped pressure hulls was carried out in case that wall thickness varies from 10-80 mm with 5 mm increment. Series of numerical simulations were performed to systematically study the buckling of egg-shaped pressure hulls, along with the effect of wall thickness on the buckling. Volume and mass equivalent spherical pressure hulls were also proposed to make a like-for-like comparison with egg-shaped pressure hulls.

Finally, a family of laboratory scale egg-shaped shells were proposed to perform

experimentation. To validate the proposed numerical approach and post buckling modes, three nominally identical CNC-machined steel egg-shaped shells were tentatively fabricated, accurately measured, slowly tested, and numerically studied. Additionally, to confirm the imperfection assumption and obtain a highly accurate experimental models, a range of resin egg-shaped shells with local imperfections and perfect geometries were considered using rapid prototyping.

4.1 Effect of shape index on buckling of egg-shaped pressure hulls

4.1.1 Geometry of egg-shaped pressure hulls

The geometry of a typical egg-shaped pressure hull is illustrated in Fig.4-1. It consists of a sharp end, equator, and blunt end arranged along the major axis (axis of revolution).

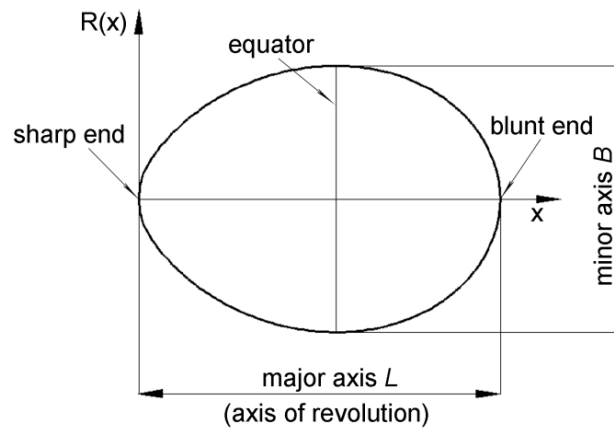


Fig.4-1 Sketch of a typical egg-shaped pressure hull

The radius of the circumference of a shell of revolution is provided in Cartesian coordinates by Eq. (4-1), which is an egg-shaped equation obtained in Chapter 3:

$$R(x) = \pm \sqrt{L^{\frac{2}{n+1}} x^{\frac{2n}{n+1}} - x^2} \quad (4-1)$$

where

$$n = 1.057(L/B)^{2.372} \quad (4-2)$$

L is the major axis, and B is the minor axis. This equation has been widely applied for describing the contour of eggshells. Consequently, this equation is used to define the geometry of the middle surface of egg-shaped pressure hull. To facilitate the creation of a family of egg-shaped pressure hulls, the following variable named shape

index for determining the SI (i.e., the ratio of the minor B to major L axis) is introduced:

$$SI = B / L . \quad (4-3)$$

This parameter determines the geometry of egg-shaped pressure hull. As shown in Fig.4-2, for $SI = 0$, the egg-shaped pressure hull is an infinitely long cylindrical pressure hull. When $0 < SI < 1$, an egg-shaped pressure hull is obtained. For $SI = 1$, the egg-shaped pressure hull approximates a spherical pressure hull. Therefore, the cylindrical pressure hull and spherical pressure hull, which are described by the dashed lines in Fig.4-3, can be treated as particular instances of the egg-shaped pressure hull.

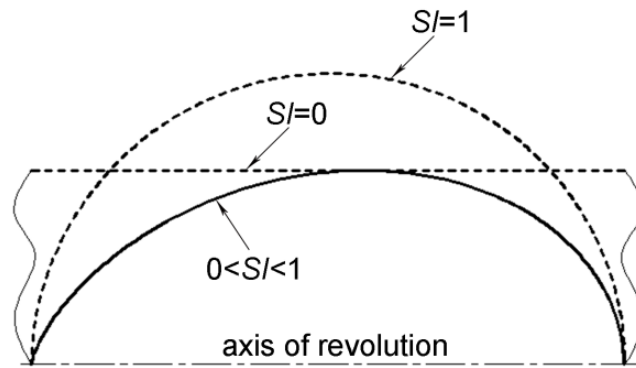


Fig.4-2 Meridian of an egg-shaped shell

Egg SI s differ greatly among the world's bird species [1]. Our previous studies have demonstrated that the goose egg can provide a guide for developing a new type of manned pressure hull [2]. The range of SI s in this study was determined on the basis of the experimental results of 333 eggs (6 days old) from 2-year-old geese. The eggs were selected from Jiangshan farm, located in Zhejiang Province, China. To obtain the SI s, the major L and minor B axes of the eggs were carefully measured using a digital caliper. The SI results are shown in Fig.4-3; they approximate a normal distribution. The SI value is most frequently in the 0.65 to 0.72 range. This range was selected for creating a family of egg-shaped pressure hulls with a constant capacity and mass. Besides, to extend the range of SI , the shells with SI s of 0.4, 0.5, 0.6, 0.8, 0.9 and 1 were also proposed.

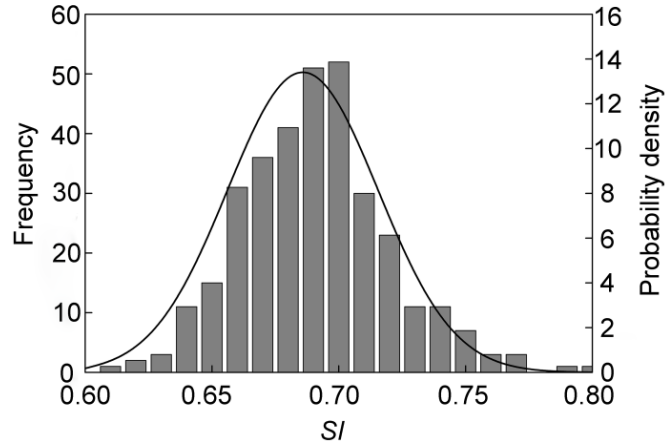


Fig.4-3 Distribution of the shape index of tested goose eggshells after transformation with normally distributed curve

4.1.2. Capacity and mass of egg-shaped pressure hull

The capacity of the egg-shaped pressure hull is determined as follows:

$$V = \frac{\pi}{6} LB^2 . \quad (4-4)$$

The mass of the egg-shaped pressure hull is calculated using the following relationship:

$$m = At\rho , \quad (4-5)$$

where t is the shell thickness, and ρ is the mass density of the material. The surface area A is determined using a modified version of Mohsein [3-4]:

$$A = k\pi \left(LB^2 \right)^{\frac{2}{3}} , \quad (4-6)$$

where $k = 1.02$ is a correction coefficient. Using (4-4), (4-5), and (4-6), the major (L) and minor (B) axes are calculated as follows:

$$L = \sqrt[3]{\frac{6V}{\pi(SI)^2}} , \quad (4-7)$$

$$B = \sqrt{\frac{6V}{L\pi}} . \quad (4-8)$$

Thus, L and B are respectively determined using (4-7) and (4-8) by retaining the capacity (V) and mass (m) of the egg-shaped pressure hull constant. It is assumed that $V = 3.1809 \text{ m}^3$, $A = 10.4598 \text{ m}^2$, $t = 15 \text{ mm}$. According to (4-7) and (4-8), a family of

egg-shaped pressure hulls with a constant capacity and mass can be created by calculating the major L and minor B axes. The meridian of this family of pressure hulls is identified in Fig.4-4.

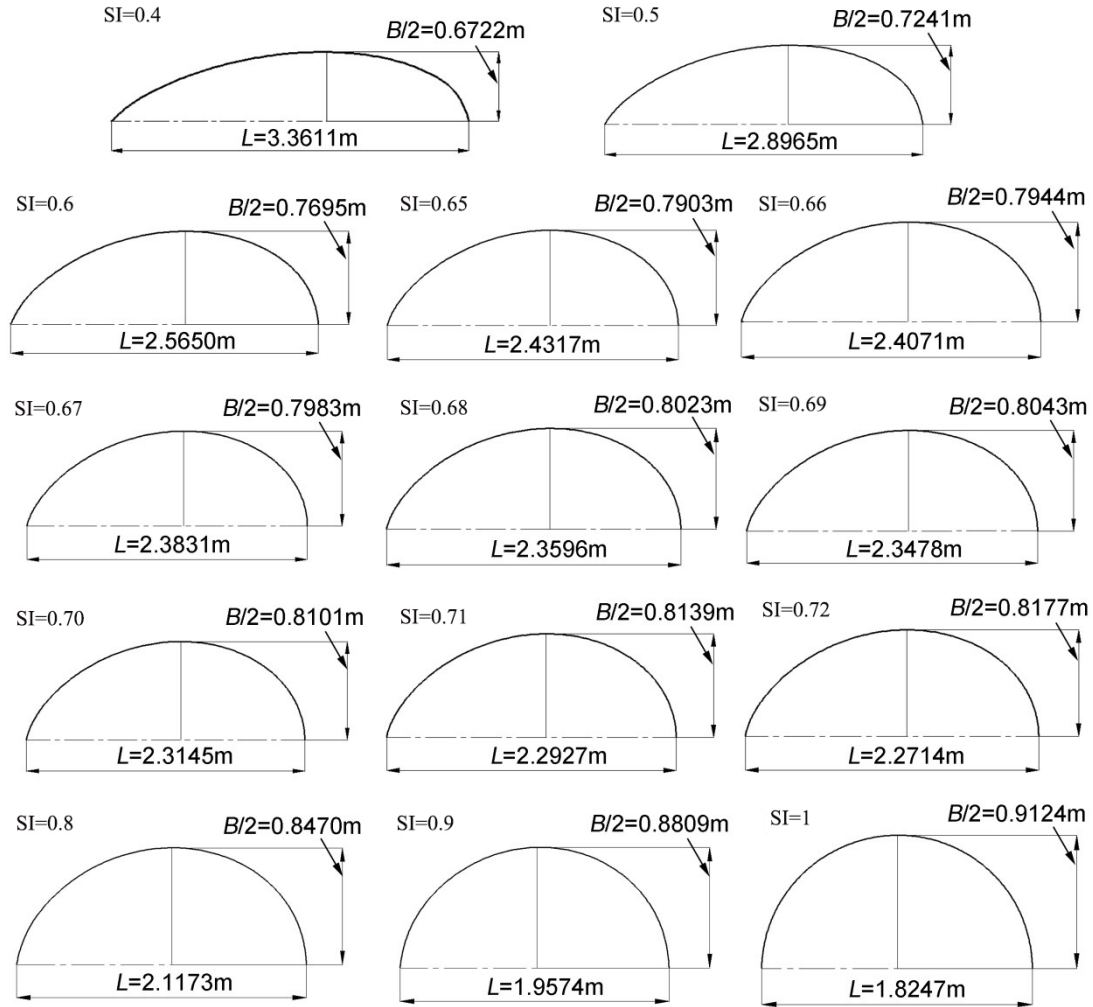


Fig.4-4 A family of egg-shaped pressure hulls with a constant capacity and mass

4.1.3 Numerical modeling of egg-shaped pressure hulls

To examine the effect of egg SI on the load carrying capacity of egg-shaped shells, both linear buckling analysis and nonlinear buckling analysis with imperfections included were performed. Fourteen egg-shaped pressure hulls with a constant capacity and mass were analyzed. The analysis was performed using the finite element method in Abaqus. The fully integrated S4 shell element was selected to avoid hourglassing. The number of elements was determined using mesh convergence analysis. Thus, the finite element model of each egg-shaped shell has the same hull elements of 7584 and

nodes of 7586. The uniform pressure $p_0 = 1\text{MPa}$ was externally applied to the whole surface area of the egg-shaped shells. This is a typical load for underwater pressure hulls, underground pressure vessels, and underpressure tanks. To avoid rigid displacements, for example of the egg-shaped pressure hull with SI of 0.69, constraints were applied at three random spatial points and the support condition of each point from left to right as follows: $U_y=U_z=0$, $U_x=U_y=0$, $U_y=U_z=0$, as shown in Fig.4-5; this was identical for all analyzed egg-shaped pressure hulls. These constraints were in line with CCS2013 [5] and did not cause excessive constraint of the models because the pressure was equally applied. The reaction forces at these points were zero. Ti alloy (Ti-6Al-4V) was used to construct the egg-shaped pressure hulls. Details of this material can found in Chapter 2.

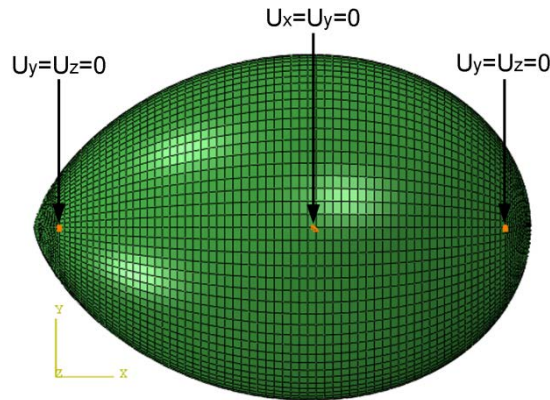


Fig.4-5 FE mesh and support conditions for the egg-shaped pressure hull with SI of 0.69

4.1.4. Linear buckling of egg-shaped pressure hulls

This section focuses on the linear buckling loads and modes of egg-shaped pressure hulls. Linear eigenvalue buckling analysis was conducted numerically using a Lanczos eigensolver implemented in Abaqus/Standard. A semianalytical formula developed by Mushtari [6] was adopted for calculating the elastic buckling loads; thus,

$$p_{cr} = \frac{2Et^2}{(\overline{2R_1} - \overline{R_2})\overline{R_2}} \sqrt{\frac{1}{3(1-\mu^2)}} , \quad (4-9)$$

where $\overline{R_1}$ is the mean value of the principle meridional radius of curvature for the

shell section bounded by the nodal curves of the local buckling forms; likewise, \bar{R}_ϕ is the mean of the principle circumferential radius of curvature. Details of this formula are provided in [7-9]. According to these previous studies, (4-9) can be used to predict the linear buckling load of the thin, convex shells of revolution with a membrane stress and with a number of waves along the parallels. When $R_1 = R_2$, (4-9) can be simplified to the equation used for the classical buckling problem of spherical shells developed by Zoelly [10]. However, when $R_1 = \infty$, p_{cr} is zero and does not correspond to the elastic buckling load of infinitely long cylindrical shells. In all analyses, only the elastic properties of the material were used. The numerical and analytical results are shown in Fig.4-6 and Table 4-1.

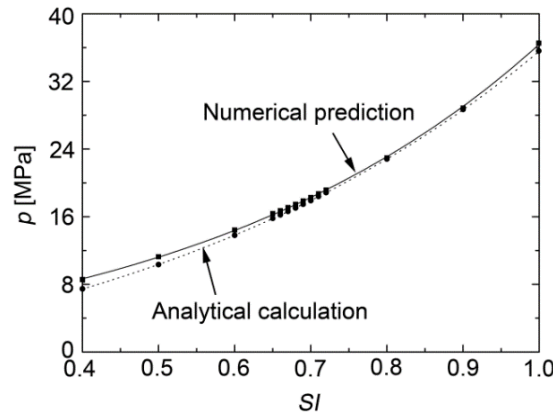
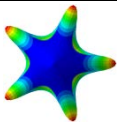
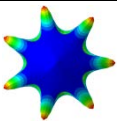
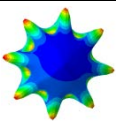
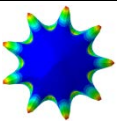
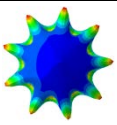
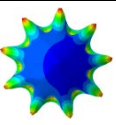
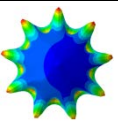


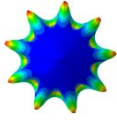
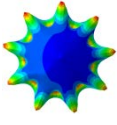
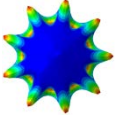
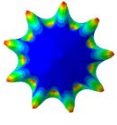
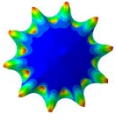
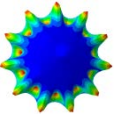
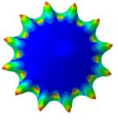
Fig.4-6 Linear buckling loads of egg-shaped pressure hulls versus egg shape index (SI) obtained from numerical predictions and analytical calculations

Using the analytical and numerical approaches, the linear buckling load was found to increase monotonically in conjunction with increases in the SI , as shown in Fig.4-6. The analytical calculations underestimated the numerical buckling loads by 0.5%–12.2%. When the egg SI increased, this difference initially decreased and then slightly increased. In all cases, the buckling mode exhibited the similar form. As can be seen from Table 4-1, the shells with SI s of 0.4, 0.5, 0.6, 0.8, 0.9 and 1.0 take the form of ($n=$) 5, 7, 8, 10, 11 and 12 circumferential waves, respectively; the hulls with an SI ranging from 0.65 to 0.72 take the same form of nine circumferential waves ($n = 9$). All of the egg-shaped pressure hulls analyzed take the same form of one meridional half-wave ($m = 1$) at the equator. These are typical buckling modes for axisymmetric

shells with positive Gaussian curvature, such as barreled shells [11-12].

Table 4-1 Linear buckling modes for all analyzed egg-shaped shells.(View along major axis).

<i>SI</i>	0.4	0.5	0.6	0.65	0.66	0.67	0.68
modes							
<i>n</i>	5	7	8	9	9	9	9

<i>SI</i>	0.69	0.7	0.71	0.72	0.8	0.9	1
modes							
<i>n</i>	9	9	9	9	10	11	12

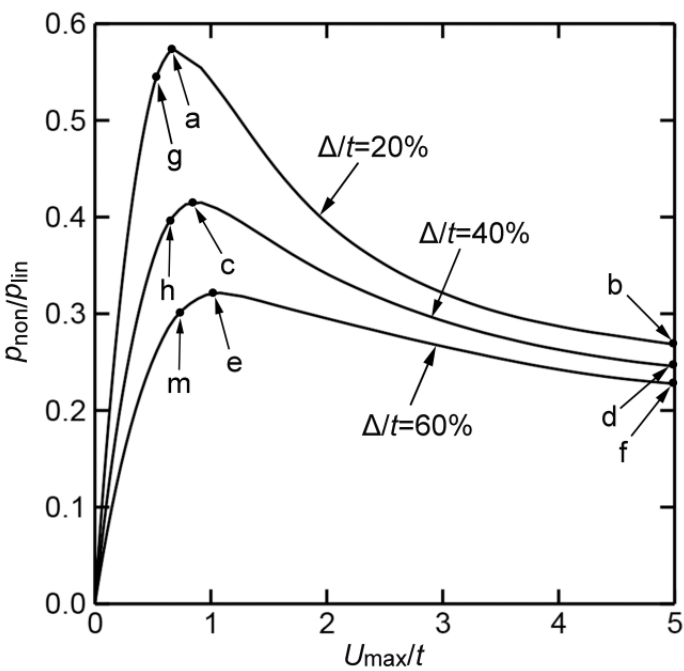


Fig.4-7 Equilibrium paths for the egg-shaped shell with $SI=0.69$

4.1.5. Nonlinear buckling of egg-shaped pressure hulls

The egg-shaped shells considered in this work correspond to a medium-thick walled structure. Both nonlinear material properties and initial geometric

imperfections play a crucial role in the buckling behavior of the shell structure. To determine the nonlinear buckling behavior of egg-shaped shells, the geometrically and materially nonlinear analysis with imperfections included was performed using the modified Riks method implemented in Abaqus/Standard. The analysis is in line with ENV 1993-1-6 (2007) [13]. Thus, the realistic buckling resistance could be obtained without adding any additional reduction factors [14]. In each case, the initial equivalent geometric imperfection in the form of the first linear buckling mode was introduced into the perfect model. The size of imperfection (Δ) was set at 20%, 40%, and 60% of the shell thickness (t). The material was assumed to be elastic plastic. The numerical results are illustrated in Fig.4-7.

Detailed results are obtained for $SI = 0.69$ only, because the nonlinear buckling behavior was identical for all analyzed shells. Fig.4-7 demonstrates the equilibrium paths for an egg-shaped shell that has an SI of 0.69; the applied load (p_{non}) normalized by the linear buckling load (p_{lin}) is plotted against the maximum deflection (U_{max}) normalized by the shell thickness (t). The characteristic of these paths is unstable. For each path, the load initially increases monotonically and exhibits an increase of deflection up to a critical buckling load, beyond which a substantial decrease of the load is displayed. This is a typical characteristic for shells of revolution with positive Gaussian curvature [11–12]. As shown in the same figure, the critical buckling load significantly decreased as the imperfection size increased. This result indicates that the egg-shaped shell is sensitive to initial geometric imperfections; therefore, the control of machining accuracy is essential.

In the same figure, the first yield points (g, h, m) of the eggshell with different imperfection sizes were marked at the paths, which was obtained using the same postprocessing procedure as in Ref. [15]. The first yield loads for these marks (g, h, m) corresponding to Fig.4-7 were also tabulated in Table 4-2. As can be seen from Fig.4-7 and Table 4-2, for the shell with Δ/t of 20%, 40% and 60%, the first yield loads were approximately 96%, 95% and 92% of the critical buckling loads respectively. Similar trend was found for other cases. It was suggested that all of the egg-shaped shells could lose stability within the elastic-plastic regime, which was

similar to the results of medium-thick conical shells subjected to external pressure [16].

Table 4-2 First yield load p_{fyd} values of egg-shaped shells and the ratio of the first yield and critical buckling load $p_{fyd} / p_{elastic-plastic}$.

Δ/t	p_{fyd}	$p_{fyd} / p_{elastic-plastic}$
20%	9.82	0.96
40%	7.01	0.95
60%	5.28	0.92

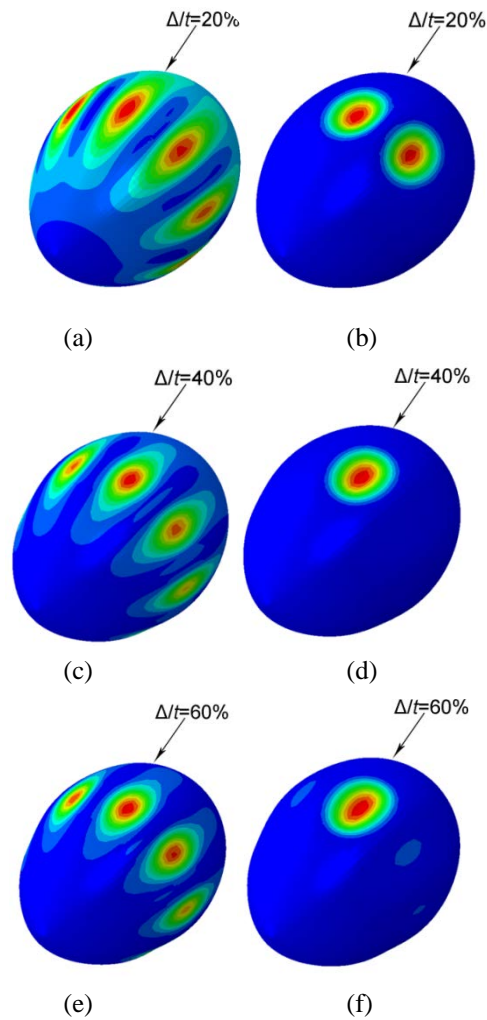


Fig.4-8 Critical buckling modes (a, c, e) and postbuckling modes (b, d, f) for the egg-shaped shell with $SI=0.69$

Fig. 4-8 contains the critical buckling modes (a, c, e) and postbuckling modes (b, d, f) for the egg-shaped shell that has an SI of 0.69; the marks (a–f) correspond to

Fig.4-7. All of the critical buckling modes for different imperfection sizes appear identical and have the shape of nine circumferential waves and one meridional half-wave; these results resemble those for the linear buckling mode of the shell. Moreover, all of the postbuckling modes at the end of the paths appear identical and in the form of local dents. This final failure mode appears consistent with that of the two ellipsoidal shells reported by Healey [17], as shown in Fig.4-9.

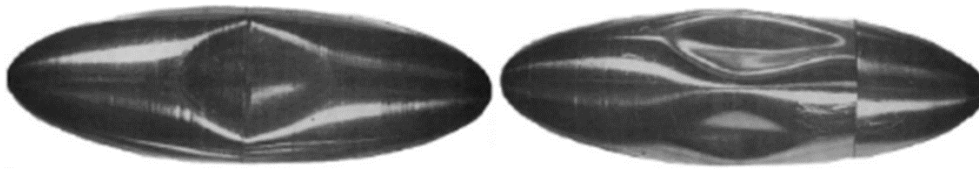


Fig.4-9 View of two ellipsoidal shells after collapse by external hydrostatic pressure [17]

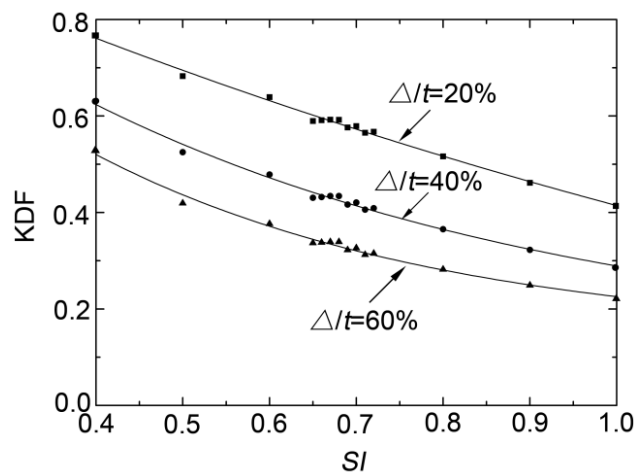


Fig.4-10 KDFs versus egg-shaped index (SI) for the egg-shaped shells of different imperfections sizes

The results of the nonlinear buckling analysis for all of the egg-shaped shells are demonstrated in Fig.4-10. The vertical axis corresponds to the knock down factors (KDFs) of the shell, which are the critical buckling load of imperfect shell normalized by the numerical linear buckling load of the corresponding perfect shell. The KDF value decreases considerably in conjunction with increases in the SI and imperfection size. These findings extend those of Jasion [12], confirming that the imperfection sensitivity of egg-shaped shells increases as they become more spherical. However, comparing Fig.4-6 and Fig.4-10 reveals that, for the shells with an SI range of 0.65 to

0.72, although they may lead to the significant variation of the linear buckling load, changes in the SI result in a relatively small variation in the load carrying capacity. For example, the difference between the nonlinear buckling load of an egg-shaped shell with an SI of 0.65 and that of an egg-shaped shell with an SI of 0.72 is only 9.4% for $\Delta/t = 60\%$. Therefore, from a bionic perspective, we can select a rational SI range according to design requirements such as space utilization and hydrodynamics without causing safety concerns.

4.2 Effect of wall thickness on buckling of egg-shaped pressure hulls

In this section, it is assumed that the major axis, $L = 2.561\text{m}$, the minor axis, $B = 1.767\text{m}$, and the wall thickness, $t = 10, 15, 20, 25, 30, 35, 40, 45, 50, 55, 60, 65, 70, 75$, and 80 mm respectively. In this case, the shape index, SI , is about 0.69, falling into the most frequent range of goose eggs. Also, assume that the egg-shaped pressure hulls are made of Ti alloy (Ti-6Al-4V).

4.2.1 Buckling of geometrically perfect egg-shaped pressure hulls

A total of 42 numerical experiments were carried out for geometrically perfect egg-shaped pressure hulls in this section, including 15 linear elastic bifurcation analyses (LBA), 12 geometrically and materially nonlinear analyses (GMNA), and 15 linear elastic perfect shell analyses (LPA).

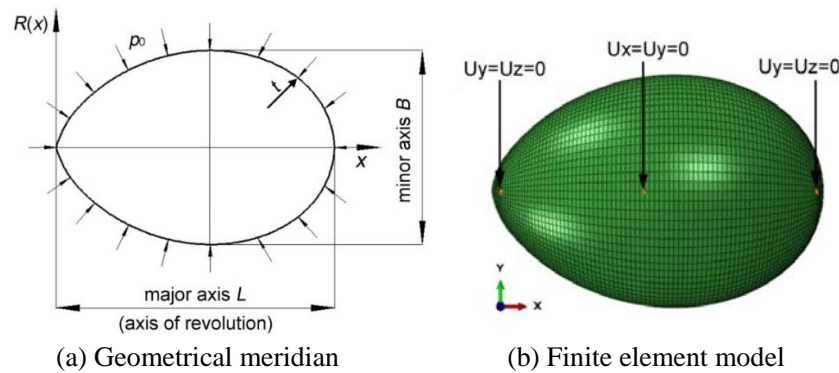


Fig.4-11 Mathematical model of an egg-shaped pressure hull

The analyses are essentially identical with ENV 1993-1-6 [13], which were performed based on the FE code ABAQUS 6.13. The fully integrated S4 shell element was employed in FE models. The number of elements was determined using mesh density convergence analysis by LBA [12]. As a result, each numerical model

has the same element number of 9310. To prevent the rigid body motion, three spatial points of each model were fixed as specified in CCS2013 [5], in the following: $U_y=U_z=0$, $U_x=U_y=0$, $U_y=U_z=0$, see Fig. 4-11, leading to no excessive constraint as the pressure is uniformly applied. The uniform external pressure, $p_0 = 1$ MPa was applied on the whole surface of each egg-shaped pressure hull. In this case, the eigenvalue obtained from LBA corresponded directly to the linear buckling load, while the arc length value obtained from GMNA belongs to the nonlinear buckling load.

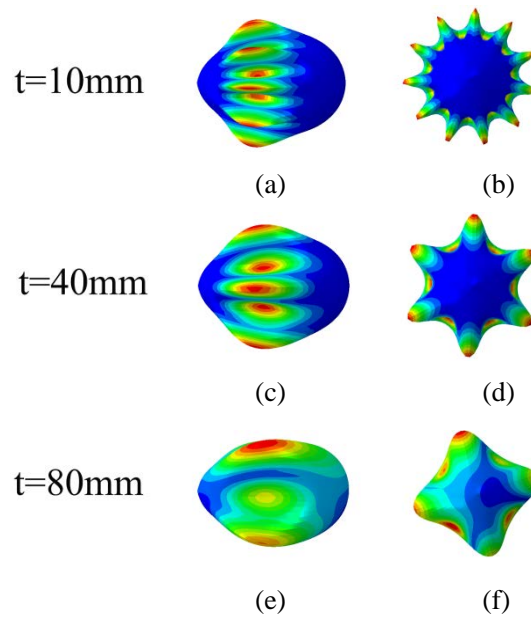


Fig.4-12 Linear buckling modes for the 10 mm, 40 mm, and 80 mm egg-shaped pressure hulls obtained from linear elastic bifurcation analysis (LBA); a, c, e = front view; b, d, f = left view.

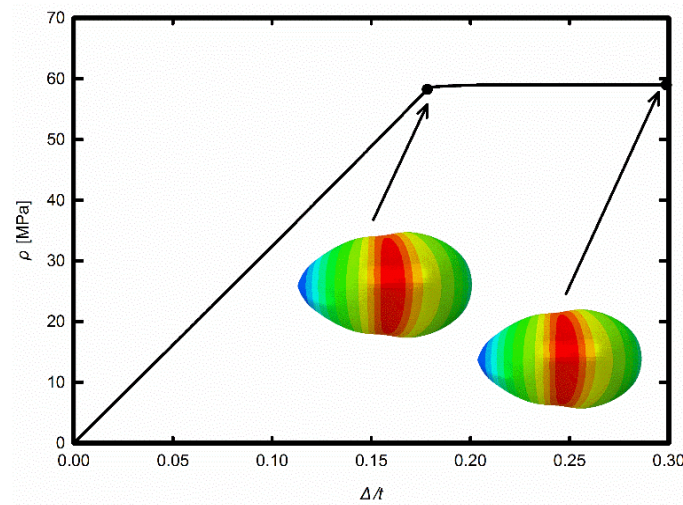


Fig.4-13 Equivalent path for the 40 mm egg-shaped pressure hull obtained from geometrically and materially nonlinear analysis (GMNA), along with its critical and post buckling modes

Also, dividing the yield stress of the material by the maximum Von Mises stress given by LPA, the yielding load of each egg-shaped pressure hull can be obtained in accordance with the mechanics of elasticity. In addition, the material model was assumed to be elastic for both LBA and LPA, and to be elastic-plastic for GMNA. Table 4-3 and Figs.(4-12)-(4-13) illustrate the results obtained from the numerical experiments.

Table 4-3 Buckling and yielding loads for egg-shaped pressure hulls.

t [mm]	Perfect geometry [MPa]			Imperfect geometry[MPa]		
	$p_{LBA}(n)$	$p_{GMNA}(k_p)$	p_{LPA}	$p_{GNIA} (k_{im})$	$p_{GMNIA} (k_{df})$	$p_{LIA}(k_{yl})$
10	6.65(11)	N/A	14.40	2.70(0.41)	2.68(0.40)	2.68(0.19)
15	14.94(9)	N/A	21.59	7.53(0.50)	7.12(0.48)	6.68(0.31)
20	26.58(8)	N/A	28.77	15.42(0.58)	13.3(0.50)	11.98(0.42)
25	41.80(7)	36.64(0.88)	35.93	26.38(0.63)	20.68(0.49)	18.08(0.50)
30	60.21(7)	44.08(0.73)	43.07	40.30(0.67)	27.96(0.46)	23.87(0.55)
35	82.46(6)	51.74(0.63)	50.21	56.59(0.69)	36.35(0.44)	30.79(0.61)
40	107.49(6)	58.96(0.55)	57.36	76.16(0.71)	43.83(0.41)	36.38(0.63)
45	137.15(6)	66.66(0.49)	64.49	100.36(0.73)	51.67(0.38)	42.33(0.66)
50	170.33(5)	73.99(0.43)	71.61	131.05(0.77)	64.01(0.38)	53.30(0.74)
55	205.04(5)	81.59(0.40)	78.67	160.91(0.78)	71.81(0.35)	59.46(0.76)
60	244.06(5)	90.64(0.37)	85.77	193.73(0.79)	79.25(0.32)	65.49(0.76)
65	287.69(5)	98.99(0.34)	92.85	232.42(0.81)	87.03(0.30)	71.44(0.77)
70	336.19(5)	103.99(0.31)	99.92	277.72(0.83)	95.12(0.28)	78.71(0.79)
75	391.41(5)	113.11(0.29)	106.97	329.44(0.84)	103.31(0.26)	85.31(0.80)
80	442.08(4)	123.70(0.28)	114.02	380.66(0.86)	114.89(0.26)	99.42(0.87)

Notes: p_{LBA} =buckling load obtained from linear elastic bifurcation analysis (LBA); p_{GMNA} = buckling load obtained from geometrically and materially nonlinear analysis (GMNA); p_{LPA} = yielding load obtained from linear perfect elastic shell analysis (LPA); p_{GNIA} = buckling load obtained from geometrically nonlinear elastic analysis with imperfections included (GNIA); p_{GMNIA} = buckling load obtained from geometrically and materially nonlinear elastic analysis with imperfections included (GMNIA); p_{LIA} = yielding load obtained from linear imperfect elastic shell analysis (LIA); n =number of circumferential waves; $k_p = p_{GMNA}/p_{LBA}$; $k_{im} = p_{GNIA}/p_{LBA}$; $k_{df} = p_{GMNIA}/p_{LBA}$; $k_{yl} = p_{LIA}/p_{LPA}$. These notations are the same for Table 4-4 and Table 4-5.

Comparing the results from linear elastic bifurcation analysis (LBA), geometrically and materially nonlinear analysis (GMNA), and linear elastic perfect shell analysis (LPA), the buckling of geometrically perfect egg-shaped pressure hulls can be divided into two regimes: elastic buckling regime and elastic-plastic buckling regime. As can be observed in the first four columns of Table 4-3, for the shallow egg-shaped

pressure hulls ($10 < t < 20$ mm), the yield load, p_{LPA} , is more than the linear buckling load, p_{LBA} , suggesting that the hulls may buckle in an elastic buckling regime. In this circumstance, results of geometrically and materially nonlinear analysis (GMNA) are neglected for the 10mm, 15mm, and 20mm pressure hulls. For the deep egg-shaped pressure hulls ($25 < t < 80$ mm), the yield load, p_{LPA} , is less than the linear buckling load, p_{LBA} , and the elastic-plastic buckling load, p_{GMNA} , suggesting that the hulls may buckle in an elastic-plastic buckling regime. These findings indicate that the deep egg-shaped pressure hulls appear to exhibit an elastic-plastic buckling instability due to the subjected high external pressure and the relatively large wall thickness.

For geometrically perfect egg-shaped pressure hulls, both the linear and elastic-plastic buckling loads are strongly affected by their wall thicknesses. They significantly increased with an increase in the wall thickness (Column 2 and 3 of Table 4-3). Besides, the value in the parenthesis in Column 3 of Table 4-3 corresponds to the ratio (k_p) of the elastic-plastic buckling load, p_{GMNA} , to the linear buckling load, p_{LBA} , which indicates the sensitivity of the critical buckling load of hulls to the material plasticity; as can be seen the thicker the egg-shaped pressure hull, the more sensitive to material plasticity the critical buckling load. Fig. 4-12 shows that the linear buckling modes of all pressure hulls take the similar form of a number of circumferential waves (n) along with one longitudinal half-wave ($m=1$), which is typical for shells of revolution with positive Gaussian curvature. Whereas, Fig.4-13 plots the applied load, p , versus the ratio of the maximum deflection, Δ , to the wall thickness, t for the 40 mm egg-shaped pressure hull; the equivalent path has a metastable character - the applied load first increased linearly with an increase in the deflection, after a critical value (the elastic-plastic buckling load); both the critical buckling and post-buckling modes were identical and took the form of one longitudinal half-wave ($m=1$); this was similar to other cases considered.

4.2.2 Buckling of geometrically imperfect egg-shaped pressure hulls

A total of 45 numerical experiments were carried out for geometrically imperfect egg-shaped pressure hulls in this section, including 15 geometrically nonlinear elastic

analyses with imperfections included (GNIA), 15 geometrically and materially nonlinear elastic analyses with imperfections included (GMNIA), and 15 linear elastic imperfect shell analyses (LIA). For each model, the eigenmode imperfection obtained from corresponding linear elastic bifurcation analysis (LBA) was introduced into the perfect one. This kind of geometrical imperfection often results in a conservative result and has been widely used to examine the load carrying capacity of shells of revolution in the preliminary design stage. The imperfection size was assumed to be 5 mm, which is in line with the previous studies [17-18] and the current rules. Besides, the mesh, load, boundary conditions, material modelling, analysing tool and method of imperfect egg-shaped pressure hulls were the same as those of perfect pressure hulls. Table 4-3 and Fig.4-14 illustrate the results obtained from the numerical experiments.

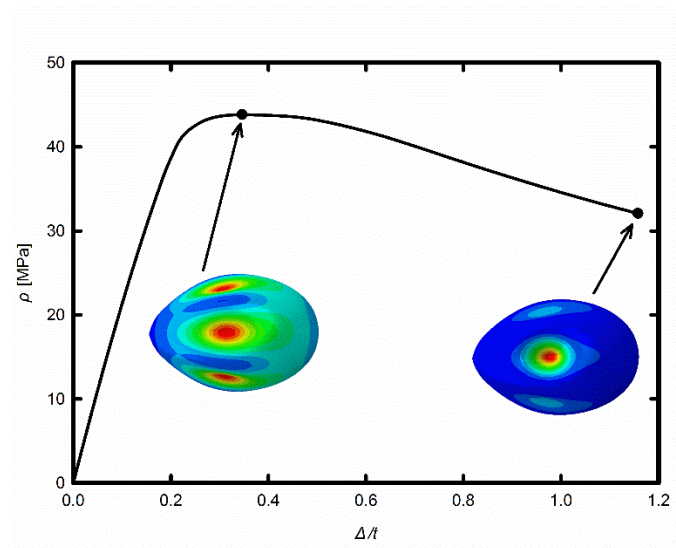


Fig.4-14 Equivalent path for the 40 mm egg-shaped pressure hull obtained from geometrically and materially nonlinear elastic analysis with imperfections included (GMNIA), along with its critical and post buckling modes

Comparing the results from geometrically nonlinear elastic analysis with imperfections included (GNIA), geometrically and materially nonlinear elastic analysis with imperfections included (GMNIA), and linear elastic imperfect shell analysis (LIA), all geometrically imperfect egg-shaped pressure hulls buckle in an elastic-plastic buckling regime. This is due to the fact that the yield load, p_{LIA} , is less than the nonlinear elastic buckling load, p_{GNIA} , and the elastic-plastic buckling load,

p_{GMNIA} (last three columns of Table 4-3). These findings are different from those of geometrically perfect egg-shaped pressure hulls mentioned in Section 3 because of the existence of geometric imperfections. Moreover, the yield load, p_{LIA} , of imperfect pressure hull is less than that, p_{LPA} , of perfect pressure hull. The ratio (k_{yl}) of the yield load, p_{LIA} , of imperfect pressure hull to that, p_{LPA} , of perfect pressure hull increases with an increase in the wall thickness (the parenthesis in the last column of Table 4-3). This finding indicates that the sensitivity of the yielding load to the shape deviation decreases with an increase in the wall thickness.

Identical with the perfect egg-shaped pressure hulls, the geometrically nonlinear elastic buckling behaviours of imperfect egg-shaped pressure hulls are strongly affected by their wall thickness. The geometrically nonlinear elastic buckling load, p_{GINA} , significantly increases with an increase in the wall thickness (see Column 5 of Table 4-3), which is similar to linear elastic bifurcation analysis (LBA). The value in the parenthesis in Column 5 of Table 4-3 corresponds to the ratio (k_{im}) of the geometrically nonlinear elastic buckling load, p_{GINA} , to the linear buckling load, p_{LBA} , which indicates the sensitivity of the critical buckling load of hulls to the shape deviation. As can be seen, the value is 41% for the 10 mm egg-shaped pressure hull, while the value is 86% for the 80 mm egg-shaped pressure hull; this indicates that thicker the egg-shaped pressure hull, the less sensitive to shape deviation the critical buckling load, which is, however, reverse to that of the material plasticity.

The load carrying capacity of imperfect egg-shaped pressure hulls, the elastic-plastic buckling load, p_{GMNIA} , is listed in Column 6 of Table 4-3. As can be inferred, the elastic-plastic buckling load, p_{GMNIA} , increases linearly with an increase in the wall thickness. This trend is similar to results obtained from geometrically and materially nonlinear analysis (GMNA) and to the previous studies into spherical pressure hulls [18-19]. The parenthesis in the same column corresponds to the knock down factor (k_{df}) – the ratio of the elastic-plastic buckling load of imperfect egg-shaped pressure hull, p_{GMNIA} , to the linear buckling load of perfect one, p_{LBA} , which involves the effect of both material plasticity and shape deviation to the

buckling. The knock down factor (k_{df}) first increases with an increase in the wall thickness, after a critical value ($t=20$ mm) it decreases with an increase in the wall thickness. This finding suggests that the shape deviation is the main affecting factor for the relatively shallow pressure hulls, while the material plasticity is the main affecting factor for the relatively deep pressure hulls

In addition, the equivalent paths of all imperfect pressure hulls obtained from GNIA and GMNIA are similar and have an unstable character. For example of the 40 mm egg-shaped pressure hull in Fig.4-14, the applied load first increases monotonically with an increase in the deflection, after a critical value the applied load significantly decreases with an increase in the wall thickness. As can be seen in the same figure, the critical buckling mode is similar to the linear buckling one of perfect pressure hull. The post buckling mode takes the form of one or more local dimples, which is typical for shells of revolution with positive Gaussian curvature. This findings are similar to other cases obtained from GNIA and GMNIA.

4.2.3 Comparison between egg-shaped and spherical pressure hulls

To examine the potential application of egg-shaped pressure hulls, this section investigates the buckling of volume and mass equivalent spherical pressure hulls, which are widely used in deep sea submersibles [18-21]. The spherical pressure hulls have the same volume/mass, wall thickness, and material as the egg-shaped pressure hulls. A total of three typical thicknesses were considered in the following: 10 mm, 40mm and 80 mm. For the volume equivalent spherical pressure hulls, the radius, $r = 1$ m, was determined from the volume equation of spherical shell, $v = 4\pi r^3/3$ and the volume equation of egg-shaped shell. For the mass equivalent spherical pressure hulls, the radius, $r = 1.0004$ m, was determined from the mass equation of spherical shell, $m = 4\pi r^2 t \rho$ and the mass equation of egg-shaped shell.

A total of 34 numerical experiments were carried out in this section. Sixteen of them were performed for geometrically perfect spherical pressure hulls, involving linear elastic bifurcation analysis (LBA), geometrically and materially nonlinear analysis (GMNA), and linear elastic perfect shell analysis (LPA). The others were performed for geometrically imperfect spherical pressure hulls, involving

geometrically nonlinear elastic analysis with imperfections included (GNIA), geometrically and materially nonlinear elastic analysis with imperfections included (GMNIA), and linear elastic imperfect shell analysis (LIA). The imperfection shape was assumed to be the corresponding linear buckling mode. The imperfection size was assumed to be 5 mm as well. Each numerical model had 6534 S4 shell elements according to the mesh density analysis. The load, boundary conditions, material modelling, analysing tool and method of spherical pressure hulls were the same as those of egg-shaped pressure hulls. Table 4-4, Table 4-5 and Figs.(4-15)-(4-16) illustrate the results obtained from the numerical experiments.

Table 4-4 Buckling and yielding loads for volume equivalent spherical pressure hulls.

t [mm]	Perfect geometry [MPa]			Imperfect geometry [MPa]		
	$p_{LBA}(n)$	$p_{GMNA}(k_p)$	p_{LPA}	$p_{GNIA} (k_{im})$	$p_{GMNIA} (k_{df})$	$p_{LIA}(k_{yl})$
10	13.68(17)	N/A	16.59	4.58(0.34)	4.51(0.33)	4.35(0.26)
40	211.62(9)	67.46(0.32)	66.40	125.44(0.59)	59.11(0.28)	47.41(0.71)
80	827.73(6)	147.35(0.18)	132.8	670.64(0.81)	132.82(0.16)	112.00(0.84)

Table 4-5 Buckling and yielding loads for mass equivalent spherical pressure hulls.

t [mm]	Perfect geometry [MPa]			Imperfect geometry [MPa]		
	$p_{LBA}(n)$	$p_{GMNA}(k_p)$	p_{LPA}	$p_{GNIA} (k_{im})$	$p_{GMNIA} (k_{df})$	$p_{LIA}(k_{yl})$
10	13.67(17)	N/A	16.43	4.98(0.36)	4.89(0.36)	4.88(0.30)
40	211.45(9)	67.44(0.32)	66.14	120.72(0.57)	55.96(0.26)	43.61(0.66)
80	827.10(6)	134.89(0.16)	132.44	682.64(0.81)	133.37(0.16)	116.70(0.88)

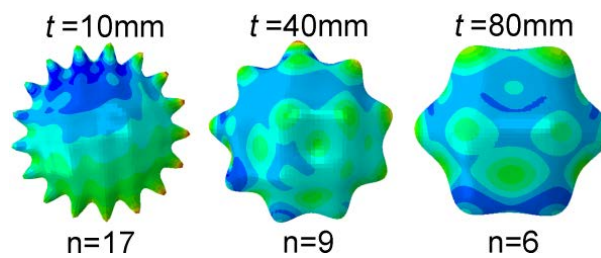


Fig.4-15 Linear buckling modes for volume equivalent spherical pressure hulls obtained from linear elastic bifurcation analysis (LBA)

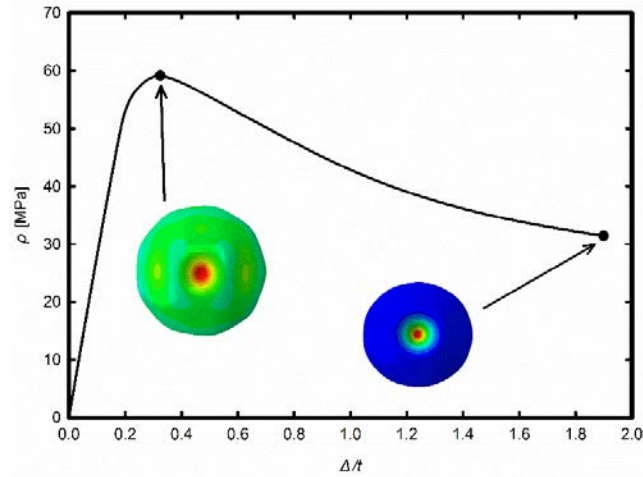


Fig.4-16 Equivalent path for the 40 mm volume equivalent spherical pressure hull obtained from geometrically and materially nonlinear elastic analysis with imperfections included (GMNIA), along with its critical and post buckling modes

As can be seen, the thickness of volume equivalent spherical pressure hulls strongly affects their buckling and yielding behaviours, which is similar to egg-shaped pressure hulls. Comparing Table 4-3 and Table 4-4, the linear buckling load, p_{LBA} , of spherical pressure hulls is about twice as much as that of egg-shaped pressure hulls. This is because the spherical pressure hull has a central symmetric geometry, leading to the extremely efficient stress and displacement distributions in the material. In this case, the linear buckling modes of all spherical pressure hulls resemble a number of circumferential and meridional half waves (Fig.4-15). The number of wave crest (n) decreases with an increase in the wall thickness. On the other hand, the difference between the elastic-plastic buckling loads, p_{GMNA} , of spherical and egg-shaped pressure hulls significantly decreases with an increase in the wall thickness. The plasticity reduction factor, k_p , of spherical pressure hulls is much less than that of egg-shaped pressure hulls, suggesting that spherical pressure hulls are much more sensitive to the material plasticity than egg-shaped ones. Similarly, we can find that spherical pressure hulls are more sensitive to the shape imperfection than egg-shaped ones.

As can be inferred from Column 6 of Table 4-3 and Table 4-4, the load carrying capacity, p_{GMNIA} , of the egg-shaped pressure hull is only 59.4% of the volume

equivalent spherical one at 10 mm wall thickness, 74.1% at 40 mm wall thickness, and as much as 86.5% at 80 mm wall thickness. This indicates that egg-shaped pressure hulls appear to be applicable to deep sea submersibles, especially to full ocean depth ones (11000 m). In the full ocean depth case, the wall thickness may exceed 80 mm to ensure the safety, and the load carrying capacity of egg-shaped pressure hulls can be much closer to that of spherical pressure hulls. Not only that, the inner space efficiency and hydrodynamics of egg-shaped pressure hulls can be better than those of spherical pressure hulls [2, 22]. If the non-uniform or variable thickness, closely spaced eigenmode imperfections, or the shape index change [23] are taken into account, the load carrying capacity of egg-shaped pressure hulls may be nearly the same as or possibly even better than that of spherical pressure hulls. This is outside the scope of this paper and will be further studied in our future work. In addition, all equivalent path of imperfect spherical pressure hulls are similar and have an unstable character, for example of the 40 mm volume equivalent spherical pressure hull in Fig.4-16. Also, the critical buckling mode is nearly identical with the linear buckling one, while the post-buckling mode is of the form of a local dimple. Similar results and discussions can be obtained for the mass equivalent spherical pressure hulls (Table 4-5), except a distinct difference between the buckling and yielding loads of the mass and volume equivalent spherical pressure hulls.

4.3 Buckling of CNC-machined egg-shaped shells under uniform external pressure

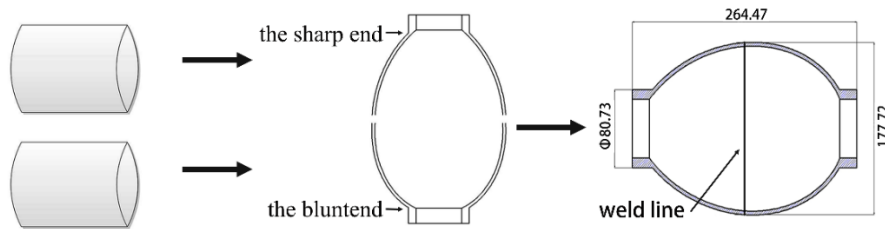
4.3.1 Experimental buckling of CNC-machined egg-shaped shells

Consider a steel egg-shaped shell with major axis $L = 254.38 \text{ mm}$ and minor axis $B = 177.72 \text{ mm}$. Three nominally identical egg-shaped shells labeled as ES1, ES2, and ES3, were cut, CNC-machined (Computer Numerical Control), and welded from a Q235 steel bar. This material has high ductility, and it can enable a satisfactory collapsed mode of shells without fracture. Fig. 4-17 shows the manufacturing process in detail. Owing to the lack of reasonable fixture tools, it is difficult to simultaneously control the machining quality in terms of shape and thickness. The present study

focuses more on the shape of the egg-shaped shell. For the ease of fabrication, each egg-shaped shell was divided into two domes at the equator: sharp dome and blunt dome. The top of each dome was replaced by a thick ring to enable accurate holding and positioning during fabrication. This ring structure may slightly influence the buckling of the egg-shaped shell because the instability of the shell initiates near the equator. After fabrication, the two domes were welded together and polished around the equator. Both rings were welded with heavy plates to seal the egg-shaped shell. Also, there was no stress relieving during the fabrication and welding.



(a) Photographs

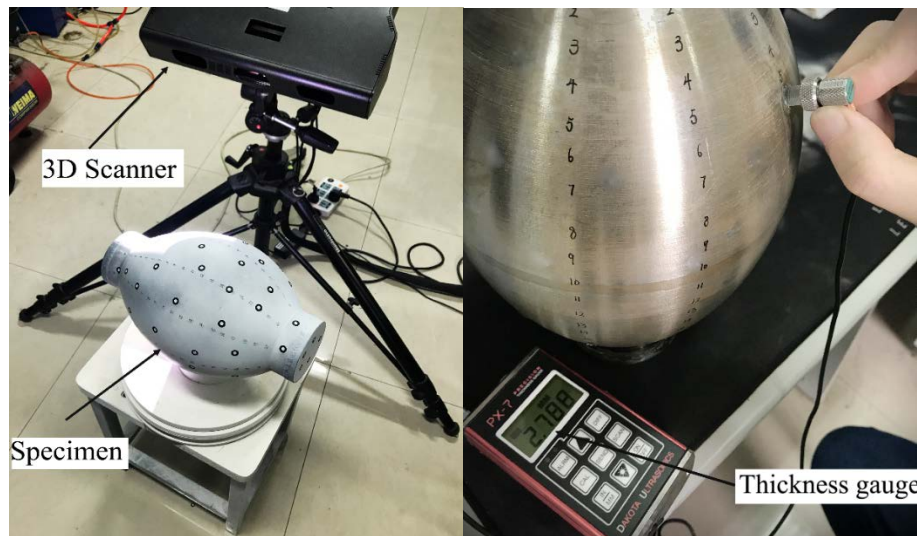


(b) Schematic

Fig.4-17 Fabricating process of egg-shaped shell

Before the test, each egg-shaped shell assembly was optically scanned and ultrasonically measured to determine its real geometry and real wall thickness, respectively. Fig. 4-18 shows these scanning and measuring processes. Through these processes, the external surface of the shell assembly, including the deterministic geometric imperfections produced during fabrication, was determined using the optimal scanning tool developed by Open Technologies Corporation (accuracy: ≤ 0.02 mm). Fig. 4-19 shows the obtained geometries along with the deviation of the radius of the fabricated shells from that of the perfect ones. As seen in this figure, the fabricated egg-shaped shells are nominally identical, indicating the satisfactory repeatability of the fabrication process. The egg-shaped shell itself shows high

geometric accuracy, although large deviations are found at the conjunction between the ring and the shell owing to the rounded corner.



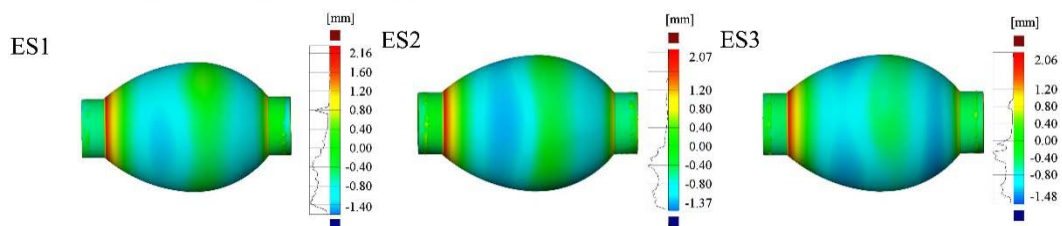
(a) Shape Scanning

(b) Thickness measurement

Fig.4-18 Photographs of geometrical measuring processes



(a) CAD models



(b) Deviations

Fig.4-19 Scanned data of fabricated egg-shaped shells

On the other hand, the wall thicknesses of the shell can be obtained at 21 equidistant points along a meridian for a total of 8 equally spaced meridians. Fig. 4-20 shows the plots of the minimum, average, and maximum wall thicknesses at the circumference along the axis of revolution. As seen in this figure, the wall thickness distributions of all egg-shaped shells are identical, indicating the satisfactory

repeatability of the fabrication process. The wall thickness of each shell differs slightly at the circumference. However, at the meridians, it first increases smoothly, then fluctuates slightly at weld seam, and finally decreases greatly. This variation in the fabricated models causes a significant deviation in the wall thickness distributions although their distributions are reasonably identical. Therefore, this section only focuses on the buckling of the fabricated models; it is numerically analyzed to verify the implemented FEM.

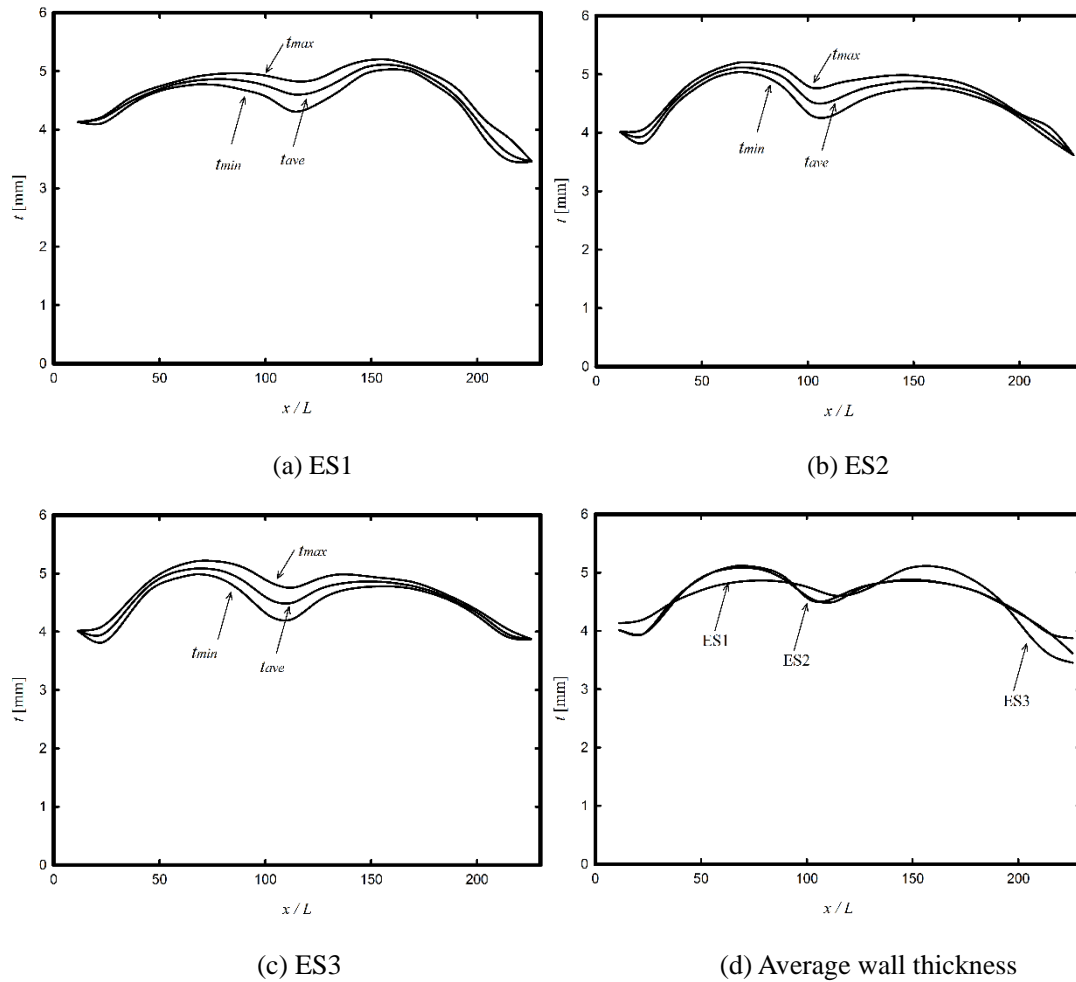


Fig.4-20 Variations of wall thickness of fabricated egg-shaped shells along the axis of revolution

After the measurement, each egg-shaped shell was immersed into a pressure chamber and tested until collapse under hydrostatic pressure. Fig.4-21 shows a schematic and photograph of the test chamber. The chamber is a cylindrical pressure vessel that uses water as the pressure medium and an O-shaped ring as the seal. The water release valve is used to exhaust the small amount of trapped air before the test

and to release the pressure after the test. Pressure was applied slowly through the inlet hose and was recorded accurately by using a pressure gage.

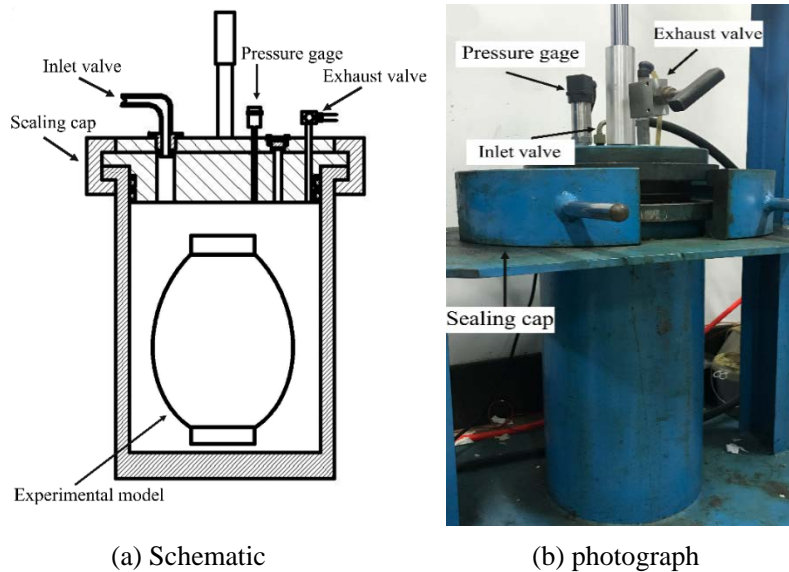


Fig.4-21 Schematic and photograph of the test chamber

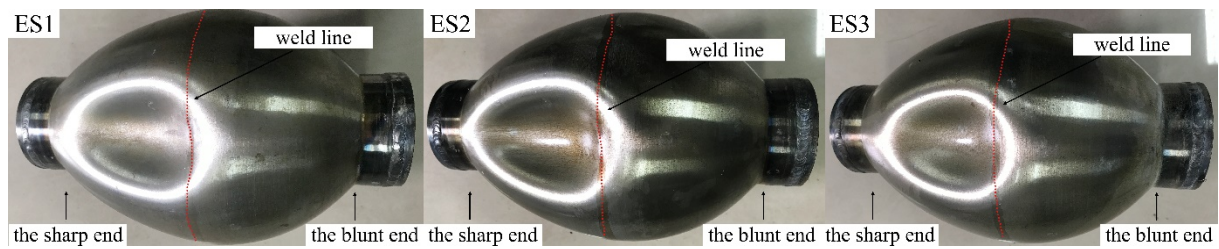


Fig. 4-22 Photographs of three tested egg-shaped shells

Table 4-6 Experimental collapse loads p_{test} and computational buckling loads p_{comput} of tested egg-shaped shells.

Specimen	p_{test}	p_{comput}		
		p_{lb}	p_{nlb}	p_{fyi}
		(MPa)		
ES1	18.99	246.11	18.23	17.50
ES2	18.46	231.19	17.51	17.04
ES3	18.26	230.49	17.45	16.58

Because of empty cavity, all the egg-shaped shells collapse suddenly at a critical point with a significant decrease in pressure. Consequently, the collapse pressures correspond to the maximum value recorded by the pressure gage during the test. As listed in Table 4-6, the experimental buckling loads of these shells range from 18.26

to 18.99 MPa, whereas their post-buckling modes are similar and take the form of a local dent, as shown in Fig.4-22. These results indicate the satisfactory repeatability of the test.

4.3.2 Numerical buckling of CNC-machined egg-shaped shells

According to the measurement results, comprehensive finite element models of the experimental egg-shaped shells were created and computed by using linear bifurcation analysis and nonlinear Riks analysis function available in ABAQUS. The measured shells' external geometry is the basis of FE models. The mesh was generated on the measured geometry, which is a mid-surface of shell from theoretical view of point. However, the wall thickness of shell was defined inward in ABAQUS environment to ensure the FE model consistent with reality. Notably, each tested shell includes thin-walled egg-shaped shell as the main part, heady rings (thick-walled shells) at both ends, and heavy plates weld to rings. All of these parts were modelled using shell element (Fig.4-23). Mesh convergence analysis was performed for each shell, resulting in 14201 S4 and 2820 S3 shell elements for the ES1 shell, 12851 S4 and 2198 S3 shell elements for the ES2 shell, and 2609 S3 and 14667 S4 shell elements for the ES3 shell.

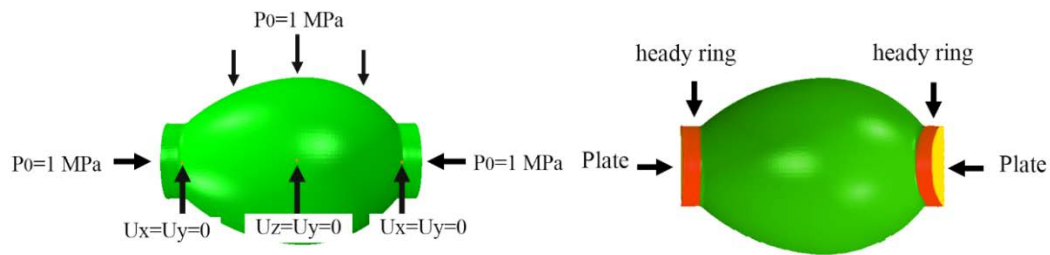


Fig.4-23 FE model of ES1 egg-shaped shell

The wall thickness was defined as the average value at the circumference and the variable value along the axis of revolution, as shown in Fig.4-20. This thickness definition is attributed to the fact that the wall thickness of each shell differs slightly at the circumference but varies significantly along the axis of revolution. The material properties were assumed to be as follows: Young modulus $E = 210$ GPa, Poisson ratio $\mu = 0.3$, and yield strength $\sigma_y = 235$ MPa. As be seen in Fig.4-23, the uniform pressure was applied on the external surface of each model, as well as on the two

heavy plates for the tested shells. In this way, axial compression due to external pressure is automatically included in the computations.

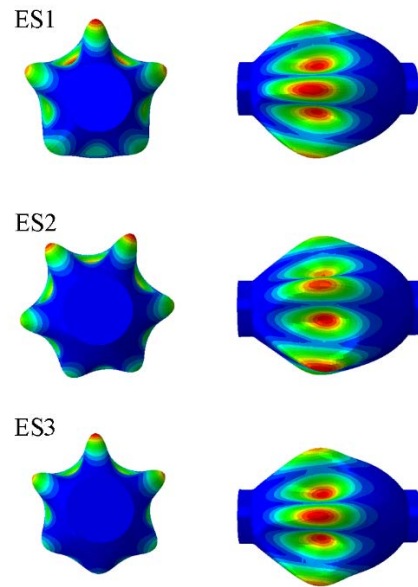


Fig.4-24 Linear buckling modes of three tested egg-shaped shells

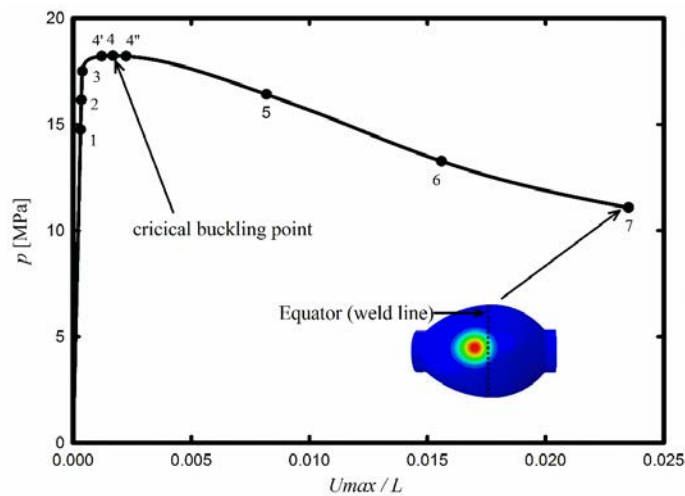


Fig.4-25 Equilibrium path of the ES1 egg-shaped shell and its post-buckling mode

In addition, the first yield pressure was evaluated numerically based on the same mesh as the corresponding buckling model. On this basis, using the mechanics of elasticity, the first yield loads of perfect and imperfect shells were determined by dividing the yield stress of the material by the maximum Mises-Huber stress given by linear analysis for an external pressure of 1 MPa. The stress was obtained from external surface, which may lead to a relatively conservative evaluation because the internal stress is slightly more than the external one for externally pressurized

thin-walled shells. Figs.(4-24)-(4-26) and Table 4-6 show the obtained computational results.

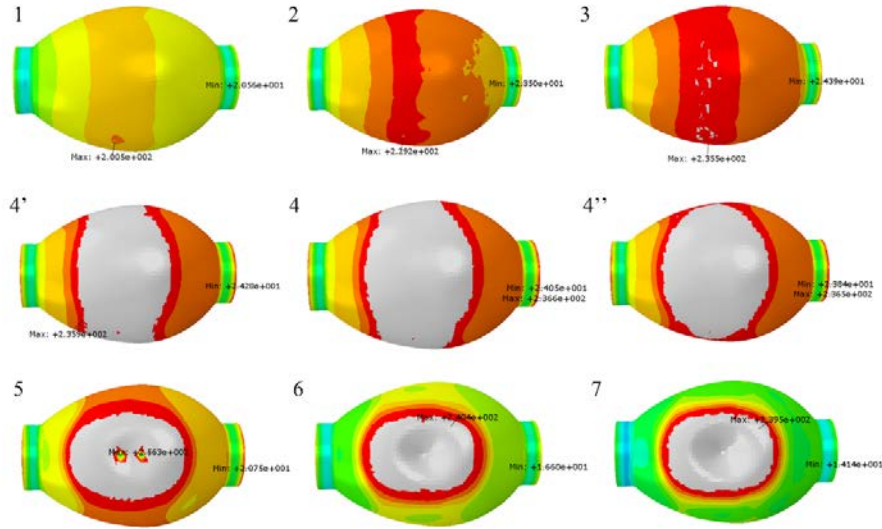


Fig.4-26 History of Mises-Huber stress distributions of ES1 egg-shaped shell, all numbers of sub pictures correspond to Fig.4-26

As can be seen from Table 4-6, the linear bifurcation load of shells ranges from 230.49 to 246.11 MPa, which is even higher than the experimental or nonlinear buckling data. Also, the linear bifurcation modes of shells are similar and take the form of several circumferential waves and one meridional half-wave (Fig.4-24). These modes are similar to those obtained from linear buckling analyses of perfect geometry, indicating that the fabricated egg-shaped shells are nearly perfect. Nevertheless, these modes are quite different from the experimental observations, suggesting that the nonlinear buckling analysis is required.

The post-buckling paths of all tested egg-shaped shells show an unstable character. This character can be indicated from the equilibrium path of the ES1 egg-shaped shell shown in Fig.4-25, which plots the applied load p versus the ratio of the maximum deflection Δ to the major axis L . Obviously, the applied load decreases significantly after the critical point. The post-buckling mode of the ES1 egg-shaped shell takes the form of a local dimple near the equator; the computational results show good agreement with the experimental results. Similar findings are also obtained for the other experimental egg-shaped shells.

Table 4-6 lists the critical buckling loads of all tested egg-shaped shells at the peak of the path. These loads range from 17.45 to 18.23 MPa, which are 94.9%–96.0% of the experimental ones. This slight underestimation has also been found in previous studies of the buckling of spherical shells [21], extending NASA's current viewpoint that the buckling of a fabricated shell of revolution can be accurately determined from the computational analysis of its actual measured shape and wall thickness [24-26].

Furthermore, the small difference between the computational and experimental results indicates their good agreement, confirming the previous finding that the buckling resistance of a stability-endangered shell can be determined from fully nonlinear analysis that includes imperfections [5, 13]. As listed in the same table, the first yield loads of egg-shaped shells are 95%–97% of their critical buckling loads, suggesting that all shells collapse in an elastic-plastic regime.

In addition, to further study the buckling mechanism of shells, the history of Mises-Huber stress distributions of ES1 egg-shaped shell in the pre-buckling, buckling, and post-buckling state is provided by Fig.4-26. The gray area indicates yielding, whilst the red area corresponds to a relative large stress. As can be seen from 3 and 4' of Fig.4-26, yield phenomenon is found near the equator of shell before the critical (buckling) point. This location is also the collapse zone in post buckling state, indicating that shells appear to lose stability in the maximum stress area and the egg-shaped shell buckles in the elastic-plastic range. Similar findings are found in the remaining cases as well.

4.4 Buckling of rapid prototyping egg-shaped shells under uniform external pressure

As can be seen from the previous experimentation in Section 4.3, nonlinear elastic-plastic buckling regime of steel egg-shaped shells are confirmed as well as unstable equilibrium path and local post buckling mode. However, due to the limitations of fabrication, all CNC-machined steel egg-shaped shells show a large variation in the wall thickness, although the fabrication has a good repeatability. Also, it is very expensive to fabricate an egg-shaped shell with precise geometrical

imperfections using CNC-machine technique.

Therefore, to confirm the effect of imperfection on the buckling and improve the accuracy of experimental sample, a rapid prototyping technique is inexpensively adopted to obtain a more accurate egg-shaped shells with perfect geometry and imperfect geometry. This technique has the obvious advantages of fabricating various forms of untypical shells with a small number.

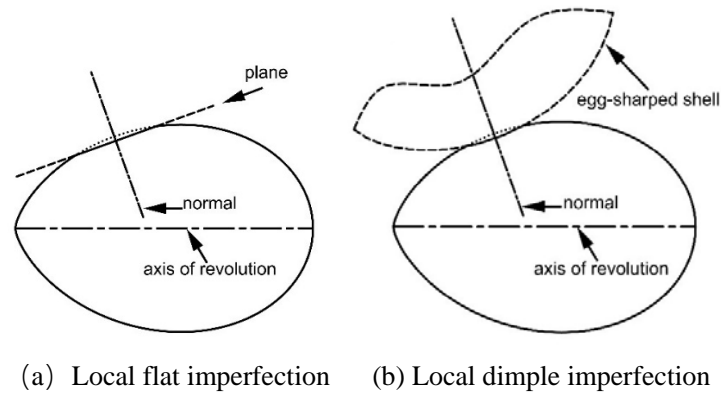


Fig.4-27 Schematic of imperfect egg-shaped shells

4.4.1 Experimental buckling of rapid prototyping egg-shaped shells

Consider a geometrically perfect egg-shaped shell with the major axis, $L = 256mm$, the minor axis, $B = 180mm$, and uniform wall thickness, $t = 2mm$. Two kinds of locally geometrical axisymmetric imperfections, namely local dimple and local flat, were affine to the perfect model, respectively. The imperfection size was assumed to be the wall thickness of shells. According to the previous studies into externally pressurized barreled shells, the higher the meridian radius, the lower the load bearing capacity. Similar findings can be found for egg-shaped shells. Therefore, the centers of both imperfections locate near the sharp end, which corresponds to the highest principle meridional radius. The axisymmetric axis of each imperfection coincides with the normal of perfect egg-shaped shell, as illustrated in Fig.4-27. For typical shells of revolution, functions resembling cosine, circle, and polynomial can be defined as local dimple imperfections due to the single curvature of geometry [27-30]. However, egg-shaped shells correspond to multifocal surfaces of positive Gaussian curvature. It is very difficult to define the dimple geometry using current functions. Consequently, an egg-shaped local dimple imperfection was assumed in

present work, which takes the same shape as the perfect geometry, as shown in Fig.4-27(b).

Assume that egg-shaped shells are made of stereolithography resin, which has been extensively implemented in rapid prototyping technology [31-33]. The prototyped samples reveal stable and reproducible mechanical performances meanwhile the prototyping cost is economic and affordable. Therefore, all of the egg-shaped samples in this study were fabricated vertically from the blunt end to the sharp one using rapid prototyping technology – stereo lithography appearance (SLA), although there exist some influence due to the fabricating direction. To facilitate the removal of typing support, a circular hole with a radius of 12.5mm was engineered at the sharp end of each shell, which was docked with a separately typed dome by using cyanoacrylate adhesive. To make a like-for-like comparison, all egg-shaped shells were fabricated using the same prototyping parameters. Details of the fabricating procedure can be found in [31, 33]. To ensure the repeatability of fabrications, measurements, and tests, three identical samples were fabricated for each imperfect egg-shaped shell. Further, to examine the knock-down effect of local imperfections on the buckling of egg-shaped shells, three geometrically perfect samples are fabricated as well.

In this case a total of nine egg-shaped samples were obtained in laboratory scale, including three imperfect samples with local flat imperfections designated as FS1, FS2, and FS3, three imperfect ones with local dimple imperfections designated as DS1, DS2, and DS3, and three perfect ones designated as PS1, PS2, and PS3, respectively. Representative photographs of the fabricated egg-shaped shells are provided in Fig.4-28. Since the parent material properties of rapid prototyped components are strongly dependent on material formula, ambient environment, and prototyping parameters, in order to accurately obtain such properties, three tensile flat coupons were fabricated vertically along the longitudinal direction using the same prototyping parameters as egg-shaped samples.

Then, all fabricated egg-shaped shells were geometrically measured for external surface and wall thickness, and then hydrostatically tested to collapse, while the three fabricated tensile flat coupons were respectively stretched in the longitudinal direction

to obtain Poisson ratio and Young's modulus of resin.

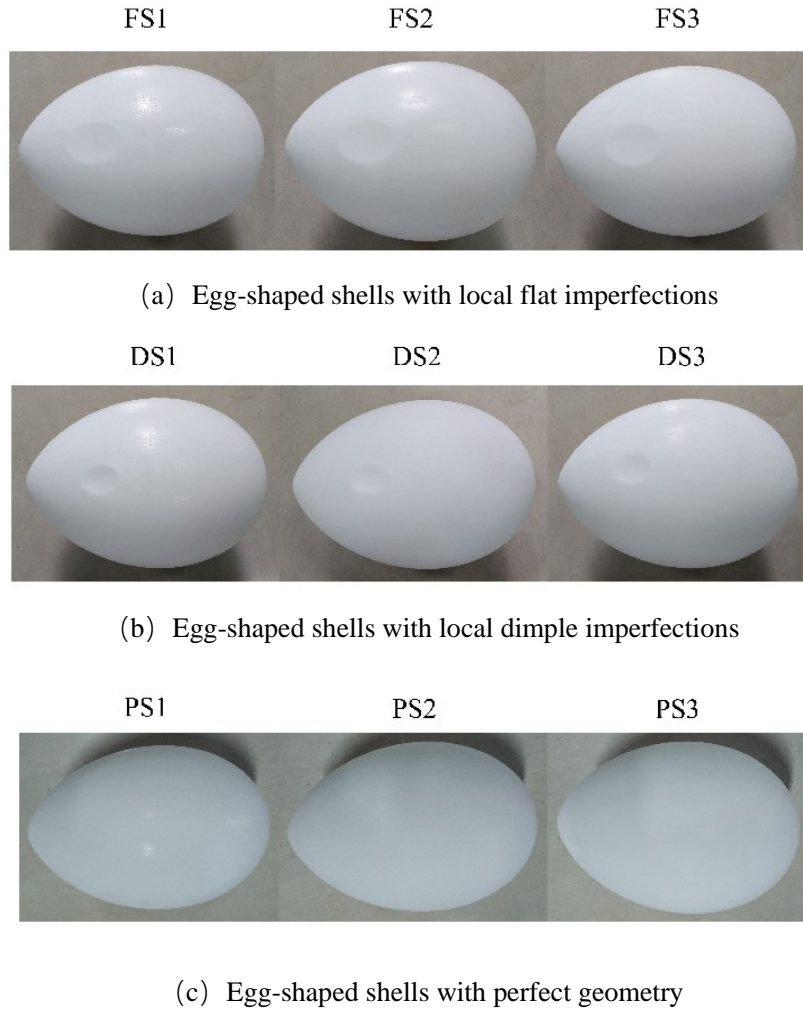
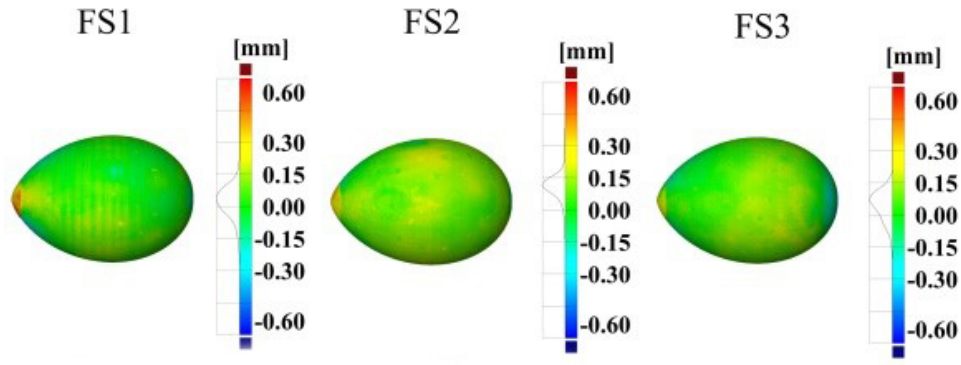
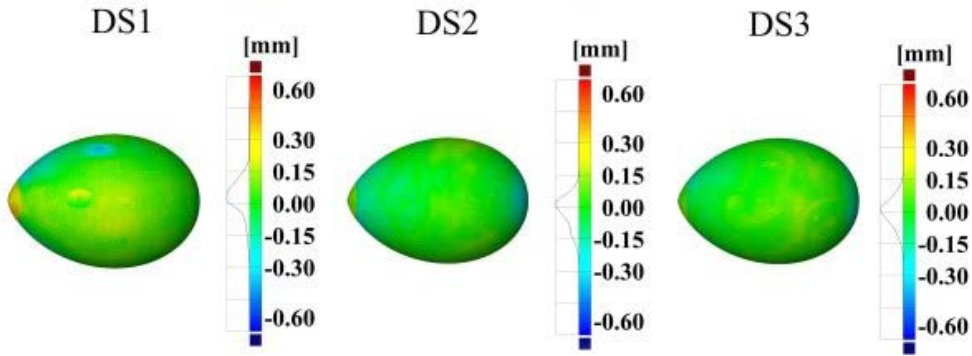


Fig.4-28 Representative photographs of fabricated egg-shaped shells

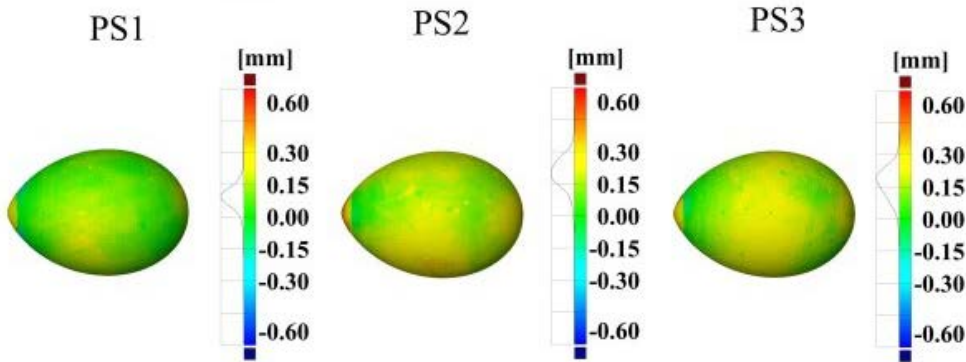
Before the test, the external surface of each egg-shaped shell was optically measured using a three-dimensional laser scanner (Open Technologies Corporation, accuracy: $\leq 0.02mm$). In this way, the CAD model of egg-shaped shell can be established based on numerous obtained point clouds, which may include slight geometrical imperfection inevitably caused by fabrication. Details of the measuring procedure can be found in [34]. The measured geometries of perfect, dimple imperfection-shaped, and flat imperfection-shaped egg-shaped shells are shown in Fig.4-29 as well as the fabricated deviations from the perfect geometries. As can be seen from Fig.4-29, there are considerably slight differences between fabricated and engineered shells.



(a) Egg-shaped shells with local flat imperfections



(b) Egg-shaped shells with local dimple imperfections



(c) Egg-shaped shells with perfect geometry

Fig.4-29 Measured geometries and fabricated deviations of egg-shaped shells

After the surface measurements, the wall thickness of each egg-shaped shell was ultrasonically measured using a nondestructive thickness gauge (Sonatest Corporation, accuracy: $\leq 0.001\text{mm}$). Measurements were conducted at 8 equidistant points along a meridian for a total of 22 equally spaced meridians, leading to $8 \times 22 + 1 = 177$ measuring points for each shell. The obtained magnitudes of minimum, t_{min} , maximum, t_{max} , and average wall thickness, t_{ave} , are listed in Table 4-7, along with the

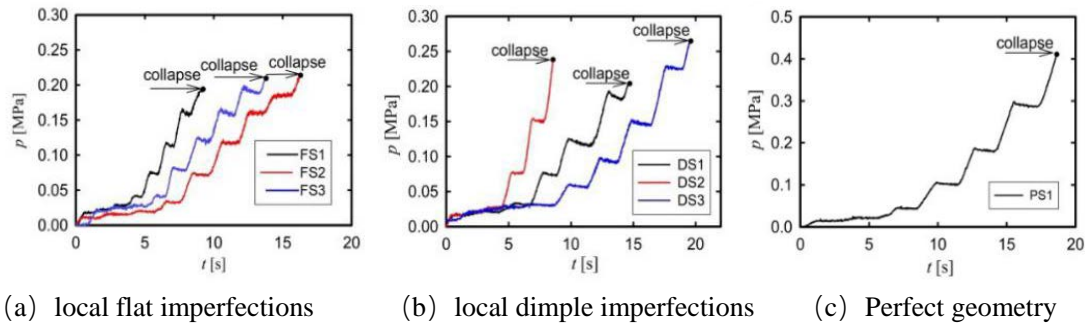
corresponding standard deviations, t_{dev} . As can be seen from Table 4-7, the fabricated wall thicknesses are very close to the nominal one (2 mm), indicating that the average wall thickness can be adopted in the subsequent numerical analysis of tested egg-shaped shells.

Table 4-7 Minimum, t_{min} , maximum, t_{max} , and average wall thickness, t_{ave} , of fabricated egg-shaped shells, along with the corresponding standard deviations, t_{dev} .

Sample	t_{min} [mm]	t_{max} [mm]	t_{ave} [mm]	t_{dev} [mm]
FS1	1.844	2.084	2.007	0.049
FS2	1.868	2.058	1.986	0.042
FS3	1.876	2.064	1.983	0.037
DS1	1.872	2.084	1.999	0.040
DS2	1.896	2.048	1.966	0.034
DS3	1.884	2.046	1.975	0.030
PS1	1.928	2.050	1.977	0.031
PS2	1.930	2.048	1.980	0.030
PS3	1.934	2.048	1.980	0.027

Finally, each fabricated egg-shaped shell was immersed into a cylindrical pressure vessel and slowly pressurized to collapse using water as the medium. Such vessel has an internal radius of 100 mm, an internal length of 800 mm, and a maximum testing capacity of 40 MPa. The pressure was imposed using a hand-operated pump, which was simultaneously recorded using a pressure gauge (HH-K10KB, accuracy: ≤ 0.04 MPa). Also, to minimize the effect of potential concentrated force due to buoyancy on the buckling and avoid some small collapsed pieces falling into the vessel, each egg-shaped shell was enclosed by a fine string bag with a bullet pig connected. Details of the testing procedure can be found in [31, 33]. During the test, an audible bang can be heard and a sharp pressure reduction can be captured when collapse happens to each shell. The obtained pressure – time curves are shown in Fig.4-30. As can be seen from the loading profiles in Fig.4-30, the applied pressure of each tested egg-shaped shell first increases steadily with an increase in the time, which continues up to implosion or collapse, and after that it decreases considerably. There appears to be apparent difference among the increasing grades of loading profiles due to the manual operation of hand-operated pump. Nevertheless, the

loading period varies from 8 to 20s, indicating a quasi-static loading case of experiments.



(a) local flat imperfections (b) local dimple imperfections (c) Perfect geometry

Fig.4-30 Pressure versus time of egg-shaped shells

Table 4-8 Element information and numerical buckling pressures, $p_{critical}$, of fabricated and designed egg-shaped shells, along with experimental buckling pressures, p_{test} .

Sample	P_{test} [MPa]	Element number		$p_{critical}$ [MPa]	$p_{critical}/p_{test}$
		S4	S3		
FS1	0.194	18850	3618	0.215	1.11
FS2	0.214	19318	1068	0.218	1.02
FS3	0.210	19288	1250	0.219	1.04
DS1	0.277	18142	4534	0.278	1.00
DS2	0.267	17906	5028	0.267	1.00
DS3	0.265	18354	3934	0.271	1.02
PS1	0.406	18510	3188	0.415	1.02
PS2	0.418	20094	1338	0.423	1.01
PS3	0.410	18198	3848	0.423	1.03
FS	N/A	21352	356	0.227	N/A
DS	N/A	20870	348	0.283	N/A
PS	N/A	22803	212	0.448	N/A

It must be noted that there may have some failures for data acquisition line during testing Sample 2 and 3 of perfect egg-shaped shells. Therefore, the pressure – time curves of these two samples were not recorded. Nevertheless, the maximum applied pressure, corresponding to the buckling load, was recorded (Table 4-8) from the digital display of pressure gauge itself by the tester. As can be identified from buckling pressures in Table 4-8, the experimental buckling pressure varies slightly from 0.194 to 0.214 MPa for egg-shaped shells with local flat imperfections, from 0.265 to 0.277 MPa for egg-shaped shells with local dimple imperfections, and from 0.406 to 0.418 MPa for perfect egg-shaped shells. In this way, the classical knock down factor (KDF) can be obtained, which is defined as the ratio of the buckling load

of imperfect shell to that of perfect one. As can be inferred, the average *KDF* for local flat imperfection is 50.1%, which is 15.5% lower than that for local dimple imperfection (65.6%). This observation suggests that egg-shaped shells are even more sensitive to local flat imperfection than local dimple imperfection.

After the test, the collapse mode of each egg-shaped shell can be observed in Fig.4-31. as can be observed from the collapse photographs in Fig.4-31, the collapse modes of all tested shells are similar; each is pressurized into a local hole because of the material brittleness. These local collapse modes are typical of shells of revolution, such as spheres [34], barrels [35], and Cassini ovals [31]. Moreover, above slight variations in the buckling pressures and similar collapse modes of nominally identical shells indicate a good repeatability of experiments. Further investigations on the buckling performances of nine egg-shaped shells are provided in the subsequent numerical analysis section.

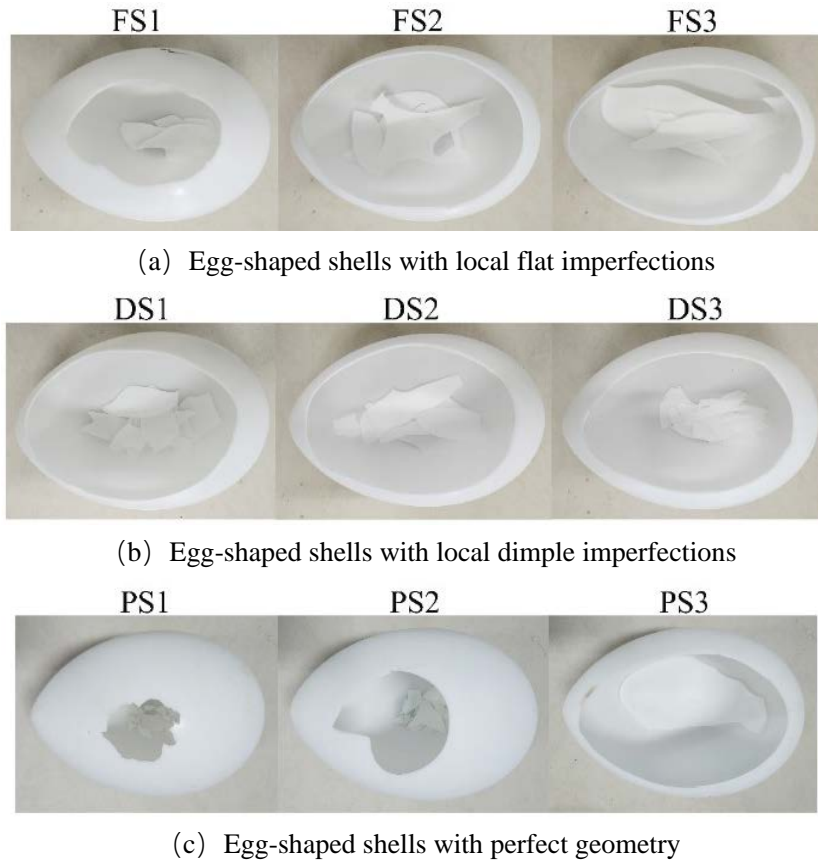


Fig.4-31 Collapse modes of egg-shaped shell

In addition, uniaxial tensile tests were carried out on three tensile flat coupons

through a modified version of ASTM D638 [36]. The obtained average material properties are as follows: Poisson ratio, $\nu = 0.32$, Young's modulus, $E = 1779 \text{ MPa}$.

4.4.2 Numerical buckling of rapid prototyping egg-shaped shells

To further study the buckling performances of imperfect and perfect egg-shaped shells, geometrically nonlinear elastic analyses were carried out for nine tested shells with fabricated real geometries (FS1, FS2, FS3, DS1, DS2, DS3, PS1, PS2, and PS3) and three designed shells with nominal geometries (FSN, DSN, PSN). Finite element code ABAQUS was employed for all analyses using arc length method, which is in line with ENV 1993-1-6 (2006) and CCS 2013 [31-32].

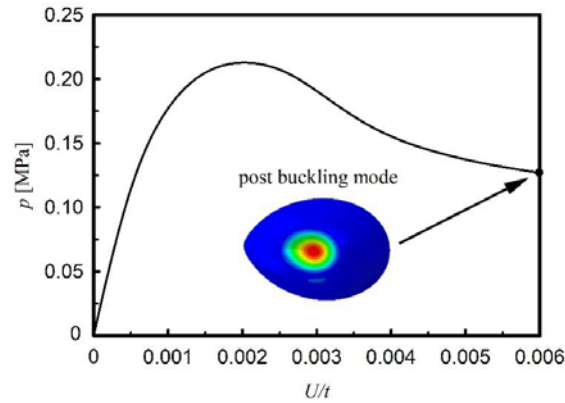


Fig.4-32 Applied pressure versus maximum deflection within the collapse zone of the FS1 egg-shaped shell, along with its post buckling mode

Each geometrical model was discretized mainly using quadrilateral shell elements S4, along with a few triangular shell elements S3. The element density was determined using mesh convergence studies. Details of element information are listed in Table 4-8. Boundary conditions were set to avoid rigid body displacement as follows: $U_y = U_z = 0, U_x = U_y = 0, U_y = U_z = 0$. A unit uniform pressure was applied on the external surface of shells. The solving parameters are as follows: the initial increment in the arc length along the static equilibrium path in the scaled load–displacement space is 0.01; the total arc length scale factor associated with this step is 200; the minimum arc length increment was $1\text{E-}050$, and the maximum arc length increment was 0.03. Also, the average experimental elastic material properties obtained in Section 3.2 were adopted in the analysis, which have been extensively implemented in the buckling analysis of resin shells of revolution and can lead to

accurate predictions [31]. The obtained numerical results are presented in Fig.4-32 and Table 4-8.

All analyzed egg-shaped shells have typical unstable post-buckling behavior and classical post buckling modes. For example, as can be seen from Fig.4-32, the pressure-deflection curve, typically named equilibrium path, show an unstable character. The applied pressure first increases linearly and then increase nonlinearly with an increase in the deflection, which corresponds to the pre-buckling stage. Such nonlinear relationship may be attributed to the geometrical nonlinearity of shell. This increase phenomenon continues up to the peak point, which corresponds to the maximum pressure – critical buckling pressure. After this point, the applied pressure decreases considerably, which corresponds to the post-buckling stage. The post-buckling mode at the end of the pressure-deflection curve takes the form of local dimple, which locates at the imperfection site. Such post-buckling mode is similar to the corresponding experimental one (Fig.4-31). Similar observations are found for other cases as well. Also, the critical buckling modes, corresponding to the peak point of pressure-deflection curve, take the form of local dimple for imperfect egg-shaped shells. On the other hand, the critical buckling modes of perfect egg-shaped shells take the form of several circumferential waves and one half-meridional wave resembling eigenmode, which is consistent with previous studies [33].

The critical buckling pressures of egg-shaped shells, corresponding to the peak points of pressure-deflection curves, are listed in Table 4-8. As can be observed from Table 4-8, the ratio of the numerical buckling load to the experimental one ranges from 1.00-1.11, showing a good agreement and indicating the validity of adopted numerical approach. The small difference between numerical prediction and experimental data may be mainly associated with the assumption of average wall thickness and variation in the material properties of shells. Further, like experimental observations, it also is inferred from the numerical data that egg-shaped shells are even more sensitive to local flat imperfection than local dimple imperfection. In addition, the critical buckling pressures of designed shells with nominal geometries are always less than those of tested shells with fabricated real geometries. It is

indicated that egg-shaped shell is sensitive to the slight fabricated geometrical imperfections.

4.4.3 Effects of imperfection shape and size on buckling of egg-shaped shells

To study the sensitivity of local geometrical imperfections to the buckling of egg-shaped shells, 12 sizes, including 0.05t, 0.1t, 0.15t, 0.2t, 0.25t, 0.5t, 0.75t, 1t, 1.25t, 1.5t, 1.75t, and 2t, were taken into account for egg-shaped shells with local dimple and local flat imperfections. Further, the first eigenmode imperfection was also introduced for a comparison. In this case, a total of 36 imperfect egg-shaped shells were examined numerically using ABAQUS code. The material modeling and properties, loading and boundary conditions, element type and density, meshing and solving approaches of these shells were identical to previous sections. Moreover, the wall thicknesses of shells were assumed to be the nominal one (2 mm). The knock down factors (*KDFs*), the numerical critical buckling pressure of imperfect egg-shaped shell normalized by that of the perfect one (0.448 MPa), are identified in Fig.4-33.

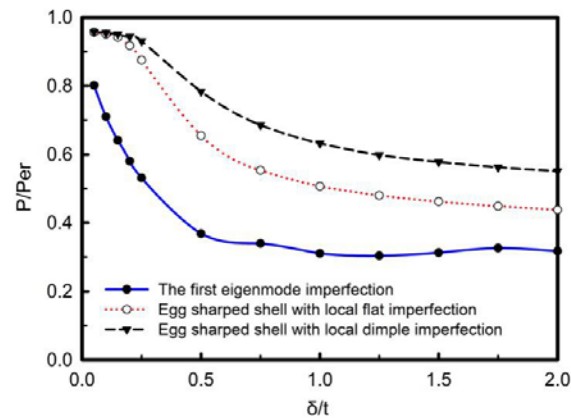


Fig.4-33 Knock down factors of imperfect egg-shaped shells versus imperfection sizes

As can be seen from Fig.4-33, there is a ‘threshold insensitivity’ of egg-shaped shells to both local imperfections because the critical buckling pressure appears not to decrease in the case of small imperfection size. Similar ‘threshold insensitivity’ phenomenon is found for tori spherical domes with local increased-radius imperfections [28, 37]. After the threshold, the critical buckling pressure continuously decreases with an increase in the imperfection size. The decreasing speed tends to

decline as the size increases.

On the other hand, for eigenmode imperfections, the critical buckling pressure decreases significantly in the case of small imperfection size (less than $0.5t$), after which it tends not to decrease and even slightly increase. These findings indicate that egg-shaped shells are highly sensitive to small eigenmode imperfections and extremely insensitive to large eigenmode imperfections, which is typical of shells of revolution under uniform external pressure.

Comparing buckling pressures obtained from local and eigenmode imperfections, eigenmode is the worst form of egg-shaped shells either in the case of small size or large size, which seems to be unfamiliar to the results of tori spherical domes. For tori spherical domes, the local increased-radius imperfection is worse than the eigenmode imperfection [28, 37]. This unfamiliarity may be due to the different shell geometries, boundary conditions, or local imperfection configurations. Nevertheless, it is confirmed that the eigenmode imperfection assumption in previous studies into egg-shaped shells [28] can generate the most conservative predictions.

4.5 Summary

The present chapter provides the results of the effect of geometrical parameters on the buckling of egg-shaped pressure hulls, along with corresponding experimentations. The following conclusions can be obtained:

(1) The results of the numerical and analytical analyses of the buckling behavior of fourteen egg-shaped pressure hulls are provided under various shape indices. The numerical linear buckling loads of the egg-shaped pressure hulls increase monotonically in conjunction with increases in the shape index; this agrees with the analytical results. The linear buckling shape of the egg-shaped pressure hulls has the form of several circumferential waves and one meridional half-wave. This is typical for shells of revolution with positive Gaussian curvature. The imperfection sensitivity increases as the shapes become more spherical. The equilibrium path of all of egg-shaped pressure hulls has an unstable characteristic. The critical buckling shape is identical to the linear buckling shape. The postbuckling mode has the form of local

dents; this finding is consistent with results obtained in previous studies.

(2) The elastic-plastic buckling load of the egg-shaped pressure hull increases linearly with an increase in the wall thickness. The thicker the egg-shaped pressure hull is, the more sensitive to material plasticity the buckling load is, the less sensitive to shape deviation the yielding and buckling loads are. For the perfect egg-shaped pressure hulls, the elastic buckling regime is found at relatively small wall thickness (10-20 mm), while the elastic-plastic buckling regime is found at relatively thick wall thickness (25-80 mm). However, all imperfect egg-shaped pressure hulls exhibit an elastic-plastic buckling instability. Similar results have been found for equivalent spherical pressure hulls. In addition, a reasonable agreement between the experiment and predictions is obtained.

(3) The egg-shaped pressure hull is less sensitive to the material plasticity and shape deviation than the spherical one, especially in the case of thick wall. As a result, the difference between the load carrying capacities of egg-shaped and spherical pressure hulls significantly decreases with an increase in the wall thickness. This finding suggests that egg-shaped pressure hulls appear to be applicable to deep submersibles, especially to full ocean depth ones. In this case, the load carrying capacity of egg-shaped pressure hulls may be nearly the same as or possibly even better than that of spherical pressure hulls, but their space efficiency and hydrodynamics can be better than those of spherical pressure hulls.

(4) Numerical and experimental results on the buckling performances of stainless egg-shaped shells demonstrate a materially and geometrically nonlinear instability regime. The experimental collapse load of three nominally identical egg-shaped shells ranges from 18.26 to 18.99 MPa, and the post-buckling modes of shells take the form of a local dent. These experimental results compare well with the numerical results, validating the proposed computational approach.

(5) Nine resin egg-shaped shells are obtained using rapid prototyping. Several quasi-static loading profiles and all buckling pressures are obtained, which suggest that the egg-shaped shell is even more sensitive to local flat imperfection than to local dimple imperfection. The numerical results agree well with the experimental ones.

The equilibrium path of each shell is unstable. The knock down factors of nominal egg-shaped shells with local flat, local dimple, and eigenmode imperfections are obtained numerically under 12 imperfection sizes. It is found that eigenmode imperfection is the worst either at small size or large size. Interestingly, a threshold insensitivity of egg-shaped shells to both local imperfections is found, which is similar to externally pressurized tori spherical domes with local increased-radius imperfections.

However, this chapter only considers egg-shaped pressure hulls with uniform wall thickness. As can be known from previous chapter, non-uniform wall thickness may strongly enhance the load carrying capacity of egg-shaped pressure hulls. This enhancement still requires further investigation and validation, which will be concentrated in the next chapter.

References

- [1]. M.E. Hauber, The book of eggs: A life-size guide to the eggs of six hundred of the world's bird species, Chicago, 2014.
- [2]. J. Zhang, M.L. Wang, W.B. Wang, W.X. Tang, Y.M. Zhu, Investigation on egg-shaped pressure hulls, *Mar. Struct.* 52 (2017) 50-66.
- [3]. N.N. Mohsenin, Physical properties of plant and animal material, Gordon and Breach, New York, 1970.
- [4]. J. Zhang, W. Peng, W.X. Tang, M.L. Wang, Experimental Study on the Geometrical and Mechanical Properties of Goose Eggshells, *Braz. J. Poultry Sci.* 19 (2017) 455-464.
- [5]. [CCS] China Classification Society, Rules for the Classification and Construction of Diving Systems and Submersibles, Beijing: CCS. (2013).
- [6]. H.M. Mushtari, On elastic equilibrium of a thin shell with initial irregularities of the form of a middle surface, *PMM (in Russian)*.15 (1915) 743-750.
- [7]. S.N. Krivoshapko, Research on general and axisymmetric ellipsoidal shells used as domes, pressure vessels, and tanks, *Appl. Mech. Rev.* 60 (2007) 336-355.
- [8]. D.V. Babich, Stability of shells of revolution with multifocal surfaces, *Int. Appl. Mech.* 29 (1993) 935-938.
- [9]. E.I. Grigolyuk, Plastic buckling of shells of revolution, *Izv. Akad. Nauk SSSR, Otd. Tekh. Nauk*, (in Russian). 2 (1958) 130-132.
- [10]. R. Zoelly, Über ein Knickungsproblem an der Kugelschale, Thesis, Zürich, 1915.
- [11]. P. Jasion, K. Magnucki, Elastic buckling of Cassini ovaloidal shells under external pressure – theoretical study, *Archives of Mechanics* 67 (2005) 179-192.
- [12]. P. Jasion, K. Magnucki, Elastic buckling of clothoidal-spherical shells under external pressure – theoretical study, *Thin-Walled Struct.* 86 (2015) 18-23.

- [13]. [CEN] Comité Européen de Normalisation, EN 1993-1-6: Eurocode 3 – Design of steel structures – Part 1.6: Strength and Stability of shell structures. Brussels: CEN. (2007).
- [14]. H. Schmidt, Stability of steel shell structures: General Report, *J. Constr. Steel Res.* 55 (2000) 159-181.
- [15]. J. Blachut, O. Ifayefunmi, Buckling of unstiffened steel cones subjected to axial compression and external pressure, *J. Offshore Mech. Arct. Eng.* 134 (2012) 031603.
- [16]. J. Blachut, A. Muc, J. Ryś, Plastic buckling of cones subjected to axial compression and external pressure, *J. Press. Vessel. Technol.* 135 (2013) 011205.
- [17]. J.J. Healey, Hydrostatic tests of two prolate spheroidal shells, *J. ship res.* 9 (1965) 77-78.
- [18]. W.C. Cui, Development of the Jiaolong deep manned submersible, *Mar. Technol. Soc. J.* 47 (2013) 37-54.
- [19]. B.B. Pan, W.C. Cui, Y.S. Shen, T. Liu, Further study on the ultimate strength analysis of spherical pressure hulls, *Mar. Struct.* 23 (2010) 444-461.
- [20]. B.B. Pan, W.C. Cui, A comparison of different rules for the spherical pressure hull of deep manned submersible, *J. Ship Mech.* 15 (2011) 276-285.
- [21]. B.B. Pan, W.C. Cui, Y.S. Shen, Experimental verification of the new ultimate strength equation of spherical pressure hulls, *Mar. Struct.* 29 (2012) 169-176.
- [22]. J. Zhang, J.C. Zhu, M.L. Wang, W.B. Wang, Y.M. Zhu, Design and analysis of egg-shaped pressure hulls, *J. Mech. Eng. [in Chinese]* 52 (2016) 155-161.
- [23]. J. Zhang, M.L. Wang, W.B. Wang, W.X. Tang, Buckling of egg-shaped shells subjected to external pressure, *Thin-Walled Struct.* 113 (2017) 122-128.
- [24]. O. Ifayefunmi, Buckling behavior of axially compressed cylindrical shells: Comparison of theoretical and experimental data, *Thin-Walled Struct.* 98 (2016) 558-564.
- [25]. M.W. Hilburger, M. P. Nemeth, J.H. Starnes, “Shell Buckling Design Criteria Based on Manufacturing Imperfection Signatures”, *AIAA J.* 44(2006) 654-663.
- [26]. M.W. Hilburger, “Developing the Next Generation Shell Buckling Design Factors and Technologies”, *AIAA J.* (2012) 2012-1686.
- [27]. S.G.P. Castro, R. Zimmermann, M.A. Arbelo, R. Khakimova, M.W. Hilburger, R. Degenhardt, Geometric imperfections and lower-bound methods used to calculate knock-down factors for axially compressed composite cylindrical shells, *Thin-Walled Struct.* 74 (2014) 118-132.
- [28]. J. Blachut, G.D. Galletly, Influence of local imperfections on the collapse strength of domed end closures, *Proc. Instn. Mech. Engrs.* 207 (1993) 197-207.
- [29]. J. Blachut, Buckling of composite domes with localised imperfections and subjected to external pressure, *Compos Struct.* 153 (2016) 746-754.
- [30]. J. Blachut, Locally flattened or dented domes under external pressure, *Thin-Walled Struct.* 97 (2015) 44-52.
- [31]. J. Zhang, W. Wang, F. Wang, W. Tang, W Cui, W. Wang, Elastic buckling of externally pressurized Cassini oval shells with various shape indices, *Thin-Walled Struct.* 122 (2018) 83-89.
- [32]. J. Zhang, Z. Hua, W. Tang, F. Wang, S. Wang, Buckling of externally pressurised egg-shaped shells with variable and constant wall thicknesses, *Thin-Walled Struct.* 132 (2018) 111-119.
- [33]. M. Wang, J. Zhang, W. Wang, W. Tang, Linear and nonlinear elastic buckling of

- stereolithography resin egg-shaped shells subjected to external pressure, *Thin-Walled Struct.* 127 (2018) 516-522.
- [34]. J. Zhang, M. Zhang, W. Tang, W. Wang, M. Wang, Buckling of spherical shells subjected to external pressure: a comparison of experimental and theoretical data, *Thin-Walled Struct.* 111 (2017) 58-64.
- [35]. J. Blachut, Optimal barreling of steel shells via simulated annealing algorithm, *Comput. Struct.* 81 (2003) 1941-1956.
- [36]. ASTM International, ASTM D638-14: Standard test method for tensile properties of plastics, West Conshohocken: ASTM Int. 08 (2003) 1-17.
- [37]. O. Ifayefunmi, J. Blachut, Imperfection sensitivity: a review of buckling behaviour of cones, cylinders and domes, *J. Press. Vessel. Technol.* 140 (2018) 1-8.

Chapter 5 Enhancement of egg-shaped pressure hulls using non-uniform wall thickness

In previous chapter, from the bionic viewpoint, the author systematically investigated the nonlinear elastic–plastic buckling of egg-shaped pressure hulls with various shape indices and wall thicknesses by using a combination of analytical, numerical, and experimental approaches. An egg-shaped shell was found to have an overall superior performance compared with a spherical one. However, all of these egg-shaped pressure hulls have been considered under uniform wall thickness, and less attention has been paid to enhancement of egg-shaped pressure hulls using non-uniform wall thickness. Also, in Section 4.4, it appears that egg-shaped shells with accurate geometrical shape and wall thickness distribution can be easily obtained using rapid prototyping approach. This finding can provide an experimental approach to study the buckling of egg-shaped pressure hulls with any engineered thickness.

Therefore, this chapter is devoted to an equivalent comparison between the buckling of mass equivalent egg-shaped pressure hulls with non-uniform and uniform wall thicknesses under uniform external pressure. First, a pair of resin egg-shaped pressure hulls with non-uniform and uniform wall thicknesses were designed and fabricated using rapid prototyping. Subsequently, the geometrical and buckling performance of the shells and the parent material properties of the shells were experimentally studied. Finally, the nonlinear elastic buckling performances of fabricated shells with measured imperfections and perfect shells with first eigenmode imperfections were numerically explored using the arc length method. The results revealed that the load-carrying capacity of egg-shaped pressure hulls is significantly improved when the shells have non-uniform wall thicknesses.

5.1 Design and fabrication of egg-shaped pressure hulls

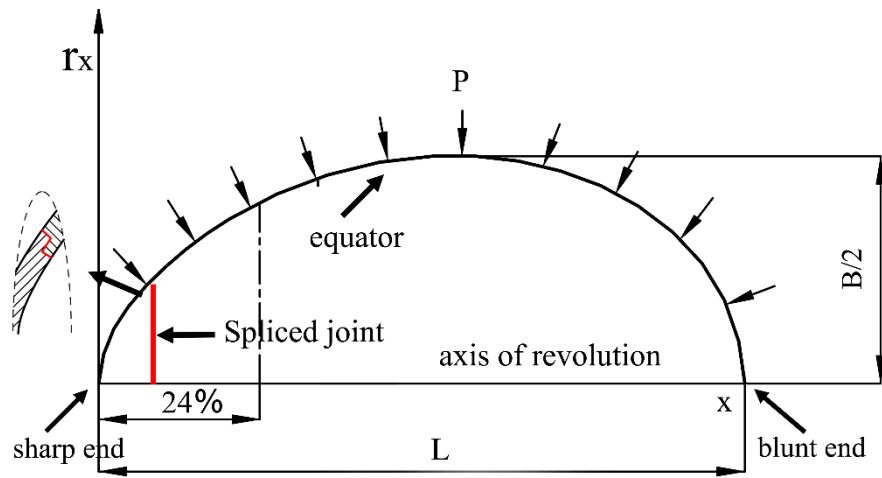
5.1.1 Geometrical design

Consider an externally pressurised egg-shaped pressure hull prepared using photosensitive resin under uniform external pressure, p , with a nominal major axis

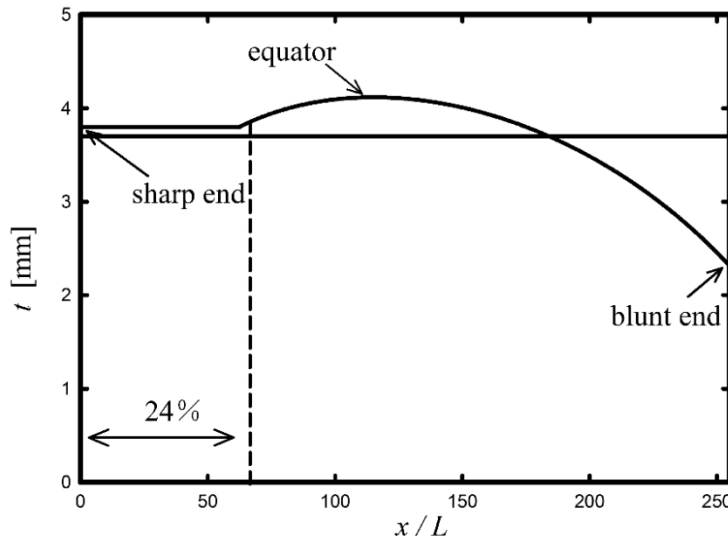
(axis of revolution) $L = 260.36$ mm and a nominal minor axis $B = 181.32$ mm. Fig.5-1a illustrates the radius of the prepared shell in Cartesian coordinates, which is defined as follows:

$$r_x = \pm \sqrt{L^{\frac{2}{n+1}} x^{\frac{2n}{n+1}} - x^2} \quad (5-1)$$

where $n = 1.057(L/B)^{2.372}$. Equation (5-1) was initially developed to describe the shape of eggs based on experimental results obtained from goose eggs [1-2]. Recently, the equation has been implemented to model the geometry of egg-shaped pressure hulls from the bionic viewpoint [3-6].



(a) Meridian



(b) Wall thickness

Fig.5-1 Schematic of an egg-shaped shell

Two types of egg-shaped pressure hulls were used in this study. The first type of shell had a uniform wall thickness with a nominal value of 3.7 mm, and the second

type of shell had a non-uniform wall thickness (Fig.5-1b) along the major axis with the same material volume as the first shell. A study on egg-shaped pressure hulls demonstrated that the meridional stress on these hulls is even higher than the circumferential stress [3]. In these cases, the variation in the wall thickness of the second shell is determined on the basis of the principle that the meridional stress, σ_θ , is approximately constant across the majority of the shell.

$$\sigma_\theta = \frac{p}{2t} \frac{2R_{1x}R_{2x} - (R_{2x})^2}{R_{1x}} \quad (5-2)$$

where the meridional radius of curvature R_{1x} and the circumferential radius of curvature R_{2x} are given as follows:

$$R_{1x} = -\frac{\left[1 + (dr_x / dx)^2\right]^{3/2}}{d^2r_x / dx^2} \quad (5-3)$$

$$R_{2x} = r_x \sqrt{1 + (dr_x / dx)^2} \quad (5-4)$$

Thus, the normalised value of the wall thickness is obtained as follows:

$$\frac{t_x}{t_{max}} = \left| \frac{2R_{1x}R_{2x} - (R_{2x})^2}{R_{1x}} \right| / \left| \frac{2R_{1x}R_{2x} - (R_{2x})^2}{R_{1x}} \right|_{max} \quad (5-5)$$

The derivation of the Eq.(5-5) was in line with Kruselecki's claim that the instability of shells can be determined by the stress state and that buckling is initiated at the weakest point (zone) of a structure [7-8]. Moreover, because the meridional radius of an egg-shaped shell near the sharp end is relatively large, the wall thickness in this area is assumed to be constant to avoid buckling failure in the sharp zone.

5.1.2 Sample fabrication

Fig.5-2 displays four egg-shaped pressure hulls that were fabricated upright along the axis of revolution through rapid prototyping—stereo lithography appearance (SLA). Two shells (ES1 and ES2) had uniform wall thicknesses, whereas the remaining shells (ES3 and ES4) had non-uniform wall thicknesses. All shells were fabricated using the same building parameters. Subsequently, the shells were cleaned and UV cured. The combined duration of the processes was 8 min. During fabrication, a fine point support was incorporated inside the shell to obtain an extremely smooth

surface. Hand grinding was used to smooth the outer surface. Moreover, a small hole with a diameter of 30 mm was designed at the sharp end to facilitate the removal of this support. The hole was closed with a domed cap by using a cyanoacrylate adhesive ($\text{CH}_2 = \text{C}(\text{CN}) - \text{COO} - \text{C}_2\text{H}_5$). The cap was fabricated separately by using SLA on the basis of Fig.5-1. Moreover, to ensure a strong connection between the hole and the shell, a stair-shaped margin between the components was implemented, as displayed in Fig.5-1(a). As the buckling initiates far from the sharp end [5], the designed hole may have a slight effect on the buckling of shell. Photosensitive resin was selected as the fabrication material, which was adopted to study the buckling capacity of Cassini oval and spherical shells[9-10].The fabricated egg-shaped pressure hulls are illustrated in Fig.5-2.

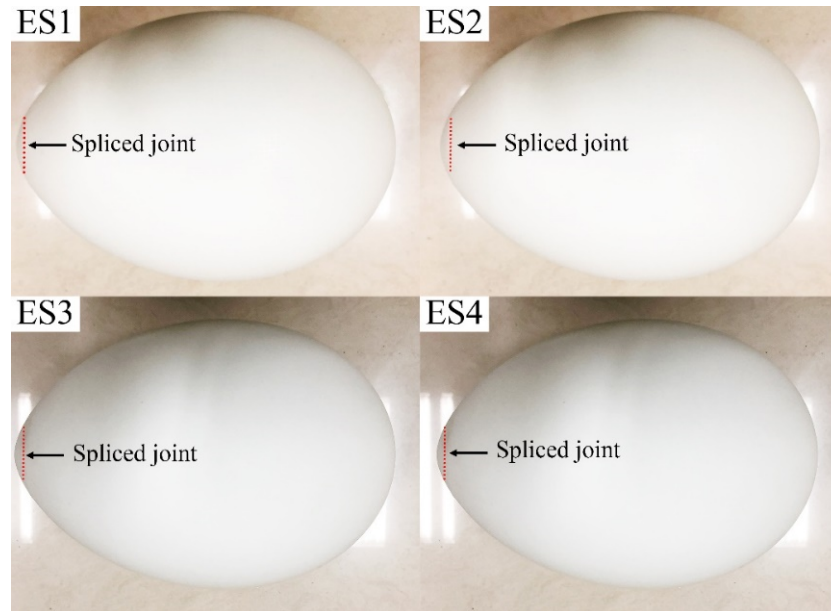


Fig.5-2 Photographs of fabricated egg-shaped shells with uniform (ES1 and ES2) and non-uniform (ES3 and ES4) wall thicknesses

5.2 Measurement and test

5.2.1 Shape scanning of samples

Before conducting the test, the external surface of each fabricated shell was accurately measured using a three-dimensional optical scanner (Open Technologies Corporation). The accuracy of the scanner was less than 0.02 mm according to the operating manual. Before the measurement, the external surface of shell was sprayed

with a thin layer of contrast aid to avoid light refraction and then pasted with several marker points to facilitate the stitching of pictures (Fig.5-3a). Thus, the accurate geometry of each fabricated shell was automatically obtained by transforming numerous point clouds into a CAD model, which included the initial geometric imperfections caused by the fabrication. The obtained geometries of the four egg-shaped pressure hulls are displayed in Fig.5-4 along with the deviations from the perfect geometries. Moreover, the obtained sizes of the egg-shaped pressure hulls from the scanned models are listed in Table 5-1.

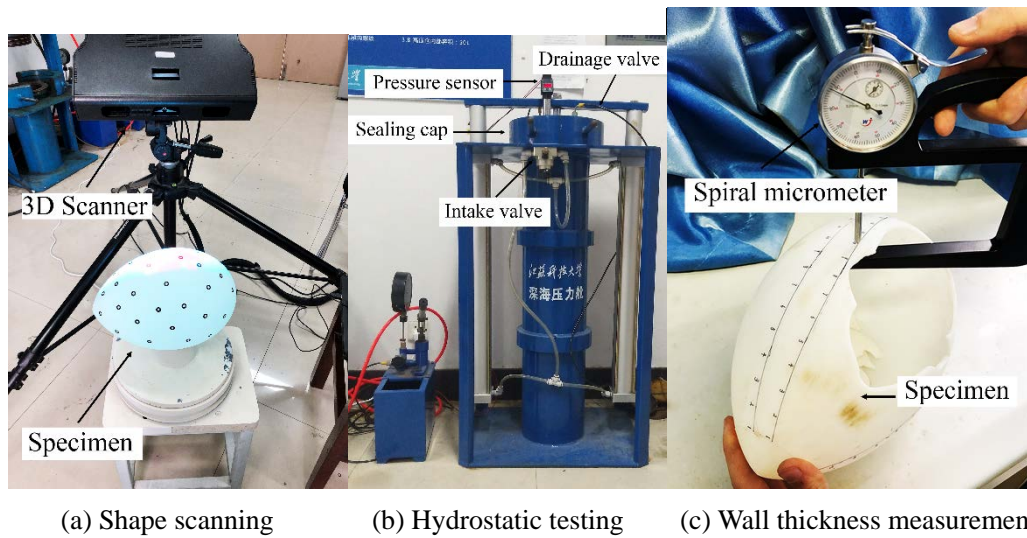


Fig.5-3 Experimental scene of egg-shaped shell

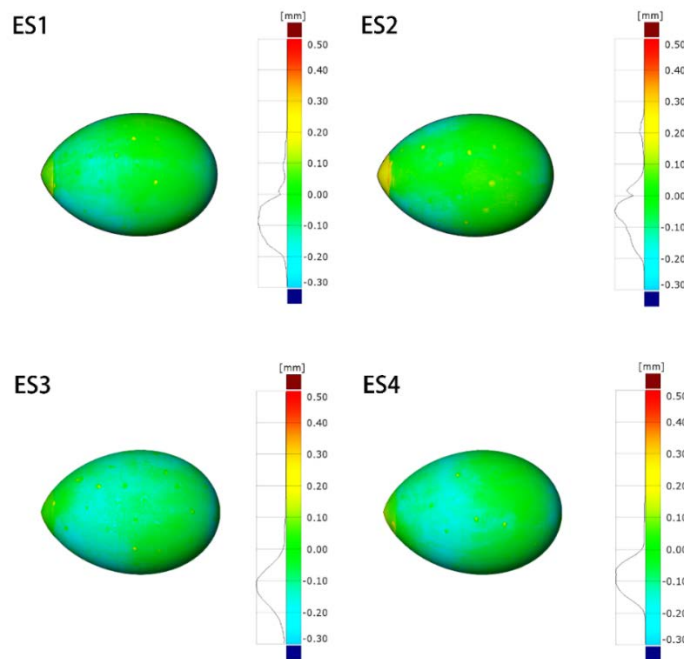


Fig.5-4 Fabrication deviations of the fabricated egg-shaped shells from perfect geometries

Table 5-1 Nominal and measured length, L , width, B , and mass, m , of the fabricated egg-shaped shells and their tested collapse pressure, p_{test} .

Specimen	L	B	m	p_{test}
	(mm)		(g)	(MPa)
Nominal	260.36	181.32	570	N/A
ES1	259.22(-1.14)	181.37 (0.05)	545(-25)	1.52
ES2	260.23(-0.14)	181.12 (-0.20)	550(-20)	1.63
ES3	260.34(-0.02)	181.08 (-0.24)	540(-30)	2.04
ES4	260.05(-0.31)	181.04 (-0.31)	540(-30)	2.11

5.2.2 Hydrostatic test of samples

After the measurement, each egg-shaped shell was carefully placed in a pressure chamber and slowly tested to destruction at room temperature. Two O-shaped rings were used to seal the chamber, and water was used as the pressure medium (Fig.5-3b). The chamber had an inner diameter of 200 mm, a total length of 800 mm, and a maximum pressure of 40 MPa. The pressure inside the chamber was slowly applied through a hand-operated pump and recorded by a pressure gauge (≤ 4 MPa). Because the shells were empty, they could float in the chamber if their buoyancy was higher than the gravitational force exerted on them. The buoyancy of perfect shells was approximately 10.22 N, as determined using the following formula:

$$F = \rho_{water} g \pi \int_0^L r_x^2 dx \quad (5-6)$$

where ρ_{water} , g , and π are equal to 1000 kg/m^3 , 9.8 m/s^2 , and 3.14, respectively. Conversely, the gravity of perfect shells was only 5.586 N, as determined using the following formula:

$$W = 2\pi\rho g \int_0^L \sqrt{1 + \left(\frac{dr_x}{dx}\right)^2} r_x t_x dx \quad (5-7)$$

where ρ is equal to 1.147 kg/m^3 . The floating may have had a significant effect on the buckling performances of shells because a concentrated force may have been applied on the tested shell [11-12]. To minimise this effect, each shell was wrapped in

a string bag with a bullet pig connected. The drainage valve was kept open before the test so that the air trapped inside the chamber could be expelled. Subsequently, the drainage valve was closed, and the pressure was manually applied until the shell collapsed. All the shells collapsed suddenly with an audible sound and a sudden decrease in the pressure. The recorded pressure during the experiment is listed in Fig.5-5, and the value of the peak point corresponds to the collapse pressure (Table 5-1). The variations in the test time resulted from manually operations because the pressure was slowly applied via a hand-operated pump. Therefore, it was not difficult to understand this observed phenomenon. However, each loading period was relatively long, which could achieve a quasi-static loading and might have a neglect impact on the results. Each collapsed shell was removed from the pressure chamber after the test; the collapse modes of the tested egg-shaped pressure hulls are shown in Fig.5-6. Owing to the brittleness of the material, each shell collapsed into several pieces. To facilitate observation, large pieces were pasted together by using cyanoacrylate adhesive, and the pasting seams were highlighted using dotted lines in the figure.

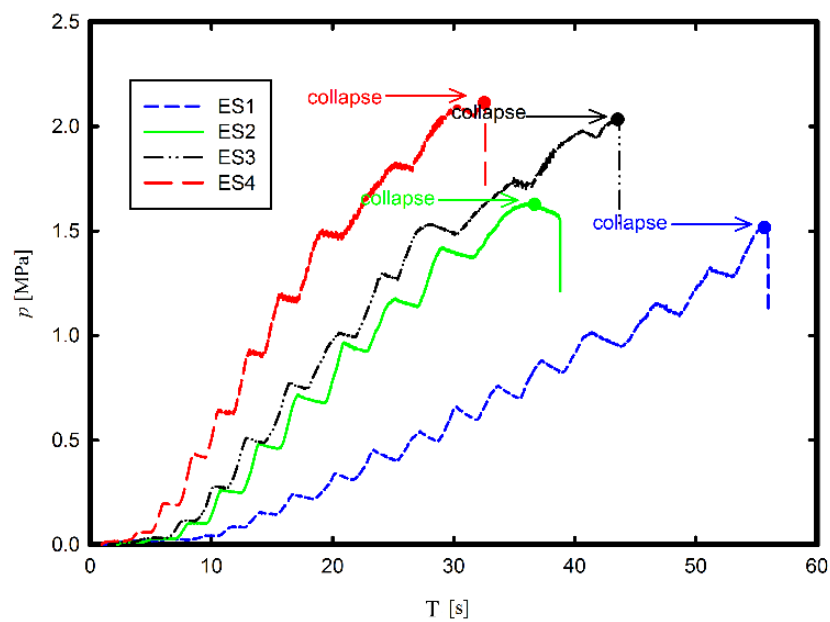


Fig.5-5 Recorded pressure of the tested egg-shaped shells

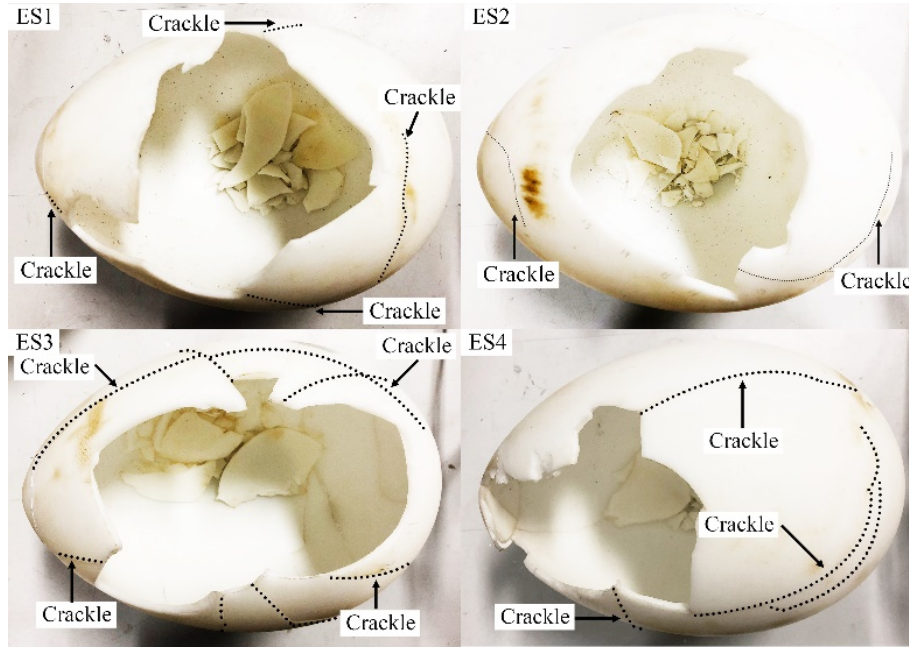


Fig.5-6 Collapse modes of the tested egg-shaped shells

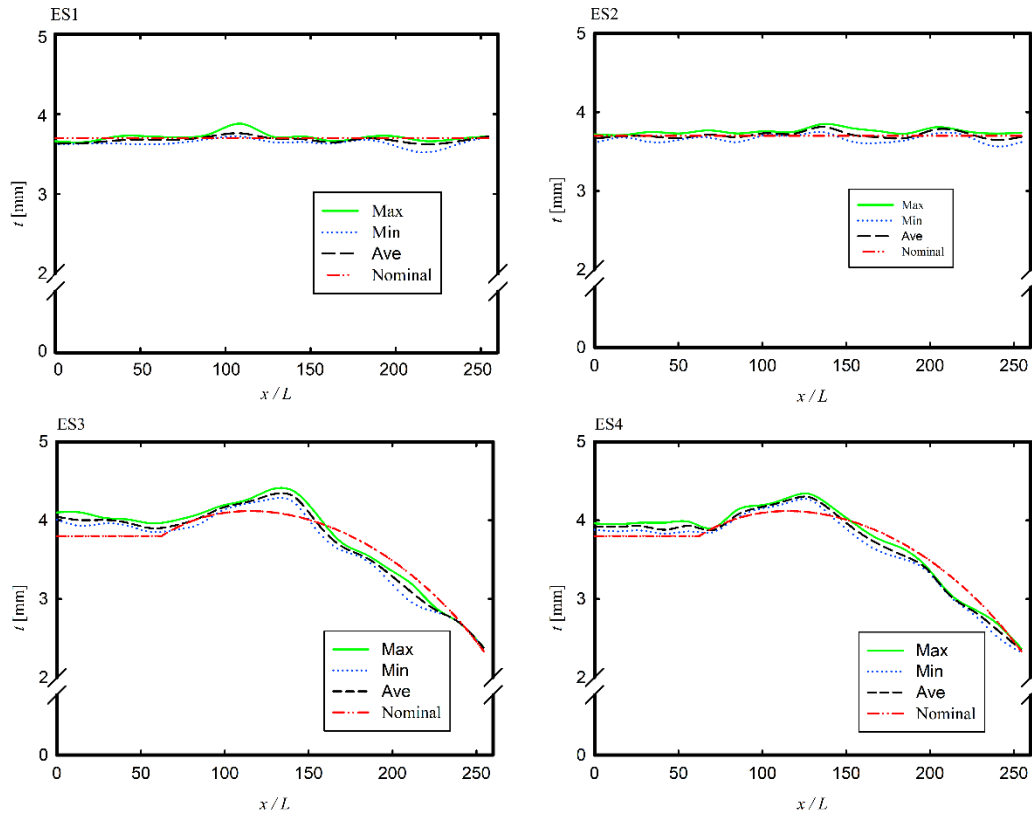


Fig.5-7 Measured wall thicknesses and nominal wall thicknesses of the tested egg-shaped shells

Finally, the wall thickness of each collapsed shell was measured along the collapse zone by using a micrometre gauge. Fig.5-3c reveals that the measuring points were

located at the four meridians of each shell; each meridian included 20 equidistant points. In this case, a total of 81 points ($4 \times 20 + 1 = 81$) were measured for the wall thickness. The measurement results are presented in Fig.5-7 and Table 5-2.

Table 5-2 Minimum, t_{min} , maximum, t_{max} , and average, t_{av} , wall thicknesses of the fabricated egg-shaped shells with the standard deviation, t_{std} .

Specimen	t_{min} [mm]	t_{max} [mm]	t_{av} [mm]	t_{std} [mm]
ES1	3.52	3.88	3.67	0.05
ES2	3.57	3.85	3.70	0.06
ES3	2.38	4.39	N/A	N/A
ES4	2.32	4.34	N/A	N/A

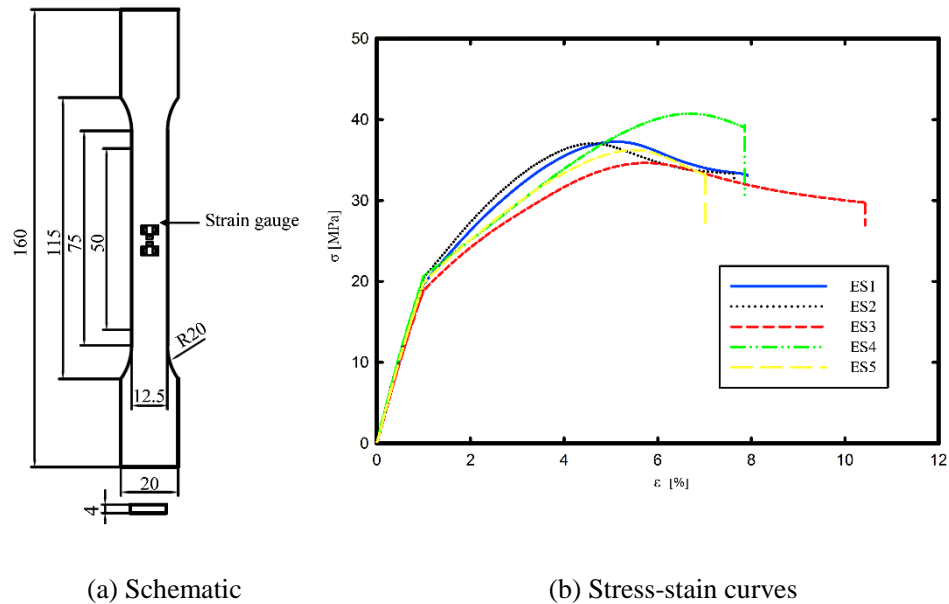


Fig.5-8 Schematic diagram and stress-stain curves of five fabricated coupons

Table 5-3 Material properties of five tested tensile coupons.

Specimen	E	μ
	(MPa)	
ES1	2076.6	0.323
ES2	2174.6	0.336
ES3	2063.8	0.303
ES4	2199.3	0.339
ES5	2100.3	0.341
AVE	2122.92	0.3284
Standard deviation	54.1426	0.014165

5.2.3 Tensile tests of material

To obtain the material properties, uniaxial tensile tests were conducted on five flat tension coupons through a modified version of ASTM D638 [13], and the tests were partially based on previous studies pertaining to the mechanical properties of parts fabricated through rapid prototyping [14-17]. These coupons were fabricated upright along the longitudinal direction by using SLA and tested at room temperature; the test was performed using the same method used for the fabricated egg-shaped pressure hulls. Fig.5-8 reveals that the coupons had a gauge length of 50 mm, a gauge width of 12.5 mm, and a wall thickness of 4 mm, in which the stress-strain curves were also included. The Young's moduli determined from the test are listed in Table 5-3.

To obtain the value of Poisson ratio, each coupon was strain gauged by using two general strain gauges. One strain gauge was pasted using cyanoacrylate adhesive in the longitudinal direction, and the other was pasted in the transverse direction. On the basis of the service instruction, the sensitivity of the strain gauge was 1.86–2.20. The sensitive grid length on the strain gauge was 1.0 mm, and the width was 1.9 mm. The base length of a strain gauge was 4.3 mm and the width was 3.5 mm. The strain variations during the test were recorded using a dynamic strain measuring instrument. The Poisson ratios determined from the recorded strains are listed in Table 5-3.

5.3 Experimental analysis of egg-shaped pressure hulls

The measured results pertaining to the shape, size, mass, and wall thickness suggested that the fabricated egg-shaped pressure hulls were nearly perfect, thus demonstrating the repeatability and high accuracy of the fabrication process. For example, Fig.5-4 demonstrates that the fabrication deviation of the four fabricated egg-shaped pressure hulls from the nominal shells was relatively small. The wall thickness deviation between most of the fabricated shells and nominal shell was less than 0.4 mm, which is a small fraction of the shell size. Table 5-2 reveals that the maximum size difference between the fabricated and nominal shells was <0.44%, whereas the maximum mass difference between the shells was <5.3%. The mass was measured using an electronic balance, whereas the nominal mass was determined

using Eq.(7). The mass difference may have been due to the relatively small deviation in the wall thickness between the fabricated shells and the nominal shell.

Fig.5-7 and Table 5-2 reveals that for a uniform wall thickness, the wall thickness values of egg-shaped pressure hulls with uniform wall thicknesses (ES1 and ES2; 3.52 to 3.88 mm with a small standard deviation) were nearly equal to that of the nominal shell (3.7 mm). Conversely, for the shells with non-uniform wall thicknesses (ES3 and ES4), the thickness measurements displayed an optimal degree of axis-symmetry. The thickness distributions of the fabricated shells were identical to that of the nominal shell along the meridian. The wall thickness was almost uniform near the sharp end of shells. Then, the thickness increased up to a peak value and decreased monotonously. Although there were some fluctuations in the wall thickness distribution values of the fabricated shells along the meridian compared with the thickness distributions values of the nominal shell, the material volumes (mass) of the egg-shaped pressure hulls with non-uniform wall thickness were approximately equal to those of the egg-shaped pressure hulls with uniform wall thickness.

The pressure–time curves displayed in Fig.5-5 demonstrate that the pressure of the tested egg-shaped pressure hulls increased monotonously up to a critical point (collapse) and decreased sharply thereafter. The variations in the curve slope were attributed to the varying loading rates of the hand-operated pump. Table 5-1 lists that the collapse pressure, p_{test} , which varied from 1.52 to 1.63 MPa for the egg-shaped pressure hulls with uniform wall thickness and from 2.04 to 2.11 MPa for the egg-shaped pressure hulls with non-uniform wall thickness. These differences may have been due to the slight deviations in the material properties, local radius, and wall thickness of the fabricated egg-shaped pressure hulls. The average collapse pressure of the egg-shaped pressure hulls with non-uniform wall thickness was approximately 24% higher than that of the egg-shaped pressure hulls with uniform wall thickness. This phenomenon indicated that the load-carrying capacity of egg-shaped pressure hulls was significantly improved using the non-uniform thickness principle presented in Eq.(5), which confirms the previous speculation that a non-uniform wall thickness may be an effective method for improving the buckling capacity of barrelled shells

[18-19].

Owing to the brittleness of the material used in this study at room temperature, all tested egg-shaped pressure hulls were pressurised into several pieces on one side. Fig.5-6 demonstrates that the shells seemed to collapse near the equator by forming a local dent. This collapse form can be also confirmed by experimental results that were obtained by externally pressurising egg-shaped pressure hulls prepared using 304 stainless steel and barrelled shells composed of mild steel [20-21]. This type of asymmetric collapse form is mainly attributed to the slight initial geometric imperfections caused by the fabrication. Moreover, the crackle on the tested shells (dotted lines) may have been due to the tearing load applied during the formation of the local dent.

5.4 Numerical analysis of egg-shaped pressure hulls

To further study the buckling of egg-shaped pressure hulls with non-uniform and uniform wall thicknesses, geometrically nonlinear elastic analyses were conducted for four fabricated shells with measured imperfections and two perfect shells with first eigenmode imperfections. Measured imperfections could be considered by directly meshing the scanned shell geometries, while eigenmode-shaped imperfections could be imposed by introducing the first eigenmode into the perfect geometries.

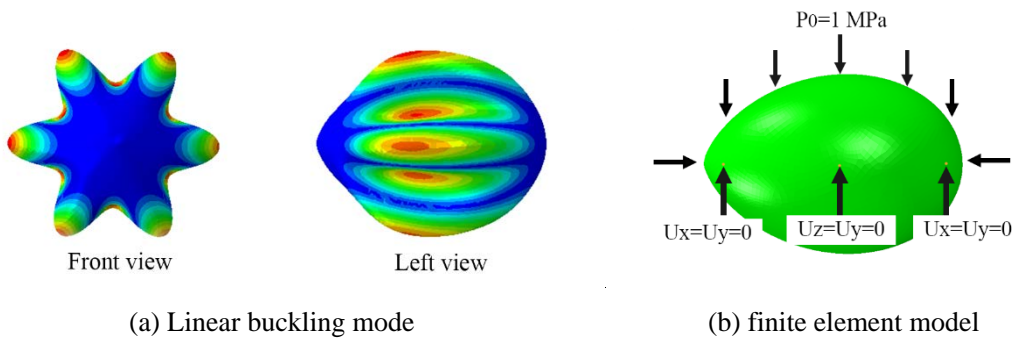


Fig.5-9 Linear buckling mode and finite element model of the egg-shaped shell

This study was performed numerically by using the arc length method available in the ABAQUS code and was based partly on ENV 1993-1-6 (2007) and CCS 2013 [22-23]. The calculating parameters are defined as follows. The initial increment in the arc length along the static equilibrium path in the scaled load–displacement space

was 0.01; the total arc length scale factor associated with this step was 200. Moreover, the minimum arc length increment was 1E-035, and the maximum arc length increment was 0.1. The first eigenmode imperfections were extracted from the linear elastic bifurcation analyses of perfect shells by using the Lanczos eigensolver available in the ABAQUS code due to its superior accuracy, as illustrated in Fig.5-9a. The imperfection size, the depth of the imperfection, was assumed to be 0.1 mm on the basis of the shape measuring results in Fig.5-4.

The finite elements of each shell were generated via a commercial software ANSA. Because the shape of each fabricated shell was optically obtained in the form of several irregular surfaces [24], the quadrilateral shell elements (S4) were considered to be the main mesh type of the fabricated shells with a few evitable triangular shell elements (S3). Conversely, the perfect shells only incorporated the quadrilateral shell elements (S4) as the mesh type due to the highly regular and smooth surfaces of the perfect shells. For all shells, mesh convergence studies were conducted, and the details of the mesh are listed in Table 5-4.

Table 5-4 Linear buckling pressure, p_{lb} , and nonlinear buckling pressure, p_{nlb} , of the fabricated and perfect egg-shaped shells with their element information.

Specimen	Mesh		P_{comput}			
	S3	S4	p_{lb}	p_{lb}/p_{test}	p_{nlb}	p_{nlb}/p_{test}
ES1	2778	8598	1.70	1.12	1.70	1.12
ES2	2944	9376	1.72	1.06	1.72	1.06
ES3	2268	7489	2.12	1.04	2.09	1.02
ES4	3572	10528	2.09	0.99	2.07	0.98
Non-uniform thickness	0	9366	2.13	N/A	1.92	N/A
Uniform thickness	0	9366	1.79	N/A	1.63	N/A

For all cases, elastic material modelling was adopted with the average tested material properties (Table 5-3) as follows: Young modulus $E = 2122.92$ MPa and Poisson ratio $\mu = 0.3284$. A uniform pressure p_0 of 1 MPa was externally applied

on the entire surface of each shell. In this case, the maximum arc length value obtained from the geometrically nonlinear elastic analysis corresponds to the critical buckling load. To eliminate the rigid body motion, three spatial nodes of each model were constrained on the basis of CCS 2013; the details of this elimination are displayed in Fig.5-9b. This definition may not introduce an over-constraint into the model due to the uniformly applied pressure. The numerical results obtained from the ABAQUS code are displayed in Fig.5-10 and listed in Table 5-4.

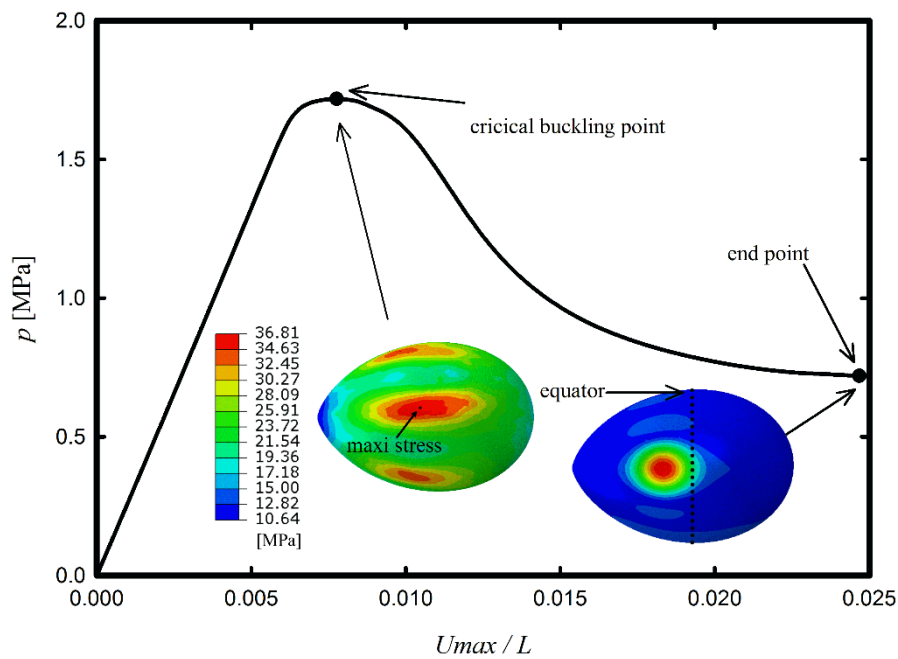


Fig.5-10 Equilibrium path of ES1 with its critical and post buckling modes, along with the critical stress distribution, which is a result of measured imperfection

The fabricated egg-shaped pressure hulls with the measured imperfections and the perfect shells with first eigenmode imperfections exhibited identical buckling behaviour, which is typically observed in shells of revolution with positive Gaussian curvature subjected to uniform external pressure [25-28]. For example, Fig.5-10 reveals that the equilibrium path—applied pressure versus maximum deflection—of ES1 at the collapse zone had an unstable character. The applied pressure first increased monotonously with an increase in the deflection and then decreased considerably after reaching a peak point. The critical buckling mode at the peak point exhibited several circumferential waves and one meridional half-wave, which was

similar to the linear buckling mode displayed in Fig.5-9a. The post buckling mode at the end of the path took the form of a local dent near the equator, which was in agreement with the experimental observation shown in Fig.5-6. Additionally, at the critical point of Fig.5-10, there existed stress concentration on the stress distribution graph, which could result from the initial inevitable geometric imperfections caused by fabrication. The location of maximum stress was at the centre of the collapse area, thus confirming that buckling was initiated at the weakest point (zone) of the structure. Similar findings were found for other models for measured imperfections or first eigenmode imperfections.

Table 5-4 lists the obtained critical buckling pressures corresponding to the applied pressures at the peak point of the equilibrium path, along with the linear buckling results. The numerical critical buckling pressures of ES1 and ES2 ranged from 1.70 to 1.72 MPa, which are 1.06–1.12 times the experimental critical buckling pressures. The critical buckling pressures of ES3 and ES4 ranged from 2.07 to 2.09 MPa, which are 0.98–1.02 times the experimental critical buckling pressures. An optimal agreement was obtained between the numerical and experimental results. In the same table, the critical buckling pressure of the perfect egg-shaped shell with a uniform wall thickness and first eigenmode imperfection is 1.63, which is only 70.8% of that of the perfect egg-shaped shell with non-uniform wall thickness and first eigenmode imperfection. This indicated that the buckling capacity of an egg-shaped shell is significantly improved using non-uniform wall thickness either under measured or eigenmode imperfections. Moreover, the critical buckling pressures obtained from eigenmode imperfections were less than those from measured imperfections, which seems to confirm the previous claim that first eigenmode imperfections may be the most serious and may cause overly conservative results [29-31]. This assumption regarding first eigenmode imperfections can be used in the preliminary design stage for the evaluation of the buckling of shells of revolution under uniform external pressure. Similar findings could be obtained for the linear cases except that all linear pressures were slightly higher than the nonlinear ones, which was associated with the nonlinear pre-buckling deformation of shells.

5.5 Summary

In this chapter, the buckling behaviours of mass equivalent egg-shaped pressure hulls with non-uniform and uniform wall thicknesses under uniform external pressure were obtained experimentally and numerically. The conclusions are as follows:

(1) The measured results and the test results pertaining to the shape, size, mass, and wall thickness demonstrated repeatability and high fabrication accuracy. All tested egg-shaped pressure hulls were broken into several pieces on one side, and they collapsed near the equator following the formation of a local dent. The average collapse pressure of the egg-shaped pressure hulls with non-uniform wall thickness was higher than that of the egg-shaped pressure hulls with uniform wall thickness, thus indicating that the load-carrying capacity of egg-shaped pressure hulls is significantly improved when the non-uniform wall thickness is implemented.

(2) Geometrically nonlinear elastic analyses were performed numerically for four fabricated shells with measured imperfections and two perfect shells with first eigenmode imperfections. The numerical evaluations of the four fabricated shells were in agreement with the corresponding experimental results. The critical buckling pressure of the perfect egg-shaped shell with non-uniform wall thickness is considerably higher than that of the perfect egg-shaped shell with uniform wall thickness, thus indicating that the buckling capacity of an egg-shaped shell is significantly improved when non-uniform wall thickness is used under either measured or eigenmode imperfections. Moreover, after buckling, the equilibrium paths of all shells exhibited an unstable character and their modes formed local dents, which are typically observed in shells of revolution with positive Gaussian curvature under uniform external pressure. The location of maximum stress was at the centre of the collapse area, thus confirming that buckling was initiated at the weakest point (zone) of the structure.

(3) The effects of non-uniform wall thickness on the buckling capacity of egg-shaped pressure hulls are suitable for investigation through an equivalent comparison experimental method. The obtained egg-shaped pressure hulls with

non-uniform wall thickness can be used in various externally pressurised components, such as underwater pressure hulls, underground pressure vessels, and liquid storage tanks subjected to negative pressure. Moreover, non-uniform wall thickness can be applied to improve the buckling capacity of other untypical shells of revolution with positive Gaussian curvature.

However, some limitations must be noted. Although the results of previous three chapters are encouraging and confirmed experimentally, all of them only focus on closed configurations – complete spherical pressure hulls or complete egg-shaped ones. In engineering applications, there are one or more large access holes on each pressure hull, which can be closed by domed heads. Such head are typical shells of revolution with positive Gaussian curvature, which are also susceptible to nonlinear buckling. Such factors will be taken into account in the next chapter.

References

- [1] V.G. Narushin, M.N. Romanov. "Physical characteristics of chicken eggs in relation to their hatchability and chick weight." *World's Poult. Sci. J.*, 58, 297-303. 2002.
- [2] V.G. Narushin. "Shape geometry of the avian egg." *J. Agric. Eng. Res.*, 79 (4), 441-448. 2001.
- [3] Zhang, J., Wang, M., Wang, W., Tang, W., and Zhu, Y. "Investigation on egg-shaped pressure hulls." *Marine Structures*, Elsevier Ltd, 52, 50-66. 2017.
- [4] Zhang, J., Peng, W. "Experimental Study on the Geometrical and Mechanical Properties of Goose Eggshells." *Brazilian Journal of Poultry Science*, 19(3), 455-463. 2017.
- [5] Zhang, J., Wang, M., Wang, W., and Tang, W. "Buckling of egg-shaped shells subjected to external pressure." *Thin-Walled Structures*, Elsevier, 113(July 2016), 122-128. 2017.
- [6] Zhang, J., Zhu, B., Wang, F., Tang, W., Wang, W., and Zhang, M. "Buckling of prolate egg-shaped domes under hydrostatic external pressure." *Thin-Walled Structures*, 119, 296-303. 2017.
- [7] J. Kruzelecki, P. Trzeccial. "Optimal design of axially symmetrical shells under hydrostatic pressure with respect to their stability". *Struct. Multidisc Optim.* 19, 148-154. 2000.
- [8] M. Barski, J. Kruzelecki, "Optimal design of shells against buckling under overall bending and external pressure". *Thin-Walled Struct.*, 43 (2005), 1677-1698. 2005.
- [9] Jian Zhang, Weimin Wang, Fang Wang, Wenxian Tang, Weicheng Cui, Weibo Wang. "Elastic buckling of externally pressurized Cassini oval shells with various shape indices". *Thin-Walled Struct.*, 2018, 122 :83-89.
- [10] Jian. Zhang, Weiming. Wang, Weicheng. Cui, Wenxian. Tang, Fang. Wang, Yun. Chen. "Buckling of longan-shaped shells under external pressure". *Marine Structures*, 2018, 60 :218-225.
- [11] S.G.P. Castro, R. Zimmermann, M.A. Arbelo, R. Khakimova, M.W. Hilburgerd, R.

- Degenhardt. "Geometric imperfections and lower-bound methods used to calculate knock-down factors for axially compressed composite cylindrical shells". *Thin-Walled Struct*, 74, 2014, 118-32. 2014.
- [12] Ismail, M. S., Purbolaksono, J., Andriyana, A., Tan, C. J., Muhammad, N., and Liew, H. L. "The use of initial imperfection approach in design process and buckling failure evaluation of axially compressed composite cylindrical shells." *Engineering Failure Analysis*, 51, 20-28. 2015.
 - [13] ASTM Norma. "Standard Test Method for Tensile Properties of Plastics." *Annual Book of ASTM Standards*, 1-15. 2004.
 - [14] Lee, C. S., Kim, S. G., Kim, H. J., and Ahn, S. H. "Measurement of anisotropic compressive strength of rapid prototyping parts." *Journal of Materials Processing Technology*, 187-188, 627-630. 2007.
 - [15] A. Lanzotti, M. Grasso, G. Staiano, M. Martorelli. "The impact of process parameters on mechanical properties of parts fabricated in PLA with an open-source 3-D Printer". *Rapid Prototyping J.* 21(5), 604-617. 2015.
 - [16] Chockalingam, K., Jawahar, N., and Chandrasekhar, U. "Influence of layer thickness on mechanical properties in stereolithography." *Rapid Prototyping Journal*, 12(2), 106-113. 2006.
 - [17] Puebla, K., Arcaute, K., Quintana, R., and Wicker, R. B. "Effects of environmental conditions, aging, and build orientations on the mechanical properties of ASTM type I specimens manufactured via stereolithography." *Rapid Prototyping Journal*, 18(5), 374-388. 2012.
 - [18] Blachut, J., and P Wang. "Buckling of Barreled Shells Subjected to External Hydrostatic Pressure." *Journal of Pressure Vessel Technology*, 123 (2), 232. 2001.
 - [19] Blachut, J., and P. Smith. "Buckling of Multi-Segment Underwater Pressure Hull." *Ocean Engineering*, 35 (2), 247-260. (doi:10.1016/j.oceaneng.2007.08.003), 2008.
 - [20] Blachut J. "Optimal barreling of steel shells via simulated annealing algorithm". *Comput. Struct*, 81(18-19):1941-56. 2003.
 - [21] Blachut, J., and P Wang. "Buckling of Barreled Shells Subjected to External Hydrostatic Pressure." *Journal of Pressure Vessel Technology*, 123 (2), 232. 2001.
 - [22] Rules for the classification and construction of diving systems and submersibles. Published by China Classification Society (CCS) in 2013, 2013.
 - [23] ENV 1993-1-6: Eurocode 3 - Design of steel structures - Part 1.6: Strength and Stability of shell structures. Eurocode 3 Part 1.6, CEN, Brussels, 2007.
 - [24] Zhang. J, Zhang. M, Tang. W.X, Wang. W.B, Wang. M.L. "Buckling of spherical shells subjected to external pressure: A comparison of experimental and theoretical data."
 - [25] Magnucki K, Jasion P. "Analytical description of pre-buckling and buckling states of barrelled shells under radial pressure". *Ocean Eng*, 58:217-23. 2013
 - [26] Jasion, P., and K. Magnucki. "Elastic Buckling of Barrelled Shell under External Pressure." *Thin-Walled Structures*, 45 (4), 393-99., 2007.
 - [27] P. Jasion, K. Magnucki. "Elastic buckling of Cassini ovaloidal shells under external pressure – theoretical study". *Arch. Mech*, 67(2), 179-92, 2015.
 - [28] P. Jasion, K. Magnucki. "Elastic buckling of clothoidal-spherical shells under external pressure – theoretical study". *Thin-Walled Struct*, 86, 18-23, 2015.

- [29] Rules for the classification and construction of diving systems and submersibles. Published by China Classification Society (CCS) in 2013, 2013.
- [30] ENV 1993-1-6: Eurocode 3 - Design of steel structures - Part 1.6: Strength and Stability of shell structures. Eurocode 3 Part 1.6, CEN, Brussels, 2007.
- [31] H. Schmidt.2000. "Stability of steel shell structures. " J. Constr. Steel Res. 55: 159-181.

Chapter 6 Spherical closures on access holes of pressure hulls

Previous chapters focus on either complete spherical pressure hulls or complete egg-shaped ones. In other words, all pressure hull configurations are closed shells of revolution. Actually, at least one large hole enclosed with heavy flange may be opened as an access channel of carried crews or inner equipment. Such hole can be closed by a domed head to ensure the safety of crews or equipment. Typical heads take the form of spherical, ellipsoidal, and tori spherical configurations, which are also prone to nonlinear buckling. The buckling performance is strongly influenced by the geometrical shape, initial imperfections, and wall thickness of head. Therefore, in order to provide theoretical guidance for the design of closed head, this chapter is devoted to the buckling of spherical caps under various heights, geometric imperfections, and wall-thickness reductions.

Firstly, the buckling of stainless steel spherical caps under uniform external pressure was introduced. Caps with a circular arc meridian have a nominal base diameter of 146 mm, nominal uniform wall thickness of 1 mm, and nominal height of 37 mm. Six nominally identical laboratory-scale caps were fabricated, measured precisely, and tested slowly. The buckling performances of such caps were studied experimentally and numerically, and the results show good agreement with each other. Furthermore, the buckling of 13 mass-equivalent caps of various heights were numerically analyzed to identify the cap with the best load-carrying capacity. The results suggest that a spherical cap with height-to-base diameter ratio of 0.274 supports the highest buckling load. Such a cap can be applied as an end-closure for cylindrical pressure hulls or as a manhole cover for manned cabins in deep-sea vehicles.

Then, the buckling of spherical caps with four different geometric imperfections was examined, including local inward dimple, increased-radius, force-induced dimple, and linear buckling mode. The influence of imperfection amplitude, meridional

position, and meridional extent on cap buckling was numerically explored and partially validated using experiments. The numerical and experimental data were well consistent. Results indicate that, in the case of small-sized imperfections, the linear buckling mode-shaped imperfection presented a relatively conservative cap buckling prediction compared with those of the other three imperfections. This finding contradicts previous findings that the force-induced dimple imperfection is the most unstable imperfection.

Finally, the buckling of spherical caps fabricated under different conditions of wall-thickness reduction was investigated. The spherical caps were fabricated using photosensitive resin and had a base diameter of 150 mm and height of 41.1 mm; they were subjected to uniform external pressure. In total, 42 spherical caps—6 with full thickness reduction and 36 with partial thickness reduction—were fabricated through rapid prototyping; after their external surface and wall thickness were measured, all caps were tested to collapse to experimentally and numerically evaluate their buckling properties, namely buckling pressures and collapse modes. Moreover, the effects of site, magnitude, and range of the thickness reduction on the buckling properties were evaluated. Herein, the experimental and numerical results are comparatively presented in tables and figures.

6.1 Spherical caps under various heights

This section investigated the buckling of such caps when subjected to uniform external pressure. Six nominally identical laboratory-scale caps were fabricated through cutting, stamping, and welding processes; measured for wall thicknesses and geometrical shapes; and tested to destruction. The buckling loads and corresponding post buckling modes of these caps were obtained, numerically studied, and compared with the experimental data. Furthermore, the buckling of several mass-equivalent caps of various heights was studied numerically to obtain a reasonably optimal topology with the best load-carrying capacity. The obtained optimal shape may have many potential applications in the deep-sea field

6.1.1 Geometry and fabrication

To check the repeatability of experiments, six laboratory-scale caps were fabricated from corresponding hemispherical shells by using a laser-cutting computer numerical control (CNC) system. The hemispherical shells were cut and cold stamped from 304 stainless steel sheets, as described in an earlier study [1]. This material has some advantages such as high ductility which can prevent the caps from disintegrating into small pieces, and it enables the post buckling modes to be determined conveniently. The caps have a nominal base diameter of $d = 146\text{mm}$, nominal uniform wall thickness of $t = 1\text{ mm}$, and nominal height of $h = 37\text{mm}$ (Fig.6-1). To uniform external pressure, p_0 , on the caps in the pressure chamber, each cap was welded on a heavy plate with a nominal diameter of $D = 170\text{ mm}$ and nominal wall thickness of $T = 20\text{ mm}$. During the entire fabrication process, the caps were not heat-treated because of their relatively small thickness-to-radius ratio. Before the hydrostatic test, the wall thicknesses and geometrical shapes of all caps were measured carefully.

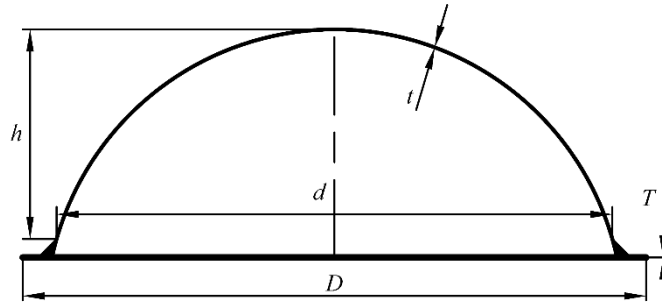


Fig.6-1 Schematic of a spherical cap

6.1.2 Pretest measurement

The wall thicknesses of the fabricated caps were obtained using an accurate ultrasonic thickness measurement gauge. Measurements were performed at 11 equidistant points along a meridian for a total of 12 equally spaced meridians, leading to $10 \times 12 + 1 = 121$ measuring points for each cap. Table 6-1 lists the nominal t_{nom} , minimum t_{min} , maximum t_{max} , and average t_{ave} wall thicknesses of the caps along with their standard deviations, t_{std} . The results show that the actual wall thickness of the fabricated caps varied from 0.978 to 1.077 mm owing to the stamping

process; this is nearly equal to the nominal value of 1 mm. This small variation suggests that the average wall thickness can be used to numerically evaluate the buckling performances of caps.

Table 6-1 Tested wall thickness of fabricated spherical caps (nominal, minimum, maximum, average, and standard deviation) and experimental and numerical buckling loads.

Sample	t_{nom} [mm]	t_{min} [mm]	t_{max} [mm]	t_{ave} [mm]	t_{std} [mm]	p_{test} [MPa]	$p_{numerics}^{e-pp}$ [MPa]	$p_{numerics}^{e-p}$ [MPa]
1	1	0.993	1.053	1.028	0.017	5.280	5.333(1.010)	5.468(1.036)
2	1	0.982	1.063	1.041	0.021	5.553	5.185(0.934)	5.310(0.956)
3	1	0.996	1.072	1.043	0.021	5.255	5.348(1.018)	5.506(1.048)
4	1	0.978	1.076	1.037	0.025	5.580	5.116(0.917)	5.257(0.942)
5	1	0.993	1.071	1.046	0.022	5.356	5.357(1.000)	5.500(1.027)
6	1	0.998	1.077	1.040	0.021	5.647	5.282(0.935)	5.429(0.961)

Notation: $p_{numerics}^{e-pp}$ = numerical buckling loads obtained from elastic-perfectly plastic modelling;
 $p_{numerics}^{e-p}$ = numerical buckling loads obtained from elastic-plastic modelling.

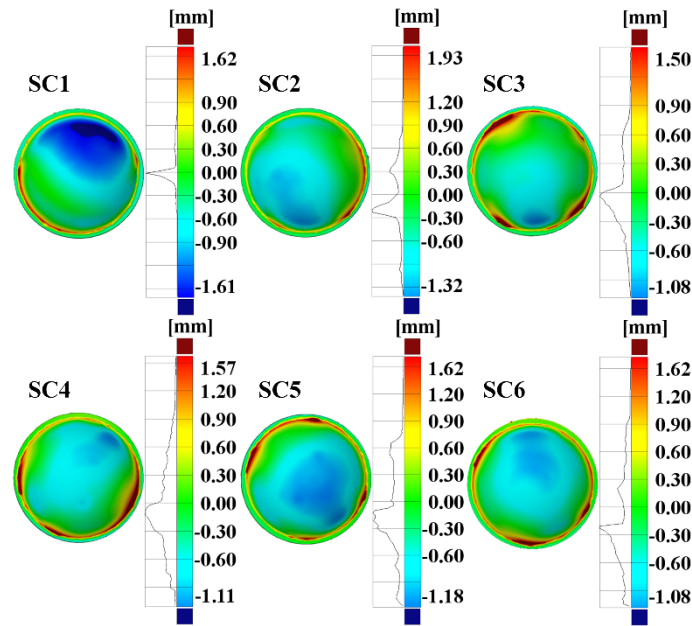


Fig.6-2 Radius deviations of fabricated caps from the perfect geometry

After the thickness measurement, the geometrical shapes of the fabricated caps were obtained using optical scans by using a scanning tool developed by Open Technologies Corporation (accuracy: ≤ 0.02 mm). The outer surface of each fabricated cap assembly, consisting of the cap, weld seam, and heavy plate, was scanned in the form of a point cloud and automatically transformed into a computer-aided design

(CAD) model. This model represents the actual shape of each fabricated cap. It includes deterministic geometric imperfections caused by the stamping, cutting, and welding processes; these were adopted to numerically evaluate the buckling performances of the caps. Fig.6-2 shows the radius deviations of all fabricated cap assemblies from the perfect one; as seen in this figure, the weld seam shows the maximum deviation, and the base of the cap also shows relatively large deviation owing to welding deformation. Nevertheless, the fabricated caps are nominally identical, indicating the reasonable repeatability of the fabrication process.

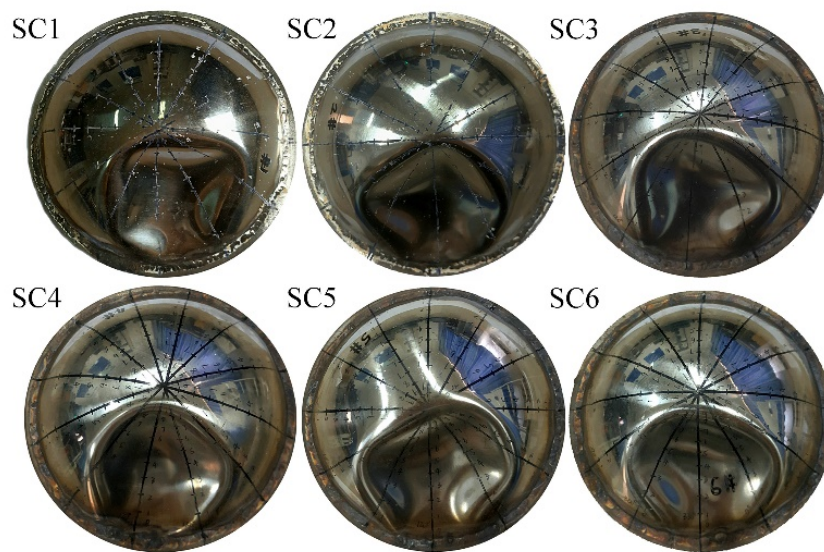


Fig.6-3 Collapse models of the tested caps

6.1.3 Hydrostatic pressure test

After the pretest measurements, the caps were slowly pressured to destruction in a pressure cylindrical chamber at Jiangsu University of Science and Technology. The chamber has an inner diameter of 200 mm, total length of 400 mm, and maximum pressure of 20 MPa, with water as the pressure medium. The pressure inside the chamber was recorded using a pressure transducer; the pressure was applied slowly in increments of ~ 0.1 MPa by using a programmable logic controller (PLC). During the test, each cap assembly could dive into the bottom of chamber, because the buoyancy of the cap assembly is much lower than its self-weight. This dive imposes a concentrated force on the cap if the heavy plate is upward in the water, and this may

affect the buckling to some extent [2]. Details of the force calculation are as reported in an earlier study [3]. To eliminate this effect, each cap assembly was carefully placed into the water with the heavy plate contacting the bottom of the chamber. All caps disintegrated immediately after buckling, which was accompanied by a sudden drop in pressure. Thus, the buckling loads of the tested caps could be obtained easily (seventh column in Table 6-1). After each test, the destroyed cap was removed from the chamber. Fig.6-3 shows the destruction modes (post buckling modes) of the caps.

6.1.4 Parent material properties

As reported in [4] previously, it is very difficult to determine the compression properties of a parent material through compression tests of thin-walled coupons. Therefore, most studies have used the tension properties to evaluate the material properties of externally pressurized revolution shells [1,3-6]. In this work, four flat tensile coupons were fabricated from the same 304 stainless steel sheets used to fabricate the caps. The coupons were designed and tested according to the Chinese Standard GB/T 228.1-2010 [7], which is in line with ISO 6892-1: 2009 [8].

During the test, both a highly accurate extensometer and a load sensor were used to generate stress–strain curves up to $\varepsilon = 50\%$. From these curves, the material properties could be derived using regression analysis and the following equations:

$$\sigma = E\varepsilon, \text{ for } \sigma < \sigma_y \quad (6-1a)$$

$$\sigma = \sigma_y \sqrt[k]{(E\varepsilon / \sigma_y - 1)^n}, \text{ for } \sigma \geq \sigma_y \quad (6-1b)$$

Table 6-2 Parent material properties (304 stainless steel) obtained from flat tension coupons tests.

Coupon	E [GPa]	σ_y [MPa]	μ	n	k
1	151.440	334.730	0.284	0.054	4.221
2	163.500	335.180	0.300	0.088	5.678
3	161.700	337.230	0.274	0.087	5.581
4	160.190	334.490	0.307	0.072	5.350
average	159.208	335.408	0.291	0.075	5.208

Notation: E = Young modulus; σ_{yp} = Yield stress; μ = Poisson ratio; n and k = strain hardening parameter.

Table 6-2 lists obtained Young modulus, E ; yield strength, σ_y ; and strain hardening parameters, n and k ; as well as their average values. Meanwhile, coupons were strain-gauged in the transverse and longitudinal directions to obtain Poisson ratio, μ (see Table 6-2), in the linear range. The average material properties were used to numerically evaluate the buckling of caps.

6.1.5 Experimental analysis of spherical caps

Table 6-1 and Fig.6-3 show the buckling loads and destruction modes of the tested caps, respectively. As seen in the seventh column of Table 6-1, the buckling load, p_{test} , of the spherical caps ranges from 5.255 to 5.647 MPa. This variation may result from imperfect shapes (Fig.6-2), inhomogeneous wall thickness (first six columns of Table 6-1), and material hardening during the stamping and welding processes as well as from variations in the wall thickness and material properties (Table 6-2) of the 304 stainless steel sheets. Nevertheless, this slight change indicates the reasonable repeatability of the experiments.

Per Zoelly's formula [9], the analytical buckling load of a complete spherical shell is

$$P_{analytical} = 2E(t/r)^2 / \sqrt{3(1-\mu^2)} \quad (6-2)$$

where r is the median radius. This buckling load of a cap with nominal dimensions is obtained as 23.723 MPa from Eq. (6-2); this is much higher than the experimental results owing to the initial deviations from a perfect geometry and to constraint difference between a complete spherical shell and a spherical cap. Therefore, NASA advocated a knock-down factor, KDF, multiplied by the analytical buckling load of a complete spherical shell to evaluate the buckling load of a spherical cap [10], as follows:

$$P_{cap} = P_{analytical} (0.14 + 3.2 / \lambda^2) \quad (6-3a)$$

as plotted in Fig.6-4. The geometry parameter, λ , is given by

$$\lambda = [12(1-\mu^2)]^{1/4} (r/t)^{1/2} 2 \sin(\theta/2) \quad (6-3b)$$

where θ is the semivertex angle. This equation is derived from a lower bound for a

large amount of experimental data on clamped shells. Applying Eq. (6-3), the obtained buckling load of the cap is 3.628 MPa, which is even lower than the experimental results. Using NASA's lower bound approach has been suggested to lead to an overconservative evaluation. This finding extends previous research results of cylindrical shells that suggest that NASA's classical lower bound approach must be updated [2].

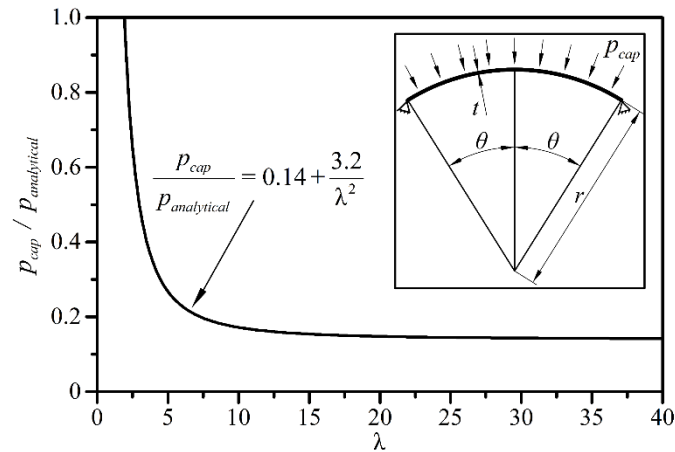


Fig.6-4 Recommended design buckling pressure of spherical caps

As seen in Fig.6-3, the destruction modes of six tested caps are similar and take the form of a local dimple near the base, confirming the high ductility of the parent material. This destruction mode is typical for revolution shells with a positive Gaussian curvature under uniform external pressure [11]. The destruction location may be associated with the clamped boundary condition imposed by the weld seam and heavy plate at the base, which is identical to the findings of previous studies on hemispherical, torispherical, ellipsoidal, and egg-shaped domes [3,5,12]. In addition, the similar destruction mode indicates the high repeatability of the experiments.

6.1.6 Numerical analysis of spherical caps

To further examine the buckling of spherical caps, the FEM was applied to the six tested specimens in line with CCS 2013 [13] and EN 1993-1-6 (2007) [14]. This was done using the modified Riks method available in Abaqus code, which involves initial deterministic shape imperfections and material and geometry nonlinearities. This concept is well aligned with NASA's ongoing research [15,16].

For each case, both the heavy plate and the corresponding weld seam were removed from the scanned CAD model. The mesh was generated freely and uniformly on each scanned cap using the general FE preprocessor ANSA. In this way, the initial deterministic shape imperfections of the fabricated caps can be automatically included in the numerical model. The fully integrated quadrilateral shell element S4, along with a few triangular S3 shell elements, was mainly chosen to prevent hourglassing. Mesh convergence examination was performed to determine the number of elements: 15,246 S4 and 51 S3 elements for SC1, 15,389 S4 and 53 S3 elements for SC2, 15,967 S4 and 57 S3 elements for SC3, 14,834 S4 and 56 S3 elements for SC4, 15,671 S4 and 52 S3 elements for SC5, and 14,957 S4 and 55 S3 elements for SC6.

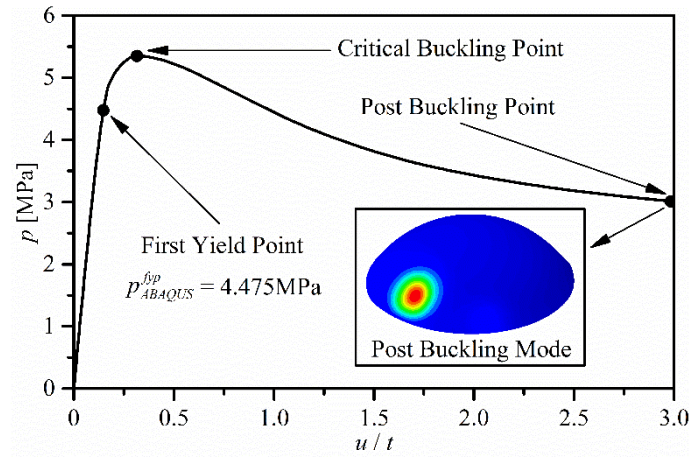


Fig.6-5 Equilibrium path of the SC1 cap along with post buckling mode

The base of each cap was fully constrained to simulate the clamped boundary condition imposed by the weld seam and the heavy plate. In practice, the junction between the cap and the pressure vessel is usually reinforced using a heavy ring [17]; this justifies the use of this clamped boundary. A unit pressure, $p_0 = 1$ MPa, was uniformly applied on the outer surface of each cap. Hence, the arc length value obtained from the numerical analysis directly corresponds to the buckling load of the cap. The elastic-plastic model following Eq.(6-1) was used in the numerical model along with the elastic-perfectly plastic model assuming that the stress remains constant after the yield point. The material properties were defined as the average values obtained from the flat coupon tests listed in the last row of Table 6-2. In

addition, the wall thickness of each cap was assumed to be the average value of measurements listed in the fifth column of Table 6-1. Table 6-1 and Fig.6-5 show the FEM results.

The numerical buckling loads, $p_{numerics}^{e-p}$, obtained from elastic–plastic modeling are listed in the last column in Table 6-1; they range from 5.257 to 5.506 MPa, which is similar to the experimental values. The ratio of the numerical load, $p_{numerics}^{e-p}$, to the experimental load, p_{test} , for each cap is listed in parentheses in the same column; the ratios range from 0.942 to 1.048. These relatively small differences may result from assumptions of the average thickness value and the use of the parent’s material properties. Nevertheless, a reasonable agreement is obtained between the numerical and the experimental results. These findings confirm that the realistic buckling resistance of a stability-endangered shell structure can be obtained through geometric and material nonlinear analysis with imperfection accounted for [18].

Meanwhile, the numerical buckling loads, $p_{numerics}^{e-pp}$, obtained from elastic–perfectly plastic modeling are listed in the second-last column in Table 6-1, along with ratio of the numerical load, $p_{numerics}^{e-pp}$, to the experimental load, p_{test} , in the parentheses. The numerical and experimental results show reasonable agreement, although the elastic–perfectly plastic values are marginally lower than the elastic–plastic ones. These findings suggest that elastic–perfectly plastic modeling can lead to relatively conservative results, and it can be used to evaluate the buckling of revolution shells under external pressure.

In addition, for either elastic–plastic analysis or elastic–perfectly plastic analysis, the equilibrium paths and critical and post buckling modes of all caps are similar, which are typical for revolution shells subjected to external pressure [11,19]. For example, the equilibrium path of the SC1 cap in Fig.6-5 as obtained from elastic–perfectly plastic analysis shows unstable performance. The path is plotted as the applied pressure, p , versus the maximum deflection, u , divided by the nominal wall thickness, $t = 1$ mm. The applied pressure initially increases with the deflection; then,

after a critical point corresponding to the buckling, it decreases significantly and transitions to the post buckling stage.

Furthermore, the cap tends to yield before buckling, suggesting that the cap may buckle in an elastic–plastic regime. This is because the critical buckling load is greater than the first yield load marked in the path, which is obtained in accordance with the mechanics of elasticity by dividing the yield stress of the material by the maximum Von Mises stress given by linear analysis for external pressure of 1 MPa. Similar phenomena are seen in other cases. In addition, the post buckling mode at the end of the path has the form of a local dimple, which is identical to the experimental destruction mode (Fig.6-3). Similar observations can be made in other caps.

6.1.7 Buckling of spherical caps of various heights

To study the effect of the height, h , on buckling, a series of mass-equivalent spherical caps of various heights are investigated. These caps have the same mass, $m = 168.533\text{g}$, base diameter, $d = 146\text{ mm}$, and material properties as the caps considered in Table 6-2. The cap height is varied from 10 to 70 mm in 5-mm increments, where the cap with $h = 70\text{ mm}$ corresponds to a hemispherical cap. The wall thickness of each mass-equivalent spherical cap is assumed to be uniform: 1.246 mm for $h = 10\text{ mm}$, 1.218 mm for $h = 15\text{ mm}$, 1.181 mm for $h = 20\text{ mm}$, 1.136 mm for $h = 25\text{ mm}$, 1.086 mm for $h = 30\text{ mm}$, 1.032 mm for $h = 35\text{ mm}$, 0.976 mm for $h = 40\text{ mm}$, 0.920 mm for $h = 45\text{ mm}$, 0.864 mm for $h = 50\text{ mm}$, 0.810 mm for $h = 55\text{ mm}$, 0.758 mm for $h = 60\text{ mm}$, 0.708 mm for $h = 65\text{ mm}$, and 0.661 mm for $h = 70\text{ mm}$.

For each cap, both linear elastic eigenvalue analysis and nonlinear Riks analysis are conducted using the FEM available in ABAQUS code. In the linear analysis, the element type and load and boundary conditions are the same as those in Section 6.1.6, except that the material is modeled as an elastic one following Eq (6-1a). The subspace iteration method is used to solve the first eigenmode of each cap and the corresponding eigenvalue that directly corresponds to the linear buckling load. In nonlinear Riks analysis, the element type, load and boundary conditions, and elastic-perfectly plastic material modeling are the same as those in Section 6.1.6,

except that the initial geometric imperfections are assumed to be the first eigenmode obtained from the linear elastic eigenvalue analysis. The small imperfection size is assumed and set to be 0, 0.05, 0.10, 0.15, 0.20, and 0.25 mm, respectively, which is often required during fabrication of the pressure hulls in subsea engineering [20,21]. According to previous studies on the buckling of externally pressurized caps with different imperfection forms [3,22], an eigenmode imperfection can result in a relatively conservative evaluation in the case of small size, although the sensitivity of buckling loads to this imperfection may diminish for a large imperfection size. In both analyses, mesh convergence examination is also performed, resulting in approximately 15,000 elements for each cap.

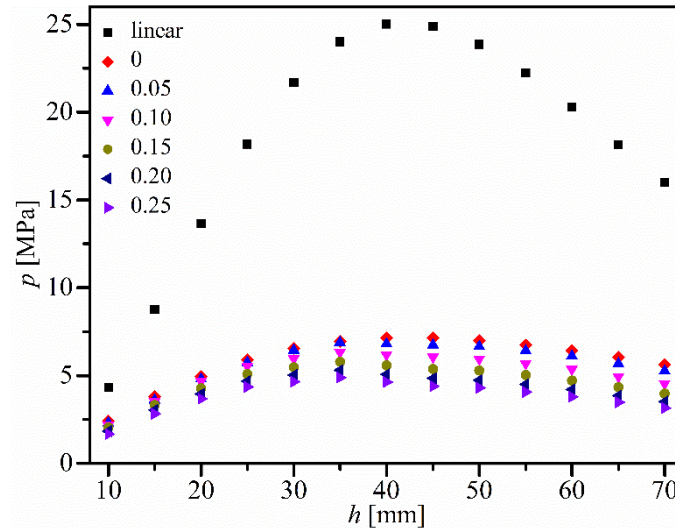


Fig.6-6 Buckling loads of mass-equivalent spherical caps of various heights and several imperfection sizes, along with their knock down factors

The linear buckling loads of the perfect geometry versus the cap height are plotted in Fig.6-6 along with the nonlinear buckling loads with several imperfection sizes. The linear buckling load initially increases greatly with height; after a critical point ($h \approx 40$ mm), it decreases significantly. Similar trends were found in the nonlinear analysis, except that these increasing and decreasing rates tend to slow down owing to the effect of geometrical and material nonlinearities on buckling. These findings indicate that the cap with $h/d \approx 0.274$ has the best load-carrying capacity among the series of mass-equivalent spherical caps. This cap has the highest buckling

load-to-mass ratio, making it suitable for application as an end-closure for cylindrical pressure hulls or manhole covers of manned cabins in deep-sea vehicles. For these vehicles, light weight and high security are two important design constraints that concern designers. In addition, both nonlinearities lead to a significant decrease in the buckling load of each cap. Furthermore, the larger the imperfection size, the lower is the nonlinear buckling load.

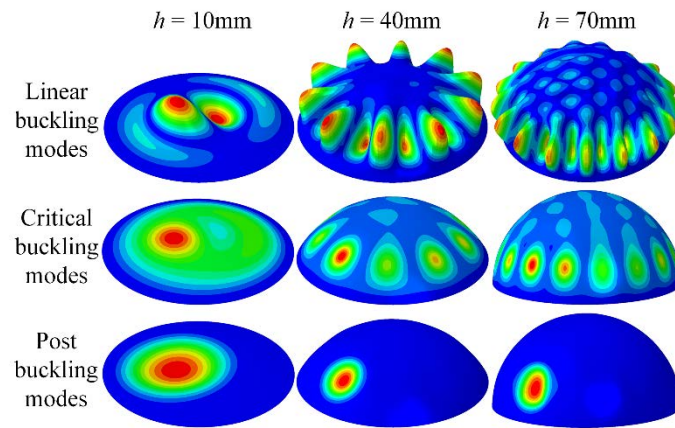


Fig.6-7 Linear, critical, and post buckling modes of 10mm, 40mm, and 70mm heights

The equilibrium paths and linear, critical, and post buckling modes of mass-equivalent spherical caps are similar; this is typical of revolution shells subjected to external pressure [1,3,19,23]. All equilibrium paths of geometrically imperfect caps are unstable, which is identical to Fig.6-5 in Section 6.1.6. The linear buckling mode of geometrically perfect caps takes the form of one half circumferential wave and several meridional waves (n). The number of meridional waves increases rapidly with the height owing to the increasing radius and decreasing wall thickness. Fig.6-7 shows some typical results; the number of meridional waves is $n = 1$ for the cap with $h = 10\text{ mm}$, $n = 10$ for the cap with $h = 40\text{ mm}$, and $n = 17$ for the cap with $h = 70\text{ mm}$. The critical buckling modes of geometrically imperfect caps are identical to those of the linear buckling modes owing to the assumption of initial eigenmode imperfections. However, all post buckling modes resemble a local dimple; this is consistent with the experimental results, although the configurations of their imperfections are completely different. It is indicated that

imperfect caps may destruct in the form of a local dimple, which is independent of their imperfection shape.

6.2 Buckling of spherical caps under various imperfections

This section used the obtained optimal spherical cap as the basic cap model [24], various imperfections, including the LIDI, IRI, FIDI, and LBMI, were implemented in this study to examine cap buckling performance, and the findings were partially validated using experiments. Section 6.2.1 introduces the geometry and proposes finite element models of caps with the four imperfections. Section 6.2.2 explores the effects of the four imperfections on buckling, and material tests, wall thickness measurements, 3D scanning tests, and hydrostatic pressure tests of caps with partial imperfections are presented. The tested caps were numerically evaluated. This paper presents the novel use of a rapid prototyping technique for investigating the buckling of imperfect caps. Moreover, the study results validated LBMI as a more unstable imperfection than FIDI in case of small-sized imperfections.

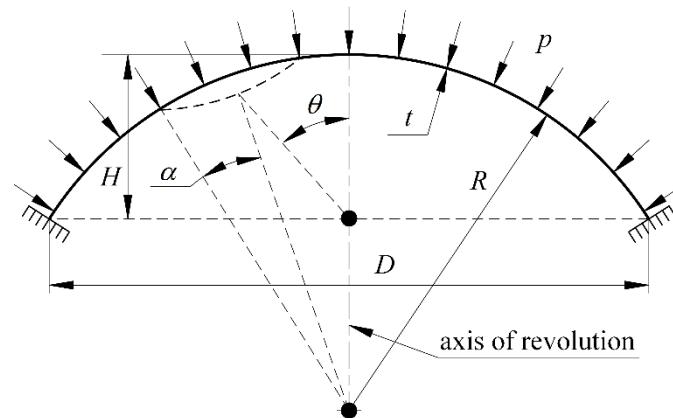


Fig.6-8 Geometry of a spherical cap

6.2.1 Geometry and imperfections

The geometry of a spherical cap under external pressure, p , is illustrated in Fig.6-8, in which t is the uniform wall thickness, R is the radius, H is the height of the spherical cap, α is the angle corresponding to the meridional extent of imperfection, and θ is the meridional position of the imperfect centre axis. Details of the profile of caps with the four types imperfections are described below.

First, the shape of the LIDI, represented in Fig.6-9a, is in accordance with descriptions by Blachut and Galletly [12,22]. This imperfection is widely adopted to study the imperfection sensitivity of hemispherical domes. The radial deviation (w) of the imperfection is presumed as

$$w = \delta_0 (1 - x^2)^3 \quad (6-4)$$

where δ_0 is the amplitude of the imperfection at the apex, $x = S/S_{imp}$, and S_{imp} is the meridional extent of imperfection, S is the varied meridional extent within S_{imp} .

Second, the shape of the IRI, illustrated in Fig.6-9b, is based on the work of Koga and Hoff [25]. As shown in Eq. (6-5b), the semi angle of imperfection (φ) can be calculated using the known nominal radius of R , the preset amplitude of imperfection (δ_0), and the given angle corresponding to the meridional extent of imperfection (α). The R_{imp} changes with the R , α , and φ , as illustrated in Eq. (6-5b), and the distance of the circles' centres for the portion of spherical caps (Δ) may be further derived, as in Eq. (6-5c).

$$\varphi = 2 \arctan((R(1 - \cos \alpha) - \delta_0) / R \sin \alpha) \quad (6-5a)$$

$$R_{imp} = R \sin \alpha / \sin \varphi \quad (6-5b)$$

$$\Delta = \sqrt{R_{imp}^2 - R^2 \sin^2 \alpha} - R \cos \alpha \quad (6-5c)$$

Third, the shape of the FIDI is characterised by the amplitude of the imperfection δ_0 at the pole of the spherical cap. The amplitude of the imperfection, in turn, depends on the axially concentrated force, as presented in Fig.6-9c. FIDIs have been used to evaluate the load-carrying capacity of cylindrical shells and hemispherical domes [2,22,26,27]. Two approaches are used to simulate FIDIs: *i*) evaluation of the spring-back after the deformation, and *ii*) application of a fixed concentrated force at one point, which was adopted in this study.

Finally, the LBMI (Fig.6-9d) in this chapter is identical to that of CCS2013 [13], and can be obtained as follows: the first eigenmode for the spherical structure is calculated using linear elastic bifurcation analysis (LBA). The eigenmode is then multiplied by a scaling factor; finally, the eigenmode is applied to a perfect model by

switching the original nodal positions, and conducting finite element analysis. The scaling factor is the amplitude of imperfection.

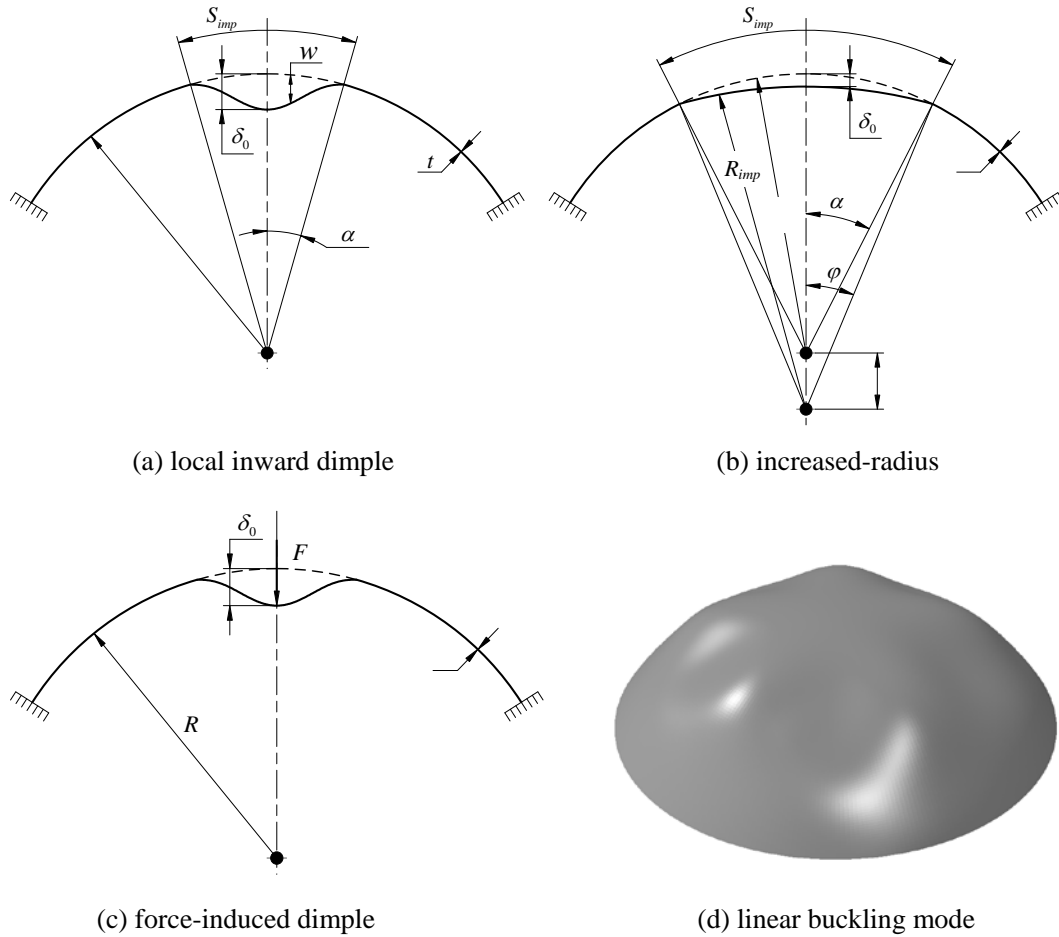


Fig.6-9 Geometries of caps with four imperfections

6.2.2 Finite element model

All spherical cap models are fabricated with the same nominal base diameter (D) of 150 mm, uniform wall thickness (t) of 2 mm, and height (H) of 41.1 mm ($H/D = 0.274$) [24]. The angle of the meridional position (θ) varied from $0^\circ - 70^\circ$ (every 10°) for the three imperfections (LIDI, IRI, and FIDI). For all imperfections, amplitudes of imperfection (δ_0) were set at 0.5 and 1 mm.

To analyse the collapse loads of spherical caps with different imperfections, a nonlinear calculation based on Riks algorithm in the Abaqus code was carried out, following the ENV 993-1-6 (2007) standard [14]. The elements of each FE model were generated freely on the geometric model including the axisymmetric or

off-axisymmetric imperfections. To accurately simulate the shape of imperfection, the mesh density was significantly increased on the imperfection area. Because of the existence of an imperfection, shell elements S4 was mainly chosen with a few S3 shell elements. Mesh convergence studies were performed to establish approximately 20 000 elements for each model [28]. The properties of the fabrication material (SOMOS 8000) were used to compute buckling loads. Further details about the material are presented in Section 6.2.4.1. In practical engineering fields, spherical caps and main cylinders are connected with heavy rings [5,29] to fully fix the bottom of the cap (Fig.6-10). This boundary condition has been used extensively to analyse dome buckling [3,24,30-35].

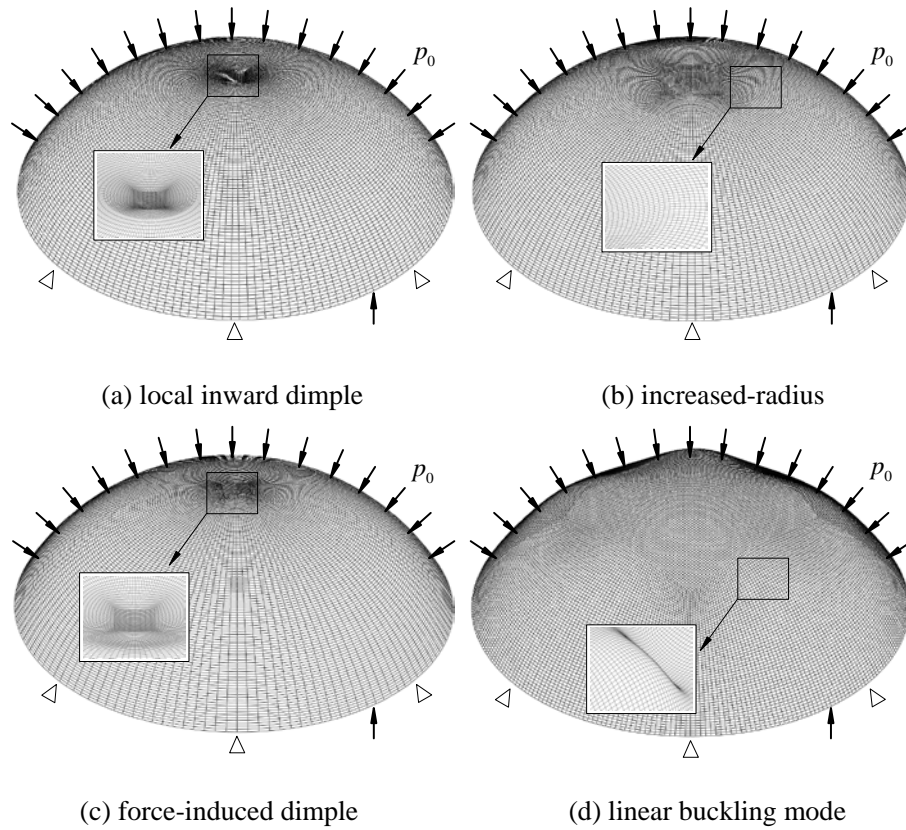


Fig.6-10 The FE models with four different imperfections

In all analyses in this study, a uniform external pressure ($p_0 = 1$ MPa) was imposed on the outer surface of each spherical cap. The LIDI and IRI were directly mapped to FE models in Abaqus with the given δ_0 and S_{imp} . The FIDI implementation in the finite element model followed a two-step process: first, a concentrated normal load

was applied to one point on the spherical cap surface; second, a uniform external pressure was applied to the surface while the concentrated force remained constant [2,22]. The LBMI was obtained by introducing a scaling factor into the first eigenmode shape, which was acquired from LBA [13]. The calculation parameters were defined as follows: the initial increment in arc length along the static equilibrium path in the scaled load-displacement space was 0.001; the total arc length scale factor associated with this step was 300; the minimum arc length increment was 1E-06; and the maximum arc length increment was 0.01.

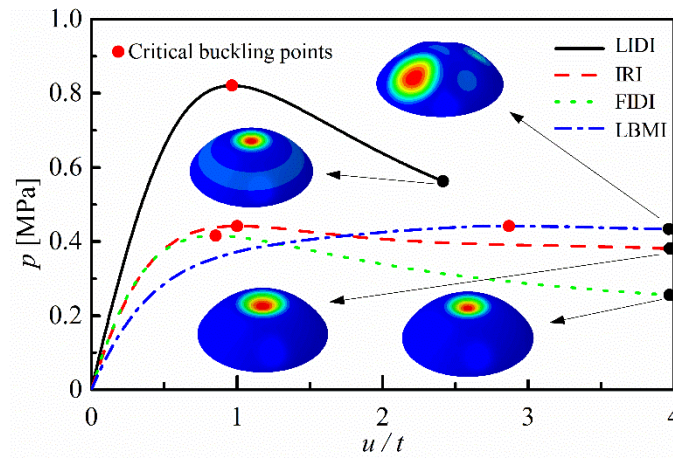


Fig.6-11 Equilibrium paths of four imperfect spherical caps and their post buckling modes

6.2.3 Numerical analysis of imperfect spherical caps

All caps exhibited similarly unstable post buckling modes, as observed from the equilibrium paths of the imperfect spherical caps in Fig.6-11 (where the deflection of imperfection, $\delta_0 = 1$ mm, is recorded at the apex, $\theta = 0^\circ$). These equilibrium paths plotted the relationship between load (p) and maximum deflection (u) divided by nominal wall thickness ($t = 2$ mm). All equilibrium paths of the remaining spherical caps with different imperfections were similar. As shown in Fig.6-11, for the cap with an LIDI, the load first increased dramatically, and then after a peak value, the buckling load, the load decreased with an increase in the maximum deflection (u). This example demonstrates the unstable characteristics of the imperfect caps. This character is typical of shells of revolution [23,36,37]. Additionally, all post buckling modes of spherical caps with different imperfections were in the form of a single local

dimple, which is a common phenomenon for domes [3,24].

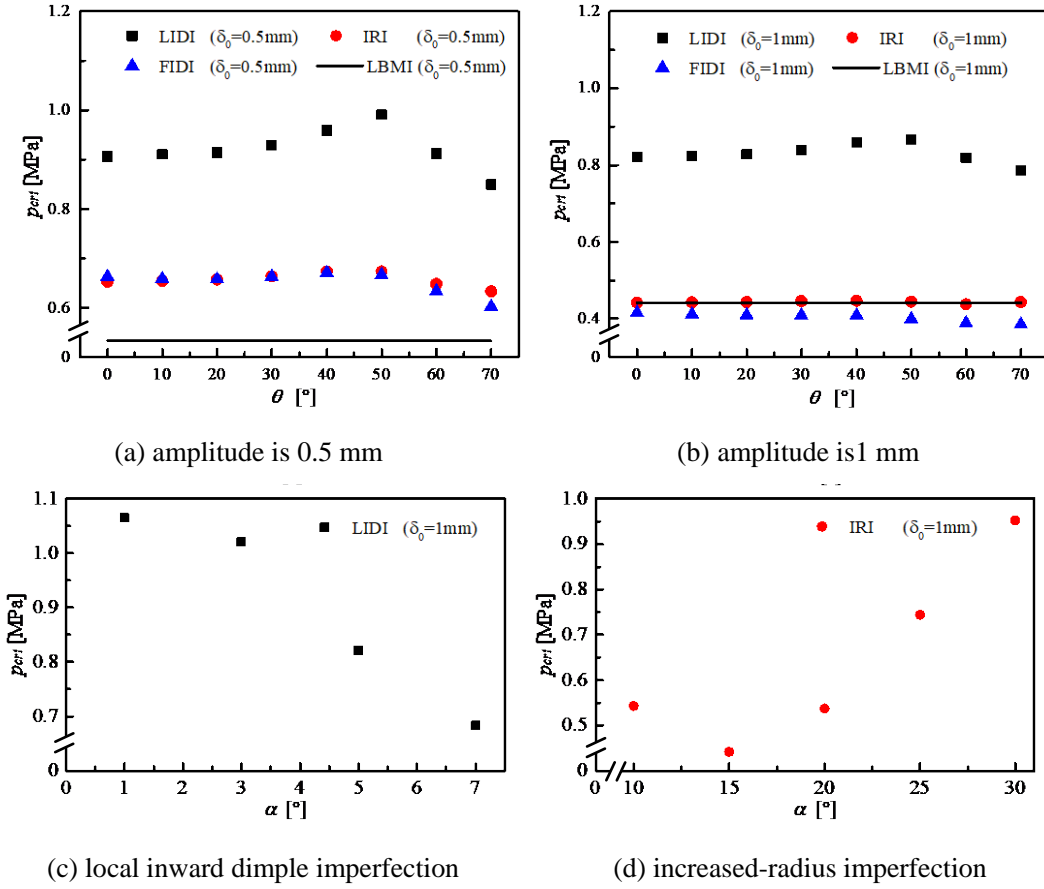


Fig.6-12 Critical buckling loads (p_{cri}) for the imperfections under various conditions

Critical buckling load (p_{cri}) varied according to imperfection form, meridional position (θ), and the meridional extent (α), as well as the amplitude (δ_0) of imperfection. As presented in Fig.6-12a, in the case in which $\delta_0 = 0.5$ mm, the buckling loads first slightly increased and then decreased with increasing θ for the LIDI, IRI, and FIDI. The mean buckling load values for the LIDI, IRI, and FIDI were 0.9240, 0.6571, and 0.6519 MPa, respectively. The buckling load of the spherical cap with an LBMI was 0.5327 MPa, which is significantly lower than the buckling loads of spherical caps with other imperfections (LIDI, IRI, and FIDI). In addition, as indicated in Fig.6-12b, the buckling loads of spherical caps with $\delta_0 = 1$ mm exhibited the same trend as those of spherical caps with $\delta_0 = 0.5$ mm. Specifically, in spherical caps with $\delta_0 = 1$ mm, the mean values of buckling loads for LIDIs, IRIs, and FIDIs were 0.8369, 0.4431, and 0.4034 MPa, respectively. The buckling load for

the LBMI was 0.4418 MPa, which is almost identical with the buckling load values of spherical caps with IRIs and FIDIs, and much lower than that for LIDIs.

Fig.6-12c and 6-12d illustrate the trend of buckling loads with the change of the meridional extent of imperfection (α) for LIDIs and IRIs. As demonstrated in Fig.6-12c, in the case where $\delta_0 = 1$ mm, the buckling loads of spherical caps with LIDIs decreased as α increased from $1^\circ - 7^\circ$ (every 2°). The buckling loads of spherical caps with IRIs first decreased and then increased (when $\alpha=15^\circ$) as α increased between 10° and 30° (every 5°), as indicated in Fig.6-12d. A possible explanation for this phenomenon is that the spherical caps with IRIs became closer to Cassini oval shells as α increased [37], leading to an increase of buckling loads. The range of α was determined by the shape of the imperfection; when $\delta_0 = 1$ mm, 8.6° was the maximum α for LIDIs, but the minimum α for IRIs.

Generally, when $\delta_0 = 1$ mm, the buckling load for caps with FIDIs was slightly smaller than those of caps with the other three imperfections, which is in accordance with the finding that the FIDI is the most unstable imperfection [22,27,38]. However, in this study, the buckling load for caps with LBMI (0.5327 MPa) was much less than that for caps with FIDIs (0.6519 MPa) when $\delta_0 = 0.5$ mm. This divergence in findings may have been due to the size of the imperfections. Moreover, the magnitude of buckling load for caps with LBMI was nearly equal to that of caps with FIDIs when $\delta_0 = 1$ mm, which indicates that LBMI may be more suitable for the buckling prediction of spherical caps with regard to small imperfections. Although, the sensitivity of buckling loads for LBMI diminished for larger amplitudes of imperfection. Because underwater pressurised hulls usually exhibit small imperfection amplitudes [20], numerous guidelines for submersibles recommend the use of LBMI to assess the load capacity of hulls [13].

6.2.4 Experimentation of imperfect spherical caps

Six imperfect spherical caps for the experimental assessment of buckling performance were fabricated. Material tests, wall thickness measurements, 3D scanning tests, and hydrostatic pressure tests were performed.

The six caps, comprising three laboratory scale models with LIDIs (L-1, L-2, L-3)

and three laboratory scale models with IRIs (I-1, I-2, I-3), were fabricated with widely used SOMOS 8000 using stereo lithography apparatus (SLA). The nominal base diameter (D), uniform wall thickness (t) and height (H) of the tested caps were 150, 2, and 41.1 mm, respectively, and were the same as the corresponding values computed in Section 6.2.3. The imperfections in the models were set at the apex ($\theta = 0^\circ$) and the amplitude of the imperfection, $\delta_0 = 1$ mm. The meridional extent of imperfections (α) with LIDIs and IRIs were 5° and 15° , respectively.

To obtain the properties of the parent material, five samples were fabricated using the same low viscosity photosensitive resin (SOMOS 8000) used to fabricate the caps. The tensile properties of the samples were examined using a universal testing machine (MZ-5001D1) at Jiangsu University of Science and Technology. Various properties of the parent material, such as Young modulus (E) and Poisson ratio (μ), obtained from tensile tests are listed in Table 6-3, and the average values of the material properties were applied to numerical evaluations of cap buckling performance.

Table 6-3 Properties of parent material (SOMOS 8000) obtained from flat tensile coupon tests.

Coupon	E [MPa]	μ
1	2063.800	0.303
2	2174.600	0.336
3	2076.600	0.323
4	2199.300	0.339
5	2100.300	0.341
average	2122.920	0.328

Notation: E = Young modulus; μ = Poisson ratio.

The thicknesses of all fabricated caps were measured using a thickness gauge. To obtain the thickness of each cap, 73 points were measured. These points comprised nine equidistant points on each of the eight equidistant meridians, as well as one point at the apex (Fig.6-13). The wall thicknesses measurements comprised nominal t_{nom} , minimum t_{min} , maximum t_{max} , average t_{ave} , and correlative standard deviations, t_{std} . The results are listed in Table 6-4. The wall thickness of the caps varied from 1.824 mm to 2.025 mm, and the average value was 1.927 mm, which was close to the nominal value of 2 mm. This finding indicates that the average wall thickness can be

adopted to numerically compute the buckling performance of the spherical caps fabricated using SLA.

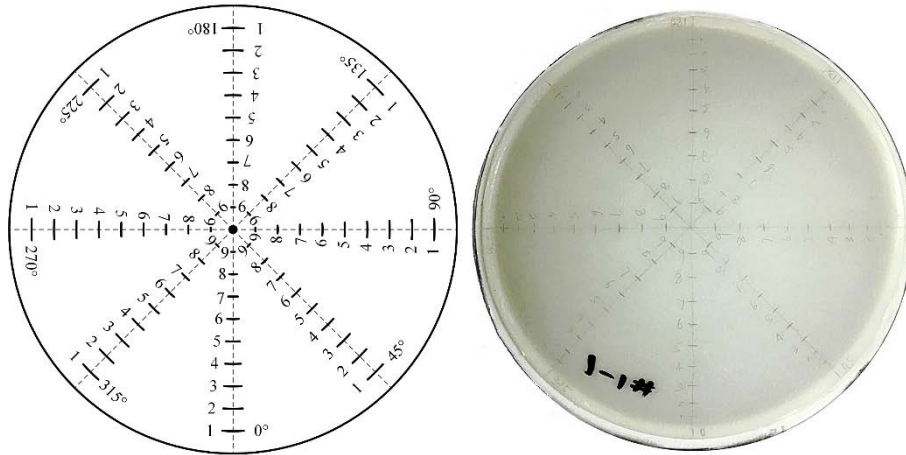


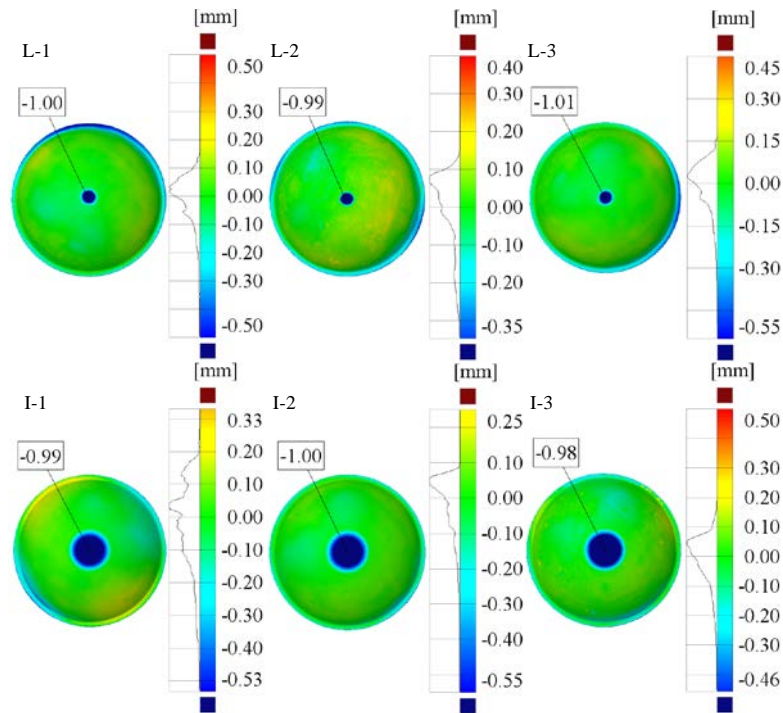
Fig.6-13 Distribution of points for measuring wall thickness; a sample of an experimental spherical cap (I-1) is displayed on the right-hand side

Table 6-4 Tested wall thicknesses of fabricated spherical caps (nominal, minimum, maximum, average, and standard deviation) as well as experimental and numerical buckling loads.

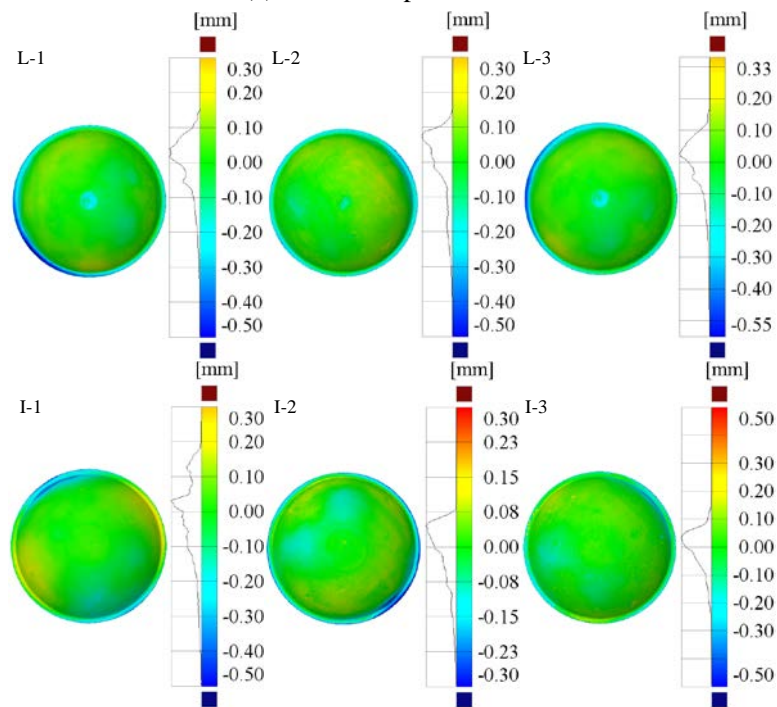
Sample	t_{nom} [mm]	t_{min} [mm]	t_{max} [mm]	t_{ave} [mm]	t_{std} [mm]	p_{coll} [MPa]	$p_{numerics}$ [MPa]
L-1	2	1.824	2.022	1.934	0.019	0.7048	0.6766(0.9600)
L-2	2	1.845	2.025	1.932	0.017	0.6976	0.7149(1.0247)
L-3	2	1.870	1.990	1.919	0.013	0.6854	0.6648(0.9699)
I-1	2	1.842	2.002	1.918	0.013	0.3735	0.4156(1.1128)
I-2	2	1.835	2.024	1.929	0.017	0.3904	0.4113(1.0535)
I-3	2	1.842	2.004	1.929	0.014	0.3963	0.4140(1.0449)

Before the hydrostatic test, the outer surface of each fabricated cap was scanned in the form of a point cloud using Open Technologies Corporation (accuracy: ≤ 0.02 mm) to acquire the geometric shapes. The point cloud was then automatically translated into a computer-aided design (CAD) model for analysis. The CAD models of caps with LIDIs (L-1, L-2, L-3) and IRIs (I-1, I-2, I-3) were compared with ideal FE models without (Fig.6-14a) and with (Fig.6-14b) corresponding imperfections. The radius deviations of the shapes for two different models are displayed in Fig.6-14. As illustrated in Fig.6-14a, the radius deviations between the fabricated and perfect caps were approximately -1.0 mm at the geometric centres. However, the radius deviations between the fabricated and corresponding imperfect caps were approximately 0 mm at

the geometric centres (Fig.6-14b). The caps with the same imperfection exhibited similar radius deviations, indicating repeatability. This finding suggests that the fabricated spherical caps were similar to the designed models.



(a) without imperfections



(b) with axisymmetric imperfections

Fig.6-14 Comparisons of radius deviations between fabricated caps and perfectly geometrical counterparts

After the pretests, a hydrostatic test rig, fabricated for the experiments, was used to characterise the collapse loads of the caps. A schematic of the rig is presented in Fig.6-15. The test rig involved a pressurised cylindrical chamber with an inner diameter of 200 mm, full length of 1000 mm, and maximum pressure of 20 MPa. Water was used as the pressure medium in the tests. The force of gravity was required to exceed the cap's buoyancy to ensure that the cap would sink to the bottom of the chamber; therefore, a plate of 304 stainless steel with a diameter of 170 mm and thickness of 4 mm was glued to the bottom of the cap using room temperature vulcanising silicone rubber. The cap was then placed in a room-temperature environment for 24 h to enhance the bonding effect. Finally, the six treated caps were sequentially immersed into the test rig. The dive of a cap may create a concentrated force, which may, in turn, influence buckling performance. Hence, the heavy plate affixed to the experimental cap was required to make contact with the bottom of the chamber to prevent an external force from affecting the results [24]. The pressure inside the vessel was recorded using a pressure sensor and was controlled with a hand-operated pump. All caps tended to collapse suddenly when pressure was substantially decreased. Fig.6-16 illustrates the curves of the relationships between the test pressure, p_{test} , and time, t , for the six tested caps. All curves first increased to a peak value and then decreased dramatically. Therefore, the pressure at which the caps collapsed was readily determined. The test results are presented in Fig.6-17 and indicate reasonable repeatability.

6.2.4.1 Experimental analysis of imperfect spherical caps

The collapse pressures p_{coll} , from the hydrostatic tests are listed in the seventh column of Table 6-4. The collapse loads (p_{coll}) of the caps with LIDIs varied between 0.6854 and 0.7048 MPa. The variations in wall thickness and shape may have caused this range in collapse loads (Fig.6-14). The p_{coll} of caps with IRIs varied from 0.3735 to 0.3963 MPa, with a small deviation but adequate repeatability. The collapse loads were slightly lower than those obtained for the ideal FE models with LIDIs (0.8207 MPa) and IRIs (0.4418 MPa); this difference may be due to small

initial geometric imperfections formed during SLA, and to variations in wall thickness. Photographs of the samples after collapse are displayed in Fig.6-17. The collapse-related damage occurred at the top centre of the caps, in line with the theoretical calculations (Fig.6-11), and collapse damage comprised local fractures due to the brittleness of the parent material. The experimental collapse loads and damage locations were consistent with those determined using numerical analyses in Section 6.2.3.

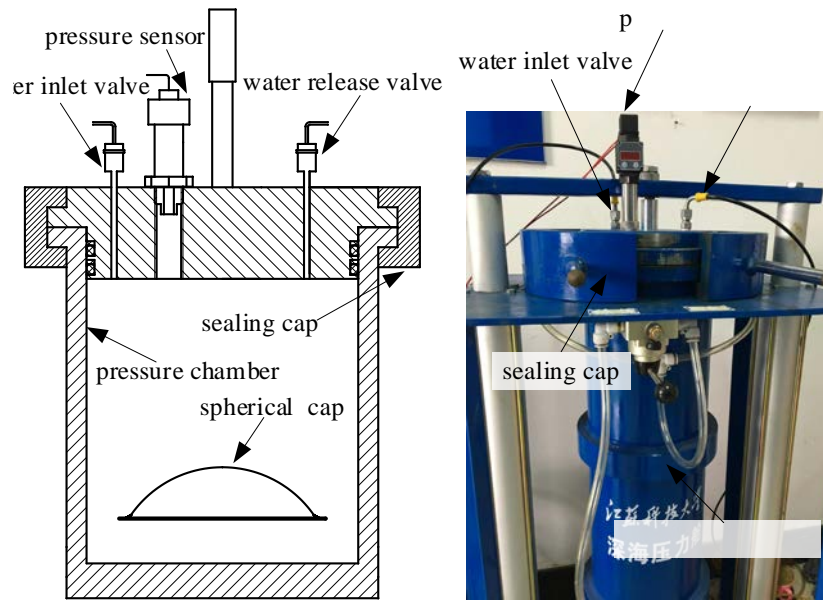


Fig.6-15 Schematic and picture of hydrostatic test rig

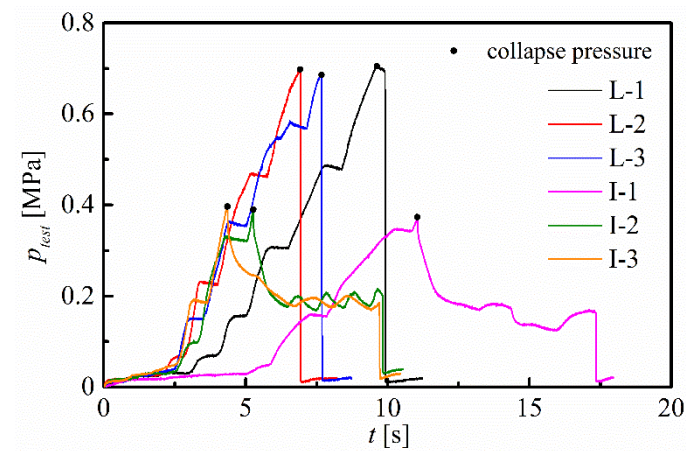


Fig.6-16 Curves of the relationships between experimental pressure, p_{test} , and time, t , for six tested caps

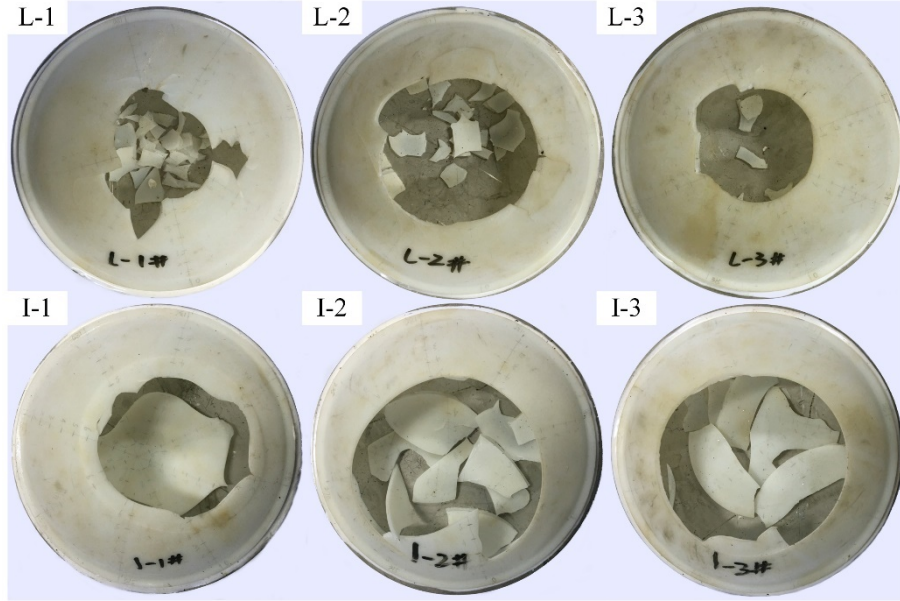


Fig.6-17 Imperfect spherical caps after collapse

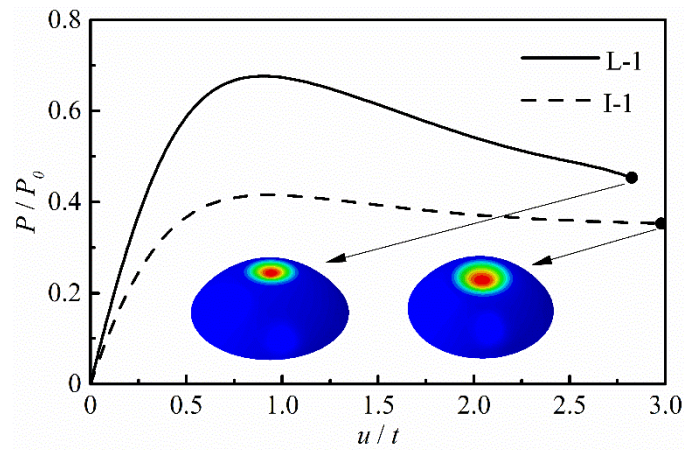


Fig.6-18 Equilibrium paths of the tested spherical caps (L-1 and I-1)

6.2.4.2 Numerical analysis of imperfect spherical caps

To evaluate the buckling performance of the spherical caps, nonlinear numerical computations of all scanned spherical caps were performed using the FE code in Abaqus. The finite elements of each cap model were generated freely and uniformly, including the deterministic initial geometrical imperfections and small imperfections caused by fabrication. The shell element S4, as well as a few shell elements of S3, were selected to prevent hourglassing. The respective numbers of shell elements S4 and S3 were 22 177 and 25 for the L-1 cap, 22 918 and 49 for the L-2 cap, 22 362 and 35 for the L-3 cap, 21 914 and 29 for the I-1 cap, 22 209 and 38 for the I-2 cap, and

22 679 and 44 for the I-3 cap. The material properties are listed in Table 6-3, and the wall thickness was assumed as the average wall thickness listed in the fifth column of Table 6-4. The applied load and boundary conditions were identical to those in Section 6.2.3.

The buckling loads ($p_{numerics}$) of the spherical caps are listed in the eighth column of Table 6-4, and the ratios of the $p_{numerics}$ to the p_{coll} are presented parenthetically. The ratios varied from 0.9600 to 1.0247 for caps with LIDIs and 1.0449 to 1.1128 for caps with IRIs. These values were almost equal to those obtained from test results, indicating relatively precise computation and agreement between the numerical and experimental results for the spherical caps. The slight differences may have resulted from average thickness value assumptions and properties of the parent material. In addition, the equilibrium paths (see Fig.6-18) of two scanned caps (L-1 and I-1) with preset imperfections were analogous with those of the imperfect caps presented in Fig.6-11, and the post buckling modes were in the form of local dimples, consistent with experimental results.

6.3 Buckling of spherical caps under various thickness reductions

This section examined the buckling performance of spherical caps with full or partial thickness reduction as well as the effect of the reduction parameters on the buckling performance. In total, 42 laboratory-scale spherical caps—6 with full thickness reduction and 36 with partial thickness reduction—were fabricated, measured, and tested. Furthermore, the collapse modes and corresponding buckling pressures of these caps were analysed under different magnitudes, ranges, and sites of wall-thickness reduction. In addition, the experimental buckling pressures were benchmarked against existing analytical and semianalytical formulae. The results reported herein can serve as a foundation for assessing corroded and defective spherical caps.

6.3.1 Design and fabrication

Consider a typical spherical cap with nominal base diameter $d = 150$ mm (nominal median radius of curvature, $r = 87.98$ mm), nominal uniform wall

thickness $t = 2 \text{ mm}$, and nominal height $h = 41.1 \text{ mm}$ [24] composed of photosensitive resin and subjected to uniform external pressure p . Assume that the wall thickness of the cap is uniformly reduced, which is achieved by 3D printing directly, across its exterior surface under a reduced magnitude t_r and a reduced range α at one of three sites (i.e., apex, middle, and base). Fig.6-19 illustrates the spherical caps with thickness reduced at these sites as well as the corresponding caps without wall-thickness reduction and with full wall-thickness reduction.

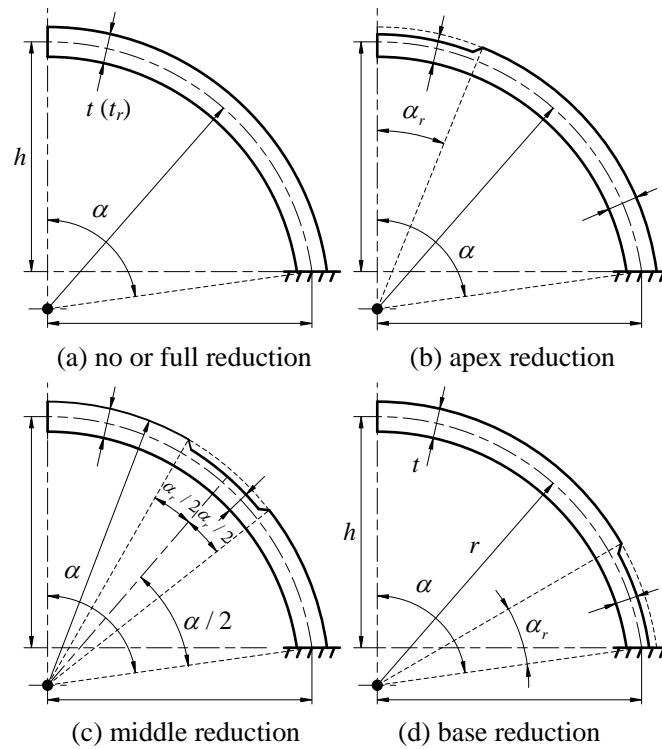


Fig.6-19 Sketch of spherical caps with four thickness reduced sites

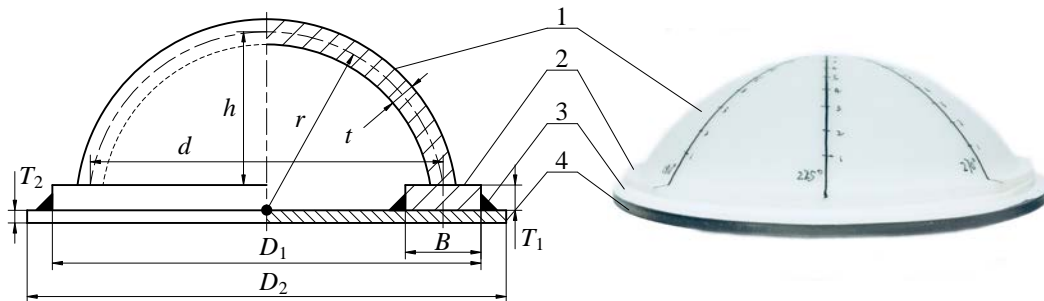


Fig.6-20 Schematic and photograph of an experimental domed cap; 1 = cap, 2 = heavy ring, 3 = vulcanising silicone rubber, and 4 = steel plate

To evaluate the effects of magnitude, range, and site of wall-thickness reduction on

the buckling properties of domed spherical caps, thickness reduction at the three aforementioned sites was analysed. For each site, the reduced magnitude, t_r/t , was set to 0.8 and 0.6, and the reduced range, α_r/α , was set to 0.1, 0.2, and 0.4. The wall thickness of caps with full thickness reduction was set to $0.8t$ and $0.6t$, which corresponded to the reduced range of $\alpha_r/\alpha = 1$. To ensure a nearly fixed constraint, a resin heavy ring of thickness $T_1 = 5$ mm, outer diameter $D_1 = 160$ mm, and width $B = 12.5$ mm was engineered on the base of each cap (Fig.6-20).

To verify the repeatability of the experiments, two spherical caps were fabricated for each parameter combination, thus yielding a total of 2 (caps) \times 3 (sites) \times 2 (magnitudes) \times 3 (ranges) = 36 spherical caps with partial thickness reduction as well as 2 (caps) \times 3 (magnitudes) = 6 spherical caps with full thickness reduction. All caps were fabricated upright along the axis of revolution, under similar fabrication parameters, through rapid prototyping (stereolithography). Details of this fabrication approach, which yields high-quality caps for hydrostatic testing, are available in [37,39,40]. Additionally, to characterize the parent material properties, five flat tension coupons were designed according to a modified version of ASTM D638 [41] and were synchronously fabricated upright along the longitudinal direction under the same fabricating parameters as those employed for the spherical caps.

6.3.2 Geometric measurement

To verify the accuracy of the geometries of the fabricated spherical caps, the external surface and wall thickness of each fabricated cap were measured using an optical scanner (Open Technologies Corporation) and an ultrasonic gauge (Sonatest Corporation), respectively; per their operating manuals, the measurement accuracy of these instruments is <0.02 and <0.001 mm, respectively. Both measurement approaches are detailed in [1,42].

Fig.6-21 depicts the deviation of each fabricated spherical cap from the corresponding perfect geometry. As evident, the geometry of all caps are highly accurate relative to the perfect geometry. By contrast, most heavy rings exhibited relatively large deviations, which may be attributed to excessive manual polishing

after rapid prototyping. Nevertheless, the effect of these large deviations on the buckling of caps is negligible because the ring functions solely as a fixed boundary condition. Moreover, as the geometry of each cap was of medium quality, the nominal median radius of the spherical caps can be used as an input parameter to study their pressure-supporting capacity.

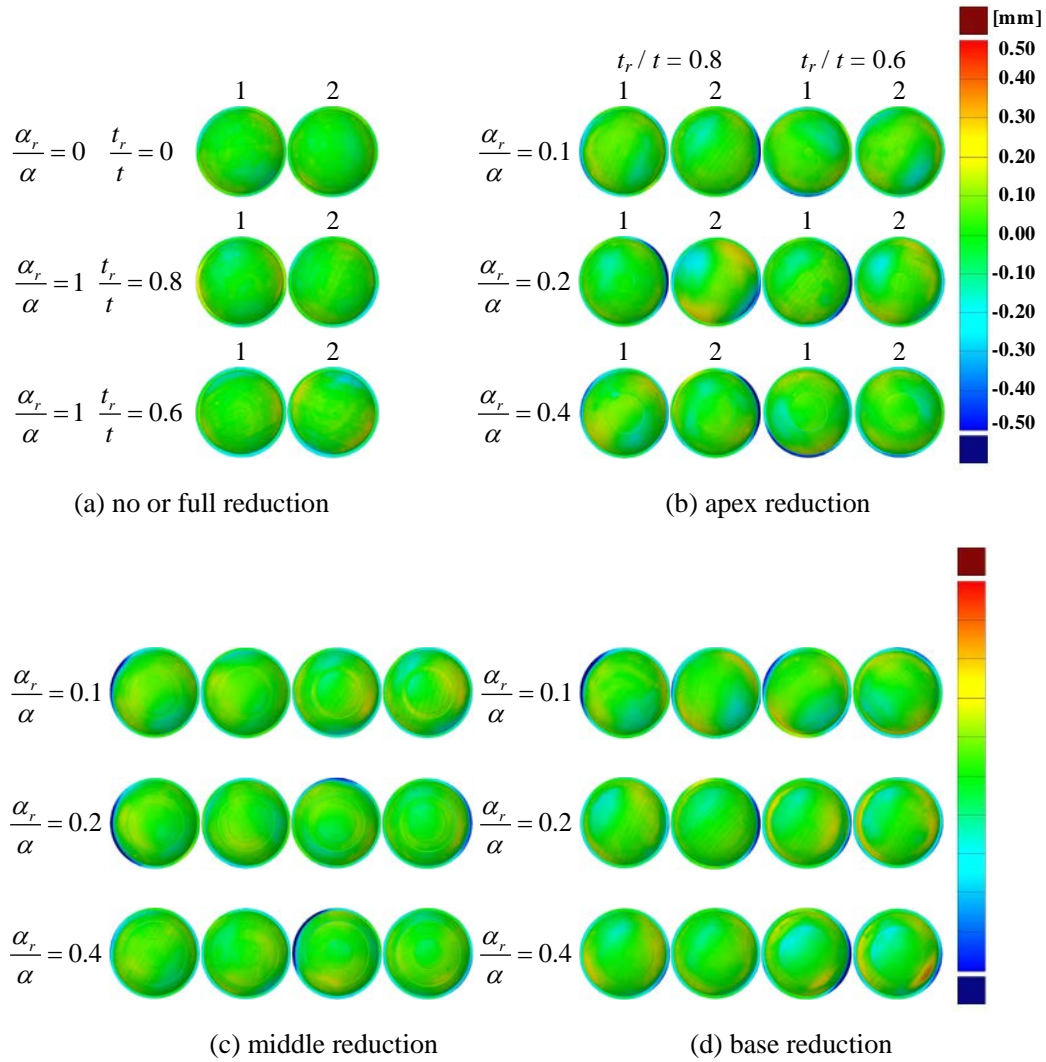


Fig.6-21 Geometric deviations of the fabricated spherical caps from the corresponding perfect geometries; all symbols correspond to those in Fig.6-19, and numbers 1 and 2 indicate the two spherical caps fabricated for each tested cap design

The wall thickness of each cap was ultrasonically measured at ten equidistant points on each of eight equally spaced meridians, yielding a total of $9 \times 8 + 1 = 73$ measurement sites on each cap. Table 1 lists the obtained minimum, t_{min} , maximum, t_{max} , and average, t_{ave} , magnitudes of wall thickness as well as the corresponding standard deviations, t_{std} , and nominal values, t_{nom} . As evident from

the table, the actual wall thicknesses of the fabricated spherical caps agree well with their nominal thicknesses, with negligible differences ranging from 0 to 0.06 mm. These measurements indicated that the wall-thickness distribution of each cap is of medium quality; thus, the nominal wall thickness of the spherical caps can be used as an input parameter to study their pressure-supporting capacity.

6.3.3 Mechanical testing

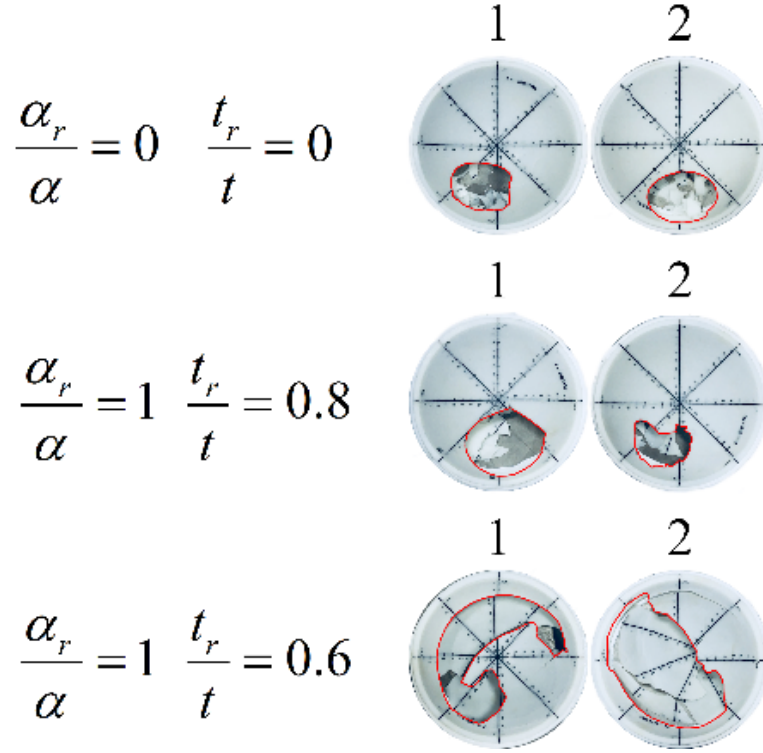
After the geometric measurements, each cap was slowly loaded to collapse under quasistatic pressure at room temperature. The pressure was manually applied through the medium of water in a cylindrical pressure vessel (inner diameter = 200 mm, total length = 1000 mm, and maximum pressure = 20 MPa) at Jiangsu University of Science and Technology. A hand-operated pump and a pressure gauge were used to apply and record the hydrostatic pressure, respectively.

To prevent water from entering the cap during the test, a heavy, circular stainless-steel plate of diameter $D_2 = 170$ mm and thickness of $T_2 = 4$ mm was attached to the bottom of the ring of each cap by using vulcanising silicone rubber (Fig.6-20); this forms a closed, partially spherical cavity that transfers the externally applied pressure to the cap during hydrostatic testing.

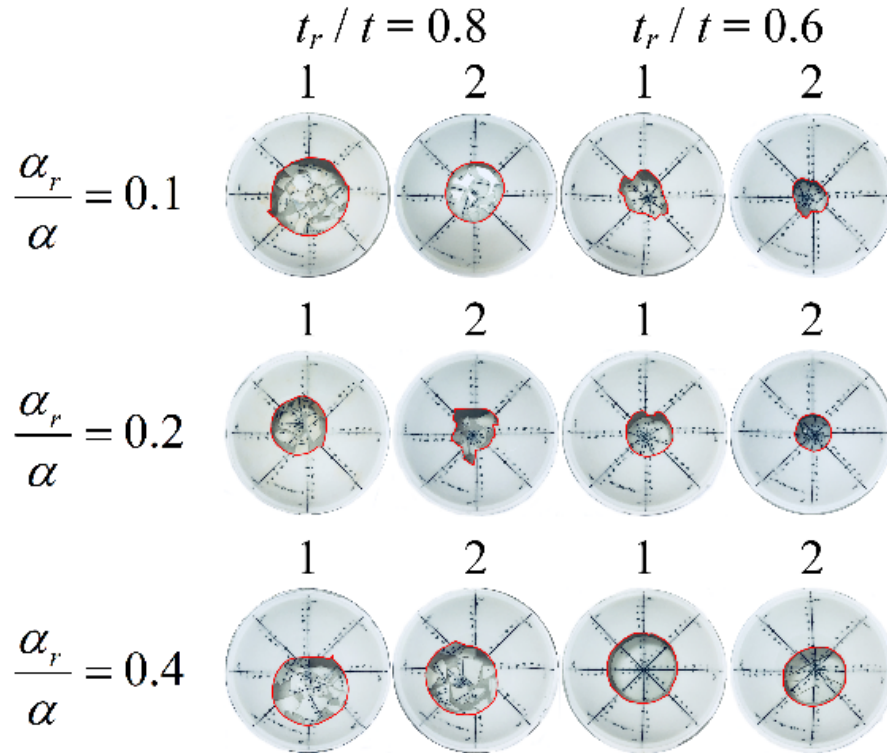
To prevent pieces of the tested spherical caps from falling into the pressure vessel, each tested cap was wrapped in a string bag. The pressure difference between the top and bottom due to the gravity of water is as follows, $\Delta p = \rho gh = 1000 \times 9.8 \times 41.1 \times 10^{-3} = 4.028 \times 10^{-4}$ MPa. This slight difference indicates a small effect of gravity on the experimental results. In all spherical caps, the buckling occurred suddenly and was accompanied by an audible bang and a sharp reduction in the pressure. Therefore, detecting buckling and the maximum recorded pressure corresponding to the buckling or collapse load of each cap (see the rightmost column in Table 6-5) was straightforward. This mechanical testing operation is detailed in [37,39,40].

After the test, the collapsed spherical caps were removed from the pressure vessel. Fig.6-22 presents vertical views of the collapse modes of the caps. Owing to the

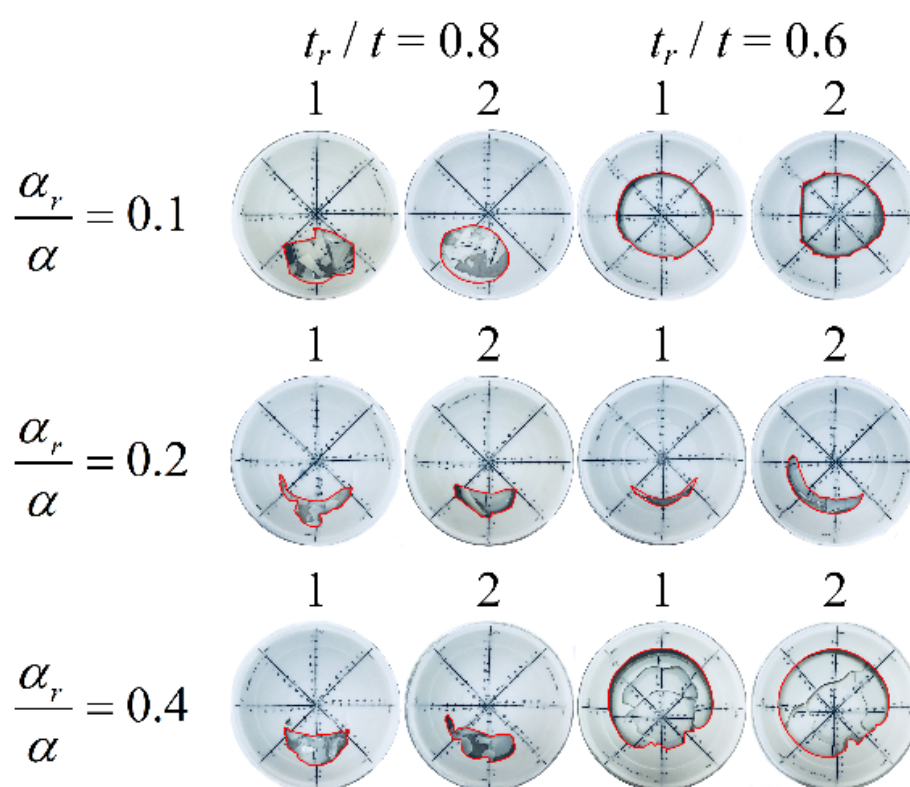
brittleness of the material, each cap shell collapsed into several pieces in a local form. To facilitate further observation, the pieces were collected and assembled at the collapse area.



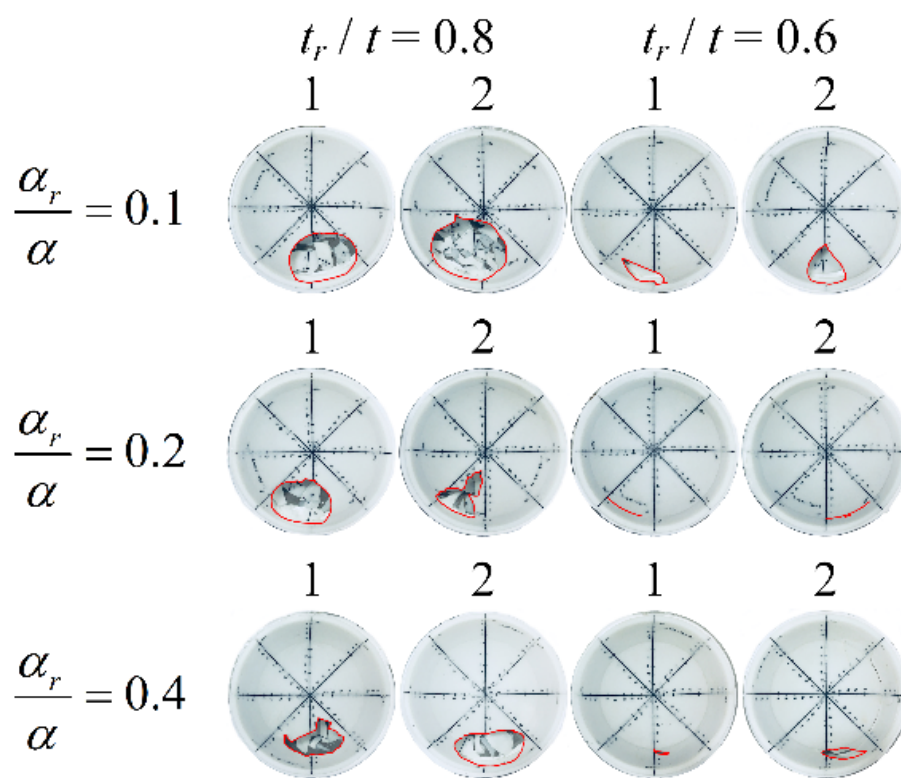
(a) no or full reduction



(b) apex reduction



(c) middle reduction



(d) base reduction

Fig.6-22 Vertical views of the spherical caps after collapse; collapse boundaries are marked in red.

To determine the caps' material properties, namely Young modulus and Poisson ratio, the five fabricated coupons were subjected to uniaxial tensile testing per ISO 6892-1: 2009 [8] and ASTM D638 [41]. Young modulus and Poisson ratio were respectively determined using the stress–strain curves and the strain recorded in the longitudinal and transverse directions. These tensile tests are explained in [40]. The calculated material properties of the five coupons, listed in Table 6-6, evidence the high repeatability of the experiments. Thus, the average material properties, that is Young modulus, $E = 2122.92$ MPa, and Poisson ratio, $\mu = 0.328$, can be adopted as input parameters to examine the pressure-supporting capacity of the spherical caps.

6.3.4 Full thickness reduction analysis of spherical caps

The buckling performance of three pairs of medium quality spherical caps with no or full thickness reduction is discussed in this subsection. These three pairs had uniformly distributed thickness of magnitude $1t$, $0.8t$, and $0.6t$. As shown in Figs.6-22a and 6-23a, all the tested spherical caps were pressurised into several small pieces due to the brittleness of the material, which collapsed in a local form near the base. This collapse phenomenon is mainly attributed to the base of each cap being fully constrained. In addition, this collapse form can result in a typical local dimple if the parent material has high ductility, as reported in studies on steel spherical shells [1,24]. Moreover, with decreasing wall thickness, the size of the collapse zone increased and the zone shape became increasingly irregular. Specifically, nearly 50% of the $0.6t$ -magnitude spherical caps ripped inward along the base because the small wall thickness may have led to a significant change in stiffness at the base.

As listed in the Tables 6-5 and 6-7, similar to the collapse modes, the buckling pressures of each pair of spherical caps with the same nominal wall thickness were nearly identical, evidencing the high repeatability of the experiments.

To identify a rational design criterion for these spherical caps, four analytical and semianalytical formulae were adopted for benchmarking against the experimental results. These formulae include the analytical linear buckling or empirical plus analytical buckling predictions.

Table 6-5 Nominal, t_{nom} , maximum, t_{max} , minimum, t_{min} , average, t_{ave} , wall thicknesses of all fabricated spherical caps and the corresponding standard deviations, t_{std} , and buckling pressures, p_{test} .

case	sample		non-reduced area						reduced area					p_{test} [Mpa]
	$\frac{\alpha_r}{\alpha}$	$\frac{t_r}{t}$	sample number	t_{nom} [mm]	t_{max} [mm]	t_{min} [mm]	t_{ave} [mm]	t_{std} [mm]	t_{nom} [mm]	t_{max} [mm]	t_{min} [mm]	t_{ave} [mm]	t_{std} [mm]	
apex reduction	0.1	0.8	1	2	2.030	1.912	1.977	0.021	1.6	1.630	1.588	1.605	0.014	0.554
			2	2	2.034	1.954	1.995	0.015	1.6	1.642	1.602	1.616	0.013	0.547
		0.6	1	2	2.058	1.950	2.005	0.023	1.2	1.244	1.184	1.210	0.017	0.375
			2	2	2.038	1.886	1.997	0.022	1.2	1.212	1.196	1.204	0.004	0.373
	0.2	0.8	1	2	2.052	1.940	1.994	0.027	1.6	1.626	1.594	1.610	0.010	0.537
			2	2	2.068	1.964	2.011	0.025	1.6	1.660	1.602	1.628	0.016	0.554
		0.6	1	2	2.074	1.942	1.993	0.021	1.2	1.212	1.186	1.200	0.007	0.255
			2	2	2.052	1.958	2.008	0.022	1.2	1.244	1.202	1.217	0.011	0.257
	0.4	0.8	1	2	2.052	1.978	2.007	0.016	1.6	1.666	1.586	1.619	0.020	0.553
			2	2	2.068	1.948	2.005	0.026	1.6	1.666	1.598	1.632	0.017	0.557
		0.6	1	2	2.052	1.968	2.004	0.019	1.2	1.232	1.188	1.210	0.009	0.296
			2	2	2.016	1.972	1.998	0.012	1.2	1.224	1.194	1.206	0.007	0.295
middle reduction	0.1	0.8	1	2	2.064	1.886	2.015	0.031	1.6	1.642	1.582	1.607	0.020	0.632
			2	2	2.092	1.946	2.018	0.031	1.6	1.624	1.568	1.601	0.018	0.589
		0.6	1	2	2.032	1.956	1.988	0.017	1.2	1.216	1.168	1.181	0.014	0.270
			2	2	2.062	1.954	1.999	0.022	1.2	1.214	1.170	1.198	0.016	0.300
	0.2	0.8	1	2	2.052	1.960	2.016	0.021	1.6	1.624	1.582	1.608	0.011	0.539
			2	2	2.032	1.956	2.000	0.017	1.6	1.612	1.568	1.593	0.012	0.519
		0.6	1	2	2.066	1.952	2.027	0.028	1.2	1.244	1.168	1.206	0.020	0.269
			2	2	2.048	1.952	2.009	0.022	1.2	1.208	1.174	1.195	0.010	0.237
	0.4	0.8	1	2	2.032	1.972	1.998	0.014	1.6	1.614	1.568	1.591	0.012	0.419
			2	2	2.038	1.938	2.008	0.023	1.6	1.614	1.578	1.597	0.010	0.402
		0.6	1	2	2.048	1.962	2.005	0.018	1.2	1.214	1.172	1.196	0.012	0.231
			2	2	2.034	1.976	2.009	0.015	1.2	1.216	1.182	1.197	0.010	0.235
base reduction	0.1	0.8	1	2	2.048	1.992	2.011	0.011	1.6	1.622	1.582	1.601	0.015	0.605
			2	2	2.024	1.980	2.004	0.013	1.6	1.616	1.582	1.594	0.011	0.632
		0.6	1	2	2.064	1.984	2.012	0.014	1.2	1.238	1.146	1.200	0.028	0.389
			2	2	2.042	1.936	2.007	0.017	1.2	1.224	1.182	1.198	0.012	0.390
	0.2	0.8	1	2	2.032	1.918	1.997	0.026	1.6	1.628	1.484	1.572	0.042	0.465
			2	2	2.024	1.960	1.995	0.013	1.6	1.608	1.556	1.590	0.015	0.500
		0.6	1	2	2.042	1.982	2.009	0.013	1.2	1.208	1.184	1.192	0.008	0.188
			2	2	2.078	1.924	2.005	0.032	1.2	1.208	1.182	1.193	0.009	0.199
	0.4	0.8	1	2	2.058	1.988	2.027	0.016	1.6	1.632	1.558	1.596	0.021	0.376
			2	2	2.078	1.998	2.033	0.021	1.6	1.624	1.518	1.593	0.022	0.361
		0.6	1	2	2.062	1.978	2.010	0.013	1.2	1.210	1.172	1.193	0.010	0.147
			2	2	2.046	1.976	2.003	0.016	1.2	1.194	1.138	1.173	0.013	0.150
no reduction	0	0	1	2	2.008	1.870	1.940	0.029	N/A					0.727
			2	2	2.002	1.898	1.946	0.024						0.725
full reduction	1	0.6	1	N/A					1.6	1.604	1.490	1.548	0.030	0.411
			2						1.6	1.592	1.500	1.543	0.027	0.410
			1						1.2	1.200	1.112	1.157	0.024	0.180
			2						1.2	1.190	1.098	1.152	0.022	0.170

Table 6-6 Material properties of photosensitive resin obtained through uniaxial tensile testing.

coupon	E [MPa]	μ
1	2063.800	0.303
2	2174.600	0.336
3	2076.600	0.323
4	2199.300	0.339
5	2100.300	0.341
min	2063.800	0.303
max	2199.300	0.341
std	54.143	0.014
ave	2122.920	0.328

Notation: E = Young modulus; μ = Poisson ratio.

These formulae include the analytical linear buckling formula, p_{Zoelly} , derived by Zoelly [9]; the classical knockdown factor formula, p_{NASA} , developed by NASA [10], the empirical formula, p_{Evkin} , recently reported by Evkin [43], and the new knockdown factor formula, p_{Wagner} , deduced by Wagner [44]. The formulae are as follows:

$$p_{Zoelly} = 2E(t_r / t)^2 / \sqrt{3(1 - \mu^2)}, \quad (6-6)$$

$$p_{NASA} = p_{Zoelly}(0.14 + 3.2 / \lambda^2), \text{ for } \lambda > 2, \quad (6-7)$$

$$p_{Evkin} = p_{Zoelly} 0.693 / (1 - \mu)^{1/5} \lambda^{2/5}, \text{ for } \lambda \geq 5, \text{ and} \quad (6-8)$$

$$p_{Wagner} = p_{Zoelly}(5.172\lambda^{-1.464} + 0.1296), \text{ for } \lambda \geq 5.5. \quad (6-9)$$

Here, λ is the geometry parameter given by $\lambda = [12(1 - \mu^2)]^{1/4} (r / t_r)^{1/2} 2 \sin(\alpha / 2)$, the median radius, r , and reduced wall thickness, t_r , are assumed to the nominal magnitudes of the caps because of the highly accurate fabrication, as explained earlier. It should be mentioned that all formulae (6-7) – (6-9) are considered as attempts to provide lower bound estimations of design buckling pressure for plastic materials, while the formula (6-6) corresponds to the linear elastic buckling pressure that is always non-conservative. Also, where they are valid for brittle materials or not is unclear. The properties of the cap material measured experimentally are presented in Table 6-6 (Young modulus, $E = 2122.92$ MPa, and Poisson ratio, $\mu = 0.328$), and

those calculated using the aforementioned formulae are presented in Table 6-7; the data in parentheses in Table 6-7 are the ratios of the theoretical loads to the experimental loads.

Table 6-7 Experimental and theoretical buckling pressures of spherical caps with no or full thickness reduction.

t [mm]	λ	p_{ave} [MPa]	p_{Zoelly} [MPa]	p_{NASA} [MPa]	p_{Evkin} [MPa]	p_{Wagner} [MPa]
2	11.533	0.726	1.341(1.848)	0.220(0.303)	0.378(0.521)	0.367(0.506)
1.6	12.894	0.411	0.858(2.090)	0.137(0.333)	0.232(0.564)	0.216(0.527)
1.2	14.889	0.175	0.483(2.759)	0.075(0.426)	0.123(0.703)	0.110(0.631)

Notations: p_{ave} = Average experimental buckling pressure of each pair of caps (one pair for each case); the experimental results are presented in the bottom six rows of Table 1. Data in parentheses are the ratios of the theoretical loads to the experimental loads.

As evident from Table 6-7, the thinner the spherical cap, the higher the aforementioned ratio. Predictions made using Zoelly's formula were the most dangerous, whereas those made using NASA's formula were the most conservative; these findings are consistent with those of previous studies on spherical shells and caps [1,24,45]. Furthermore, predictions made using Evkin's and Wagner's formulae are similar, which yield the much less conservative safe design than NASA's formula. Nevertheless, Evkin's predictions are slightly more than Wagner's, both of them have a large safety margin that ensures design and operation reliability.

6.3.5 Partial thickness reduction analysis of spherical caps

The buckling performance of three groups of medium quality spherical caps, namely those with thickness reduction at the apex, middle, and base, is discussed in this subsection. At each of these three sites, reduced wall thickness of $0.8t$ and $0.6t$ was studied (with $1t$ being the full wall thickness). Similarly, at each site, the reduction range was 0.1α , 0.2α , and 0.4α . Fig.6-22 presents the vertical views of all pairs of collapsed caps. To analyse the collapse mechanism, the collapse margin, cap base, and reduction range of the caps are respectively indicated using red lines, black

lines, and blue zones in Fig.6-23.

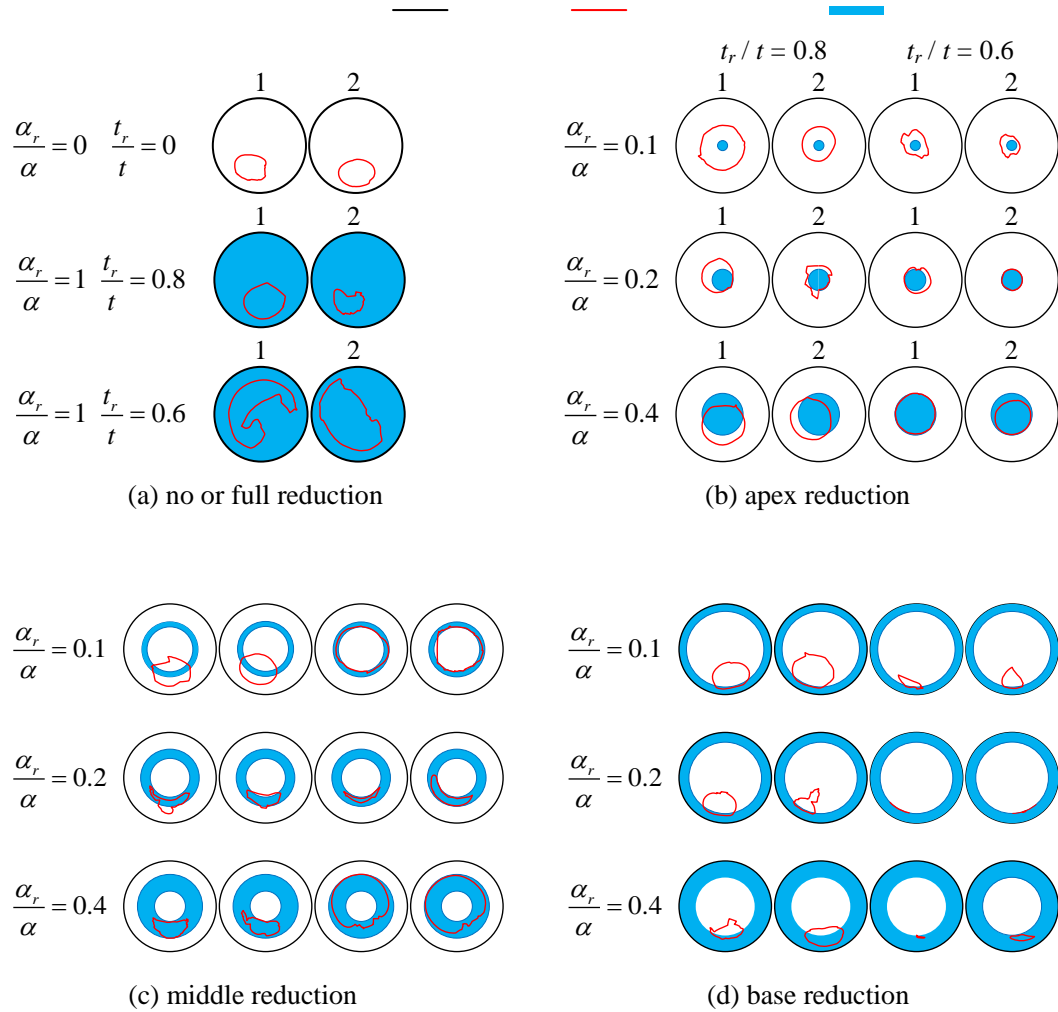


Fig.6-23 Collapse margins (marked in red) and reduced areas (blue zones) of the spherical caps, extracted from Fig.6-22

As evident from Figs.6-22 and 6-23, identical to the results seen in the analysis for full thickness reduction, most spherical caps collapsed into several small pieces due to the brittleness of the parent material. All collapses initiated near the thickness-reduced area, but the collapse sites and configurations differed in different configurations of caps. For example, in the case of thickness reduction at the apex, most spherical caps collapsed in the form of a near-circle, and the collapse area and thickness-reduced apex area appeared to nearly share the same centre. This finding becomes more apparent in the cases of large magnitude and range of thickness reduction. In addition, with increase in the magnitude and range, the collapse margin tended to approach the

margin of the reduced-thickness area. These results indicate that at low thickness-reduction magnitude and range, the caps buckle with overall stability, mainly because of the reduced local stiffness, whereas at high magnitude and range, the caps buckle with only local stability around the margin of the reduced-thickness area, mainly because of stress concentration in the margins of the thickness-reduced areas.

In the case of thickness reduction at the middle region of the cap, the spherical cap with the lowest magnitude and range of thickness reduction exhibited the same collapse mechanism as did the cap with full thickness reduction. The other spherical caps with similar configuration buckled along the margin of the thickness-reduced areas, either in a local form on the flank or in an overall form at the apex, depending on the magnitude and range of thickness reduction. Finally, regarding thickness reduction at the base, all spherical caps appeared to buckle in a local form along the margins of the thickness-reduced areas, mainly because of stress concentration at the margins. These results confirmed that the buckling of shells of revolution subjected to uniform external pressure is initiated at the weakest point (zone) of the structure [45,46].

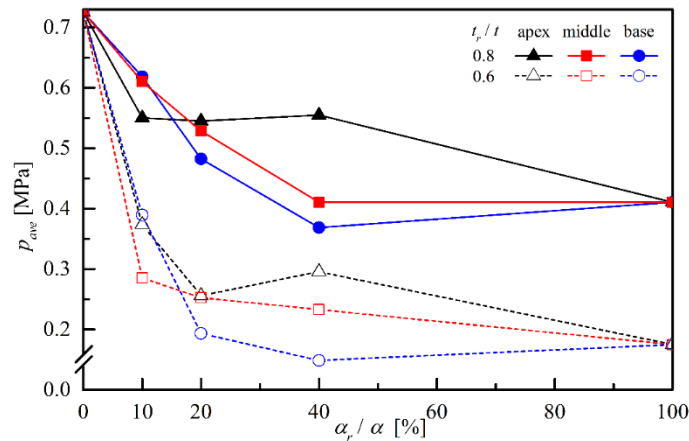


Fig.6-24 Average buckling pressure of a pair of caps for each cap configuration, p_{ave} , versus the range of thickness reduction, α_r / α for two magnitudes, t_r / t , and three sites (apex, middle, and base) of thickness reduction

Fig.6-24 depicts a plot of the collapse pressures of spherical caps versus the range of thickness reduction for two magnitudes and three sites of thickness reduction; the

figure also presents the results for full thickness reduction. The $1t$ spherical cap (i.e., without thickness reduction) refers to the caps not subject to thickness reduction, whereas the $0.8t$ and $0.6t$ spherical caps with full thickness reduction are special configurations with 100% reduced range. Fig.6-24 clarifies that for a given range of thickness reduction, the thinner the spherical cap, the lower the buckling pressure. For a given magnitude of thickness reduction, in most cases, the buckling pressure first considerably decreases with increase in the range, following which (over 0.4α) it slightly increases with increase in the range. This subsequent slight increase in buckling pressure suggests the presence of a threshold range beyond which the cap can support a certain level of pressure. This finding can be used as a guide to evaluate whether the pressure hull of an underwater vehicle can continue to work safely after corrosion or damage. Additionally, thickness reduction at the apex has the least effect on the pressure-supporting capacity of spherical caps, whereas thickness reduction at the base has the strongest effect. Therefore, corrosion or damage near the base of a spherical-cap structure warrants immediate attention.

To determine a rational design criterion for spherical caps with partial thickness reduction, four analytical and semianalytical formulae (Eqs. 6-6–6-9) were benchmarked against all experimental buckling pressures; Fig.6-25 presents the results along with the experimental data of the spherical caps with full thickness reduction. In the case of partial thickness reduction, the wall thickness was reduced to examine the pressure-supporting capacity of spherical caps. As evident from the figure, of the four examined formulae, both Wagner's and Evkin's formulae yields nearly the same optimal performance, providing a large safety margin to ensure design and operation reliability while being less conservative than the formula developed by NASA. As explained in Section 6.3.4, Zoelly's formula may yield unreliable predictions for spherical caps in the preliminary design stage. Thus, Wagner's and Evkin's formulae can be used to assess not only spherical caps with uniform wall thickness but also spherical caps with partial thickness reduction caused by such factors as corrosion or low-quality fabrication.

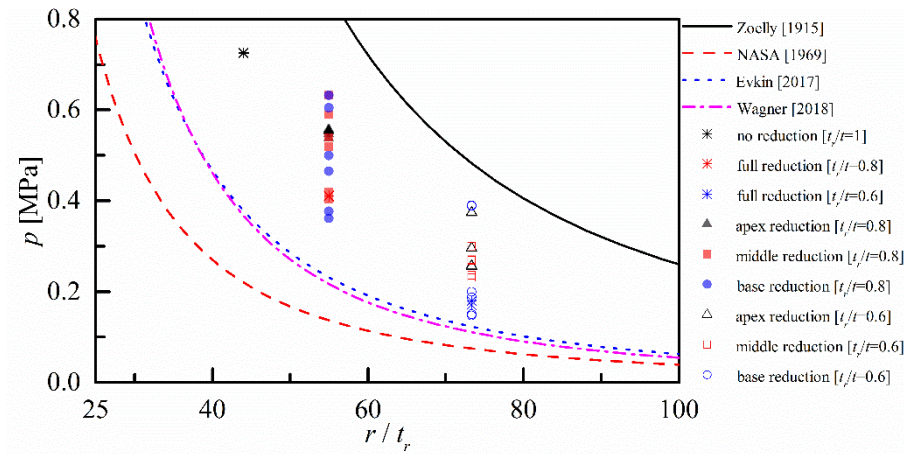


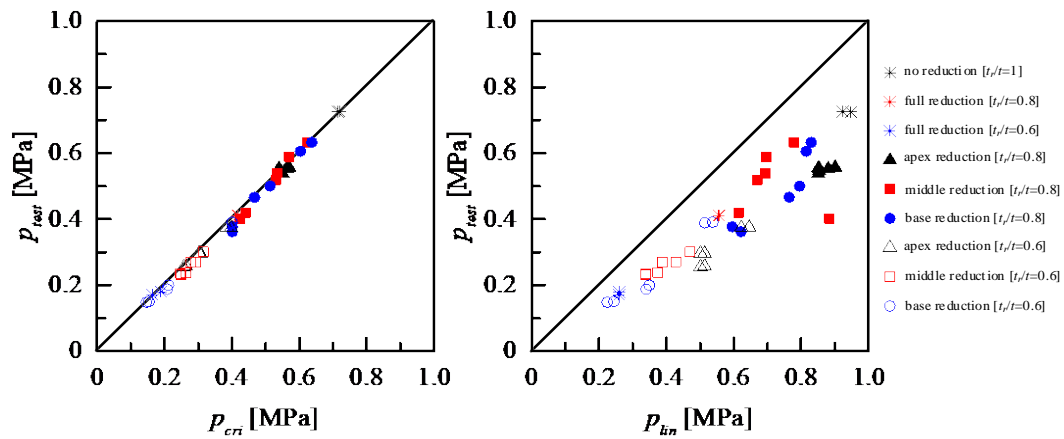
Fig.6-25 Buckling pressures of experimental spherical caps versus their median radius-to-reduced wall thickness ratio as well as the corresponding analytical or semianalytical results

6.3.6 Numerical analysis of the tested caps

Previous works have confirmed the role of the FE method in predicting buckling behaviours and pressure-supporting capacity of thin-walled shells [37,40]. To evaluate the buckling mechanism of above tested spherical caps, both linear and nonlinear computations of all 42 scanned caps were carried out using the FE code ABAQUS. The finite elements of caps were generated freely and uniformly on the measured geometries. The S4 shell elements and few S3 elements were selected to prevent hourglassing. Mesh convergence studies were performed to establish approximately 20 000 elements for each model [24,37,28]. The material properties were the same as the average values in Section 6.3.3. For each reduced region or unreduced one, the wall thickness was assumed to be the average value of corresponding region listed in the Table 6-5. Clamped boundary conditions were applied, which has been extensively used to examine dome buckling [3,5,6,12,24,31,32,34,35].

The relationship of buckling loads (p_{test}) of tested caps versus critical buckling loads (p_{cri}) obtained from the nonlinear arc length method and linear buckling loads (p_{lin}) obtained from linear bifurcation analysis are presented in Fig.6-26. As demonstrated in Fig.6-26a, the values of critical buckling loads agree well with those obtained from experimental results. However, Fig.6-26b illustrates that the magnitude of linear buckling loads is much more than that for p_{test} . These findings can indicate that the shell buckling occurs in a nonlinear-elastic regime. As presented in Fig.6-27,

some typical instability modes for four thickness reduced sites are provided. All critical buckling modes and post buckling modes of scanned caps resemble a local dimple which is consistent with the experimental results, but the linear buckling modes appear to be far from them, although each maximum deformation occurs near the collapse zone.



(a) experimental versus critical buckling loads (b) experimental versus linear buckling loads

Fig.6-26 Experimental buckling loads of 42 spherical caps versus critical and linear buckling loads obtained from numerical analysis

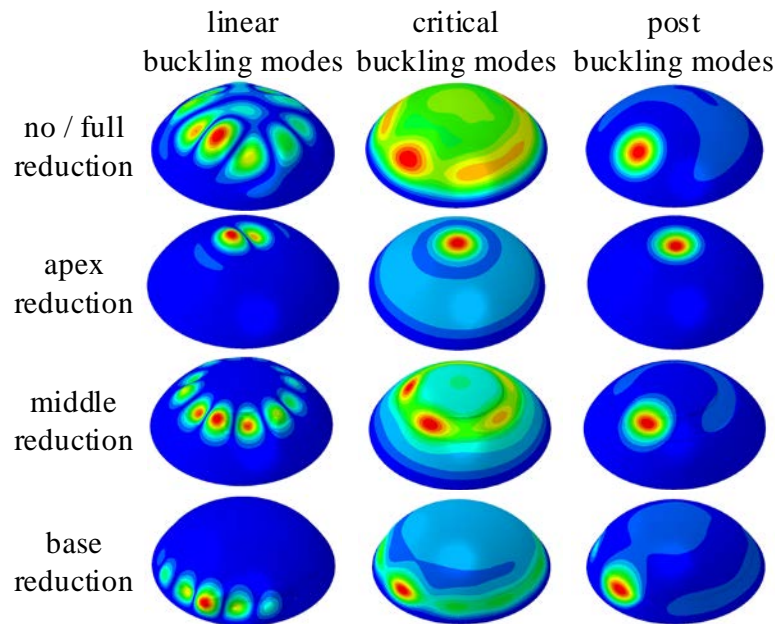


Fig.6-27 Typical linear, critical, and post buckling modes of experimental spherical caps with four thickness reduced sites

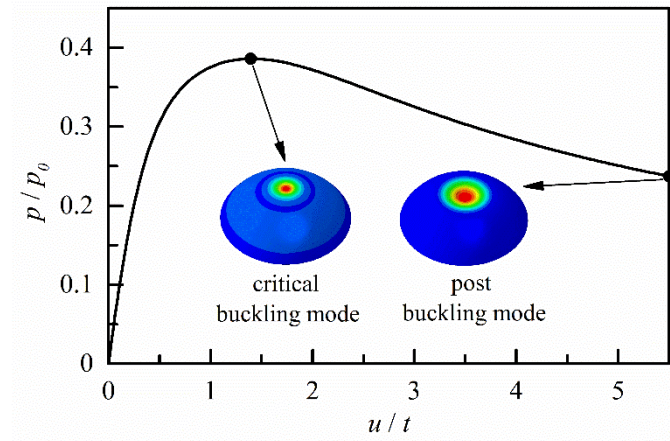


Fig.6-28 Equilibrium path, critical buckling mode, and post buckling mode of an apex reduction ($t_r/t = 0.6$, $\alpha_r/\alpha=0.1$) spherical cap

Fig.6-28 illustrates the equilibrium path of an apex reduction ($t_r/t = 0.6$, $\alpha_r/\alpha=0.1$) cap, which plots the relationship between buckling load (p) normalised by the initial applied pressure ($p_0 = 1\text{MPa}$) and maximum deflection (u) divided by nominal wall thickness (t). The curve first increases linearly and then nonlinearly, after a peak value it decreases suddenly. The nonlinear relationship suggests the obvious effect of geometrically nonlinear pre-buckling deformations on the buckling of shell. It appears that both the critical buckling mode and the post buckling mode have the same form of a local dimple, consistent with the experimental result. This unstable character is typical of shells of revolution [3,37,40,47]. Similar findings are found for the remaining cases.

6.4 Summary

In this chapter, firstly, experimental and numerical results of the buckling performances of six spherical laboratory-scale caps were obtained; furthermore, numerical results for the buckling of several mass-equivalent spherical caps of various heights were obtained. Secondly, the numerical results of buckling loads and shapes of spherical caps with different imperfections were provided. For each model, various positions, meridional extents, and two amplitudes of the models' imperfections (LIDIs, IRIs, FIDIs, and LBMIIs) were considered. Thirdly, the buckling behaviours of nearly perfect spherical caps with wall-thickness reduction were experimentally and numerically investigated; in addition, the effects of various reduction parameters on

the buckling properties were examined. Geometric measurements evidenced that the fabrication was of high accuracy, and hydrostatic testing demonstrated the high repeatability of the experiments. The results are as follows.

(1) The experimental buckling loads of spherical caps with deterministic imperfections vary from 5.255 to 5.647 MPa; the corresponding post buckling modes are similar and have the shape of a local dimple. The relatively small load variation and consistent destruction shape suggest good repeatability of the experiments. The nonlinear numerical buckling loads obtained from elastic–plastic and elastic–perfectly plastic analyses show reasonable agreement with the experimental ones. Elastic–perfectly plastic modeling can lead to relatively conservative results, and these can be used to evaluate the buckling of revolution shells under external pressure. The obtained numerical post buckling modes of all spherical caps take the form of a local dimple; this is consistent with the experimental results.

(2) The linear buckling of mass-equivalent spherical caps of various heights was studied numerically along with their nonlinear buckling under first eigenmode imperfections. The linear buckling loads initially increase with height and then decrease after a critical point. Similar phenomena are seen in nonlinear cases. The spherical cap with $h/d \approx 0.274$ is an optimal configuration, and it can be applied as an end-closure for cylindrical pressure hulls or as a manhole cover for manned cabins in deep-sea vehicles. The linear buckling modes of all caps take the form of one half circumferential wave and several meridional waves, and the post buckling modes of all imperfect caps resemble a local dimple; this is consistent with the experimental results despite the different imperfection forms between them.

(3) No significant differences were identified between the results obtained for different positions. The various tested values of the meridional position, θ , exhibited similar effects on the sensitivity of buckling load. By contrast, the same meridional extent for different imperfections (LIDIs and IRIs) exhibited opposite effects on buckling loads (LIDI buckling loads decreased, whereas that of IRI first decreased and then increased). This phenomenon was attributed to the geometries of the various imperfections. Additionally, for $\delta_0 = 0.5$ mm or $\delta_0 = 1$ mm, the mean buckling

load values of caps with LBMI was significantly lower than those of caps with LIDIs (by approximately 43% and 48%, respectively). Furthermore, the buckling load magnitudes of caps with LBMI were much less than those of caps with IRIs and FIDIs when $\delta_0 = 0.5$ mm (by approximately 20%), and similar when $\delta_0 = 1$ mm (those of caps with LBMI were approximately 0.3% less than those with IRIs and 9% more than those with FIDIs). This finding suggests that the LBMI achieved relatively conservative results and is thus more suitable for spherical cap buckling prediction analyses than the other three imperfections. LBMI may be especially useful for testing small imperfections, which have potential applications in deep sea fields. For example, these tests may be used for assessing domes connected to cylindrical pressure shells and hatches covering the access holes of pressurised subsea vessels.

(4) To validate the numerically calculated data for the spherical caps, six cap models were fabricated using SLA. For each cap model, wall thickness was measured and the real surface was scanned. Results of buckling load analyses of these cap models are presented numerically and experimentally. The ratios of the $p_{numerics}$ to the p_{coll} were 0.9600 to 1.0247 for caps with LIDIs and 1.0449 to 1.1128 for caps with IRIs, indicating agreement between the numerical and experimental results. Thus, FE analysis calculations used in this study were reliable and efficient. However, this study had some limitations. Although our discoveries provide valuable reference points for further investigations, only experiments on spherical caps with LIDIs and IRIs were performed. Other imperfections such as FIDIs and LBMI, and perfectly spherical caps should be experimentally investigated in future studies. In addition, the amplitudes of studied imperfections should be more diverse.

(5) All spherical caps buckled or collapsed in a local form, and all caps were pressurised into several small pieces due to the brittleness of the parent material. In the case of full thickness reduction, spherical caps collapsed near the base owing to the fully fixed boundary condition. With reduction in the wall thickness, the size of collapse zone appeared to increase, and the shape of the zone became increasingly irregular. In the case of partial thickness reduction, all collapses initiated near the thickness-reduced areas, but the collapse sites and forms differed for different

thickness-reduction configurations. At small magnitudes and ranges of thickness reduction, most caps buckled with overall stability, whereas at large magnitudes and ranges, the caps buckled locally around the margins of the thickness-reduced area.

(6) Similar to spherical caps with partial thickness reduction, the buckling pressure of the spherical caps with full thickness reduction increased linearly with increase in wall thickness for a given range of thickness reduction. For a given magnitude, the buckling pressure of most spherical caps with partial thickness reduction first considerably decreased with increase in the range and then slightly increased with increase in the range (over 0.4α). Moreover, thickness reduction at the apex exerted the weakest effect on the pressure-supporting capacity of spherical caps, whereas thickness reduction at the base exerted the strongest effect.

(7) Among the four analytical and semianalytical formulae examined in this study, Wagner's and Evkin's formulae appeared to yield the optimal performance in cases of both full and partial thickness reduction, providing a large safety margin to ensure design reliability while being much less conservative than the formula developed by NASA. Zoelly's formula may yield unreliable predictions for spherical caps in the preliminary design stage. Additionally, the numerical results indicated a nonlinear elastic buckling regime of caps, which agreed well with experimental results. To our knowledge, this study is the first to experimentally and numerically investigate the buckling of medium quality spherical caps with partial wall-thickness reduction as well as their design criterion. The results thus serve as a foundation for the assessment of corroded and defective spherical caps.

References

- [1] J. Zhang, M. Zhang, W. Tang, W. Wang, M. Wang, Buckling of spherical shells subjected to external pressure: A comparison of experimental and theoretical data, *Thin-Walled Struct.* 27111 (2017) 58-64.
- [2] S.G.P. Castro, R. Zimmermann, M.A. Arbelo, R. Khakimova, M.W. Hilburger, R. Degenhardt, Geometric imperfections and lower-bound methods used to calculate knock-down factors for axially compressed composite cylindrical shells, *Thin-Walled Struct.* 74 (2014) 118-132.
- [3] J. Zhang, B. Zhu, F. Wang, W. Tang, W. Wang, M. Zhang, Buckling of prolate

- egg-shaped domes under hydrostatic external pressure, *Thin Walled Struct.* 119 (2017) 296-303.
- [4] H.Schmidt, P.Swadlo, Part C - Shells of revolution with Arbitrary meridional shapes - Buckling design by use of computer analysis, ECSC contract No.7210-SA/208: Enhancement of ECCS design recommendations and development of Eurocode 3 parts related to shell buckling, Final Rep, Universität GH Essen, FB Bauwesen • Stahlbau. (1996).
 - [5] J. Blachut, G.D. GALLETTY, D.N. MORETON, Buckling of near-perfect steel torispherical and hemispherical shells subjected to external pressure, *AIAA J.* 28 (1990) 1971-1975.
 - [6] P. Smith, J. Blachut, Buckling of externally pressurized prolate ellipsoidal domes, *J Press Vessel Technol.* 130 (2008) 11210.
 - [7] [SAC] Standardization Administration of the People's Republic of China, GB/T 228.1: Metallic materials – Tensile Testing – Part 1: Method of Test at Room Temperature, China: SAC. (2010)
 - [8] [ISO] International Organization for Standardization, SO 6892-1: Metallic Materials – Tensile Testing - Part 1: Method of Test at Room Temperature. Geneva: ISO. (2009)
 - [9] J. Blachut, P. Smith, Tabu search optimization of externally pressurized barrels and domes, *Eng. Optim.* 39 (2007) 889-918.
 - [10] NASA, NASA SP-8032: Buckling of thin-walled doubly curved shells, Washington (DC): NASA Space Vehicle Design Criteria (Structures). (1969).
 - [11] J. Blachut, Experimental perspective on the buckling of pressure vessel components, *Appl. Mech. Rev.* 66 (2013) 010803.
 - [12] J. Blachut, G.D. Galletly, Buckling strength of imperfect steel hemispheres, *Thin-Walled Struct.* 23 (1995) 1-20.
 - [13] [CCS] China Classification Society, Rules for the Classification and Construction of Diving Systems and Submersibles, Beijing: CCS. (2013).
 - [14] [CEN] Comité Européen de Normalisation, EN 1993-1-6: Eurocode 3 – Design of steel structures – Part 1.6: Strength and Stability of shell structures. Brussels: CEN. (2007)
 - [15] M.W. Hilburger, M.P. Nemeth, J.H. Starnes, Shell Buckling Design Criteria Based on Manufacturing Imperfection Signatures, *AIAA J.* 44 (2006) 654-663.
 - [16] M.W. Hilburger, Developing the next generation shell buckling design factors and technologies, *AIAA Pap.* 2012-1686, NF1676L-13283. (2007) 1-15.
 - [17] J. Blachut, K. Magnucki, Strength, Stability, and Optimization of Pressure Vessels: Review of Selected Problems, *Appl. Mech. Rev.* 61 (2008) 60801.
 - [18] H. Schmidt, Stability of steel shell structures, *J. Constr. Steel Res.* 55 (2000) 159-181.
 - [19] P. Jasion, Stability analysis of shells of revolution under pressure conditions, *Thin-Walled Struct.* 47 (2009) 311-317.
 - [20] W. Cui, Development of the *Jiaolong* Deep Manned Submersible, *Mar. Technol. Soc. J.* 47 (2013) 37-54.
 - [21] B.B. Pan, W.C. Cui, Y.S. Shen, T. Liu, Further study on the ultimate strength analysis of spherical pressure hulls, *Mar. Struct.* 23 (2010) 444-461.
 - [22] J. Blachut, Locally flattened or dented domes under external pressure, *Thin-Walled Struct.* 97 (2015) 44-52.

- [23] P. Jasion, K. Magnucki, Elastic buckling of Cassini ovaloidal shells under external pressure - Theoretical study, *Arch. Mech.* 67 (2015) 179-192.
- [24] J. Zhang, Y. Wang, F. Wang, W. Tang, Buckling of stainless steel spherical caps subjected to uniform external pressure, *Ships Offshore Struct.* 13 (2018) 779-785.
- [25] Koga T, Hoff NJ. The axisymmetric buckling of initially imperfect complete spherical shells. *Int J Solids Struct* 1969;5:679-697.
- [26] J.M.T. Thompson, *Advances in Shell Buckling: Theory and Experiments*, *Int. J. Bifurc. Chaos.* 25 (2014) 1530001.
- [27] M.A. Arbelo, R. Degenhardt, S.G.P. Castro, R. Zimmermann, Numerical characterization of imperfection sensitive composite structures, *Compos Struct.* 108 (2014) 295-303.
- [28] P. Jasion, K. Magnucki, Elastic buckling of barrelled shell under external pressure, *Thin-Walled Struct.* 45 (2007) 393-399.
- [29] J. Blachut, G. Galletly, Influence of local imperfections on the collapse strength of domed end closures, *J Mech Eng Sci.* 207 (1993) 197-207.
- [30] A. Lee, F. López Jiménez, J. Marthelot, J.W. Hutchinson, P.M. Reis, The geometric role of precisely engineered imperfections on the critical buckling load of spherical elastic shells, *J. Appl. Mech.* 83 (2016) 1-11
- [31] J. Blachut, Buckling of multilayered metal domes, *Thin-Walled Struct.* 47 (2009) 1429-1438.
- [32] J. Blachut, Buckling of composite domes with localised imperfections and subjected to external pressure, *Compos. Struct.* 153 (2016) 746-754.
- [33] J. Blachut, Buckling of externally pressurized steel toriconical shells, *Int. J. Press. Vessel. Pip.* 144 (2016) 25-34.
- [34] B. Warrington, *The buckling of torispherical shells under external pressure*, Ph. D thesis, The University of Liverpool, Liverpool. 1984.
- [35] G.D. Galletly, J. Kruzelecki, D.G. Moffat, B. Warrington, Buckling of shallow torispherical domes subjected to external pressure – a comparison of experiment, theory, and design codes, *J Strain Anal Eng.* 22 (1987) 163-175.
- [36] J. Blachut, Buckling of externally pressurised barrelled shells: a comparison of experiment and theory, *Int J Pres Ves Pip.* 79 (2002) 507-517.
- [37] J. Zhang, W. Wang, F. Wang, W. Tang, W. Cui, W. Wang, Elastic buckling of externally pressurized Cassini oval shells with various shape indices, *Thin-Walled Struct.* 122 (2018) 83-89.
- [38] C. Hühne, R. Rolfes, J. Tessmer, A new approach for robust design of composite cylindrical shells under axial compression, *European Conference on Spacecraft Structures, Materials & Mechanical Testing 2005 (ESA SP-581)*, Noordwijk, Netherlands. 2005.
- [39] M. Wang, J. Zhang, W. Wang, W. Tang, Linear and nonlinear elastic buckling of stereolithography resin egg-shaped shells subjected to external pressure, *Thin-Walled Struct.* 127 (2018) 516-522.
- [40] J. Zhang, Z. Hua, W. Tang, F. Wang, S. Wang, Buckling of externally pressurised egg-shaped shells with variable and constant wall thicknesses, *Thin-Walled Struct.* 132 (2018) 111-119.
- [41] ASTM International, *ASTM D638-14: Standard test method for tensile properties of plastics*, West Conshohocken: ASTM Int. 08 (2003) 1-17.

- [42] M. Zhang, W. Tang, F. Wang, J. Zhang, W. Cui, Y. Chen, Buckling of bi-segment spherical shells under hydrostatic external pressure, *Thin-Walled Struct.* 120 (2017) 1-8.
- [43] A.Y. Evkin, O. V. Lykhachova, Energy barrier as a criterion for stability estimation of spherical shell under uniform external pressure, *Int. J. Solids Struct.* 118-119 (2017) 1339-1351.
- [44] H. N. R. Wagner, C. Hühne, S. Niemann, Robust knockdown factors for the design of spherical shells under external pressure: Development and validation, *Int. J. Mech. Sci.* 141 (2018) 58-77.
- [45] J. Kruzelecki, P. Trzeciak, Optimal design of axially symmetrical shells under hydrostatic pressure with respect to their stability, *Struct. Multidiscip. Optim.* 19 (2000) 148-154.
- [46] M. Barski, J. Kruzelecki, Optimal design of shells against buckling under overall bending and external pressure, *Thin-Walled Struct.* 43 (2005) 1677-1698.
- [47] J. Blachut, Externally pressurized toricones - Buckling tests, in: *Shell Struct: Theory Appl.* – Proc. 10th SSTA 2013 Conf. 2014 (3) 183-186.

Chapter 7 Conclusions and future work

7.1 Conclusions

In this thesis, results of a bionic, numerical, analytical, and experimental study into egg-shaped pressure hulls of deep manned submersibles are presented, along with the analytical, numerical, and experimental results of spherical pressure hulls and spherical caps. The main conclusions are as follows:

Firstly, an analytical, numerical, and experimental study into the buckling of spherical pressure hulls is carried out under different wall thicknesses, material properties, and imperfection amplitude. It is indicated that deep spherical pressure hulls are highly imperfection-sensitive structures, which tend to buckle in elastic – plastic regime due to the relatively high thickness-to-radius ratio. The plasticity reduction factor is a negative exponential function of the wall thickness-to-radius ratio, whilst the geometrical imperfection reduction factor is a piecewise linear function of the wall thickness-to-radius ratio pieced in three ranges. In this basis, a mechanism formula to predict the load-carrying capacity of spherical pressure hulls is derived semi-analytically. Also, experimental and numerical data of ten stainless spherical shells under uniform external pressure confirm the obtained post buckling mode, the adopted material modelling, and imperfection assumption.

Secondly, a bionic study into egg-shaped pressure hulls is performed based on goose eggs. A like-for-like comparison is made between spherical and egg-shaped hulls. First of all, the geometric properties of goose eggshells are examined, from which shape index distribution, shape function, volume, and surface equations are obtained. Based on the shape function, egg-shaped shell theory is derived to determine linear elastic stresses and buckling. On this basis, two egg-shaped pressure hulls respectively with the uniform and non-uniform thickness are proposed, along with the equivalent spherical pressure hull for comparison. Buckling of these pressure hulls with geometric imperfections are further studied using numerical analyses at a given design load. It is found that, with respect to hull strength, buoyancy reserve, and

space efficiency etc., egg-shaped pressure hulls could be optimally coordinated, which appear to be leading to overall better performance than the spherical pressure hull. Especially, the egg-shaped pressure hull is quite less sensitive to the geometric imperfections, making it more convenient and low costly to form the hull in manufacturing or to open holes in applications.

Thirdly, the effects of geometrical shape and wall thickness on the linear and nonlinear buckling of pressure hulls are deeply explored, along with corresponding experimentations. The imperfection sensitivity increases as the shapes become more spherical. For each hull, the post buckling mode at the end of the paths has the form of local dents. The thicker the egg-shaped pressure hull is, the more sensitive to material plasticity the buckling load is, the less sensitive to shape deviation the yielding and buckling loads are. The egg-shaped pressure hull is less sensitive to the material plasticity and shape deviation than the spherical one, especially in the case of thick wall. As a result, the difference between the load-carrying capacities of egg-shaped and spherical pressure hulls significantly decreases with an increase in the wall thickness. This finding suggests that egg-shaped pressure hulls appear to be applicable to deep submersibles, especially to full ocean depth ones. Additionally, experimental data of egg-shaped shells under uniform external pressure proves the validity of the adopted analyzing approach.

Subsequently, in order to examine the effect of non-uniform wall thickness distribution the load carrying capacity of pressure hulls, an equivalent comparison between the buckling of mass equivalent egg-shaped pressure hulls with non-uniform and uniform wall thicknesses is conducted under uniform external pressure. All tested egg-shaped pressure hulls are broken into several pieces on one side, and they collapsed near the equator following the formation of a local dent. The average collapse pressure of the egg-shaped pressure hulls with non-uniform wall thickness is higher than that of the egg-shaped pressure hulls with uniform wall thickness, thus indicating that the load-carrying capacity of egg-shaped pressure hulls is significantly improved when the non-uniform wall thickness is implemented. It appears that non-uniform wall thickness can be applied to improve the buckling capacity of other

untypical shells of revolution with positive Gaussian curvature.

Finally, the buckling of spherical caps under various heights, geometric imperfections, and wall-thickness reductions are numerically and experimentally studied. A good agreement is obtained between simulation and experiment. The post buckling modes of spherical caps take the form of a local dimple. The spherical cap with $h/d \approx 0.274$ is an optimal configuration, and it can be applied as an end-closure for cylindrical pressure hulls or as a manhole cover for manned cabins in deep-sea vehicles. Moreover, the initial geometrical imperfection resembling first linear buckling mode achieves relatively conservative results and is thus more suitable for spherical cap buckling prediction analyses than the other three imperfections. Additionally, Wagner's and Evkin's formulae appear to yield the optimal performance in cases of both full and partial thickness reduction, providing a large safety margin to ensure design reliability while being much less conservative than the formula developed by NASA.

7.2 Future works

Although the obtained results are encouraging, there are still some limitations in this these. Details are as follows:

(1) All egg-shaped pressure hulls are taken into account in the case of isotropic material. However, there is a large difference between meridional and circumferential mechanical performances. It appears that orthogonal material like composite material can be more effective for such untypical shell of revolution with positive Gaussian curvature. Therefore, the buckling of egg-shaped shells with such material requires further investigation.

(2) The present work only focuses on a single egg-shaped shell structure, which is difficult to enlarge capacity by increasing the shell size. In this case, segmented egg-shaped configuration, including several identical single egg-shaped shells, may be an optimal selection. Different segment can play different function and can be fabricated with different material. Therefore, further works should focus on the buckling of segmented egg-shaped pressure hulls.

(3) Eggshell is a closed shell of revolution with multifocal surfaces of positive Gaussian curvature. It is extremely difficult to fabricate egg-shaped pressure hulls using traditional manufacturing techniques. Although the rapid prototyping can lead to a high accuracy, the fabricating cost is very high and the fabricating quality cannot be ensured compared with other fabrication approaches. Therefore, how to effectively fabricate egg-shaped pressure hulls is another research topic.

Publications associated with the thesis

1. **Jian Zhang**, Meng Zhang, Wenxian Tang, Weibo Wang, Minglu Wang. Buckling of spherical shells subjected to external pressure: A comparison of experimental and theoretical data. Thin-Walled Structures. vol.111, pp58-64, 2017. **(2018 Impact Factor: 2.881)** ← Chapter 2
2. **Jian Zhang**, Wei Peng, Wenxian Tang, Minglu Wang. Experimental Study on the Geometrical and Mechanical Properties of Goose Eggshells. Brazilian Journal of Poultry Science. vol.19, pp455-464, 2017. **(2018 Impact Factor: 0.463)** ← Chapter 3
3. **Jian Zhang**, Minglu Wang, Weibo Wang, Wenxian Tang, Yongmei Zhu. Investigation on egg-shaped pressure hulls. Marine Structures. vol.52, pp50-66, 2017. **(2018 Impact Factor: 2.491)** ← Chapter 3
4. **Jian Zhang**, Benyi Zhu, Fang Wang, Wenxian Tang, Weibo Wang, Meng Zhang. Buckling of prolate egg-shaped domes under hydrostatic external pressure. Thin-Walled Structures. vol.119, pp296-303, 2017. **(2018 Impact Factor: 2.881)** ← Chapter 3
5. **Jian Zhang**, Minglu Wang, Weibo Wang, Wenxian Tang. Buckling of egg-shaped shells subjected to external pressure. Thin-Walled Structures. vol.113, pp122-128, 2017. **(2018 Impact Factor: 2.881)** ← Chapter 4
6. **Jian Zhang**, Meng Zhang, Weicheng Cui, Wenxian Tang, Fang Wang, Binbin Pan. Elastic-plastic buckling of deep sea spherical pressure hulls. Marine Structures. vol.57, pp38-51, 2018. **(2018 Impact Factor: 2.491)** ← Chapter 2
7. **Jian Zhang**, Weiming Wang, Weicheng Cui, Wenxian Tang, Fang Wang, Yun Chen. Buckling of logan-shaped shells under external pressure. Marine Structures. vol.60, pp218-225, 2018. **(2018 Impact Factor: 2.491)** ← Chapter 3
8. **Jian Zhang**, Weimin Wang, Fang Wang, Wenxian Tang, Weicheng Cui, Weibo Wang. Elastic buckling of externally pressurized Cassini oval shells with various shape indices. Thin-Walled Structures. vol.122, pp83-89, 2018. **(2018 Impact Factor: 2.881)** ← Chapter 3
9. **Jian Zhang**, Minglu Wang, Weicheng Cui, Fang Wang, Zhengdao Hua, Wenxian Tang. Effect of thickness on the buckling strength of egg-shaped pressure hulls. Ships and Offshore Structures. vol.13(4), pp375-384, 2018. **(2018 Impact Factor: 1.685)** ← Chapter 4
10. Minglu Wang, **Jian Zhang**, Weimin Wang, Wenxian Tang. Linear and nonlinear elastic buckling of stereolithography resin egg-shaped shells subjected to external pressure. Thin-Walled Structures.

vol.127, pp516-522, 2018. **(2018 Impact Factor: 2.881) ← Chapter 4**

11. **Jian Zhang**, Zhengdao Hua, Wenxian Tang, Fang Wang, Shuyan Wang. Buckling of externally pressurised egg-shaped shells with variable and constant wall thicknesses. *Thin-Walled Structures*. vol.132, pp111-119, 2018. **(2018 Impact Factor: 2.881) ← Chapter 5**

12. **Jian Zhang**, Yueyang Wang, Fang Wang, Wenxian Tang. Buckling of stainless steel spherical caps subjected to uniform external pressure. *Ships and Offshore Structures*. vol.13(7), 779-785, 2018. **(2018 Impact Factor: 1.685) ← Chapter 6**

13. **Jian Zhang**, Zhengdao Hua, Fang Wang, Wenxian Tang. Buckling of an egg-shaped shell with varying wall thickness under uniform external pressure, *Ships and Offshore Structures*, (doi.org/10.1080/17445302.2018.1524553)accept, **Online publishing (2018 Impact Factor: 1.685) ← Chapter 5**

14. **Jian Zhang**, Yuewen Zhang, Fang Wang, Xilu Zhao, Weicheng Cui, Yongmei Zhu. Strength Characteristics of maraging steel spherical pressure hulls for deep manned submersibles. *Journal of ship mechanics*. vol.22(12), pp1508-1526, 2018. **(2018 Impact Factor: 0.446) ← Chapter 2**

15. Wenxian Tang, Xinlong Zuo, **Jian Zhang**, Xilu Zhao, Yongmei Zhu. Buckling of multi-segment egg-shaped pressure hull. *Journal of ship mechanics*. vol.22(12), pp1557-1574, 2018. **(2018 Impact Factor: 0.446) ← Chapter 3**

16. **Jian Zhang**, Yueyang Wang, Wenxian Tang, Yongmei Zhu, Xilu Zhao. Buckling of externally pressurised spherical caps with wall-thickness reduction. *Thin-Walled Structures*. vol.136, pp129-137, 2019. **(2018 Impact Factor: 2.881) ← Chapter 5**

Acknowledgements

Firstly, the author would like to express the deep gratitude to his supervisor Professor Xilu Zhao for the patience and encouragement throughout this work. Zhao's way of thinking, working, and researching has significantly affected the author for nearly 10 years. Without his smart inspirations, critical comments and valuable suggestions, it is impossible to complete this thesis.

Secondly, the author was very grateful to the Chinese famous scientist Professor Weicheng Cui, who was ever the first deputy general designer of Chinese deep manned submersible 'Jiao Long' (7 km) and is now the general designer of Chinese hadal manned submersible 'Rainbow Fish' (11 km). Cui provided the author engineering background, experimental data and research ideas.

Thirdly, the author was obliged to his diligent master students such as Minglu Wang, Xinlong Zuo, Meng Zhang, Yueyang Wang, Zhengdao Hua, Shengqiu Li, Jiawei Tan, and so forth. Their hard works considerably push forward the research process. Further, the author would like to express their gratefulness to the anonymous reviewers of his published scientific papers whose constructive comments significantly improved the present work.

Fourthly, the author was grateful to four members of thesis examination committee including Professor Katsuyuki Konishi, Professor Yohichi Kohzuki, Professor Yoshio Fukushima, and associate Professor Alan Hase.

Subsequently, this work was supported by the National Natural Science Foundation of China [grant number 51709132], the Natural Science Foundation of Jiangsu Province [grant number BK20150469], and the Jiangsu Provincial Government Scholarship Programme. Also, the author would appreciate the experimental support from Shanghai Engineering Research Center of Hadal Science and Technology, Chinese Ship Scientific Research Center, and Jiangsu Provincial Key Laboratory of Advanced Manufacture and Process for Marine Mechanical Equipment.

Finally, the author would be grateful to his family's firm support, particularly to his kind wife Jie Xia and his lovely son Zijie Zhang.